

NORTHWESTERN UNIVERSITY

Spin Dynamics of Systems with Two or Three Unpaired Spins in Weak or Moderate Exchange

Coupling Regime

A DISSERTATION

SUBMITTED TO THE GRADUATE SCHOOL

IN PARTIAL FULFILLMENT OF THE REQUIREMENTS

for the degree

DOCTOR OF PHILOSOPHY

Field of Chemistry

By

Haochuan Mao

EVANSTON, ILLINOIS

DECEMBER 2022

Abstract

Spin Dynamics of Systems with Two or Three Unpaired Spins in Weak or Moderate Exchange Coupling Regime

Haochuan Mao

This thesis presents results on photophysics and spin dynamics of photoactive organic molecules that possess one unpaired electron spin in the ground state and two or three unpaired spins upon photoexcitation. The excited state dynamics of the systems were studied using transient optical absorption spectroscopies and non-Boltzmann population on the spin sublevels of the long-lived excited states of the systems were further interrogated using time-resolved electron paramagnetic resonance (EPR) spectroscopies and pulsed EPR spectroscopies. Despite the weak or moderate exchange couplings in these multi-spin systems, unique spin dynamics and intense spin polarization were still observed.

The thesis consists of two parts, one concerning the charge transfer and spin dynamics in a covalently linked donor-acceptor-radical system and the second half concerning the excited state dynamics, spin multiplicity and spin polarization in chromophore-radical systems.

In Chapter 2, a donor-acceptor-radical molecule that forms a triradical state upon photoexcitation is investigated. We studied charge transfer dynamics of the system in various dielectric environments and demonstrated the switching between a mono-radical state and a weakly coupled triplet-radical state in low temperature matrices. Chapter 3 and Chapter 4 discusses the spin dynamics of excited triplet states coupled with a radical in systems featuring an organic chromophore that is appended with a stable radical. In Chapter 3, we found that metalation of a porphyrin chromophore increased the exchange coupling between the excited

porphyrin triplet state and 2,2,6,6-tetramethylpiperidinoxyl doublet state, forming excited quartet state that was confirmed by pulsed EPR measurements. Chapter 4 discusses results of spin polarization of α,γ -bis(diphenylene)- β -phenylallyl (BDPA) doublet ground state by photogeneration of a C_{60} triplet state through weak exchange coupling in a series of covalently linked C_{60} -BDPA dyad. Pulse EPR techniques unambiguously measured the spin polarization dynamics and enhancement factors in these systems.

In chapter 5, a donor-acceptor molecule that serves as a candidate for two-qubit operation was investigated. Photoexcitation of the donor generates a long-lived radical pair that has distinct g factors for each radical component. Deuteration of the donor and aligning the molecule in a liquid crystal further simplify the EPR spectrum of the radical pair, allowing for qubit specific operation and detection. Further, single-qubit and two-qubit CNOT gate was performed on this radical pair, demonstrating the feasibility of the complete set of qubit gates for molecular qubit.

Acknowledgements

I would like to begin by thanking my advisor, Professor Michael Wasielewski, for providing me with the opportunity to explore the world of physical organic chemistry in the last five years. I always enjoy perceiving coincidences and their intertwined connections. Somehow, joining the Wasielewski's group seems to have composed of many coincidences, which for example, can be to have decided to initiate a group presentation on Marcus theory in physical chemistry class back in my junior year of college, to have read Dr. Yilei Wu's paper on a triangular molecule in my senior year, to happen to have sit next to Dr. Michelle Chen's friend on a bus during the recruitment weekend and learned that the Wasielewski's group does research on spin chemistry, etc. I am very grateful Mike, to have received mentorship and support of yours in the last five years. Your wealth of knowledge on photochemistry and chemistry in general have led to many exciting projects that I really enjoyed working on. Having conversations with you is a fun experience in many ways and I could not benefit more from various meetings with you.

I would also like to thank my committee members Professor Lin Chen and Professor Franz Geiger for your help and great questions you brought up during my qualifying exam.

I want to acknowledge the work of my collaborators and co-authors: **Chapter 2** – Dr. Ryan Young for transient absorption measurements, Dr. Brandon Rugg and Dr. Jinyuan Zhang for providing precursors and suggestions on organic synthesis and data interpretations, Dr. Matt Krzyaniak for the discussion and training on EPR, Dr. Brian Phelan and Dr. Brandon Rugg for the training on cryostat for optical measurements; **Chapter 3** – Professor Erin Chernick for the opportunity to collaborate on this project, Dr. Norbert Grzegorzec for providing all the samples, Emmaline Lorenzo and Dr. Ryan Young for transient absorption measurements, and Dr. Matt

Krzyaniak for the discussion on EPR; **Chapter 4** and **Chapter 5** – Dr. Ryan Young for transient absorption measurements, and Dr. Matt Krzyaniak for the discussion on EPR.

I have received numerous help from previous and current members of Waz group throughout the five years. Dr. Brandon Rugg, I was very lucky to have you as my mentor in my first two years. Although you complained multiple times how you don't like teaching, your mini lectures or training sessions were always easy to follow, and the questions you prepared always helped me understand the concepts better; I also want to thank Dr. Jiawang Zhou and Dr. Youn Jue (Eunice) Bae for training me on the fluorometer. Dr. Jinyuan Zhang and Dr. Jordan Nelson, thank you for various scientific discussions and useful life hacks that helped me survive my first year in the US. Dr. Jacob Olshansky, although I did not end up being your mentee and doing DNA related research, I did appreciate your group meetings and learned how to better present my research. Dr. Jenna Logsdson and Amanda Mahoney, various events and activities hosted by you really brought the group together and it could have been harder for me to fit in without you two. Dr. Natalia Powers-Riggs, thank you for taking me to those theater events. I am glad that I met a musical and Sondheim's fan in the graduate school. Dr. Michelle Chen and Dr. Yilin Wu, thank you for all the conversations in the A lab and office, I always felt encouraged talking to you after giving group meetings. Dr. Matt Krzyaniak and Dr. Ryan Young, thank you for all the help on TA, EPR and discussions on various projects. I really appreciate your scientific contributions and mentorship. I would also like to thank Dr. Adam Coleman, Chenjian Lin, Fangbai Xie, Dr. Yunfan Qiu and Dr. Jon Schultz for all kinds of conversations that makes the experience more enjoyable.

I would also like to thank my previous roommate Dr. Yuanning Feng for keeping me sane and drunk on numerous Saturday nights and building a social network that include many friends

at the department of chemistry. In addition, thank you Dr. Yue Wu, Dr. Wenjie Zhou, Dr. Xiaoyu Cheng and Dr. Su Chen for all the chatting and advice.

I would also like to thank my girlfriend Keyu Zeng for mutual support in the last five years. We have been through the same process, but yours have been more of a rollercoaster. However, your journey from inorganic chemistry to theoretical physics inspires me to keep learning new things and pursue the research on spectroscopy after my Ph.D.

Finally, I want to thank my parents for their support, inspirations and being great parents. As a spoiled kid, I am always too shy to say such words to my family. But during those sleepless night at grad school, I would occasionally recall the stories of your childhoods, high school, and college years that you would tell tirelessly at family dinners, then realized, that spending five years doing *challenging* research in such comforting and inclusive environments is way easier than walking miles of mountainous and muddy road to schools carrying bags of rice and pickled vegetables, failing college entrance exam and redoing it the next year for three times, being admitted to colleges in Shanghai or Beijing but getting laughed at the accent by surrounding classmates and etc. You both mentioned that what motivated you to go to college was simply to get out of the mountains surrounding you and make more money, which I laughed at as a kid. But at the end of the day, doing research and pursuing a Ph.D. degree is simply another form of *getting out of mountains*, except that getting a Ph.D. degree is something that you two could have achieved if you were born at a different time.

Table of Contents

Abstract.....	3
Acknowledgements	5
Table of Contents	8
List of Figures.....	12
List of Tables	21
Chapter 1 – Introduction	22
1.1 Motivations	23
1.2 Spin-Spin Interactions.....	24
1.3 Strong and weak coupling regime of exchange interactions.....	26
1.4 Optical Spin Polarization in Molecular Qubits	27
1.5 Dissertation Outline	28
Chapter 2 – Controlling the Dynamics of Three Electron Spin Qubits in a Donor-Acceptor-Radical Molecule using Dielectric Environment.....	31
2.1 Introduction.....	32
2.2 Experimental Details.....	33
2.2.1 Design and Synthesis	33
2.2.2 Thermodynamic Driving Forces.....	34
2.2.3 Optical Spectroscopy	35
2.2.4 EPR spectroscopy	35
2.3 Results and Discussion.....	36
2.3.1 Transient Absorption Spectroscopy.....	36
2.3.2 Time Resolved Electron Paramagnetic Spectroscopy	41
2.4 Conclusion	44
2.5 Supplementary Information	44
2.5.1 Synthesis and Characterization.....	44

	9
2.5.2 Steady-State Optical Spectroscopy	48
2.5.3 Electrochemistry and Energetics	48
2.5.4. Transient absorption spectroscopy and kinetics	51
2.5.5. EPR Spectroscopy	60
2.5.6. Computational Data	62
Chapter 3 – Metallated Porphyrin Stable Free Radicals: Exploration of Electron-Spin Communication and Dynamics.....	64
3.1 Introduction	65
3.2 Experimental Details	70
3.2.1 Steady State Absorption Spectroscopy	70
3.2.2 Electron Paramagnetic Resonance Spectroscopy	70
3.2.3 Transient Absorption Spectroscopy	71
3.3 Results and Discussion.....	71
3.3.1 Steady State Continuous Wave EPR Spectroscopy	71
3.3.2 Time Resolved EPR Spectroscopy	72
3.3.3 Pulsed Transient Nutation EPR Spectroscopy.....	74
3.3.4 Transient Absorption Spectroscopy.....	77
3.4 Conclusion	79
3.5 Supplementary Information	80
3.5.1 Synthesis	80
3.5.2 Time-Resolved Continuous-Wave Electron Paramagnetic Resonance (TREPR) Spectroscopy	91
3.5.3 Echo-Detected Transient Nutation Spectra	93
3.5.4 Transient Absorption Spectra	94
3.5.5 Computational Data	97
Chapter 4 – Optical Spin Polarization of a Radical Serving as a Molecular Qubit through Weak Exchange Coupling to Photogenerated Triplet States.....	100

	10
4.1 Introduction.....	101
4.2 Experimental Details.....	103
4.2.1 Steady-State Spectroscopy.....	103
4.2.2 Transient Absorption Spectroscopy.....	103
4.2.3 Continuous-Wave EPR Spectroscopy	103
4.2.4 Pulsed EPR.	104
4.3 Results and Discussion.....	105
4.3.1 Synthesis.....	105
4.3.2 Steady-State Spectroscopy.....	105
4.3.3 Transient Absorption Spectroscopy.....	106
4.3.4 Time-Resolved EPR spectroscopy.	109
4.3.5 Spin Dynamics of Spin Polarized BDPA.	111
4.3.6 Ground State Spin Polarization Enhancement at Room Temperature.....	114
4.4 Conclusion	116
4.5 Supplementary Information	117
4.5.1. Synthesis and Characterization.....	117
4.5.2. Transient Absorption Spectroscopy.....	128
4.5.3 Electron Paramagnetic Resonance (EPR) Spectroscopy	137
4.5.4 Computational Data	141
Chapter 5 – Quantum Gate Operation on a Spectral Addressable Photogenerated Molecular Electron Spin-Qubit Pair	148
5.1 Introduction.....	149
5.2 Experimental Methods	151
5.2.1 Synthesis.....	151
5.2.2 Steady-state optical spectroscopy	152
5.2.3 Steady-state continuous-wave EPR spectroscopy (CW-EPR)	152

	11
5.2.4 Time-resolved EPR (TREPR) spectroscopy.....	152
5.2.5 Pulse-EPR spectroscopy	153
5.3 Results and Discussion.....	153
5.3.1 Steady-state absorption spectroscopy	153
5.3.2 Transient absorption spectroscopy.	154
5.3.3 Steady-state EPR spectroscopy.....	156
5.3.4 TREPR spectroscopy	156
5.3.5 EPR spectral readout with nonselective pulses	158
5.3.6 Single-qubit operation	160
5.3.7 The three-pulse CNOT gate.....	162
5.4 Conclusions	165
5.5 Supplementary Information	165
5.5.1. Synthesis and Characterization.....	165
5.5.2. Transient Absorption Spectroscopy.....	172
5.5.3. Electron Paramagnetic Spectroscopy	176
Reference	180
Curriculum Vitae.....	200

List of Figures

- Figure 1.1. Matrix representation of the Hamiltonian in equation 1. The colored blocks represent non-zero matrix elements..... 25
- Figure 1.2. Simulated X-band EPR spectra of two electron spin with different exchange couplings..... 26
- Figure 2.1. Kinetic pathways and energies for the relevant states of 1 in (a) 9/2 v/v PrCN/EtCN at 140 K and in (b) PrCN at 105 K. 37
- Figure 2.2. FsTA (a) and nsTA (b) transient absorption spectra of 1 in 9/2 PrCN/EtCN at 140 K following $\lambda_{\text{ex}} = 450$ nm excitation. 37
- Figure 2.3. FsTA (a) and nsTA (b) transient absorption spectra of 1 in a PrCN glass at 105 K following $\lambda_{\text{ex}} = 450$ nm excitation. 39
- Figure 2.4. TREPR spectrum of 1 at X-band in PrCN glass at 105 K, 100 ns after a 7 ns, 450 nm laser pulse. Simulation is shown in red..... 41
- Figure 2.5 Schematic for EPR transitions in all three canonical orientations with $m_s = \pm 1/2$ sublevels overpopulated. Grey circles represent the population differences of spin sublevels relative to the least populated sublevel, downward arrows represent emissive transitions, and upward arrows represent absorptive transitions..... 43
- Figure 2.6. UV-Vis absorption spectra recorder using a Shimadzu 1800 spectrophotometer. Spectra of 1 and its non-radical precursor 1H in toluene at 295 K..... 48
- Figure 2.7. Cyclic (a) and differential-pulse (b) voltammetry of 1 in CH₃CN (0.1 M tetrabutylammonium hexafluorophosphate). Results are reported vs. SCE. 49
- Figure 2.8. FsTA (a) and nsTA (b) species-associated spectra of 1 in a 9/2 PrCN/EtCN at 140 K following $\lambda_{\text{ex}} = 450$ nm excitation. c) and d) Comparison of the kinetic traces to the fit at selected probe wavelengths for the fsTA and nsTA data, respectively. The resulting from the global fitting of the data to a model that includes spin-selectivity and an $A \rightarrow B \rightarrow G$ model. 53

Figure 2.9. FsTA (a) and nsTA (b) species-associated spectra of 1 in a PrCN at 105 K following $\lambda_{\text{ex}}= 450$ nm excitation. The resulting from the global fitting of the data to a model that includes spin-selectivity and an $A \rightarrow B \rightarrow C \rightarrow \text{GS}$ model. c) and d) Comparison of the kinetic traces to the fit at selected probe wavelengths for the fsTA and nsTA data, respectively..... 54

Figure 2.10. Transient absorption spectra of 1H. a) fsTA data of 1H at 140K in PrCN/EtCN 9:2 solution b) Comparison of the kinetic traces to the fit at selected probe wavelengths c) species-associated spectrum resulting from the global fitting of the data to an $A \rightarrow B \rightarrow \text{GS}$ model..... 55

Figure 2.11. Transient absorption spectra of 1H. a) fsTA data of 1H at 105 K in PrCN. b) Comparison of the kinetic traces to the fit at selected probe wavelengths c) species-associated spectrum resulting from the global fitting of the data to an $A \rightarrow B \rightarrow \text{GS}$ model. 56

Figure 2.12. Transient absorption spectra of 1H. a) nsTA data of 1H at 105K in PrCN. b) Comparison of the kinetic traces to the fit at selected probe wavelengths c) decay-associated spectrum resulting from the global fitting of the data to two exponential decays. 57

Figure 2.13. (a) FsTA spectra of 1 in toluene at 295 K following $\lambda_{\text{ex}}= 450$ nm excitation. (b) Species-associated spectra for the data in (a) resulting from the global fitting of the data to a model that includes spin-selectivity and an A G model. (c) and (d) The corresponding nsTA data and species-associated spectra, respectively..... 58

Figure 2.14. (a) FsTA spectra of 1H in toluene at 295 K following $\lambda_{\text{ex}}= 450$ nm excitation. (b) Species-associated spectra for the data in (a) resulting from the global fitting of the data to a $A \rightarrow B \rightarrow \text{G}$ model. (c) Kinetic fits at selected wavelengths..... 59

Figure 2.15. (a) NsTA spectra of 1H in toluene at 295 K following $\lambda_{\text{ex}}= 450$ nm excitation. (b) Species-associated spectra for the data in (a) resulting from the global fitting of the data to a $A \rightarrow B \rightarrow \text{G}$ model. (c) Kinetic fits at selected wavelengths. 60

Figure 2.16. TREPR spectrum of 1 at X-band in PrCN at 105 K, 100 ns after a 7 ns, 450 nm laser pulse. Simulation is shown in red..... 61

Figure 2.17. TREPR spectra obtained using direct detection at 85 K in mTHF for PXX (~100 μM) after a 7 ns laser pulse, with the fit to a standard spin-orbit intersystem crossing model shown in red..... 61

Figure 3.1. Synthetic route of 3 and 3(Zn) used in this study.....	68
Figure 3.2. Synthetic route of 3(Cu) and 3(Ni). used in this study.....	69
Figure 3.3. Steady-state CW EPR of (a) 3 (b) 3(Zn) (c) 3(Ni) (d) 3(Cu) in mTHF at X-Band (9.5 GHz), obtained at 85K with 0.1 mT modulation amplitude.	72
Figure 3.4. TREPR spectra in frozen mTHF at 85 K, at 40 ns following a 7 ns laser pulse, for: (a) 2 and 3; (b) 2(Zn) and 3(Zn).	74
Figure 3.5. Echo-detected transient nutation spectra collected at 85K in mTHF for (a) 3, (b) 3(Zn) following the 510 nm and 550 nm, 7 ns, 2.5 mJ laser pulse, respectively. Peak positions are marked with dashed lines.	76
Figure 3.6. Transient absorption spectra and species-associated spectra of 3 and 3(Zn). (a) Transient absorption spectra of 3 and 3(Zn) in 2-methyl THF at 85 K following $\lambda_{\text{ex}} = 550$ nm and $\lambda_{\text{ex}} = 510$ nm respectively. (b) Species-associated spectra of 3 and 3(Zn) resulting from the global fitting of the data to an $A \rightarrow B$ model.	78
Figure 3.7. TREPR spectra obtained using direct detection at 85K in mTHF for (a) 2, (b) 2(Zn) after a 7 ns laser pulse, with the fit to ISC-Triplet models.	91
Figure 3.8. TREPR spectra obtained using direct detection at 85K in mTHF for (a) 3, (b) 3(Zn) after a 7 ns laser pulse.	92
Figure 3.9. Echo-detected transient nutation spectra collected at 85K in mTHF for (Top) 3(Zn), (Bottom) 3 following the 510 nm and 550 nm, 7 ns, 2.5 mJ laser pulse, respectively. Peak positions are marked with dashed lines.	93
Figure 3.10. Transient absorption spectra, species-associated spectra and the global fitting of 3 and 3(Zn). (a) Transient absorption spectra of 3 and 3(Zn) in 2-methyl THF at 85 K following $\lambda_{\text{ex}} = 550$ nm and $\lambda_{\text{ex}} = 510$ nm respectively. (b) Species-associated spectra of 3 and 3(Zn) resulting from the global fitting of the data to an $A \rightarrow B$ model. (c) Population curves and the fitting for 3 and 3(Zn) yielded from singular value decomposition to an $A \rightarrow B$ model.....	94

Figure 3.11. Transient absorption spectra, species-associated spectra and the global fitting of 2 and 2(Zn). (a) Transient absorption spectra of 2 and 2(Zn) in 2-methyl THF at 85 K following $\lambda_{\text{ex}} = 550$ nm and $\lambda_{\text{ex}} = 510$ nm respectively. (b) Species-associated spectra of 2 and 2(Zn) resulting from the global fitting of the data to an $A \rightarrow B$ model. (c) Population curves and the fitting for 2 and 2(Zn) yielded from singular value decomposition to an $A \rightarrow B$ model..... 95

Figure 3.12. Femtosecond transient absorption spectra, species-associated spectra and the global fitting of 3(Cu) and 3(Ni). (a) Femtosecond transient absorption spectra of 3(Cu) and 3(Ni) in 2-methyl THF at 85 K following $\lambda_{\text{ex}} = 550$ nm and $\lambda_{\text{ex}} = 525$ nm respectively. (b) Species-associated spectra of 3(Cu) and 3(Ni) resulting from global fitting of the data to an $A \rightarrow B \rightarrow C \rightarrow \text{GS}$ model. (c) Time traces at specified wavelengths for 3(Cu) and 3(Ni) and the global fitting to an $A \rightarrow B \rightarrow C \rightarrow \text{GS}$ model. 96

Figure 3.13. Nanosecond transient absorption spectra, species-associated spectra and the global fitting of 3(Ni). (a) Nanosecond transient absorption spectra of 3(Ni) in 2-methyl THF at 85 K following $\lambda_{\text{ex}} = 550$ nm. (b) Species-associated spectra of 3(Ni) resulting from global fitting of the data to an $A \rightarrow \text{GS}$ model. (c) Time traces at specified wavelengths for 3(Ni) and the global fitting to an $A \rightarrow \text{GS}$ model..... 97

Figure 4.1. Structural formulas of the compounds 1 (C_{60} -BDPA), 2 (C_{60} -ph-BDPA), 3 (m- C_{60} -BDPA) and 4 (m- C_{60} -ph-BDPA)..... 105

Figure 4.2. UV-vis spectra of compound 1-4 in toluene solution at room 106

Figure 4.3. Transient absorption spectra of 1 (a), 2 (b), 3(c) and 4(d) in toluene at 298 K following $\lambda_{\text{ex}} = 450$ nm excitation. 107

Figure 4.4. (a) TREPR spectrum of 1, 2, 3 and 4 at X-band in toluene solution at 298 K, 100 ns after a 7 ns, 450 nm laser pulse. b) Energy level diagrams of triplet-radical pair in the weak exchange coupling regime with $J > 0$ (left) or $J < 0$ (right). The arrows indicate possible flip-flop transitions in the excited states and the ISC from the excited states to the ground states. The blue and red circles indicate the initial and final populations respectively. 110

Figure 4.5. Spin dynamics of ground state polarization of BDPA probed by the pulse sequence shown at the top. 113

Figure 4.6. Spin echo of 1, 3 and 4 detected at 341.7 mT using the pulse sequence shown at the top with $T_{\text{daf}} \sim 8 \mu\text{s}$. The signal was normalized to the spin echo without laser pulse i.e., at thermal equilibrium..... 115

Figure 4.7. Temperature dependence of SP of a ground-state spin doublet in the presence of 0.34 T external field at thermal equilibrium (black curve). The dotted line marked the ground-state SP and the corresponding effective temperature of BDPA in 1 (red), 3 (blue) and 4 (purple) $8 \mu\text{s}$ after the photoexcitation. 116

Figure 4.8. Transient absorption spectra of 1. a) FsTA data of 1 at 298 K in toluene solution following $\lambda_{\text{ex}} = 450 \text{ nm}$ excitation. b) Evolution-associated spectra (EAS) of 1. c) Comparison of the kinetic traces to the fit at selected probe wavelengths. d) Population models for the species in the EAS. 129

Figure 4.9. Transient absorption spectra of 2. a) FsTA data of 2 at 298 K in toluene solution following $\lambda_{\text{ex}} = 450 \text{ nm}$ excitation. b) Evolution-associated spectra (EAS) of 2. c) Comparison of the kinetic traces to the fit at selected probe wavelengths. d) Population models for the species in the EAS. 130

Figure 4.10. Transient absorption spectra of 3. a) FsTA data of 3 at 298 K in toluene solution following $\lambda_{\text{ex}} = 450 \text{ nm}$ excitation. b) Evolution-associated spectra (EAS) of 3. c) Comparison of the kinetic traces to the fit at selected probe wavelengths. d) Population models for the species in the EAS. 131

Figure 4.11. Transient absorption spectra of 4. a) FsTA data of 4 at 298 K in toluene solution following $\lambda_{\text{ex}} = 450 \text{ nm}$ excitation. b) Evolution-associated spectra (EAS) of 4. c) Comparison of the kinetic traces to the fit at selected probe wavelengths. d) Population models for the species in the EAS. 132

Figure 4.12. Transient absorption spectra of 1. a) NsTA data of 1 at 298 K in toluene solution following $\lambda_{\text{ex}} = 450 \text{ nm}$ excitation. b) Species-associated spectra (SAS) of 1. c) Comparison of the kinetic traces to the fit at selected probe wavelengths. d) Population models for the species in the SAS. 133

Figure 4.13. Transient absorption spectra of 2. a) NsTA data of 2 at 298 K in toluene solution following $\lambda_{\text{ex}} = 450 \text{ nm}$ excitation. b) Species-associated spectra (SAS) of 2. c) Comparison of the kinetic traces to the fit at selected probe wavelengths. d) Population models for the species in the SAS. 134

Figure 4.14. Transient absorption spectra of 3. a) NsTA data of 3 at 298 K in toluene solution following $\lambda_{\text{ex}} = 450$ nm excitation. b) Species-associated spectra (SAS) of 3. c) Comparison of the kinetic traces to the fit at selected probe wavelengths. d) Population models for the species in the SAS. 135

Figure 4.15. Transient absorption spectra of 4. a) NsTA data of 4 at 298 K in toluene solution following $\lambda_{\text{ex}} = 450$ nm excitation. b) Species-associated spectra (SAS) of 4. c) Comparison of the kinetic traces to the fit at selected probe wavelengths. d) Population models for the species in the SAS. 136

Figure 4.16. Time-Resolved EPR of 1 (a), 3 (b) and 4 (c) in toluene at room temperature. 137

Figure 4.17. Transient nutation of 1 (a), 3 (b) and 4 (c) with (red) and without (black) light excitation ($T_{\text{daf}} = 1\mu\text{s}$) 138

Figure 4.18. T_2 relaxation measurement of the steady state BDPA in 1 (a), 3 (b) and 4 (c) using the pulse sequence $\pi/2-\tau-\pi-\tau$ -echo, where $\tau = 160$ ns and π pulse is 32 ns..... 139

Figure 4.19. Exchange coupling dependence of energies of spin sublevels of a radical-triplet pair system (top) and the doublet (quartet) character in percentage of the $T_0\beta$ and $T_0\alpha$ levels (bottom) 140

Figure 4.20. Optimized structure for 1 (a), 2 (b), 3 (c) and 4 (d) with B3LYP/6-31G* level of theory 141

Figure 5.1. Structures of the compounds used in this study. 151

Figure 5.2. UV-vis spectra of 1 and 1-d9 1d9 in toluene solution at 295 K..... 153

Figure 5.3. Transient absorption spectra of 1. a) fsTA data of 1 at 85 K in mTHF solution following $\lambda_{\text{ex}} = 450$ nm excitation. b) Species-associated spectra (SAS) of 1. c) Comparison of the kinetic traces to the fit at selected probe wavelengths. 154

Figure 5.4. CW-EPR spectra of PXX radical cation and PXX-d10 radical cation in dichloromethane solution at 295 K. The spectral fitting of PXX radical cation is shown in red. 156

Figure 5.5. (a) TREPR spectra and spectral simulation of **1** in mTHF solution (top), 1-d91d9 in mTHF solution (middle) and 1-d91d9 in 5CB aligned along the magnetic field at 85 K, 200 ns after a 7 ns, 450 nm laser pulse. The vertical lines connected to the dots show the transitions of RPs whose principal axes, x, y or z, are parallel to the magnetic field, where z is defined as the direction that connects the two spins, and x and y are perpendicular to z (b) Schematics of RPs randomly orient in the solution with one of the electron spins in the RP coupled to multiple protons (top), randomly oriented RPs with one of the electron spins in the RP coupled to multiple deuterons (middle), and deuterated RPs z-axis is aligned along the magnetic field direction (bottom)..... 157

Figure 5.6. Pulse sequence used to measure the EPR spectrum of the SQP produced by photoexcitation of 1-d9. (b) Spin echo of the RP showing FID-like behavior due to the broadband microwave excitation. Both in-phase and quadrature part of the signal was collected. (c) Frequency domain of the spin echo producing the entire RP spectrum. 159

Figure 5.7. (a) Pulse sequence of single-qubit nutation. (b) Frequency spectra after a single-qubit nutation pulse on C60•-. (c) Frequency space simulation on the effect of single-qubit pulse with varying turning angles. (d) and (f) Experimental spectra slices at the dashed line in (b). (e) and (f) Spin level diagrams and level populations of the RP with and without a π pulse respectively. 161

Figure 5.8. (a) Pulse sequence for CNOT gate and detection. Frequency spectra after the three-pulse CNOT gate operation with incremental L is plotted in (b) and (c) using C60•- or PXX•+-d9 as the control qubit respectively. The slice marked by the dashed line in (b) and (c) are shown in (d) and (e) respectively and simulation is shown in red. 164

Figure 5.9. Transient absorption spectra of **1**. a) nsTA data of **1** at 85 K in mTHF solution following $\lambda_{ex} = 414$ nm excitation. b) Decay-associated spectra (DAS) of **1**. c) Comparison of the kinetic traces to the fit at selected probe wavelengths. 173

Figure 5.10 Transient absorption spectra of **1**. a) fsTA data of **1** at 294 K in toluene solution following $\lambda_{ex} = 414$ nm excitation. b) Species-associated spectra (SAS) of **1**. c) Comparison of the kinetic traces to the fit at selected probe wavelengths. 174

Figure 5.11. Transient absorption spectra of **1**. a) nsTA data of **1** at 294 K in toluene solution following $\lambda_{ex} = 414$ nm excitation. b) Decay-associated spectra (DAS) of **1**. c) Comparison of the kinetic traces to the fit at selected probe wavelengths. 175

Figure 5.12. CW-EPR of PXX•+ and PXX•+-d10 in dichloromethane solution at 294 K and the structure formula of PXX showing five chemically inequivalent protons. 176

Figure 5.13. (a) Echo detected field sweep of 1-d9 in 5CB aligned along the magnetic field. 20 ns Gaussian-shaped $\pi/2$ and π pulse are used in the experiment. Fourier transform of the echo at each field position gives the corresponding frequency spectra and were plot against the magnetic field. The features with frequencies lager than 20 MHz or lower than -20 MHz belong to 3^*C60 . (b) Frequency spectra of 1-d9 1d9 at the field position indicated by the dashed line in (a) showing the complete EPR spectrum of the RP. The shaded area shows the bandwidths of Gaussian-shaped microwave pulses, indicating the feasibility of selective and non-selective excitation..... 176

Figure 5.14. Resonator profile characterized by a three-pulse nutation experiment at various frequency. The nutation frequencies versus microwave frequencies plot isare fitted with a resonator model to give the center frequency F0 and the quality factor Q..... 177

Figure 5.15. Out-of-phase ESEEM measurement on 1-d9 at 85 K in 5CB liquid crystal that is (a) aligned along the magnetic field, or (b) aligned perpendicular to the field..... 178

Figure 5.16. (a) Single-qubit gate operation using a three-pulse nutation pulse sequence with a selective nutation pulse that excites PXX•+and a non-selective Hahn echo sequence that detects the entire EPR spectrum. (b) Frequency domain simulation of the experiment..... 179

Scheme 2.1. Structure of 1H (PXX-PI-BDPAH) and 1 (PXX-PI-BDPA) 34

Scheme 2.2. Synthetic scheme for 1H (PXX-PI-BDPAH)..... 44

Scheme 4.1. Synthetic Scheme of 1H..... 118

Scheme 4.2. Synthetic Scheme of 2H..... 119

Scheme 4.3. Synthetic Scheme of 3H..... 120

Scheme 4.4. Synthetic Scheme of 4H..... 121

Scheme 5.1. Synthesis route of 1.....	166
Scheme 5.2. Synthesis route of PXX-d10.....	167

List of Tables

Table 2.1. Free energies of reaction for various charge transfer reactions in different solvents ..	50
Table 2.2. Triplet fit parameters	62
Table 2.3. Coupled triplet-doublet pair fit parameters.....	62
Table 3.1. Singlet lifetimes ($\tau = 1/k$) for 2, 2(Zn), 3 and 3(Zn) and increasement of rates for 3 and 3(Zn)	79
Table 4.1. Transient Absorption Species Associated Kinetics for 1-4 in toluene at 298 K.....	108
Table 4.2. Polarization Kinetics and Spin-Lattice Relaxation for 1,3 and 4 in toluene at 298 K	112
Table 4.3. C ₆₀ to BDPA distance measured from the center of C ₆₀ to α -carbon of BDPA	141
Table 5.1. Proton Hyperfine Couplings Extracted From CW-EPR Spectrum of PXX Radical Cation.....	176

Chapter 1 – Introduction

1.1 Motivations

Quantum information science (QIS) is drawing increasing attention for its potential to provide new computation, communication and sensing technologies.¹⁻³ Efforts are accelerating to identify and characterize new molecular systems to serve as qubits in these applications.^{4,5} Taking advantage of synthetic tunability^{6,7} and ease of spin state readout using microwave pulses,⁸⁻¹⁰ electron spins in molecular systems have motivated chemists to achieve advances in extending coherence lifetimes¹¹⁻¹³ and scaling up the number of qubits.¹⁴⁻¹⁷ These molecular systems employ multiple electron spin qubits comprising interacting organic radicals^{8,9,18-21} and/or metal complexes^{11,16,22-25} but are usually limited to thermally polarized electron spins²⁶ with well-defined initial spin states only available at high magnetic fields and temperatures <3 K.¹⁸

This thesis broadly concerns with qubit-qubit interactions in a certain regime of interaction strength and their outcomes as a function of molecular structures and other external stimuli such as dielectric constants of solvent molecules that are interacting with molecular qubits. Spin-bearing organic molecules, known as radicals, that are a kind of open-shell species, are suitable candidates for the study, for the ease of synthetic tunability and lack of spin-orbit couplings, which would otherwise reduce the spin coherence time, a key parameter that concerns QIS applications. Despite the rarity of stable organic radicals that suitable for such study, open-shelled species with long lifetimes can be readily generated through photoexcitation. Moreover, photoexcitation oftentimes generates open-shell species with spin multiplicities that are larger than two, and more than one radical can form in the process in certain molecules. Therefore, light absorbing molecules with careful design are perfect candidates for the study of qubit-qubit interactions. Moreover, by means of electron paramagnetic resonance (EPR), coherent control of electron spin states can be realized,

paving road for QIS application such as quantum sensing and quantum computing.

1.2 Spin-Spin Interactions

The electron has a characteristic magnetic moment given by $\mu_s = g\beta_e S$, where g is a dimensionless constant that relates the magnetic moment to the spin angular momentum S through units defined by the Bohr magneton, β_e (which itself is given by $\beta_e = e\hbar/2mec$). For a free electron the so-called g -factor is approximately 2. When an electron is in a magnetic field, the magnetic moment of the electron tends to align with the field. Quantum mechanically, the external magnetic field lifts the energy degeneracy of electron spins and the energies of the two states are described by the Hamiltonian in the following.

$$\mathcal{H}_z = g\beta_e BS \quad (1)$$

Where, B is the strength of magnetic field and S is the spin operator. When two electron spins are close to each other, spin-spin interactions will be considered. In general, two types of spin-spin interactions are concerned in systems composed of organic radicals. Namely, exchange couplings and dipolar couplings. The exchange coupling between two electron spins arises from the different spatial distributions of electron density, which imposes an energy gap between a singlet and a triplet state. The exchange coupling is isotropic in nature, it is often referred to as scalar coupling due to the form of its Hamiltonian.

$$\mathcal{H}_{ex} = JS_1S_2 \quad (2)$$

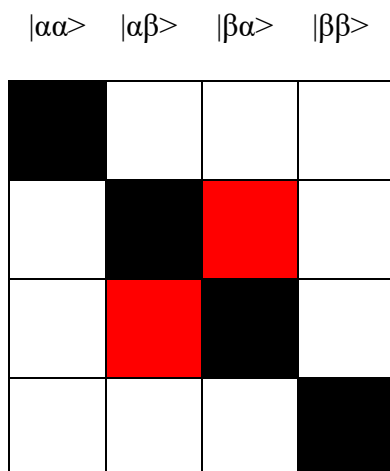


Figure 1.1. Matrix representation of the Hamiltonian in equation 1. The colored blocks represent non-zero matrix elements.

The matrix representation of this Hamiltonian in uncoupled basis (**Figure 1.1**) indicates the mixing between $|\alpha\beta\rangle$ and $|\beta\alpha\rangle$ in two of the eigenstates due to the presence of off-diagonal elements. Diagonalizing the matrix results in three eigenstates with the same energy and total spin quantum number of one, and the other eigenstate with a different energy and total spin quantum number of zero.

The dipolar couplings, as the name suggests, originate from the interactions of two magnetic dipole moments, which lift the degeneracy of the triplet states. Due to the delocalized nature of electrons in molecules, the net effect of the dipolar coupling between two electron spins is the weighted average of all possible distances between the two spins and takes the form of the following Hamiltonian:

$$\mathcal{H}_{ZFS} = \mathbf{S}_1 \mathbf{D} \mathbf{S}_2 \quad (3)$$

Where \mathbf{D} is called zero-field splitting (ZFS) tensor as the net effect of this tensor is to lift the

degeneracy of the triplet states in the absence of external magnetic field.

1.3 Strong and weak coupling regime of exchange interactions

When two electron spins that are exchange coupled to each other are present in an external magnetic field. The magnitude of the exchange coupling poses the system to either strong coupling regime if the exchange coupling is much larger than the difference of Zeeman energies of the two spins, or weak coupling regime if the exchange coupling is much smaller than the difference of Zeeman energies. Distinct EPR spectra and state mixing behavior are observed in these two regimes. **Figure 1.2** shows the simulated EPR spectra of two electron spins with g factor of 2.002 and 2.004 respectively at X-band.

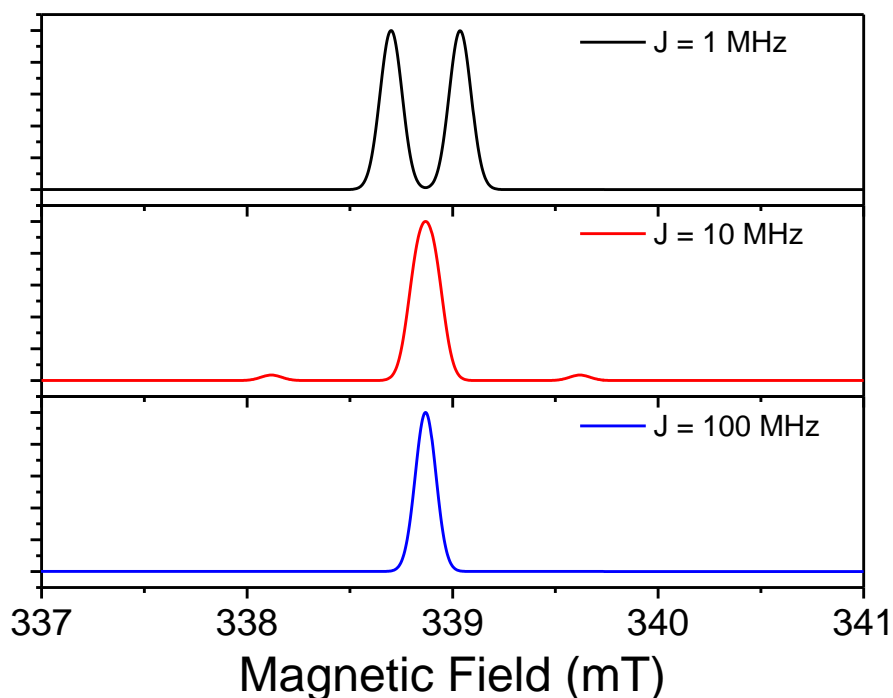


Figure 1.2. Simulated X-band EPR spectra of two electron spin with different exchange couplings

When J is negligible, the EPR spectrum of the two spin - $1/2$ radicals shows two absorption peaks

at their resonant fields that are dictated by their g values. As the exchange coupling increases, the two peaks merge while two extra satellite peaks appear. This is because the increase in exchange coupling further mix the $|\alpha\beta\rangle$ and $|\beta\alpha\rangle$ states, increasing the singlet or triplet character of the resulting eigenstates. The satellite peaks arise from the transition from the state with more singlet character to the upper T_+ and lower T_- states, with lower transition probability. In the strong coupling regime, the system becomes a pure triplet and the transition between the singlet state to T_+ and T_- states are formally forbidden. Due to the isotropic nature of the exchange coupling, the transition from T_0 to T_+ and T_0 to T_- share the same resonant field, while triplet radicals often have non-zero ZFS and shows more structure than a Lorentzian peak in solid state samples.

1.4 Optical Spin Polarization in Molecular Qubits

Molecular qubits are usually limited to thermally polarized electron spins whose initial states are ill-defined at room temperature due to the thermal fluctuations.²⁶ Thus, high magnetic field and millikelvin temperatures are often required to initialize the qubits.¹⁸ The challenge of achieving well-defined qubit state can be overcome by optical spin polarization, a strategy commonly used in qubit platforms that are based on defect centers in solid-state material such as nitrogen-vacancy (NV) center, where optical pumping of the ground state and spin-selective excited states relaxations allow for population buildup at one specific spin state to realize qubit initialization, or spin polarized initial state.²⁷⁻²⁹

Photochemical processes in molecular qubit systems are also spin-selective^{19, 30} and have shown promise to create well-defined initial qubit states. For instance, sub-nanosecond photo-induced electron transfer in donor-acceptor molecules generates entangled spin (qubit) pair with pure initial quantum state.^{20, 31-33} Resonant excitation of pseudo-tetragonal chromium (Cr^{4+})

complexes to their singlet excited states have also been shown to selectively relax back to $m_s = \pm 1$ ground state sublevels to create spin polarization (SP).^{34, 35}

Moreover, it has been demonstrated that chromophores appended with radicals can initialize the ground state doublet of the radicals through the exchange interactions between the chromophore triplet excited states and the radicals.³⁶⁻⁴¹ The initialized or, spin polarized ground state doublet was proposed to be a result of the reverse quartet mechanism³⁶ in most of the strongly coupled chromophore-radical systems, in which the exchange coupling (J) is much larger than the Zeeman splitting, yielding well-defined excited doublet and quartet states that are separated by $|3J|$.⁴² However, such chromophore-radical systems in the weak-coupling regime remain unexplored.^{43, 44} In this regime, the excited triplet states of the chromophore have vanishing orbital overlap with the singly occupied molecular orbital (SOMO) of the radical either due to relative long distance or orbital symmetry mismatch, resulting in exchange coupling magnitudes much smaller than the Zeeman splitting. Whether such weak exchange coupling in a chromophore-radical system can effectively create a spin-polarized ground-state doublet and the associated mechanism of SP in this regime both remain less explored.

1.5 Dissertation Outline

The following chapters will discuss SP phenomena, spin selectivity and dynamics in systems composed of two or three electron spins under moderate or weak exchange coupling regime.

Chapter 2 discusses the spin-dependent dynamics of a covalent donor-acceptor-radical molecule, D-A-R*, where the donor chromophore (D) is *peri*-xanthenoxanthene (PXX), the acceptor (A) is pyromellitimide (PI) and the radical (R*) is α,γ -bis(diphenylene)- β -phenylallyl

(BDPA). Selective photoexcitation of D within D-A-R* in butyronitrile/propionitrile at 140 K and butyronitrile at 105 K results in the spin-selective reactions $D-A-R^* \rightarrow D^{*+}-^1(A^{\cdot-}-R^{\cdot})$ and $D^{*+}-^3(A^{\cdot-}-R^{\cdot})$. Subsequently, at 140 K, $D^{*+}-^1(A^{\cdot-}-R^{\cdot}) \rightarrow D^{*+}-A-R^{\cdot}$, whereas $D^{*+}-^3(A^{\cdot-}-R^{\cdot}) \rightarrow D-A-R^{\cdot}$. In contrast, at 105 K, $D^{*+}-^3(A^{\cdot-}-R^{\cdot}) \rightarrow {}^3D-A-R^{\cdot}$ and $D-A-R^{\cdot}$. Time-resolved EPR spectroscopy shows that ${}^3D-A-R^{\cdot}$ is highly spin-polarized, where the $m_s = \pm 1/2$ spin sublevels of the doublet-quartet manifolds are selectively populated. The results from this chapter demonstrate dielectric environment control over different spin states in the same molecule.

We expand what is learned in Chapter 2 and examine the spin dynamics of weakly coupled triplet-doublet systems in covalently linked chromophore-radical molecules in the following chapters. In Chapter 3, a series of mesosubstituted porphyrins with a (2,2,6,6-tetramethylpiperidin-1-yl)oxyl stable free radical (SFR) appended and metalated with Cu(II), Ni(II), and Zn(II) are investigated in order to explore the interaction between the SFR doublet state and metalloporphyrin. The spin state of the porphyrin varies upon metal insertion, where Zn(II) is a diamagnetic metal, Cu(II) is paramagnetic, and Ni(II) can be switched from a diamagnetic square-planar structure to a paramagnetic octahedral state by complexation with a solvent (i.e., pyridine or tetrahydrofuran). Time-resolved electron paramagnetic resonance (TREPR) measurements reveal that upon photoexcitation, the Zn(II) and free-base porphyrin species demonstrate different magnetic exchange regimes between the porphyrin triplet excited states and the SFR doublet state, with the Zn derivative populating a quartet state (i.e., moderate magnetic exchange), whereas the free-base derivative remains a triplet (i.e., weak magnetic exchange). Transient absorption measurements corroborate the TREPR results, demonstrating a 66% increase in the singlet excited-state decay rate due to enhanced intersystem crossing for the Zn(II) derivative in comparison to a modest 14%

enhancement for the free-base porphyrin. These results enable the realization of a switchable qubit coupler, depending upon Zn metal insertion to the free-base porphyrin, which has potential QIS applications.

In Chapter 4, a series of C₆₀ fullerene derivatives containing BDPA radical are synthesized. Selective photoexcitation of C₆₀ results in over ten-fold spin polarization (SP) of BDPA that is observed by pulsed EPR spectroscopy at room temperature. Opposite SP patterns are observed for molecules with different bridges between C₆₀ and BDPA. Transient absorption spectroscopy and other pulsed EPR measurements further reveal that SP of BDPA comes from SP transfer of excited C₆₀ triplet states through weak exchange couplings over a 1 nm distance.

Chapter 2 – Controlling the Dynamics of Three Electron Spin Qubits in a Donor-Acceptor-Radical Molecule using Dielectric Environment

Adapted from: Haochuan Mao, Ryan M. Young, Matthew D. Krzyaniak, and Michael R. Wasielewski* *J. Phys. Chem. Lett.* **2021**, *12* (9), 2213–2218.

(* Corresponding Author). Copyright 2021 American Chemical Society.

2.1 Introduction

Quantum information science (QIS) is drawing increasing attention for its potential to provide new computation, communication and sensing technologies.¹⁻³ Efforts are accelerating to identify and characterize new molecular systems to serve as qubits in these applications.^{4,5} Taking advantage of synthetic tunability^{6,7} and ease of spin state readout using microwave pulses,⁸⁻¹⁰ electron spins in molecular systems have motivated chemists to achieve advances in extending coherence lifetimes¹¹⁻¹³ and scaling up the number of qubits.¹⁴⁻¹⁷ These molecular systems employ multiple electron spin qubits comprising interacting organic radicals^{8,9,18-21} and/or metal complexes^{11,16,22-25} but are usually limited to thermally polarized electron spins²⁶ with well-defined initial spin states only available at high magnetic fields and temperatures <3 K.¹⁸

Sub-nanosecond photo-driven electron transfer from a molecular donor to an acceptor has been shown to generate a radical pair having two entangled electron spins that can serve as a spin qubit pair (SQP) in a well-defined pure initial singlet quantum state^{31,32} even at room temperature.³³ Together with pulse electron paramagnetic resonance (pulse-EPR) techniques, we have shown that photo-generated SQPs can mediate quantum state teleportation,¹⁹ implement a CNOT gate,²⁰ and transfer polarization to a third spin.⁴⁵⁻⁴⁸ Moreover, qubit-specific addressability can be achieved in an SQP system using electronic g -factor engineering.^{18,21,23}

While multiple potential QIS applications are possible using such systems, different molecular designs are often required for each different application, which often entails complex chemical synthesis. However, since the SQP created using a photoinduced charge transfer (CT) reaction is a radical ion pair, the kinetic competition between SQP recombination and subsequent

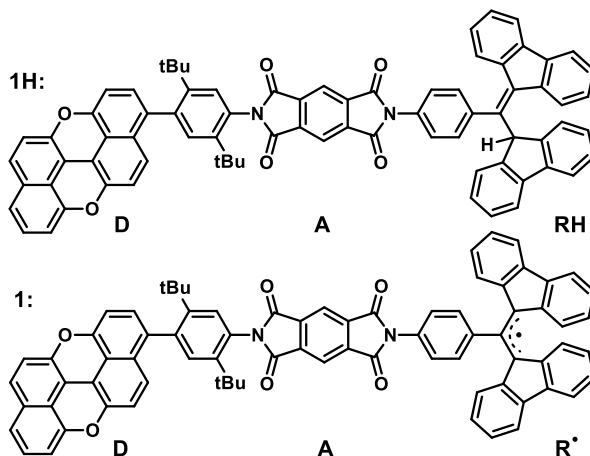
CT from the SQP to another molecule can be controlled by changing the dielectric environment of the medium surrounding the SQP.⁴⁹⁻⁵¹

In this work, we demonstrate different spin-dependent CT dynamics in a covalent electron donor-acceptor-radical molecular triad (D-A-R', **1**, Scheme 2.1) by tuning the dielectric environment, where the donor chromophore (D) is *peri*-xanthenoxanthene (PXX), the acceptor (A) is pyromellitimide (PI) and the radical (R') is α,γ -bisdiphenylene- β -phenylallyl (BDPA). PXX, PI, and BDPA were chosen because their redox potentials provide sufficient free energy of reaction⁵¹ to carry out parallel spin-dependent charge transfer processes.

2.2 Experimental Details

2.2.1 Design and Synthesis

The donor (PXX), acceptor (PI), and the radical (BDPA) were chosen such that their redox potentials provide sufficient driving force for the desired two-step electron transfer according to the Weller equation⁵¹ (see Table 2.1, page 50). The final compound **1** was attained by quantitative oxidation of **1H** which was synthesized through the imide condensation of a BDPAH-PI monoanhydride onto a PXX functionalized with 2,5-diterbutylaniline.



Scheme 2.1. Structure of **1H** (PXX-PI-BDPAH) and **1** (PXX-PI-BDPA)

2.2.2 Thermodynamic Driving Forces

The driving forces for electron transfer reactions in different solvent environments can be estimated using Weller equation, which calculates the Gibbs free energy change for ion pair (IP) states with the solvent correction accounting for different solvent environments.

$$\Delta G_{IP} = [E^{red}(D^+/D) - E^{red}(A/A^-)] + \Delta G_{Sol} \quad (1)$$

$$\Delta G_{Sol} = -\frac{e^2}{4\pi\epsilon_0} \left[\frac{1}{\epsilon_s} \cdot \frac{1}{R_{DA}} + \left(\frac{1}{\epsilon_{ref}} - \frac{1}{\epsilon_s} \right) \left(\frac{1}{2r_{A^-}} + \frac{1}{2r_{D^+}} \right) \right] \quad (2)$$

In eq 2, ϵ_0 is the vacuum permittivity, ϵ_s and ϵ_{ref} is the dielectric constants of the solvents where charge transfer reactions occur and where the redox potentials are measured respectively, R_{DA} is the electron donor-acceptor distance extracted from molecular modeling, and r_{D^+} and r_{A^-} are the ionic radii of the electron donor cation and acceptor anion respectively. The energy level diagram of **1** in toluene ($\epsilon = 2.28$) and a frozen solution ($\epsilon \approx 2$) accounting for spin selectivity is shown in Scheme 1. This diagram predicts that upon photoexcitation, D-A-R* triad **1** can readily undergo charge separation (CS) to form the D^{•+}-A^{•-}-R* state, 25 % of which, i.e. ¹(D^{•+}-A^{•-})-R*, should further charge shift to the D^{•+}-A-R⁻ state.⁵² Charge recombination of D^{•+}-A-R⁻, however can occur to either the ground or the local triplet state, depending on the relative energies of the triplet and ion pair. In a room-temperature toluene solution, the charge recombination from D^{•+}-A-R⁻ to the local triplet state of the donor (^{3*}D-A-R*) is endergonic by 0.07 eV and thus should not occur with a significant rate. However, this same reaction will be slightly exergonic in a frozen solution when the dielectric constant is closer to 2, which leads to a more positive ΔG_{Sol} .

2.2.3 Optical Spectroscopy

Steady-state absorption spectra were collected on a Shimadzu 1800 spectrophotometer. The femtosecond transient absorption (fsTA) and nanosecond transient absorption experiments have been described previously.⁵³ Details of experimental setup, the sample preparation and temperature control are summarized in 2.5.

2.2.4 EPR spectroscopy

EPR measurements were performed on 100 – 200 μM solutions. The solutions were loaded into quartz tubes (2.00 mm i.d.), subjected to three freeze – pump – thaw cycles on a high vacuum line (10^{-4} torr) and sealed with a hydrogen torch. TREPR measurements using continuous wave microwaves and direct detection were performed at X-band (~ 9.6 GHz) on a Bruker Eleksys E680 X/W EPR spectrometer with a split ring resonator (ER4118XMS3). The temperature was maintained at 105 K by an Oxford Instruments CF935 continuous flow optical cryostat with liquid nitrogen. Samples were photoexcited at 450 nm (2.0 mJ/pulse, 7 ns, 10 Hz) from an optical parametric oscillator pumped by the frequency-tripled output of a Nd:YAG laser. Following photoexcitation, kinetic traces of the transient magnetization under CW microwave irradiation were obtained in both the real and the imaginary channels (quadrature detection). Time traces were recorded over a range of magnetic fields to give 2D spectra. Spectra were processed by first subtracting the signal prior to the laser pulse for each kinetic trace (at a given magnetic field point) and then subtracting the signal average at off-resonance magnetic field points from the spectra obtained at a given time.

2.3 Results and Discussion

2.3.1 Transient Absorption Spectroscopy

Following selective photoexcitation of D within D-A-R^{*} in butyronitrile/propionitrile (PrCN/EtCN) at 140 K and PrCN at 105 K the spin-selective CT reactions D-A-R^{*} → D^{•+}-¹(A^{•-}-R^{*}) and D^{•+}-³(A^{•-}-R^{*}) occur. Subsequently, at 140 K, D^{•+}-¹(A^{•-}-R^{*}) → D^{•+}-A-R⁻, whereas D^{•+}-³(A^{•-}-R^{*}) → D-A-R^{*}. Importantly, we have shown previously that the spin dynamics of this process can be used to carry out electron spin state teleportation experiments of a spin state prepared on R^{*}.^{19, 54} In contrast, lowering the temperature to 105 K in PrCN results in the reaction D^{•+}-³(A^{•-}-R^{*}) → ³*D-A-R^{*} and D-A-R^{*}, where the spin dynamics of the weakly coupled triplet-doublet pair ³*D-A-R^{*} strongly spin-polarize R^{*}, which we observe by time-resolved EPR (TREPR) techniques.^{55,56} Thus, the latter reaction provides a means to initialize an electron spin qubit in a specific quantum state at modest temperatures. These results show that changing the dielectric environment of radical ion pair-based spin qubits can result in several outcomes useful to quantum information applications.

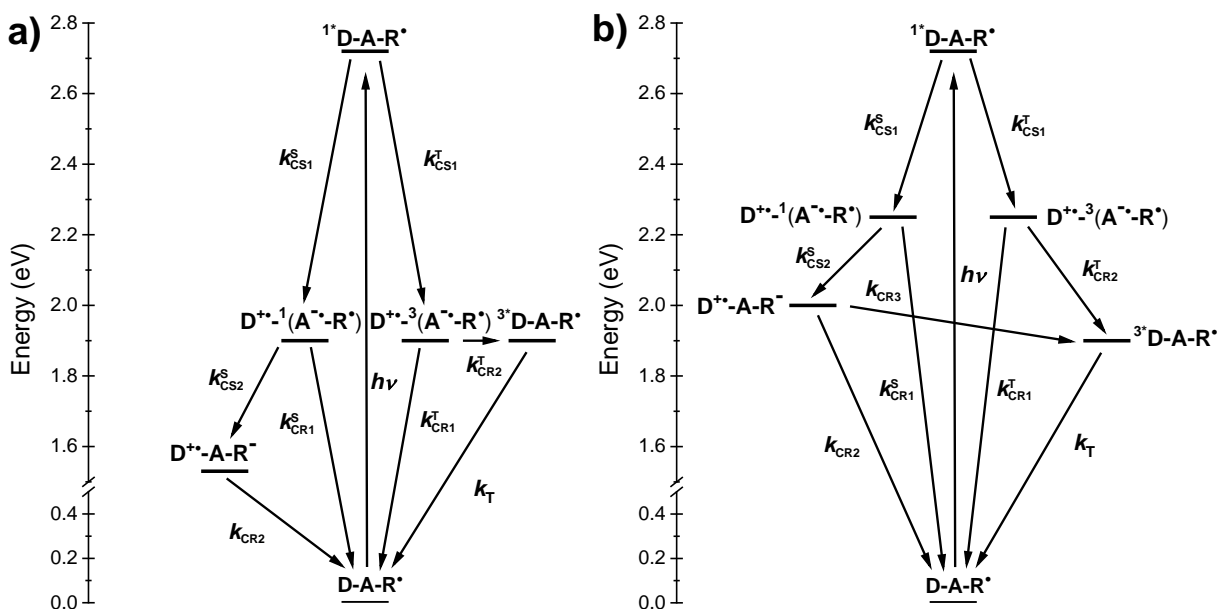


Figure 2.1. Kinetic pathways and energies for the relevant states of **1** in (a) 9/2 v/v PrCN/EtCN at 140 K and in (b) PrCN at 105 K.

D-A-R* (**1**, Scheme 2.1) was prepared by quantitative oxidation of **1H**, which was synthesized by imide condensation of a BDPAH-PI monoanhydride onto a PXX functionalized with 2,5-di-*t*-butylaniline (see Session 2.5 for details). Steady-state absorption spectra of **1** and **1H** are presented in Figure 2.6. The femtosecond transient absorption (fsTA) and nanosecond transient absorption (nsTA) spectrometers have been described previously.⁵³ Details of sample preparation and temperature control are summarized in the SI. The spin-dependent charge transfer pathways for each temperature are depicted in Figure 2.1. The specific radical ion pair energies are estimated using the Weller equation⁵¹ and will be discussed in the context of the transient spectroscopic data presented below.

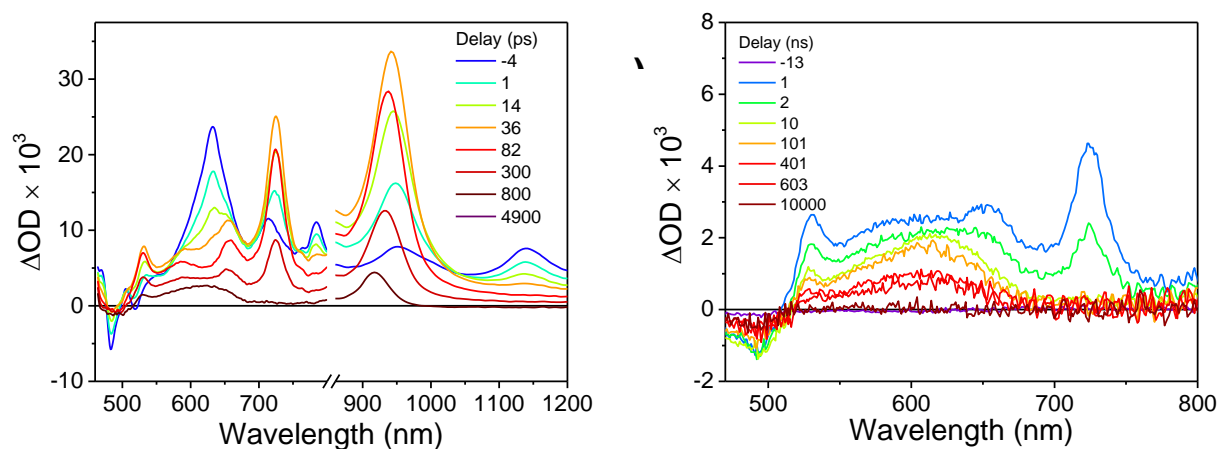


Figure 2.2. fsTA (a) and nsTA (b) transient absorption spectra of **1** in 9/2 PrCN/EtCN at 140 K following $\lambda_{\text{ex}} = 450$ nm excitation.

Selective photoexcitation of D in **1** at 414 nm in 9/2 v/v PrCN/EtCN at 140 K immediately produces the excited state of the donor ($^1D^*$), which is characterized by absorptions at 633 and 1140 nm, and stimulated emission at 482 and 518 nm (Figure 2.2). The subsequent charge

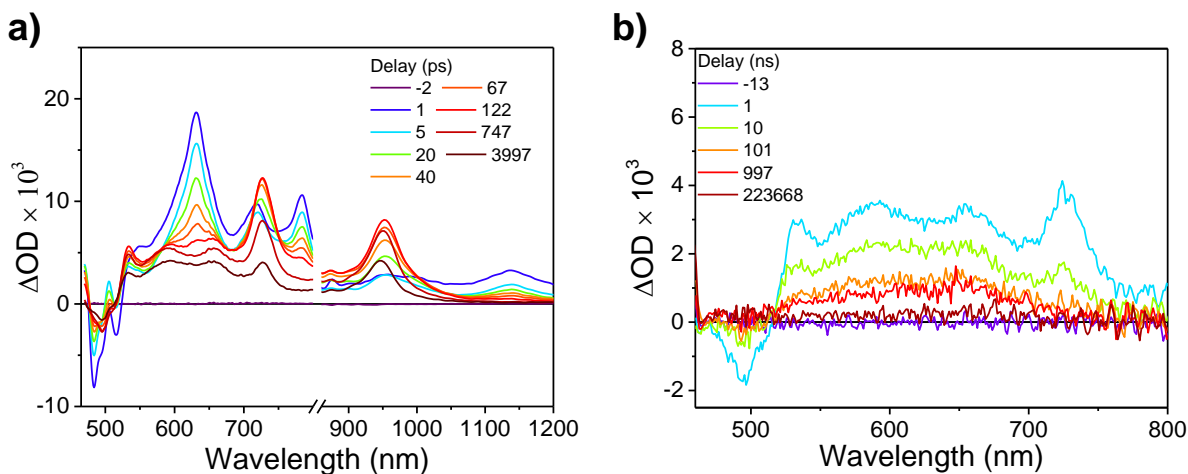
separation (CS) reaction $^1\text{D-A-R}^* \rightarrow \text{D}^{*+}\text{-A}^{\cdot-}\text{-R}^*$ results in the appearance of sharp absorptions at 723 nm, 530 and 920 nm resulting from the reduced acceptor ($\text{A}^{\cdot-}$)⁵⁷ and the oxidized donor (D^{*+}),⁵⁸ respectively. Global fitting of the fsTA data using the spin-selective model yields the species-associated spectra along with the rate constants for each process (Figure 2.8). The CS reaction occurs with $k_{\text{CS1}} = \frac{1}{4} k_{\text{CS1}}^{\text{S}} + \frac{3}{4} k_{\text{CS1}}^{\text{T}} = (55 \pm 6 \text{ ps})^{-1}$, which results in a nearly quantitative reaction yield given that the intrinsic lifetime of ^1D is 4.5 ns.⁵⁹

$\text{D}^{*+}\text{-A}^{\cdot-}$ is produced in an entangled singlet spin state due to strong exchange coupling between its two unpaired electron spins (Figure 2.1). However, the spin configuration of $\text{A}^{\cdot-}$ relative to R^* is purely statistical resulting in populations of 25% $\text{D}^{*+}\text{-}^1(\text{A}^{\cdot-}\text{-R}^*)$ and 75% $\text{D}^{*+}\text{-}^3(\text{A}^{\cdot-}\text{-R}^*)$. Thus, only the singlet secondary CS reaction, $\text{D}^{*+}\text{-}^1(\text{A}^{\cdot-}\text{-R}^*) \rightarrow \text{D}^{*+}\text{-A-R}^-$, is spin-allowed,³⁰ and is indicated by the appearance of the absorption of R^- at 600 nm³⁰ with a rate constant $k_{\text{CS2}}^{\text{S}} = (13 \pm 1 \text{ ps})^{-1}$. $\text{D}^{*+}\text{-A-R}^-$ then decays back to D-A-R^* with a rate constant $k_{\text{CR2}} = (690 \pm 10 \text{ ns})^{-1}$ (Figure 2.8), while the 75% sub-population, $\text{D}^{*+}\text{-}^3(\text{A}^{\cdot-}\text{-R}^*)$, charge recombines to the ground state with an observed rate constant $k_{\text{CR}}^{\text{T}} = (516 \pm 28 \text{ ps})^{-1}$. Since no measurable amount of $^3\text{D-A-R}^*$ is observed, $k_{\text{CR1}}^{\text{T}} \gg k_{\text{CR2}}^{\text{T}}$, thus $k_{\text{CR1}}^{\text{T}} = k_{\text{CR}}^{\text{T}}$. The nsTA spectra (Figure 2.2) show only the decrease of the $\text{D}^{*+}\text{-A-R}^-$ features over time and the corresponding rate constants for reference compound $\text{D}^{*+}\text{-A}^{\cdot-}\text{-RH}$, **1H**, are $k_{\text{CS1}} = (49.5 \pm 0.5 \text{ ps})^{-1}$ and $k_{\text{CR1}}^{\text{S}} = (464 \pm 4 \text{ ps})^{-1}$, supporting the analysis given above, see Figure S5. This also implies that $k_{\text{CR1}}^{\text{S}} \cong k_{\text{CR1}}^{\text{T}}$ as well. Moreover, since $k_{\text{CR1}}^{\text{T}} \gg k_{\text{CR2}}^{\text{T}}$, the energies of $\text{D}^{*+}\text{-}^1(\text{A}^{\cdot-}\text{-R}^*)$ and $\text{D}^{*+}\text{-}^3(\text{A}^{\cdot-}\text{-R}^*)$ in 9/2 PrCN/EtCN at 140 K are less than or equal to that of $^3\text{D-A-R}^*$, so that the reaction $\text{D}^{*+}\text{-}^3(\text{A}^{\cdot-}\text{-R}^*) \rightarrow ^3\text{D-A-R}^*$ cannot compete kinetically with $\text{D}^{*+}\text{-}^3(\text{A}^{\cdot-}\text{-R}^*) \rightarrow \text{D-A-R}^*$. The calculated ion pair energies shown in Figure 1a show that the energies of $\text{D}^{*+}\text{-}^1(\text{A}^{\cdot-}$

$-R^{\bullet}$) and $D^{\bullet+}-^3(A^{\bullet}-R^{\bullet})$ equal that of $^3D-A-R^{\bullet}$ if the solvent static dielectric constant is assumed to be $\epsilon_s = 3.4$.

Figure 2.3. FsTA (a) and nsTA (b) transient absorption spectra of **1** in a PrCN glass at 105 K following $\lambda_{ex} = 450$ nm excitation.

Lowering the temperature of **1** in PrCN to 105 K results in fsTA spectra (Figure 2.3), whose global analysis yields the initial observed CS rate constant $k_{CS1} = (34.8 \pm 0.5 \text{ ps})^{-1}$. The 25% sub-population, $D^{\bullet+}-^1(A^{\bullet}-R^{\bullet})$, charge separates further to yield $D^{\bullet+}-A-R^{\bullet}$ with a rate constant $k_{CS2}^S = (15 \pm 1 \text{ ps})^{-1}$, which decays back to $D-A-R^{\bullet}$ with an observed rate constant $k_{CR2} + k_{CR3} = (11.7 \pm 0.4 \text{ ns})^{-1}$ (Figure 2.9). The increase in overall charge recombination (CR) rate relative to that observed at 140 K is attributed to the fact that the CR rate to ground state lies far into the Marcus inverted region^{49,50} of the rate vs. free energy profile at 140 K, while the corresponding rate at 105 K is dominated by k_{CR3} that is in the Marcus normal region. Since $D^{\bullet+}-A-R^{\bullet}$ is a doublet state, it does not contribute to the spin dynamics observed at 105 K (Figure 2.1). The 75% sub-population, $D^{\bullet+}-^3(A^{\bullet}-R^{\bullet})$, charge recombines to both $^3D-A-R^{\bullet}$ and the ground state $D-A-R^{\bullet}$ with the observed



rate constant $k_{CR}^T = k_{CR1}^T + k_{CR2}^T = (902 \pm 22 \text{ ps})^{-1}$. NsTA spectroscopy further certifies that the

reaction $D^{*+}-A^{\cdot-}-R^{\cdot} \rightarrow {}^3D-A-R^{\cdot}$ occurs as evidenced by a broad feature centered around 650 nm assigned to 3D (Figure 2.4 and Figure 2.9).⁵⁹ Since the observed rate constant $k_{CR}^T = k_{CR1}^T + k_{CR2}^T$, we cannot determine k_{CR1}^T independently using the data at 105 K, and thus, cannot also assume that $k_{CR1}^S = k_{CR1}^T$. However, we can assume that $k_{CR2}^T \gg k_{CR1}^T$ and $k_{CR2}^S \gg k_{CR1}^S$ because the free energy changes for both $D^{*+}-{}^1(A^{\cdot-}-R^{\cdot})$ and $D^{*+}-{}^3(A^{\cdot-}-R^{\cdot})$ recombining directly to the ground state are about -2.25 eV, placing them both well into the Marcus inverted region for these charge transfer reactions. Comparing these data to those of **1H** in PrCN at 105 K, the initial CS occurs with a rate constant $k_{CS1} = (48.9 \pm 0.2 \text{ ps})^{-1}$, which is comparable to that of **1**, while the CR reaction displays distributed kinetics with major components of $k_{CR1} = (38.7 \pm 0.5 \text{ ns})^{-1}$ and $k_{CR1'} = (228 \pm 4 \text{ ns})^{-1}$. These slow CR rates are consistent with the arguments given above.

These observations show that the polarity of PrCN at 105 K is lower than that of 9/2/PrCN/EtCN at 140 K, which destabilizes $D^{*+}-A^{\cdot-}-R^{\cdot}$ resulting in its energy being significantly higher than that of ${}^3D-A-R^{\cdot}$. Decreasing the dielectric constant of the medium increases the radical ion pair energies relative to that of ${}^3D-A-R^{\cdot}$, making $\Delta G_{CR2}^T < 0$, such that the reaction $D^{*+}-{}^3(A^{\cdot-}-R^{\cdot}) \rightarrow {}^3D-A-R^{\cdot}$ proceeds rapidly. In order to estimate the dielectric constant of PrCN at 105 K, we measured the rate constants for **1** in toluene at 295 K for which $\epsilon_s = 2.4$ (see Figure 2.13). The rate constants obtained in toluene are somewhat faster than those measured in PrCN at 105 K, so that we assume $\epsilon_s \cong 2.3$ in the low temperature medium. The energy levels illustrated in Figure 1b are calculated using this assumption.

2.3.2 Time Resolved Electron Paramagnetic Spectroscopy

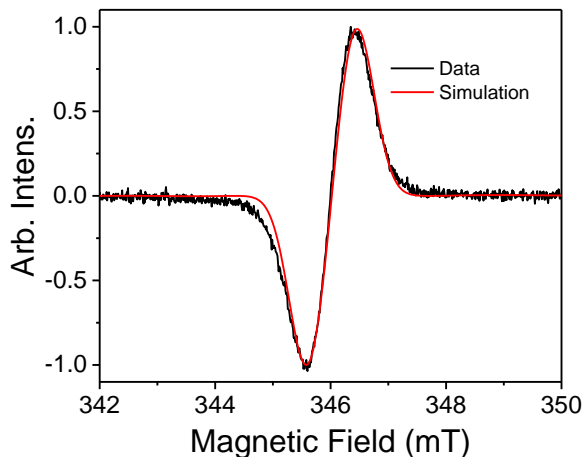


Figure 2.4. TREPR spectrum of **1** at X-band in PrCN glass at 105 K, 100 ns after a 7 ns, 450 nm laser pulse. Simulation is shown in red.

We observed an intense spin-polarized TREPR spectrum in glassy PrCN at 105 K following selective photoexcitation of D in **1** at X-band (~ 9.6 GHz). As described above, nsTA spectroscopy at 105 K shows that the only remaining species on the timescale of the TREPR experiment (> 50 ns) is $^3\text{D-A-R}^{\bullet}$. Its TREPR spectrum displays an *e, a* (*a* = enhanced absorption, *e* = enhanced emission, low to high field) polarization pattern with a 0.8 mT splitting (peak-to-peak) and a 3.2 mT width (baseline-to-baseline) (Figure 2.4). If the magnetic field range is expanded to 260-420 mT, no additional lines are obvious above the noise (Figure 2.16). In addition, the TREPR spectrum of ^3D was recorded under the same conditions as that of $^3\text{D-A-R}^{\bullet}$ to obtain the zero-field splitting parameters of ^3D needed to fit the spectrum of $^3\text{D-A-R}^{\bullet}$. The Hamiltonian for a coupled triplet-doublet pair given on eq 1 was used to fit the spectrum of $^3\text{D-A-R}^{\bullet}$:⁶⁰

$$\mathcal{H} = \omega_R \hat{S}_{R,z} + \omega_T \hat{S}_{T,z} + J_{TR} \mathbf{S}_R \mathbf{S}_T + \mathbf{S}_T \mathbf{D}_{TR} \mathbf{S}_R + \mathbf{S}_T \mathbf{D}_T \mathbf{S}_T \quad (1)$$

where ω_R and ω_T are the Larmor frequencies of the doublet (R^\bullet) and the triplet (3D) respectively; J_{TR} is the isotropic exchange coupling between the doublet and the triplet; \mathbf{D}_{TR} is the doublet- triplet dipolar interaction tensor in the point-dipole approximation; \mathbf{D}_T is the triplet zero-field splitting tensor; and $\hat{S}_{R,Z}$, \mathbf{S}_R , $\hat{S}_{T,Z}$, \mathbf{S}_T are the spin operators of the doublet and the triplet spins. \mathbf{D}_T was determined from the EPR spectrum of reference compound 3D , which yields $|D| = 1824$ MHz and $|E| = 360$ MHz (Figure 2.6 and Table 2.2. Triplet fit parameters) and is fixed during the fitting process for $^3D-A-R^\bullet$. The fit parameters for the TREPR spectrum of $^3D-A-R^\bullet$ are given in Table 2.3.

The fit indicates that the TREPR spectrum of $^3D-A-R^\bullet$ is dominated by transitions of R^\bullet owing to the comparable magnitudes of relatively weak dipolar and exchange coupling between 3D and R^\bullet , such that the transitions of 3D at much higher and lower fields are very small and do not appear above the noise level in the spectrum (see Figure 2.16). The e , a polarization pattern arises from the selective population of all four $m_s = \pm 1/2$ sublevels. This preferential population originates in spin-polarized 3D generated by the reaction $D^+-A^\bullet-R^\bullet \rightarrow ^3D-A-R^\bullet$ through the radical-pair intersystem crossing mechanism,⁶¹⁻⁶⁵ in which S-T₊₁ mixing occurs because the exchange interaction within the D^+-A^\bullet radical pair is comparable to the Zeeman splitting at X-band (Figure 2.5).⁶⁶⁻⁶⁸ Consequently, the spin polarization of 3D is transferred to R^\bullet to the four $m_s = \pm 1/2$ states in the doublet-quartet manifold.⁶⁹ Due to the relatively small population difference between $m_s = \pm 1/2$ sublevels ($D_{+1/2}$ and $D_{-1/2}$, $Q_{+1/2}$ and $Q_{-1/2}$), the population differences between

$Q_{-3/2}$ and $Q_{-1/2}$ and between $Q_{+1/2}$ and $Q_{+3/2}$ dominate, therefore, an overall e, a EPR spectrum is observed.

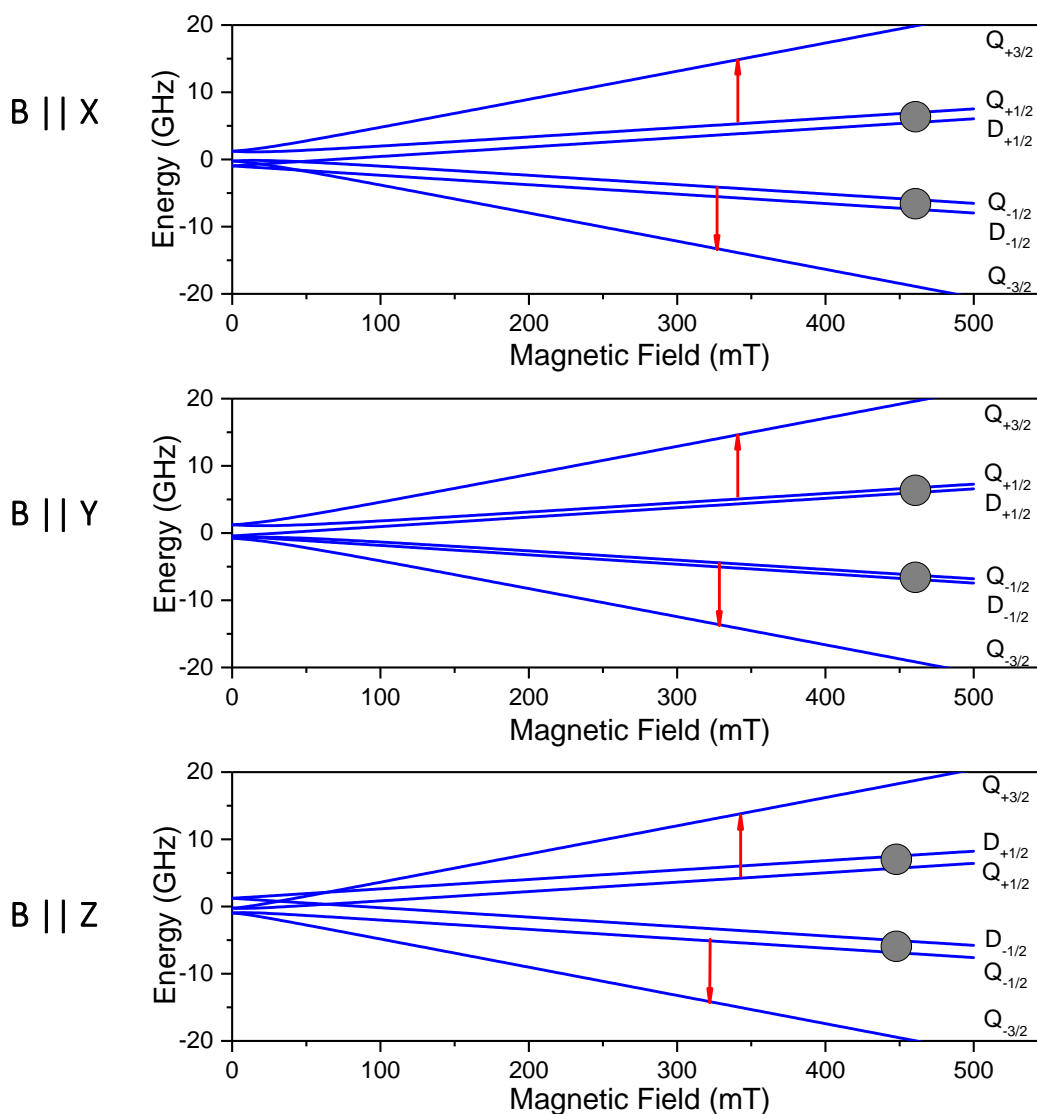


Figure 2.5 Schematic for EPR transitions in all three canonical orientations with $m_s = \pm 1/2$ sublevels overpopulated. Grey circles represent the population differences of spin sublevels relative to the least populated sublevel, downward arrows represent emissive transitions, and upward arrows represent absorptive transitions.

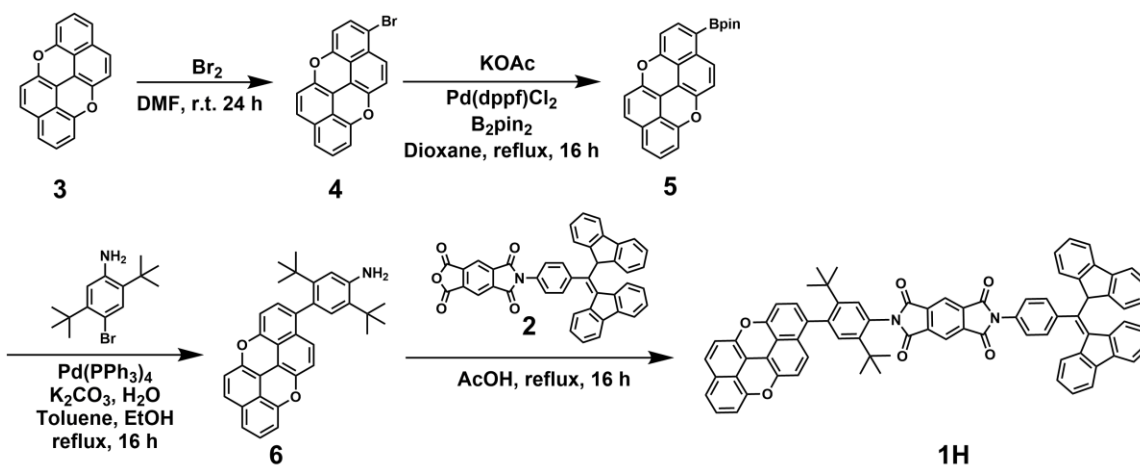
2.4 Conclusion

These results show that tuning the energetics of a D-A-R* molecule can achieve the charge transfer reaction mechanisms necessary to strongly polarize an adjacent radical to serve as a spin qubit with a well-defined spin state or to generate the intermediates necessary to carry out quantum teleportation experiments using the same molecule, thus providing a flexible three qubit system for future quantum logic gate and spin-state teleportation experiments.

2.5 Supplementary Information

2.5.1 Synthesis and Characterization

All chemicals were purchased from Sigma-Aldrich, Inc. unless noted otherwise. ^1H and ^{13}C NMR spectra were acquired with a Bruker Avance III 500 MHz instrument equipped with a DCH CryoProbe. Mass spectroscopy was performed using a Bruker Autoflex III MALDI-TOF. Purification was performed using silica gel from Sorbent Technologies (Atlanta, GA). Scheme S1 S1 outlines the syntheses of the compounds studied. The synthesis of **2**³⁰ and **3**⁷⁰ were described previously.



Scheme 2.2. Synthetic scheme for **1H** (PXX-PI-BDPAH)

Generation of **1** from its non-radical precursor **1H** was performed immediately prior to experimentation using MnO₂ and 1,5-diazabicyclo(4.3.0)non-5-ene in dry THF using methods previously described for the generation of R[•] derivatives.³⁰ The resulting samples of **1** in THF were then evaporated to dryness using a stream of N₂ before being dissolved in dry CH₂Cl₂, toluene, butyronitrile (PrCN), or butyronitrile/propionitrile (PrCN/EtCN) mixture for further study.

Compound 1H. A flame-dried round-bottom flask equipped with a magnetic stir bar was charged with **2** (23.5 mg, 37.1 μmol, 1.2 equiv.) and **6** (15.0 mg, 30.9 μmol, 1.0 equiv.), sealed with a rubber septum, and then subject to three pump-purge cycles with N₂. 3.5 ml degassed AcOH was added through the septum, and the mixture was heated to reflux for 20 h. The mixture was returned to room temperature and diluted with 20 ml of CH₂Cl₂. After three extractions with H₂O, the organic layer was collected and the solvent was removed on a rotary evaporator. The resulting crude mixture was then purified using chromatography on silica gel with 33% of hexane in CH₂Cl₂ as the eluent to yield 22.0 mg (65%) of product as a dark green solid. ¹H NMR (500 MHz, DMSO-d₆) δ: 8.54 (d, J = 8.2 Hz, 1H), 8.42-8.38 (m, 2H), 8.06 (d, J = 7.3 Hz, 1H), 7.94 (d, J = 7.7 Hz, 1H), 7.88-7.83 (d, J = 7.4 Hz, 2H), 7.69 (s, 1H), 7.68 (d, J = 7.6 Hz, 2H), 7.59-7.50 (m, 2H), 7.47-7.38 (m, 3H), 7.35 (td, J = 7.4, 1.0, 2H), 7.32-7.27 (m, 2H), 7.27-7.23 (m, 2H), 7.23-7.20 (m, 1H), 7.19 (d, J = 2.5 Hz, 1H), 7.17 (d, J = 3.7 Hz), 7.15 (s, 1H), 7.13 (s, 2H), 1.19 (s, 9 H), 1.10 (s, 9H). ¹³C NMR (126 MHz, CDCl₃) δ: 166.66, 166.58, 164.83, 160.32, 153.90, 152.68, 152.15, 148.63, 145.71, 144.45, 144.20, 143.90, 143.50, 142.13, 141.45, 140.01, 139.90, 138.91, 138.64, 137.70, 137.66, 137.07, 136.70, 133.70, 131.38, 130.26, 130.04, 129.35, 128.55, 128.45, 127.70, 127.40, 127.20, 127.10, 126.83, 125.89, 125.47, 125.26, 125.18, 121.66, 121.29, 120.26, 120.03, 119.26,

119.21, 117.46, 117.35, 111.49, 111.44, 108.71, 107.76, 36.16, 35.16, 31.97, 31.60. MS (MALDI-TOF) m/z : $[M^+]$ calculated for $C_{77}H_{52}N_2O_6$ 1102.39; found 1100.43.

Compound 4. 300 mg of **3** (1.06 mmol) and 190 mg of *N*-bromosuccinimide (NBS) (1.06 mmol, 1 equiv.) were placed in a 250 ml round-bottom flask equipped with a magnetic stir bar and sealed with a rubber septum. After three pump-purge cycles with N_2 , 100 ml of DMF was charged into the flask upon vigorous stirring at room temperature for 24 h. The reaction suspension was then diluted with H_2O and the solid was collected using vacuum filtration then washed with 20 ml of methanol three times to remove unreacted NBS. The solid was dried in the air to yield 320 mg of product as yellow solid which was used for next step without further purification.

Compound 5. 500 mg of **4** (0.69 mmol), 700 mg of bis(pinacolato)diboron (2.77 mmol, 4 equiv.), and 500 mg of potassium acetate (5.54 mmol 8 equiv.) were combined in 50 mL of 1,4-dioxane. This mixture was purged with nitrogen for 15 min. After adding 0.1 g of $Pd(dppf)Cl_2$ (0.14 mmol), the mixture was purged with nitrogen for another 15 min. The reaction mixture was then heated at 110 °C for 12 h. After the reaction mixture was cooled, the solvent was removed on a rotary evaporator. The resulting mixture was purified by silica gel column chromatography with chloromethane/hexanes/triethylamine (49/50/1) as the eluent yielding 0.4 g (71%) of yellow solid as the product. 1H NMR (500 MHz, $CDCl_3$), δ : 8.20 (d, $J = 9.5$ Hz, 1H), 7.71 (d, $J = 7.5$ Hz, 1H), 7.26 (d, $J = 9.5$ Hz, 1H), 7.08-7.04 (m, 2H), 6.94 (d, $J = 9.5$ Hz, 1H), 6.88 (d, $J = 9.0$ Hz, 1H), 6.63-6.59 (m, 2H). ^{13}C NMR (100 MHz, $CDCl_3$, δ): 155.45, 152.66, 144.26, 143.79, 137.69, 135.28, 131.39, 128.03, 127.16, 126.10, 121.46, 121.33, 119.99, 117.44, 117.19, 111.91, 111.27, 108.71, 108.56, 108.43, 83.51, 24.98. ESI-HRMS (m/z): calculated for $C_{26}H_{21}BO_4$ $[M^+]$: 408.1533; found: 408.1544.

Compound 6. A flame dried, 50 ml round-bottom flask equipped with a magnetic stir bar was charged with 100 mg of **5** (245 μmol), 84 mg of 4-bromo-2,5-di-*t*-butylaniline (294 μmol , 1.2 equiv.), 101 mg of potassium carbonate (745 μmol , 3 equiv) and 28 mg of $\text{Pd}(\text{PPh}_3)_4$ (25 μmol , 0.1 equiv.). After three pump-purge cycles, a solvent mixture of toluene/ethanol/water (2/1/1) purged with N_2 for 15 min was added to the reaction vessel and the mixture was heated at reflux for 16 h. After the reaction was cooled down, the mixture was diluted with 100 ml of CH_2Cl_2 and washed with 15 ml of water three times. The solvent in the organic layer was removed on a rotary evaporator. The crude product was then purified by silica gel column chromatography with 16% CH_2Cl_2 in hexane then 40 % CH_2Cl_2 in hexane as eluent to yield 89 mg (73 %) of orange solid as the product. ^1H NMR (500 MHz, CDCl_3), δ : 7.32 (d, $J = 9.0$ Hz, 1H), 7.12-7.06 (m, 2H), 7.00 (d, $J = 7.8$ Hz, 1H), 6.95 (d, $J = 9.0$ Hz, 1H), 6.88 (d, $J = 9.3$ Hz, 1H), 6.84-6.76 (m, 2H), 6.68 (d, $J = 7.8$ Hz, 1H), 6.66-6.60 (m, 1H), 3.86 (br, 2H), 1.38 (s, 9H), 1.11 (s, 9H).

2.5.2 Steady-State Optical Spectroscopy

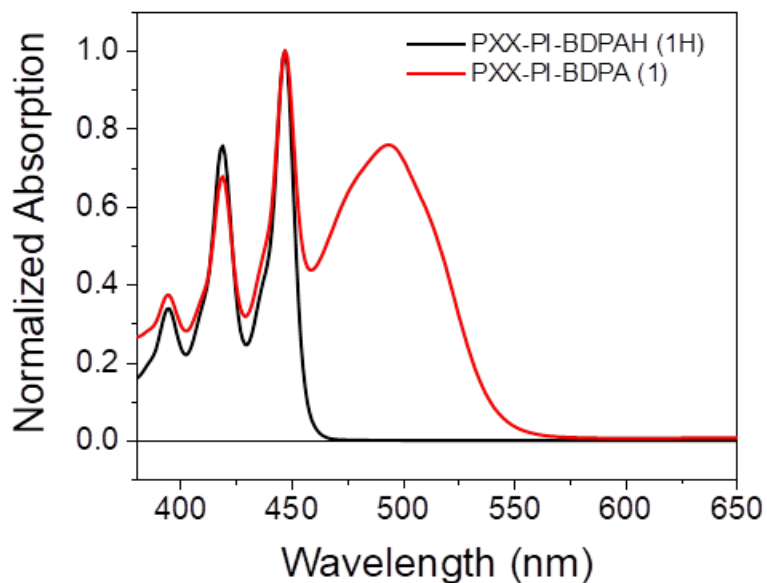


Figure 2.6. UV-Vis absorption spectra recorder using a Shimadzu 1800 spectrophotometer. Spectra of **1** and its non-radical precursor **1H** in toluene at 295 K.

2.5.3 Electrochemistry and Energetics

Measurements were performed on a CH Instruments Model 660A electrochemical workstation. Samples were measured in a solution of 0.1 M tetrabutylammonium hexafluorophosphate (TBAPF₆) in CH₂Cl₂ purged with Ar to remove oxygen. A 1.0 mm diameter platinum disk electrode, platinum wire counter electrode, and saturated calomel electrode (SCE) reference electrode were used.

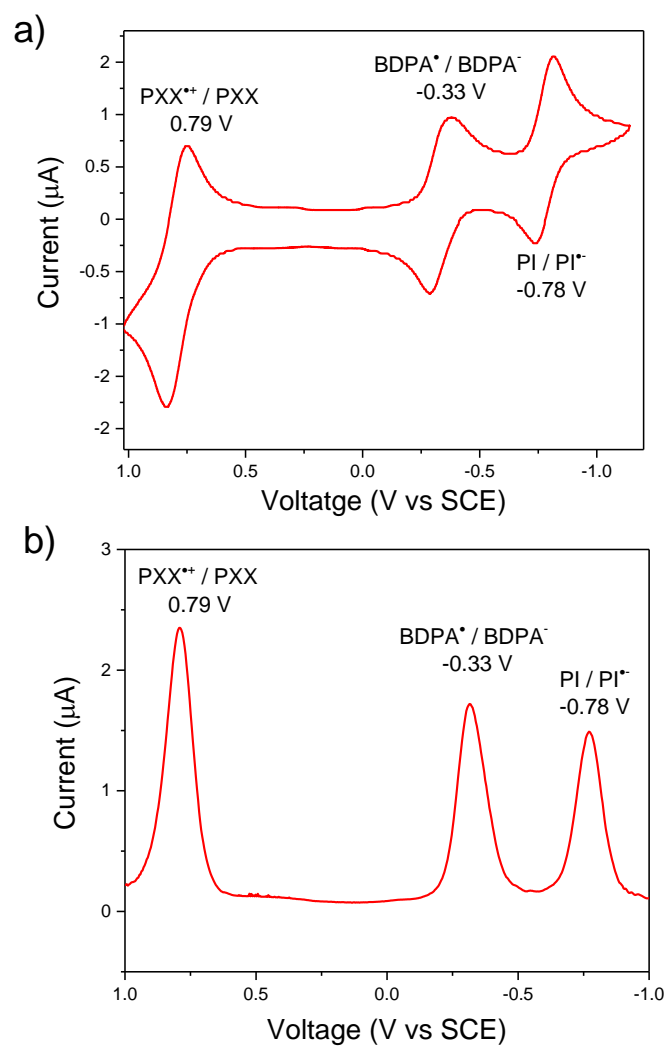


Figure 2.7. Cyclic (a) and differential-pulse (b) voltammetry of 1 in CH₃CN (0.1 M tetrabutylammonium hexafluorophosphate). Results are reported vs. SCE.

The structure of **1** was optimized using molecular mechanics with the MMFF94 force field in Avogadro 1.1.1. The ion pair distances (r_{DA}) were estimated using the distance between the centers of PXX and PI (12.9 Å), and PXX and BDPA (21.9 Å).

The free energies of reaction for the charge transfer reactions in different solvent environments can be estimated using Weller equation, which calculates the Gibbs free energy change for ion pair (IP) states with the solvent correction accounting for different solvent environments.

$$\Delta G_{IP} = [E^{red}(D^+/D) - E^{red}(A/A^-)] + \Delta G_{Sol} \quad (1)$$

$$\Delta G_{Sol} = -\frac{e^2}{4\pi\epsilon_0} \left[\frac{1}{\epsilon_s} \cdot \frac{1}{R_{DA}} + \left(\frac{1}{\epsilon_{ref}} - \frac{1}{\epsilon_s} \right) \left(\frac{1}{2r_{A^-}} + \frac{1}{2r_{D^+}} \right) \right] \quad (2)$$

In eq 2, ϵ_0 is the vacuum permittivity, ϵ_s and ϵ_{ref} is the dielectric constants of the solvents in which the charge transfer reactions occur and in which the redox potentials are measured respectively, R_{DA} is the electron donor-acceptor distance extracted from molecular modeling, and r_{D^+} and r_{A^-} are the ionic radii of the electron donor cation and acceptor anion respectively. The ionic radii are estimated from the size of the relevant π systems of PXX⁺ (r_{D^+} = 4.4 Å), PI⁻ (r_{A^-} = 3.7 Å), and BDPA⁻ (r_{A^-} = 4.4 Å). The calculated values are listed in Table S1.

Table 2.1. Free energies of reaction for various charge transfer reactions in different solvents

Reaction	ΔG (eV) ($\epsilon_s = 2.3$)	ΔG (eV) ($\epsilon_s = 3.4$)
$^1D-A-R^{\bullet} \rightarrow D^+-A^--R^{\bullet}$	-0.47	-0.82
$D^+-A^--R^{\bullet} \rightarrow D^+-A-R^-$	-0.25	-0.37
$D^+-A-R^- \rightarrow ^3D-A-R^{\bullet}$	-0.10	0.37
$D^+-A-R^- \rightarrow D-A-R^{\bullet}$	-2.00	-1.53
$D^+-A^--R^{\bullet} \rightarrow D-A-R^{\bullet}$	-2.25	-1.90

2.5.4. Transient absorption spectroscopy and kinetics

Femtosecond visible transient absorption (fsTA) spectroscopy experiments were conducted using a commercial regeneratively amplified Ti:sapphire laser system (Tsunami oscillator/Spitfire amplifier, Spectra-Physics, lab-built optical parametric amplifier⁷¹) described previously⁵³. Before interaction with the sample, the probe was split using a neutral density filter so that one portion interacted with the sample and one portion provided a reference spectrum. The pump (550 or 510 nm, 1 μ J/pulse, 120 fs) was sent through a commercial depolarizer (DPU-25-A, Thorlabs, Inc.) to suppress the effects of rotational dynamics and chopped at 500 Hz. The pump was focused to about 0.2 mm diameter and the probe to about 0.1 mm diameter at the sample. The reference probe and the transmitted probe were coupled into optical fibers and detected using a customized Helios spectrometer and Helios software (Ultrafast Systems, LLC). Nanosecond visible transient absorption (nsTA) spectroscopy experiments were performed using the pump pulse described for the fsTA experiments paired with a photonic crystal fiber ultra-broadband probe generated by a customized EOS spectrometer (Ultrafast Systems, LLC). The temporal resolution was about 120-280 fs in the fsTA experiments and about 600-900 ps in the nsTA experiments. Visible fsTA spectra were collected for 3 s at each pump-probe time delay; nsTA spectra were collected using similar durations. Samples for room-temperature TA were dissolved in toluene and prepared with an optical density of 0.8 at 450 nm in 2 mm quartz cuvettes fused to a glass bulb. This bulb was used to subject each sample to four freeze-pump-thaw cycles under vacuum (10^{-4} Torr) to remove oxygen. Samples were stirred to minimize the effects of local heating and degradation. Samples for low-temperature TA were dissolved in CH_2Cl_2 and prepared with an optical density of 0.8 at 450 nm in a 2 mm quartz cuvette. The solution was then evaporated

to dryness with a stream of N₂ in a small vial and was placed in a N₂-atmosphere glovebox. Inside the glovebox, a volume of PrCN or PrCN/EtCN 9:2 mixture equivalent to the amount of CH₂Cl₂ used previously was added to the vial to obtain a solution of similar optical density. This solution was then sealed in a sample cell consisting of two quartz windows separated by a 2 mm PTFE spacer. The sealed sample cell was then removed from the glovebox and placed inside a Janis VNF-100 cryostat (Janis Research Co. LLC) coupled to a Cryo-Con 32B (cryogenics Control Systems, Inc.) temperature controller. The sample was then cooled to 105 K or 140 K with liquid N₂ to measure the TA spectra.

All datasets were background subtracted to remove scattered pump light and spontaneous emission and corrected for group delay dispersion and time zero using Surface Xplorer (Ultrafast Systems, LLC). Data for fsTA of **1** were globally fitted to the following model that accounts for the spin selectivity, where A_T and A_S are $^1D-A-R^*$, B_T and B_S are $D^{*+1}(A^+-R^*)$ and $D^{*+3}(A^+-R^*)$ respectively, C_S is $D^{*+}A-R^-$ and C_T is an empty component to balance the matrix dimension. Since the spin statistics is assumed, the initial condition of $[A_T]:[A_S] = 3:1$ is used for the fitting.

$$\frac{d}{dt} \left[\begin{pmatrix} [A_T] \\ [B_T] \\ [C_T] \end{pmatrix} + \begin{pmatrix} [A_S] \\ [B_S] \\ [C_S] \end{pmatrix} \right] = \begin{pmatrix} -k_{CS1}^T & 0 & 0 \\ k_{CS1}^T & -k_{CR}^T & 0 \\ 0 & 0 & 0 \end{pmatrix} \begin{pmatrix} [A_T] \\ [B_T] \\ [C_T] \end{pmatrix} + \begin{pmatrix} -k_{CS1}^S & 0 & 0 \\ k_{CS1}^S & -k_{CS2}^S & 0 \\ 0 & k_{CS2}^S & -k_{CR2}^S \end{pmatrix} \begin{pmatrix} [A_S] \\ [B_S] \\ [C_S] \end{pmatrix}$$

Data for nsTA of **1** were globally fitted to a sequential model (at 105 K) or decay-associated models (at 140 K and room temperature)

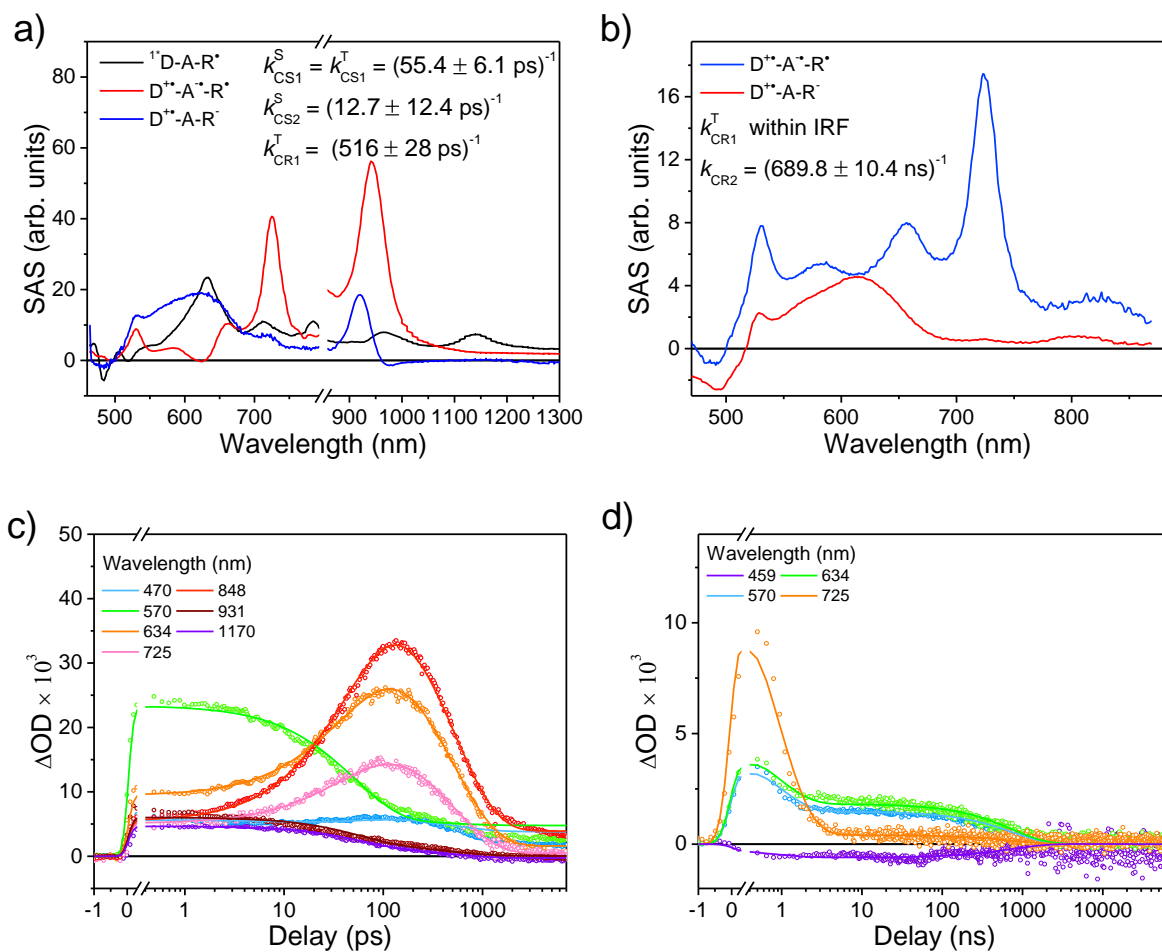


Figure 2.8. FsTA (a) and nsTA (b) species-associated spectra of 1 in a 9/2 PrCN/EtCN at 140 K following $\lambda_{ex} = 450 \text{ nm}$ excitation. c) and d) Comparison of the kinetic traces to the fit at selected probe wavelengths for the fsTA and nsTA data, respectively. The resulting from the global fitting of the data to a model that includes spin-selectivity and an $A \rightarrow B \rightarrow G$ model.

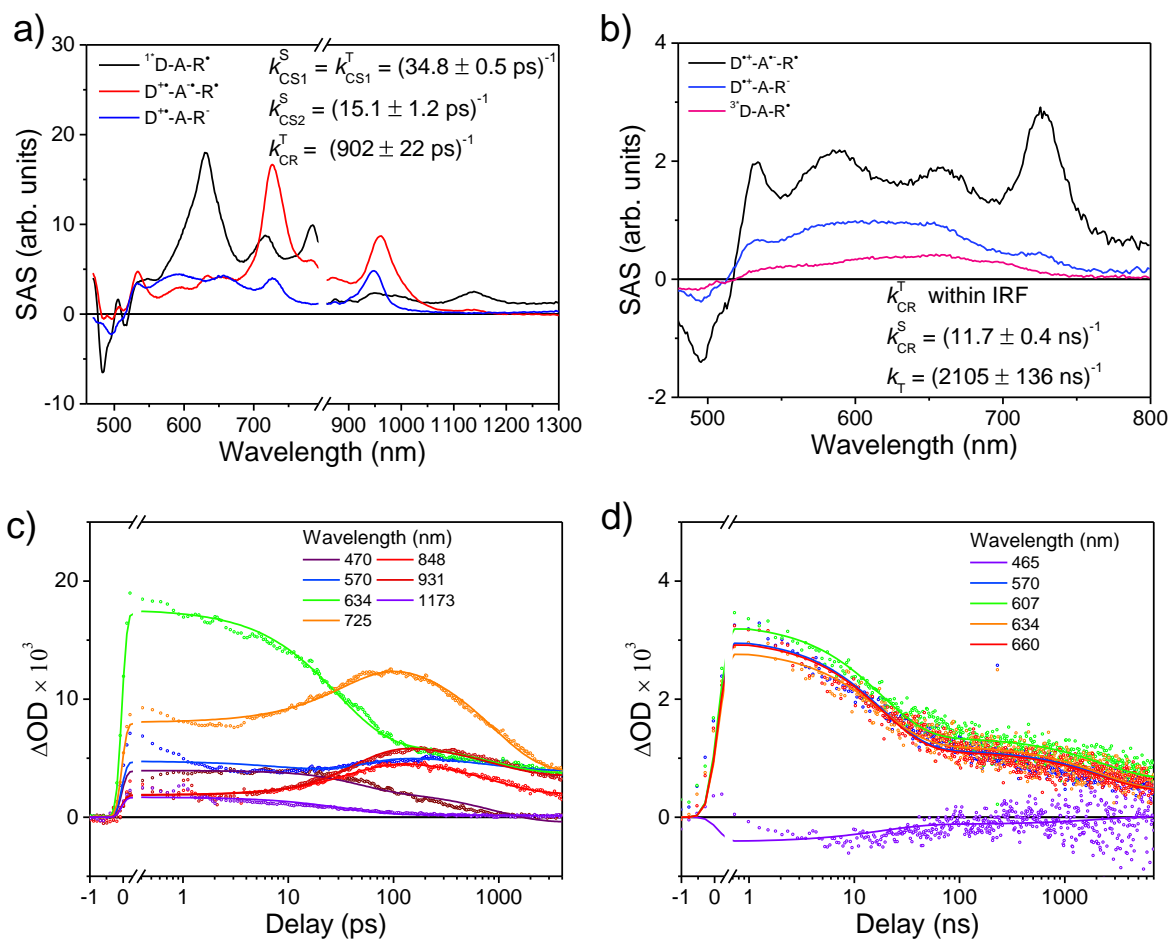


Figure 2.9. fsTA (a) and nsTA (b) species-associated spectra of 1 in a PrCN at 105 K following $\lambda_{\text{ex}} = 450 \text{ nm}$ excitation. The resulting from the global fitting of the data to a model that includes spin-selectivity and an $\text{A} \rightarrow \text{B} \rightarrow \text{C} \rightarrow \text{GS}$ model. c) and d) Comparison of the kinetic traces to the fit at selected probe wavelengths for the fsTA and nsTA data, respectively.

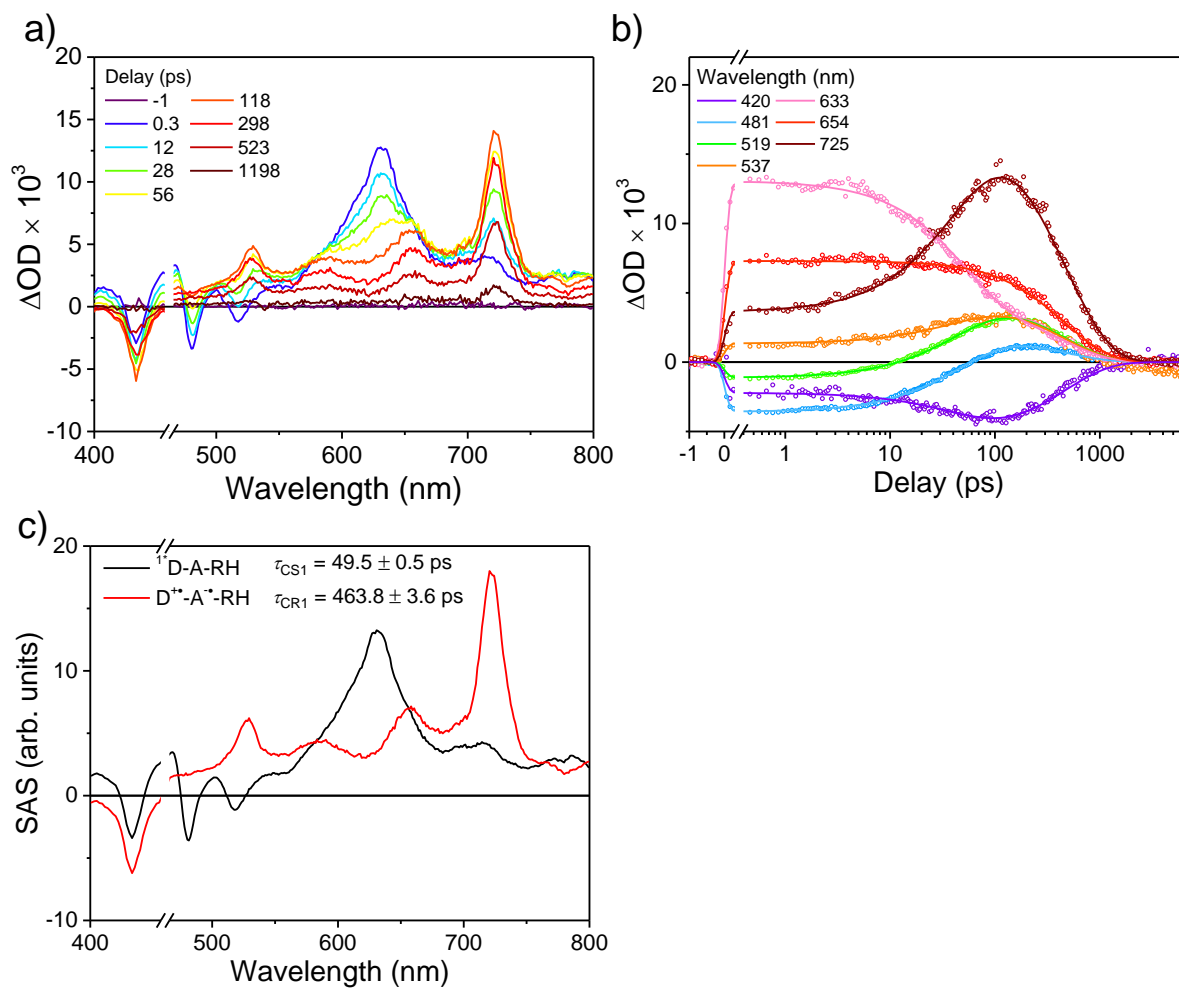


Figure 2.10. Transient absorption spectra of 1H. a) fsTA data of 1H at 140K in PrCN/EtCN 9:2 solution b) Comparison of the kinetic traces to the fit at selected probe wavelengths c) species-associated spectrum resulting from the global fitting of the data to an $A \rightarrow B \rightarrow GS$ model.

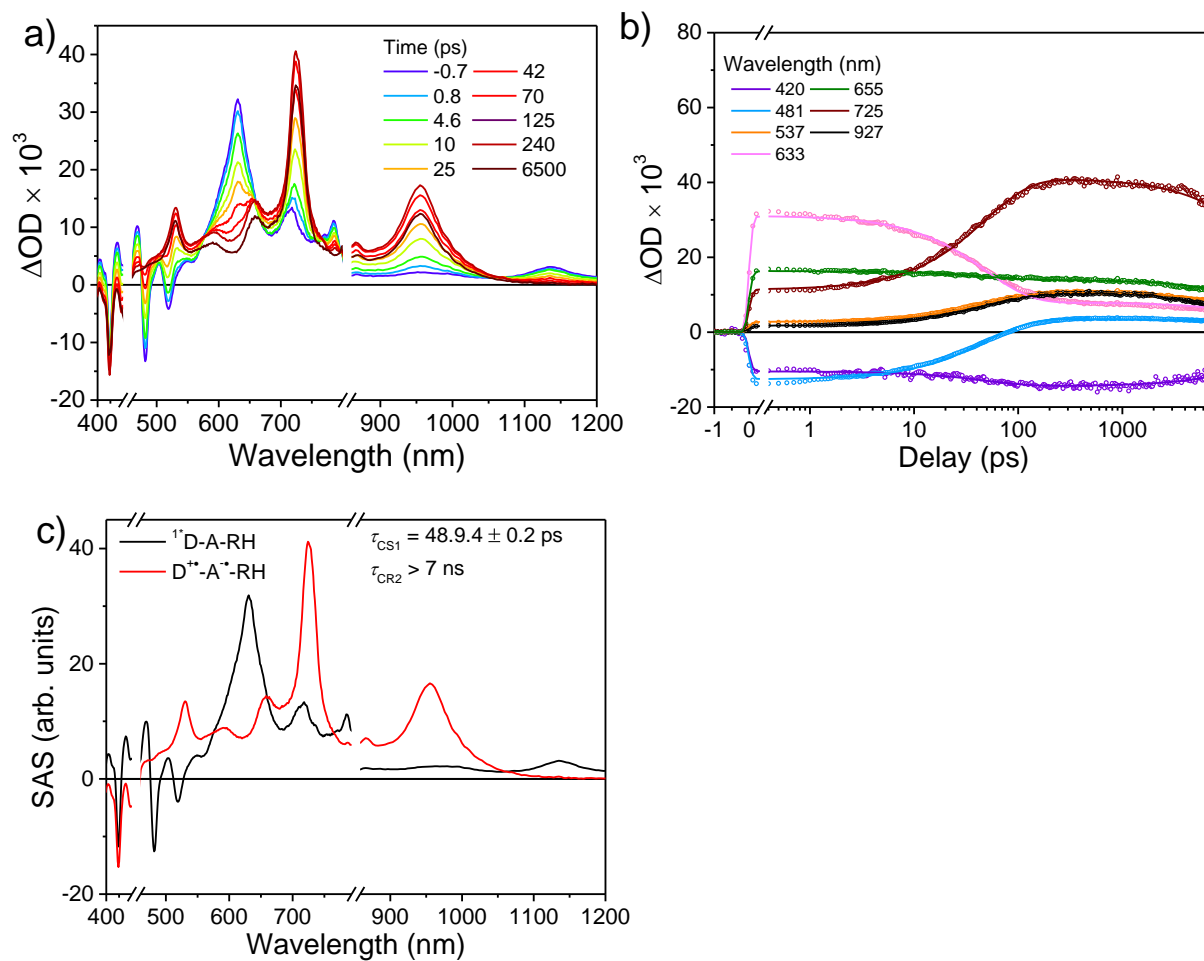


Figure 2.11. Transient absorption spectra of 1H. a) fsTA data of 1H at 105 K in PrCN. b) Comparison of the kinetic traces to the fit at selected probe wavelengths c) species-associated spectrum resulting from the global fitting of the data to an $A \rightarrow B \rightarrow GS$ model.

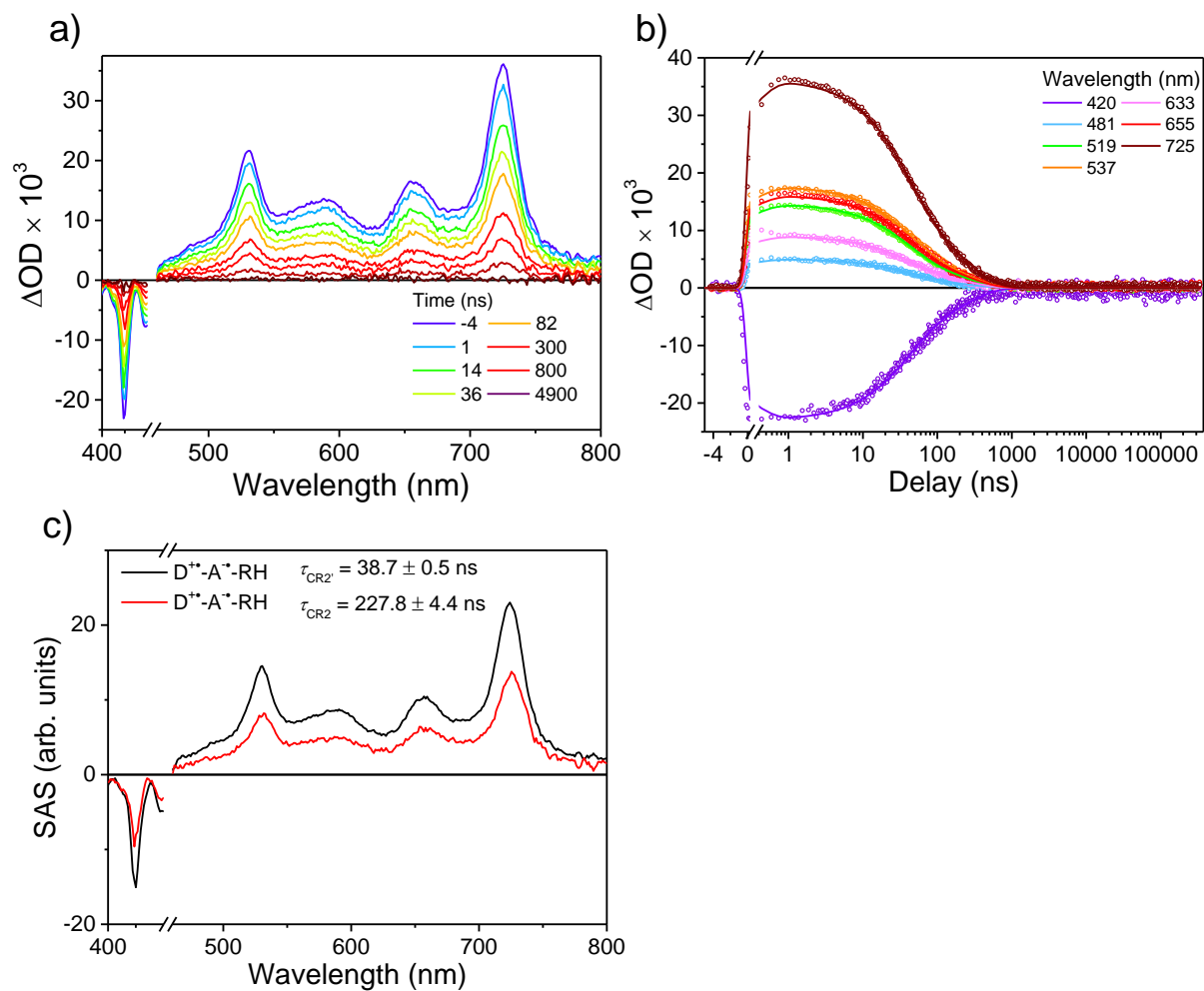


Figure 2.12. Transient absorption spectra of 1H. a) nsTA data of 1H at 105K in PrCN. b) Comparison of the kinetic traces to the fit at selected probe wavelengths c) decay-associated spectrum resulting from the global fitting of the data to two exponential decays.

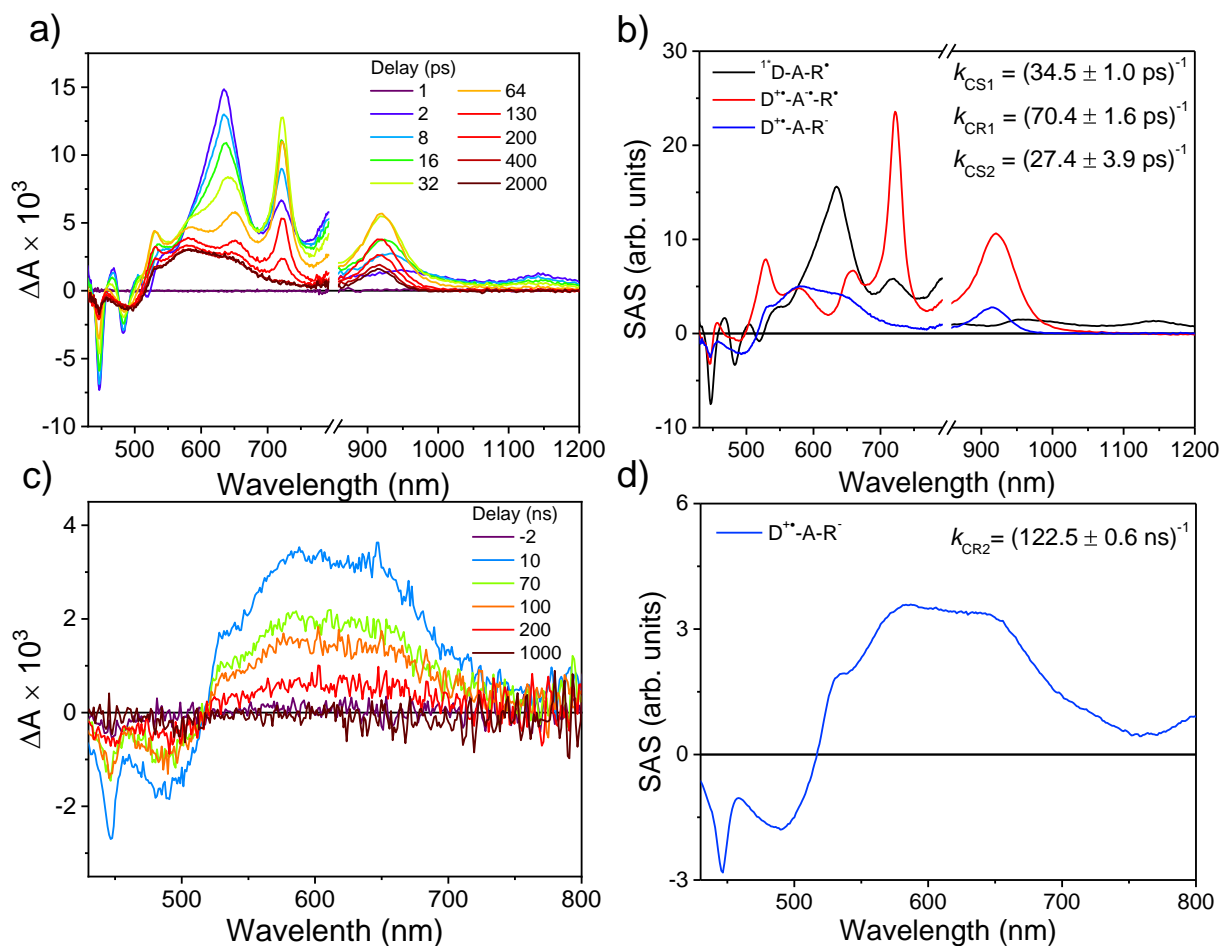


Figure 2.13. (a) FsTA spectra of 1 in toluene at 295 K following $\lambda_{\text{ex}} = 450$ nm excitation. (b) Species-associated spectra for the data in (a) resulting from the global fitting of the data to a model that includes spin-selectivity and an A G model. (c) and (d) The corresponding nsTA data and species-associated spectra, respectively.

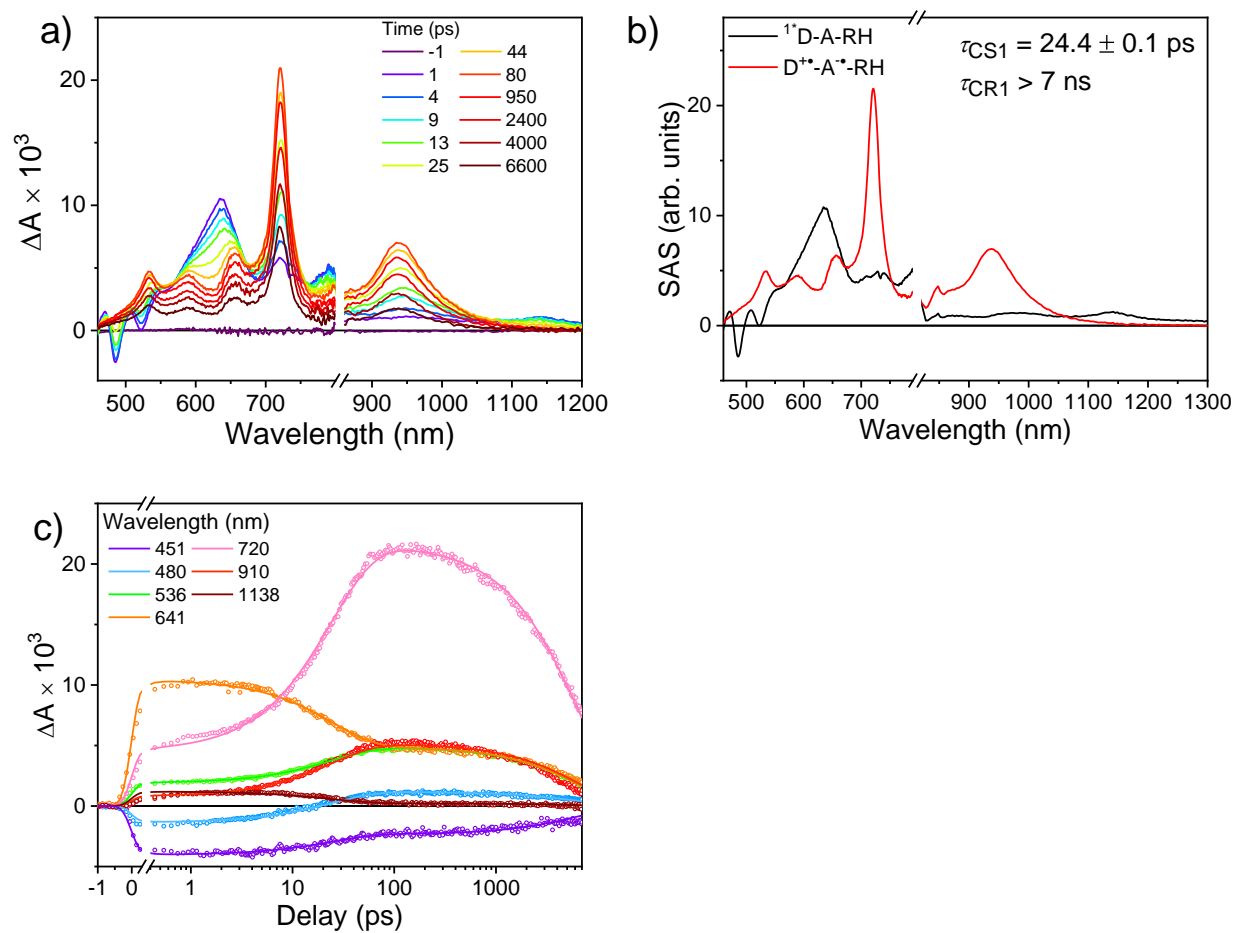


Figure 2.14. (a) FsTA spectra of 1H in toluene at 295 K following $\lambda_{\text{ex}} = 450$ nm excitation. (b) Species-associated spectra for the data in (a) resulting from the global fitting of the data to a $A \rightarrow B \rightarrow G$ model. (c) Kinetic fits at selected wavelengths.

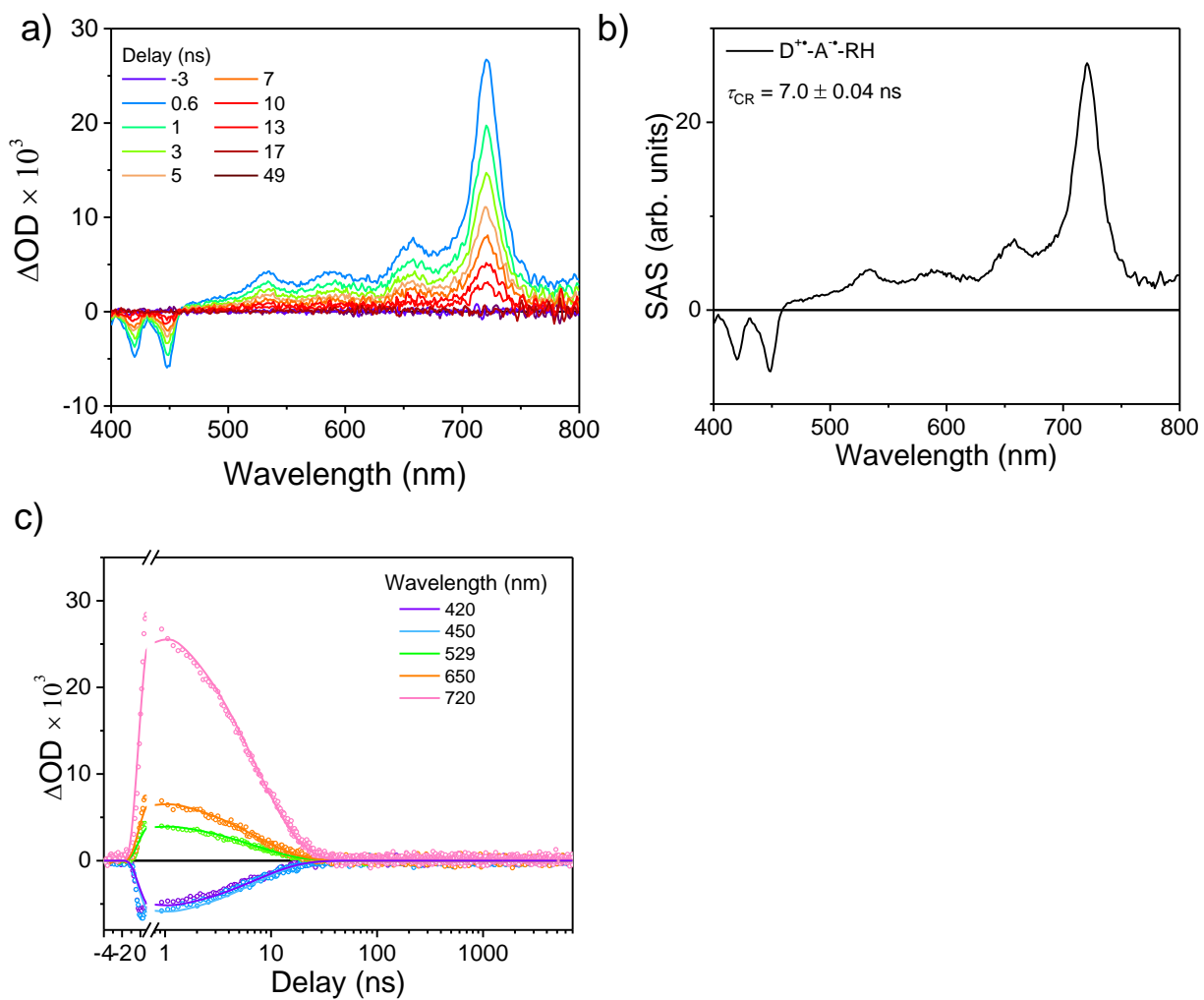


Figure 2.15. (a) NsTA spectra of 1H in toluene at 295 K following $\lambda_{ex}= 450$ nm excitation. (b) Species-associated spectra for the data in (a) resulting from the global fitting of the data to a $A \rightarrow B \rightarrow G$ model. (c) Kinetic fits at selected wavelengths.

2.5.5. EPR Spectroscopy

The TREPR spectra of PXX and 1 were fit using pepper function in EasySpin5. The model to which the spectrum of 1 was fit has been described in the main text. The fit parameters for both spectra are given in Table S2 and Table S3.

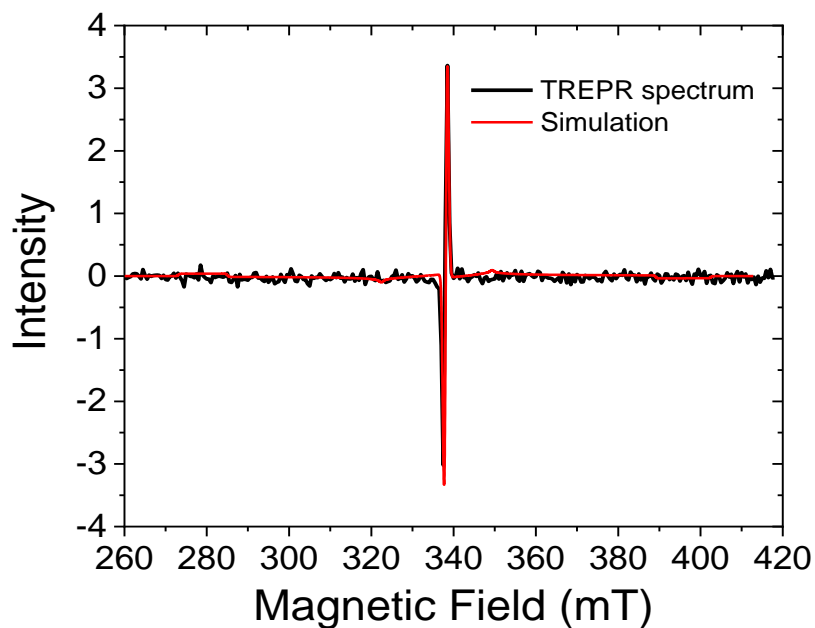


Figure 2.16. TREPR spectrum of 1 at X-band in PrCN at 105 K, 100 ns after a 7 ns, 450 nm laser pulse. Simulation is shown in red.

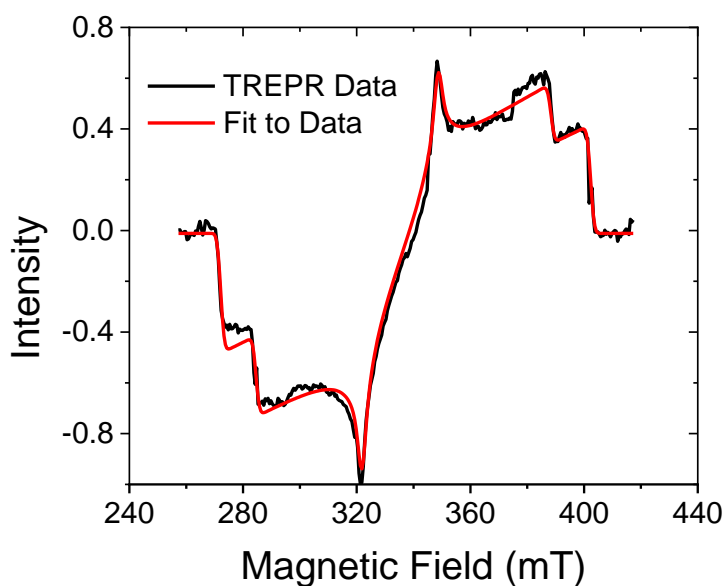


Figure 2.17. TREPR spectra obtained using direct detection at 85 K in mTHF for PXX ($\sim 100 \mu\text{M}$) after a 7 ns laser pulse, with the fit to a standard spin-orbit intersystem crossing model shown in red

Table 2.2. Triplet fit parameters

Zero-Field Splitting (MHz)	Population	Peak-Peak Linewidth (mT)
$ D = 1824$ $ E/D = 0.197$	$T_x = 1$ $T_y = 1$ $T_z = 0$	1.63

Table 2.3. Coupled triplet-doublet pair fit parameters

Exchange coupling J_{TR} (MHz)	Zero-Field Splitting D_T (MHz)	Dipolar coupling D_{TR} (MHz)	Population	Peak-Peak Linewidth (mT)
-12	$ D = 1824$ $E/D = -0.197$	5	$ Q_{3/2}\rangle = 0$ $ Q_{1/2}\rangle = 0.25$ $ D_{1/2}\rangle = 0.25$ $ D_{-1/2}\rangle = 0.25$ $ Q_{-1/2}\rangle = 0.25$ $ Q_{-3/2}\rangle = 0$	0.6

2.5.6. Computational Data

PXX-PI-BDPA (1) Doublet Ground State

O -11.7803619966	3.1035816566	-0.9358944315	C -7.4834371913	0.5260694227	3.2392608314
O -12.5780462521	-1.6284926100	0.6320559315	C -4.6420965941	-1.4478094814	-2.5993364250
O 3.4554330518	1.8805783636	-0.6964823172	C -6.3639544673	-0.5290147930	3.0896355506
O 3.7873981293	-2.5655220480	0.5423400193	C -6.3912099718	-1.2506752440	-0.7462886142
O -2.1881651661	-3.0246957920	0.4771271424	C -5.0406610655	-1.2243471889	-1.1209531458
O -2.5153749334	1.4205136446	-0.7236322777	C -4.1616007555	-0.9378608883	-0.0610240618
N 4.0209330225	-0.3108961652	-0.0711284016	C -4.6291872056	-0.7221047680	1.2366417632
N -2.7300675267	-0.8524629356	-0.2046940331	C -5.9791967457	-0.7572552766	1.6053942384
C -13.9576013191	3.9588273084	-1.3540797724	C -6.8844825020	-1.0344708381	0.5506945951
C -3.3770123768	-2.3288744975	-2.7469647966	C -14.8002087433	-0.7968823152	0.2330430527
C -4.4005649844	-0.0716534431	-3.2674694279	C -8.7175289823	1.2435931391	-0.1591442058
C -5.7678052026	-2.1622042451	-3.3833351552	C -9.5605446557	2.2691725786	-0.5455500959
C -5.1638562475	-0.0200018940	3.9214878245	C -10.9551308603	2.0697108960	-0.5426539001
C -6.8188092195	-1.8645648265	3.7264756270	C -11.4697155848	0.8513121196	-0.1516875322

C -10.6227633053 -0.2073856998 0.2472827507
C -9.2090265468 -0.0327142767 0.2492616252
C -8.3812568840 -1.1318543659 0.6550402019
C -8.9955021958 -2.3266700090 0.9939105973
C -10.3994930640 -2.4971464517 0.9985181032
C -13.1527756013 2.9151827232 -0.9484139349
C -13.7298083608 1.6793864467 -0.5550052341
C -12.8852431099 0.6231654776 -0.1469090700
C -15.3618099249 3.7792954173 -1.3714496183
C -15.9498708079 2.5893737088 -0.9937800928
C -15.1417272180 1.4996005250 -0.5724072838
C -15.6401186836 0.2271512203 -0.1633593074
C -13.4044660759 -0.5939800886 0.2388317065
C -11.2066512821 -1.4444038368 0.6293130703
C 3.1388399261 0.7503122948 -0.3971940920
C 3.3070771737 -1.4990140592 0.2274977741
C 0.5373886538 0.8134887984 -0.5071755823
C -0.5775041896 -0.0005431649 -0.3264314623
C -2.0281393941 0.3430388173 -0.4559697127
C -1.8586136171 -1.9060189616 0.1519813246
C -0.4764640108 -1.3467453379 0.0403406543
C 0.7478259449 -1.9736219579 0.2553511940
C 1.8619317796 -1.1590257204 0.0749458870
C 1.7612626712 0.1856155863 -0.2936889596
C 11.5479675585 1.9755846496 -0.0984751810
C 5.4433448540 -0.1976596322 -0.0482355361
C 6.2372948040 -1.2471780975 -0.5265797030
C 7.4324375323 1.0729784980 0.4569740038
C 6.0454141477 0.9639969581 0.4507643727
C 7.6235237385 -1.1340101949 -0.4896116737
C 10.4483392593 4.0989944014 -2.9246847871
C 9.3411470257 3.9061710833 -3.7576603486
C 8.4859620137 2.8163165830 -3.5586112808
C 8.7090324864 1.9097430117 -2.5205543689
C 9.7985026449 2.1045895088 -1.6602684936
C 10.6763511361 3.2018651711 -1.8859398861
C 11.7514991093 3.1363737005 -0.8933039668
C 12.8102045276 4.0018476129 -0.6347048412
C 13.6694781841 3.7221706446 0.4331487507
C 13.4558102730 2.5987082222 1.2403739585
C 12.3955080756 1.7264023192 0.9871920866
C 10.3264659694 1.2943802617 -0.5523668006
C 10.9471661731 -3.6466548578 3.0242828884
C 9.8029090998 -3.6168281040 3.8281072836
C 8.7982608235 -2.6706520006 3.5945497335
C 8.9088870220 -1.7478117501 2.5525682466
C 10.0379277895 -1.7811723412 1.7215823523
C 11.0632470292 -2.7335615884 1.9815427471
C 12.1409492200 -2.5197059882 1.0141539700
C 13.3188821905 -3.2258125484 0.7914565166
C 14.1552504468 -2.8340668266 -0.2590133354
C 13.8019681639 -1.7598111734 -1.0843038895
C 12.6209178509 -1.0473190545 -0.8669935087
C 11.7905932577 -1.4076846510 0.2009530388
C 10.4717766961 -0.9093627909 0.6193991473
C 9.7367538449 0.1428555667 0.0206411785
C 8.2474134339 0.0270020484 -0.0050741308
H -2.4625125430 -1.7930987828 -2.4855423002
H -3.2735074743 -2.6434837936 -3.7916240251
H -3.4380125835 -3.2281731828 -2.1253718345
H -3.6289155331 0.5077110632 -2.7541818458
H -5.3195235203 0.5251829879 -3.2607524527
H -4.0928082573 -0.2096712876 -4.3115826074
H -5.4234738795 -2.3574391916 -4.4044226740
H -6.6760240997 -1.5569492735 -3.4649417091
H -6.0328276792 -3.1235865623 -2.9288782161
H -5.5003717294 0.1806228458 4.9441520512
H -4.7487120807 0.9121140938 3.5209829963
H -4.3577671822 -0.7589214011 3.9878510104
H -6.0423495958 -2.6313428495 3.6225045948
H -7.7373352589 -2.2437538328 3.2732677305
H -7.0107579113 -1.7198449567 4.7967979184
H -7.1911410399 1.4791727087 2.7837525708
H -7.6749741515 0.7078412607 4.3035973970
H -8.4218431602 0.2074900256 2.7850410578
H -7.1364123422 -1.4582168592 -1.5031971978
H -3.8742007722 -0.5143588910 1.9831978783
H -15.1947496288 -1.7602046741 0.5405087437
H -16.7144381278 0.0636475090 -0.1658224789
H -7.6458664845 1.4096602604 -0.1685429602
H -9.1645551737 3.2315810148 -0.8540819182
H -8.3757510355 -3.1800923235 1.2529016302
H -10.8440131419 -3.4475272407 1.2743850384
H -13.5079301816 4.8989471171 -1.6537711877
H -15.9853949406 4.6088097609 -1.6931338285
H -17.0302838309 2.4758878209 -1.0155770453
H 0.4569479046 1.8581270481 -0.7894980249
H 0.8283719040 -3.0168788180 0.5426900418
H 14.5001861890 4.3898351992 0.6456656357
H 8.2348207714 -1.9536007568 -0.8549802169
H 8.0385258073 1.0680506043 -2.3925874887
H 7.8945445288 1.9782092347 0.8385328954
H 5.4341176466 1.7785750167 0.8183828565
H 5.7750095543 -2.1475934646 -0.9111012790
H 11.1232546984 4.9340594908 -3.0945880254
H 9.1497034777 4.6019375155 -4.5701408057
H 7.6357100534 2.6713061602 -4.2193530771
H 12.9625592748 4.8905727215 -1.2422409687
H 14.1202661021 2.4024042360 2.0773586910
H 12.2375145194 0.8686731105 1.6312328658
H 11.7356152487 -4.3689844993 3.2196362198
H 9.6977820142 -4.3266856699 4.6441000939
H 7.9185653775 -2.6510900897 4.2319086856
H 8.1220326971 -1.0188791403 2.3980874703
H 13.5826207530 -4.0782778372 1.4127430829
H 15.0788546227 -3.3761393879 -0.4439890665
H 14.4524369369 -1.4763787516 -1.9072184350
H 12.3557329081 -0.2270849121 -1.5247977858

**Chapter 3 – Metallated Porphyrin Stable Free Radicals: Exploration of Electron-Spin
Communication and Dynamics**

Adapted from: Norbert Grzegorzek [†], Haochuan Mao [†], Patrick Michel, Marc J. Junge, Emmaline R. Lorenzo, Ryan M. Young, Matthew D. Krzyaniak, Michael R. Wasielewski, and Erin T. Chernick* *J. Phys. Chem. A* **2020**, *124* (30), 6168–6176.

(*Corresponding Author; [†]Equal Contribution). Copyright 2020 American Chemical Society.

3.1 Introduction

World energy consumption is ever increasing, and new methods and developments are required to harvest renewable energy to keep costs down as well as preserve the Earth's natural resources. Effective organic electronic devices operating on a renewable energy platform will face challenges with time, as device operating sizes drop below the 10 nm size range.⁶ At this reduced size scale, operational principles transition to the single molecule regime, and become quantized in nature. Consequently, the research field of spintronics and quantum information science (QIS) has been gaining ever increasing momentum, where information can be manipulated, stored and transferred using the quantum properties of electron spins.^{72, 73}

The term spintronics was first introduced in the 1980's, when the giant magnetoresistance effect was realized, while more recently, electron spins have been demonstrated to serve as quantum bit (qubits) in a variety of QIS applications.⁷⁴⁻⁷⁷ However, research pertaining to this field is still in its infancy with respect to predictable and reliable molecular design for organic QIS applications. Advanced fundamental studies are required to elucidate the molecular properties necessary to achieve practical operational devices functioning to manipulate quantum information. From an organic synthesis perspective, attention has been focused on the creation of a diverse range of organic molecules with interesting open shell character, which have targeted QIS applications.^{12, 19, 78-84}

Porphyrins represent a class of aromatic, light-harvesting chromophores that can coordinate metals, transforming them to organometallic species with further unique chemical and physical properties.⁸⁵ Porphyrins can also exist as stable oxidized, reduced or neutral radicals.⁸⁶ From a biological perspective, extensive research on the oxophlorin and the *meso*-hydroxyporphyrin has been carried out to elucidate their role in the catabolism of heme.⁸⁷ Inspired

by Nature, impressive synthetic achievements have been made in the design and realization of stable porphyrin oxyl radicals with relevant magnetic properties.^{88, 89}

Porphyrins can be metallated with numerous metals, including Zn(II), Ni(II), and Cu(II). These metals can provide a platform to study the electron spin dynamics of both diamagnetic and paramagnetic porphyrin complexes: Zn(II) is a diamagnetic metal, Ni(II) can switch between diamagnetic and paramagnetic states depending on ligation^{90, 91} and Cu(II) is paramagnetic.

The intermolecular⁹²⁻⁹⁵ and intramolecular interactions^{96, 97} between a stable doublet radical and a porphyrin triplet state have both been investigated by time resolved electron paramagnetic resonance (TREPR). Different effects of a stable free radical (SFR) on a photoexcited chromophore, or charge transfer state have been observed⁹⁸ such as enhanced intersystem crossing, (EISC)⁹⁹ and electron spin polarization transfer.¹⁰⁰ These mechanisms are governed by molecular and electronic structure as well as the extent of magnetic-exchange coupling between the porphyrin triplet state and the SFR.

van der Est et. al. reported a transient EPR study on a *meso*-tetratolylporphyrin complex with a verdazyl SFR appended directly to the β -position of the porphyrin.⁹⁶ The porphyrin derivative was then metallated with vanadium to incorporate an additional unpaired spin to the system. Their TREPR spectroscopy revealed the free base porphyrin triplet state couples ferromagnetically with the doublet radical to form a quartet species. For the vanadium porphyrin, the verdazyl radical couples ferromagnetically to the porphyrin triplet, but antiferromagnetically to the unpaired spin of the vanadium metal. These results are very relevant when addressing current research efforts towards the design of molecular systems that can undergo spin hyperpolarization where the polarization of the excited state is transferred to SFR.¹⁰¹⁻¹⁰⁶

Not only does the porphyrin metal center, but also the substituents, and their position around the porphyrin periphery largely influence the spin-spin exchange between a doublet state and a porphyrin.¹⁰⁷ For example, Balch et al. reported that a β – octaethylporphyrin Ni(II) oxylradical complex demonstrated an antiferromagnetic interaction between the oxyl radical and paramagnetic Ni(II) center.¹⁰⁸ However, when Osuka et. al. substituted a porphyrin oxyl radical with pentafluorophenyl substituents in the *meso*-positions, the oxyl radical demonstrated a ferromagnetic interaction with the high-spin Ni(II).¹⁰⁹

We are specifically interested in exploring the spin-spin interactions between a SFR covalently appended to a photoexcited chromophore.^{48, 110-113} Specifically, we want to design and synthesize molecular systems where the spin-states can be manipulated such that the magnetic-exchange coupling between the radical and photoexcited chromophore can be turned “on” and “off.” The final goal is to design and synthesize functional organic molecules with controllable variable magnetic exchange regimes that may be relevant for quantum information applications.

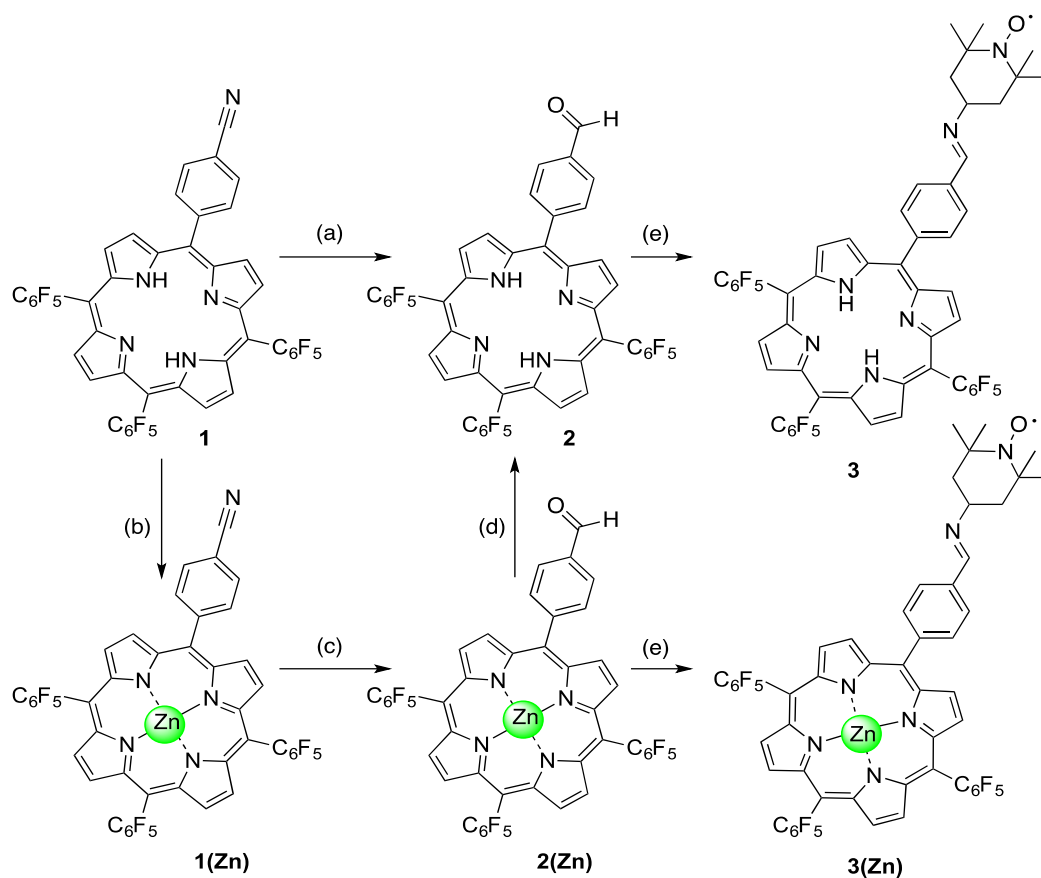


Figure 3.1. Synthetic route of **3** and **3(Zn)** used in this study

Based on the aforementioned reports, we decided to elaborate upon the porphyrin, and synthesize a series of metalloporphyrins with a stable free radical covalently appended to the *meso*-position, where the spin state of the metal can be varied. Herein reported is the synthesis of a series of *meso*-substituted porphyrins with the electron withdrawing pentafluorobenzene moiety in three positions to aid in pyridine coordination to form the Ni(II) octahedral high-spin state,¹⁰⁹ and the final *meso*-position substituted with a TEMPO SFR appended by an imine bond between a phenyl group and the porphyrin core (Figure 1). The phenyl group ensures the radical substituent assumes a near perpendicular conformation relative to the porphyrin chromophore. The porphyrin was metallated with Cu(II), Zn(II) and Ni(II), whose spin states have been described earlier. The complete synthesis and characterization of the free-base and three metalloporphyrins is reported,

in addition to TREPR and TA measurements. We have been able to show that the free base and zinc porphyrin radicals demonstrate opposite magnetic exchange regimes in the excited state. Based on transient nutation experiments, we were able to demonstrate¹⁰¹ that the Zn derivative populates a quartet state indicating the porphyrin triplet state and doublet radical are coupled, whereas, the free-base excited state is a triplet, demonstrating weak magnetic exchange. Additional TA measurements corroborate the TREPR results demonstrating a much larger increase in percentage of ISC rates of the metallated porphyrin in comparison to the free-base porphyrin. These results permit us to envision a switchable quantum state based upon metallation of the porphyrin with Zn(II).

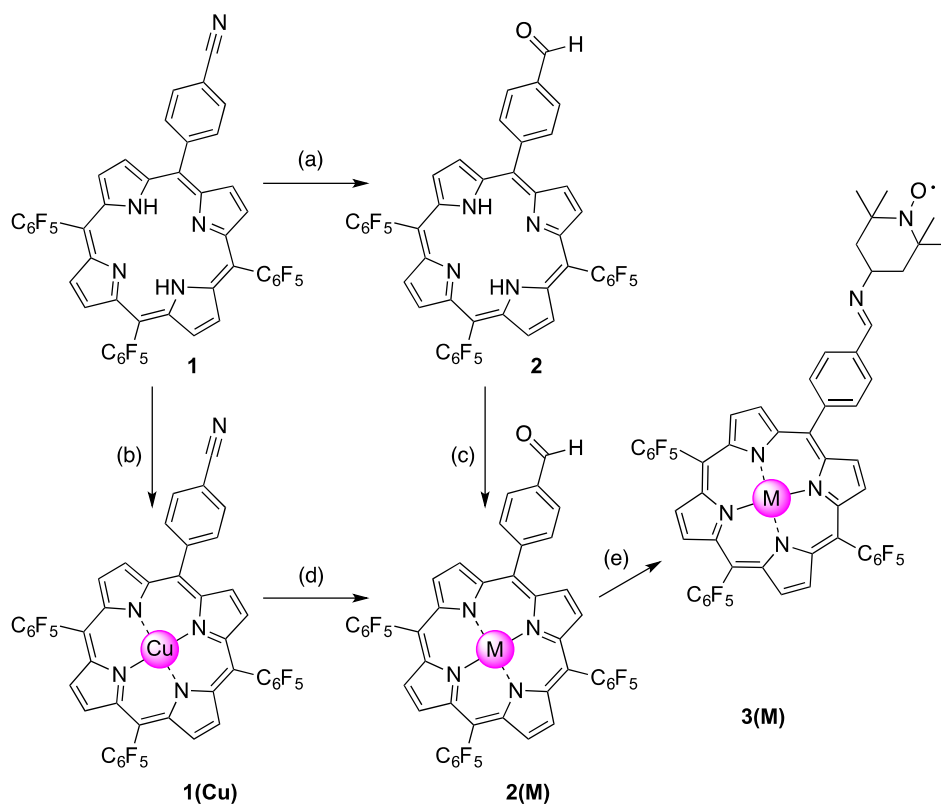


Figure 3.2. Synthetic route of 3(Cu) and 3(Ni). used in this study

3.2 Experimental Details

3.2.1 Steady State Absorption Spectroscopy

UV/Vis spectra were recorded at room temperature using a Perkin-Elmer Lambda 9 spectrophotometers.

3.2.2 Electron Paramagnetic Resonance Spectroscopy

Low temperature EPR measurements were performed on ~ 150 μM solutions of TEMPO radical porphyrins in 2-methyltetrahydrofuran (mTHF). The solutions were contained in quartz tubes with 2.40 mm o.d. and 2.00 mm i.d., subjected to three freeze—pump—thaw cycles on a vacuum line (10^{-4} Torr), and flame sealed with a hydrogen torch. EPR measurements were performed at X-band (~ 9.5 GHz) fields using a Bruker Elexsys E680-X/W spectrometer equipped with a split-ring resonator (ER4118X-MS3), or Bruker ESP300E X-Band, operating at a microwave frequency of 9.85GHz. Temperature was controlled using an Oxford Instruments CF935 continuous flow cryostat. All EPR measurements were made at X-band (~ 9.5 GHz) fields using a Bruker Elexsys E680-X/W spectrometer equipped with a split-ring resonator (ER4118X-MS3). For TREPR measurements, samples were photoexcited at 510 (Freebase), 550 (Zn), 526 (Ni) and 535 (Cu) nm (1.5 mJ/pulse, 7 ns, 10 Hz), respectively from the frequency-tripled output of a Nd:YAG laser. Continuous wave (CW) EPR spectra were measured with 0.1 mT magnetic field modulation at 100 kHz modulation frequency and non-saturating microwave power between 0.1 and 0.15 mW at 85K. TREPR measurements were performed using CW microwaves and direct detection. The kinetic traces of the transient signals were obtained using quadrature detection. Time traces were recorded over a range of magnetic field to yield 2D spectra which were processed by first subtracting the signal prior to the laser pulse for each kinetic trace at a given magnetic field

point and then subtracting the signal average at off-resonance magnetic field points from the spectra obtained at a given time.

Electron spin nutation experiments were performed through indirect detection of the longitudinal magnetization using a $P_{\text{NUT}} - t - \pi - \tau - \pi/2$ - echo pulse sequence placed 100 ns after the laser pulse, where P_{NUT} is a length incremented nutation pulse, π and $\pi/2$ are microwave pulses with widths of 16 ns and 32 ns. The time domain spectrum was then phase corrected, a constant DC offset was removed, tapered with a Hamming window and the real part was Fourier Transformed to yield the frequency nutation spectrum.

3.2.3 Transient Absorption Spectroscopy

The experimental detail of transient absorption spectroscopy was described in Section 2.5.4.

3.3 Results and Discussion

3.3.1 Steady State Continuous Wave EPR Spectroscopy

Steady-state continuous wave EPR (CW-EPR) measurements were conducted for **3**, **3(Zn)**, **3(Ni)** and **3(Cu)** at X band (9.5 GHz), as detailed in the Supporting Information, and shown in Figure 3.3. Porphyrins **3**, and **3(Zn)** are diamagnetic, hence, only the powder spectra of the TEMPO free radical are detected. For **3(Ni)**,¹¹⁴ it is assumed two mTHF molecules coordinate to the Ni, making it octahedral and paramagnetic in nature. However, the large dipolar coupling between the two unpaired electrons of the Ni renders the metal EPR silent at X-band (9.5 GHz).⁹¹ The spectra of **3(Cu)** show an additional multiplet at lower field due to hyperfine coupling of the copper unpaired electron with the four porphyrin ¹⁴N nuclei, which is characteristic of copper porphyrins.¹¹⁵

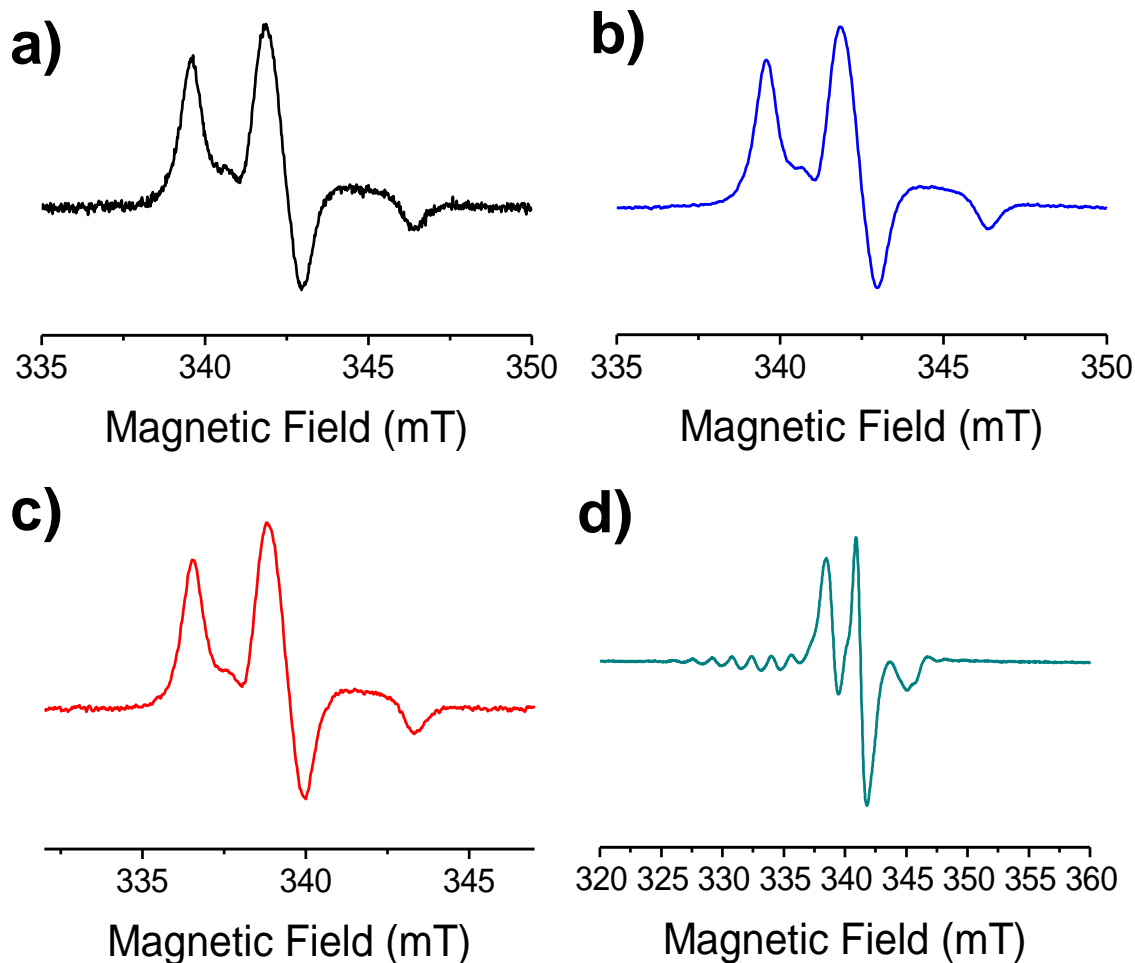


Figure 3.3. Steady-state CW EPR of (a) **3** (b) **3(Zn)** (c) **3(Ni)** (d) **3(Cu)** in mTHF at X-Band (9.5 GHz), obtained at 85K with 0.1 mT modulation amplitude.

3.3.2 Time Resolved EPR Spectroscopy

TREPR measurements were performed at 85 K in glassy mTHF following photoexcitation at the most intense Q band absorption ($S_1 \leftarrow S_0$ transition) for each sample.¹¹⁶ Porphyrins **3(Ni)** and **3(Cu)** did not yield any TREPR signals, most likely due to the strong spin-orbit (SO) coupling between the paramagnetic metal center and the porphyrin core,¹¹⁷ leading to enhanced intersystem crossing^{99, 102, 118} which shortens the lifetime of the porphyrin triplet excited states, *vide infra*. Shown in Figure 3.4 are the TREPR spectra of **2**, **3**, **2(Zn)** and **3(Zn)** recorded at 40 ns following

excitation. Free-base porphyrin, **2**, gives an EPR spectrum with an *e,a,e,a,e,a* (*a* = enhanced absorption, *e* = enhanced emission) polarization pattern (Figure 3.7), the result of selectively populating the $|T_y\rangle$ triplet sublevel due to spin-orbit intersystem crossing.¹¹⁹ Overlaid in red is a simulation of the triplet using the zero field parameters: $|D| = 1294$ MHz and $E/D = 0.118$, which falls within the range expected for a free-base porphyrin.¹²⁰ The spectrum of **3** exhibits the same polarization and has largely the same spectral shape as **2** with the exception of a small negative peak at 338 mT. This negative peak can be attributed to some nonzero coupling between the TEMPO radical and the triplet^{55,56}, however the small amplitude and lack of other spectral changes makes simulating the spectrum underdetermined. The porphyrin **2(Zn)**, Figure 3.4, shows an *a,a,a,e,e,e* polarization pattern which is consistent with selective population of the $|T_z\rangle$ triplet sublevel. Simulation of the triplet spectrum yields the zerofield parameters: $|D| = 995$ MHz and $E/D = 0.332$, the deviation of the spectrum from the simulation is due to some aggregation.¹²¹ The *D* value for **2** is around 30% larger than that of **2(Zn)**, which follows the trend of previous reported systems and is indicative of restricted spin delocalization around the porphyrin core in the presence of the two protons. The spectrum of **3(Zn)** shows significant changes relative to **2(Zn)**, a 6 mT splitting on the outer features along with a strong narrow absorptive line at 342 mT, for similar reasons to **3**, we will eschew from attempting to simulate the spectrum. The central peaks in both **3** and **3(Zn)** decay concomitantly with the broad features, Figure 3.8, which suggests that the central peak is a result of a spin coupled quartet species and not from transfer of polarization from the triplet to the TEMPO.

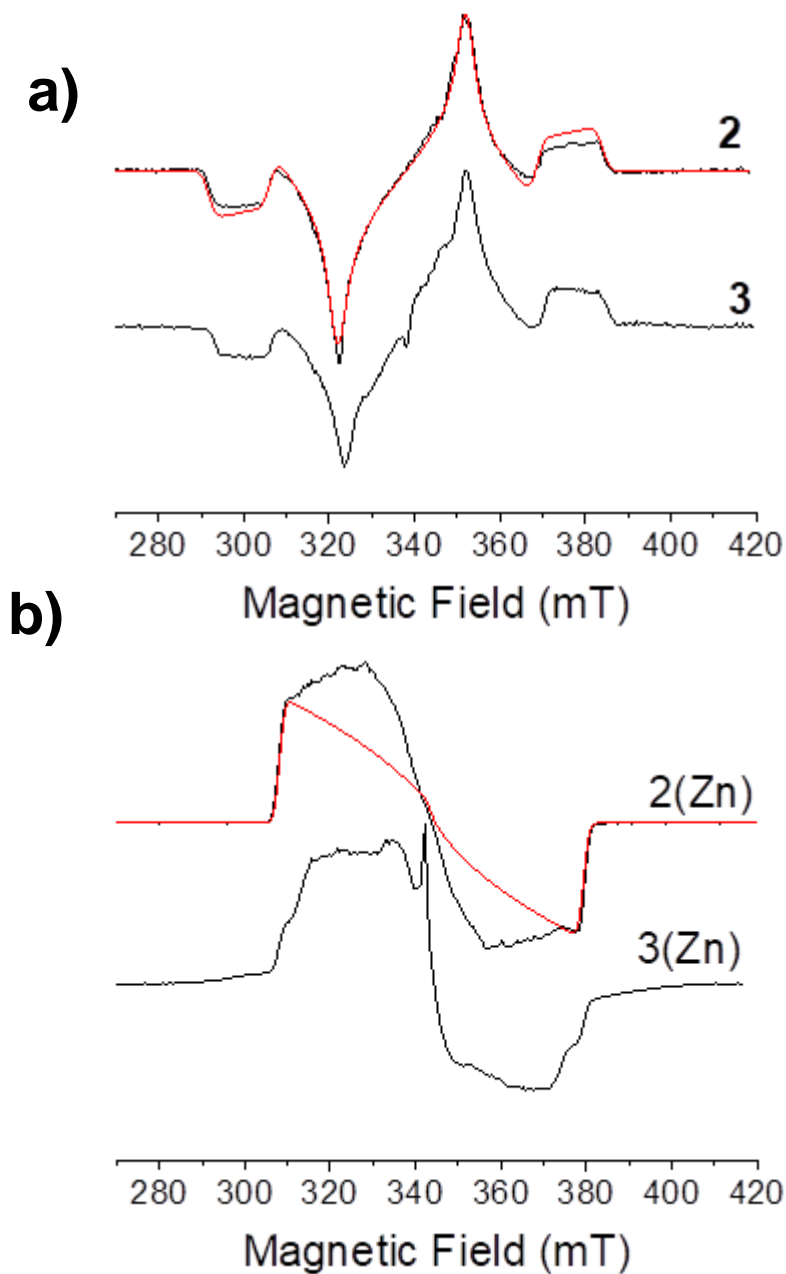


Figure 3.4. TREPR spectra in frozen mTHF at 85 K, at 40 ns following a 7 ns laser pulse, for: (a) 2 and 3; (b) 2(Zn) and 3(Zn).

3.3.3 Pulsed Transient Nutation EPR Spectroscopy

To further investigate the spin states of **3**, and **3(Zn)**, pulsed transient nutation EPR spectroscopy was performed. This technique provides information about the electron spin quantum number and the transition by measuring the nutation frequency of a spin upon irradiation with

resonant microwaves.^{122, 123} For transient nutation spectroscopy, **3** and **3(Zn)**, are ideally suited, in the dark state, they have an internal $S = 1/2$ standard by way of the TEMPO, which then allows for normalization of the nutation frequency and easy comparison to the photogenerated state. Figure 3.5 shows the nutation spectra acquired at the noted magnetic field points for **3** and **3(Zn)**, respectively. The nutation frequency of the TEMPO radical, shown in red, was collected prior to photoexcitation, following photoexcitation the nutation frequencies of the transient EPR features were collected and normalized to the frequency of the $S = 1/2$ TEMPO radical. Hence, $\omega = 1$ corresponds to the $m_s = -1/2$ to $m_s = 1/2$ transition for an $S = 1/2$ species. In Figure 4a, the feature at 329 mT for **3** has a nutation frequency of $\omega = 1.4 \approx \sqrt{2}$, which corresponds to the $m_s = \pm 1$ to $m_s = 0$ transitions of an $S = 1$ triplet state. At 333 mT and 370 mT in **3(Zn)**, Figure 4b, the nutation frequencies are: $\omega = 1.7$ and $\omega = 1.65$, respectively; which correspond closely to the expected frequency of the $m_s = \pm 1/2$ to $m_s = \pm 3/2$ transitions for an $S = 3/2$ quartet species.

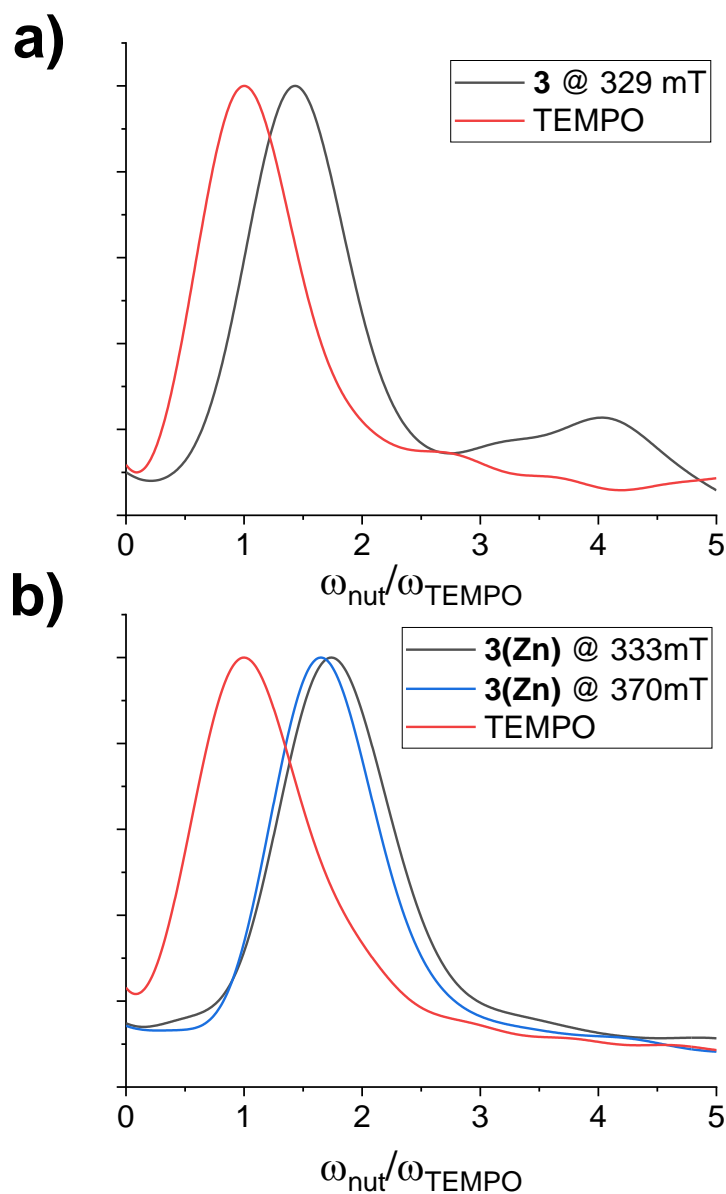


Figure 3.5. Echo-detected transient nutation spectra collected at 85K in mTHF for (a) **3**, (b) **3(Zn)** following the 510 nm and 550 nm, 7 ns, 2.5 mJ laser pulse, respectively. Peak positions are marked with dashed lines.

The combination of the TREPR and the transient nutation results provides an estimation of the magnitude of the coupling between triplet and radical in the excited states of **3** and **3(Zn)**. The TREPR spectrum of **3** shows evidence for coupling between the triplet and the radical however the transient nutation suggests that the photogenerated triplet is only weakly coupled to the

TEMPO and the EPR spectrum remains essentially that of a triplet and radical. In this case weak coupling means that the exchange coupling is much smaller than the triplet zero field splitting.^{56,}

¹²⁴ Whereas in **3(Zn)**, the TREPR more obviously demonstrates a moderate to strong coupling between the triplet and radical, and the nutation frequencies clearly demonstrate that the quartet is an eigenstate of the spin Hamiltonian. This means that the exchange coupling between triplet and radical in **3(Zn)** is greater than the zero field splitting (ZFS) of the triplet. The increase of the exchange interaction from **3** to **3(Zn)** can be explained by more delocalization of the triplet electronic structure in the presence of Zn, as evidenced by the decrease of the ZFS D value from **2** to **2(Zn)**. Freebase porphyrin is also known to have a nonplanar structure as opposed to planar zinc porphyrin molecules, which also results in less orbital overlap, thus decrease of exchange interaction with appended radical.

3.3.4 Transient Absorption Spectroscopy

Transient absorption (TA) spectroscopy studies on **2**, **3**, **2(Zn)** and **3(Zn)** determined the effect of EISC on the singlet excited-state lifetimes of free-base porphyrin and zinc porphyrin in the presence of nitroxide radicals. Comparison of the relative quenching rates provides qualitative information on the exchange coupling between nitroxide radical and porphyrin triplet state.

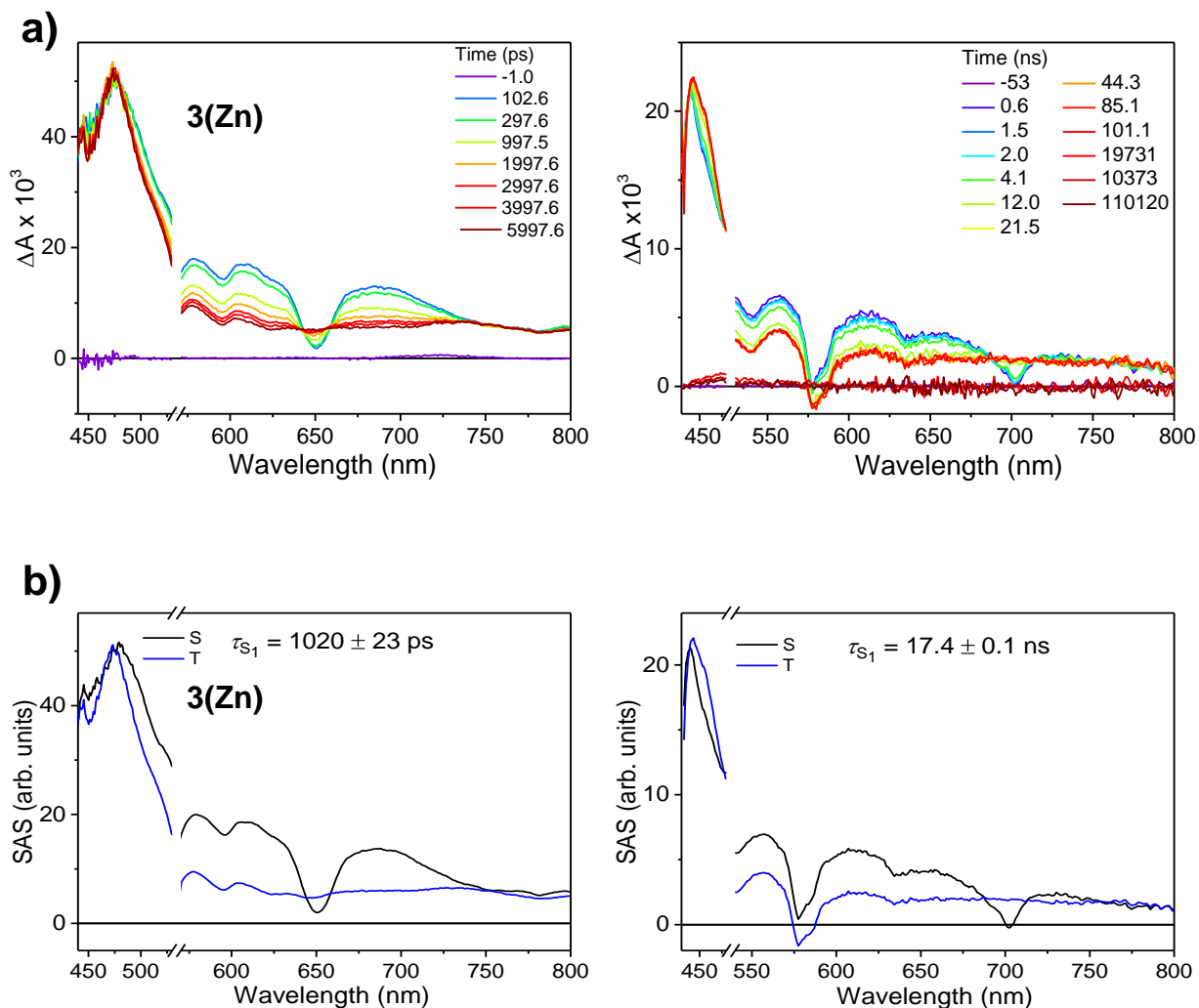


Figure 3.6. Transient absorption spectra and species-associated spectra of **3** and **3(Zn)**. (a) Transient absorption spectra of **3** and **3(Zn)** in 2-methyl THF at 85 K following $\lambda_{\text{ex}} = 550$ nm and $\lambda_{\text{ex}} = 510$ nm respectively. (b) Species-associated spectra of **3** and **3(Zn)** resulting from the global fitting of the data to an $A \rightarrow B$ model.

Photoexcitation of **3** and **3(Zn)** in mTHF at 85 K populates the excited singlet state of Zn porphyrin or free-base porphyrin, followed by intersystem crossing (ISC) to the porphyrin triplet states as seen by the depletion of the stimulated emission at 650 nm for **3** and 700 nm for **3(Zn)** (Figure 3.6.). Global fitting of the spectra to an $A \rightarrow B$ model yields the species-associated spectra (SAS) along with the singlet excited-state lifetimes of $\tau_{S_1} = 1.02$ ns for **3(Zn)** and $\tau_{S_1} = 17.4$ ns for

3. Compound **2** and **2(Zn)** yielded TA spectra with similar features but different lifetimes (See Section 3.5. Supplementary Information). The lifetimes for the four compounds and the relative enhancement of the decay rates due to EISC are summarized in the Table 3.1. The ISC rate of zinc porphyrin in **3(Zn)** is increased by 66%, whereas a relatively moderate enhancement of 14% is observed for ISC rate of free-base porphyrin in **3**. The higher increase in the ISC rate of **3(Zn)** indicates stronger exchange interaction between porphyrin triplet states and radical, which agrees with the EPR measurement of observing quartet states for **3(Zn)**.

Table 3.1. Singlet lifetimes ($\tau = 1/k$) for **2**, **2(Zn)**, **3** and **3(Zn)** and increase of rates for **3** and **3(Zn)**

Compound	S ₁ Lifetimes (ns)	Increase of decay rate %
2(Zn)	1.69 ± 0.04	
3(Zn)	1.02 ± 0.02	65.7 ± 7.2
2	19.8 ± 0.1	
3	17.4 ± 0.1	13.8 ± 0.3

3.4 Conclusion

We have investigated their photoexcited spin-state properties of a series of metallated porphyrins appended with the TEMPO SFR and. The porphyrins were fully characterized and then investigated via a series of EPR experiments. TREPR spectra for the free-base porphyrin and Zn derivatives show distinguishable polarization patterns due to change in magnitude of the exchange coupling between the porphyrin triplet state and the SFR. In addition, EPR transient nutation experiments elucidated that metalation with Zn turns on the exchange coupling between the

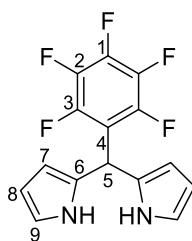
porphyrin triplet excited state and the TEMPO doublet state yielding an overall quartet state. This change in exchange coupling through metalation was further confirmed by TA experiments which determined a greater enhancement of ISC for the Zn porphyrin versus the free-base porphyrin when appended with TEMPO. Hence, we have realized a switchable exchange coupling through simple metalation. These results enable the possibility of employing metalation as switchable couplers for multi-qubit systems. Further studies will include varying the nature of the appended SFR, the number of appended SFR's, and the position of substitution (*meso* vs. β) to expand our library of multi-spin porphyrins for potential quantum information applications.

3.5 Supplementary Information

3.5.1 Synthesis

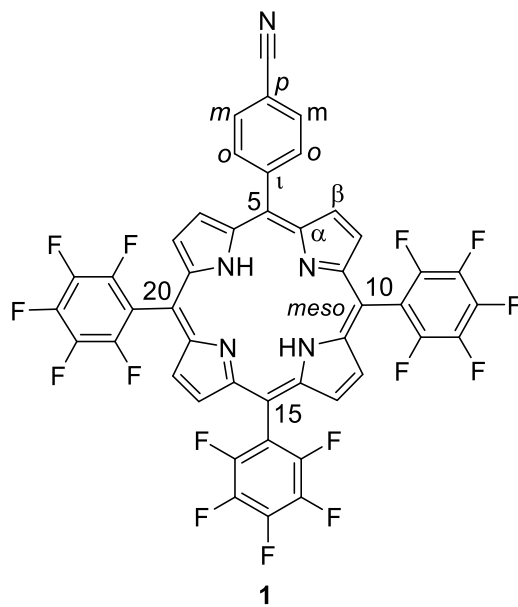
Solvents for chromatography including technical grade ethyl acetate, hexane and dichloromethane were distilled prior to use with a rotary evaporator. Dichloromethane (DCM) used for the porphyrin condensation was purified through SPS system. Methanol for the recrystallization were HPLC grade. Chloroform-*d* and pyrrole were purified directly before using by passing through a basic alumina column. Trifluoroacetic acid (TFA), 2,3,4,5,6-pentafluorobenzaldehyde, 4-cyanobenzaldehyde, 4-Amino-2,2,6,6-tetramethylpiperidinyloxy free radical, propionic acid DIBAL-H (1M solution in DCM) and 2,3-dichloro-5,6-dicyano-1,4-benzoquinone (DDQ) were used without further purification. Thin Layer Chromatography was performed on silica, or Al₂O₃ TLC plates and visualized by illumination with an UV lamp (254 nm and 365 nm wavelength). Silica gel (0.04–0.063 mm) was used as received. Al₂O₃ was used as received or deactivated with addition of water (3 mL for 100 g of Al₂O₃ for GII and 6 mL for 100 g of Al₂O₃ for GIII respectively) and shaking until warming ceased. Size exclusion chromatography was performed on Bio-Beads™ S-X3 Resin with toluene as an eluent. All NMR spectra were

recorded at 298 K on 400 MHz, 600 MHz and 700 MHz Bruker Avance III spectrometers. ^1H and ^{13}C shifts were referenced to the residual solvent signal. The ^{19}F signals were measured in the presence of an inset with TFA as the external reference. All assignments were obtained with a combination of 2D experiments (COSY, NOESY, HSQC and HMBC (^{13}C and ^{19}F)). Mass spectrometry measurements were recorded on a maXis 4G-UHR-TOF Bruker Daltonics spectrometer using the electrospray technique.



5-(pentafluorophenyl)-dipyrromethane.^{125, 126} Based on a previously reported literature procedure, 0.595 μL (4.82 mmol) of Pentafluorobenzaldehyde was added to 15 mL (216 mmol) of pyrrole (passed prior to use through basic alumina plug) and the reaction mixture was purged with nitrogen for 20 min. Then 93 μL (1.20 mmol) of TFA was added dropwise. The mixture was left stirring for additional 30 min. The reaction was diluted with ethyl acetate and quenched with 4 mL of 2 M $\text{NaOH}_{(\text{aq})}$. The organic phase was separated, washed twice with water, dried over $\text{MgSO}_{4(\text{s})}$, filtered and evaporated. The resulting greenish oil was chromatographed on a silica gel column with ethyl acetate/hexane/TEA 2:8:0.1 as the eluent. A second straw yellow fraction was the majority product ($R_f = 0.38$, ethyl acetate/hexane 2:8) and was collected and dried yielding 1.05 g of product as a white amorphous solid. Yield: 70 %. ^1H NMR (600.0 MHz, chloroform-*d*, 298 K): $\delta = 8.10$ (bs, 2H, NH), 6.73 (m, 2H, 9-pyrrole), 6.17 (m, 2H, 8-pyrrole), 6.03 (m, 2H, 7-pyrrole), 5.90 (s, 1H, 5) ^{13}C NMR (150.9 MHz, chloroform-*d*, 298 K): $\delta = 145.1$ (dm, $^1J = 253$ Hz, 3), 140.5 (dm, $^1J = 253$ Hz, 1), 137.9 (dm, $^1J = 253$ Hz, 2), 128.2 (6), 118.3 (9), 115.8 (t, $^2J = 17$ Hz, 4),

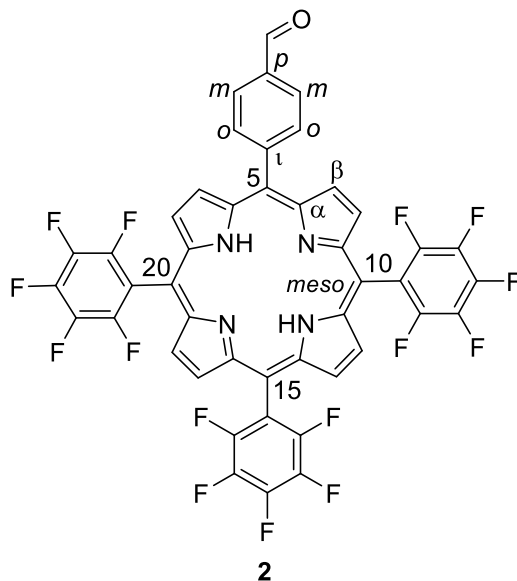
108.8 (8), 107.8 (7), 33.2 (5) ^{19}F NMR (564.7 MHz, chloroform-*d*, 298 K) δ = -140.5 (d, 2F, 3J = 21 Hz, 3), -154.7 (t, 1F, 3J = 21 Hz, 1), -160.2 (td, 2F, 3J = 21 Hz, 4J = 7 Hz, 2), HRMS *m/z*: observed 312.0693 (expected 312.0680 calculated for $[\text{C}_{15}\text{H}_9\text{N}_2\text{F}_5]^+$). m.p. 130 °C.



(5-(4-Cyanoophenyl)-10,15,20-tris(pentafluorophenyl))porphyrin (1)

(Pentafluorophenyl)dipyrromethane (0.56 g, 1.78 mmol, 2.2 equiv.) and 4-cyanobenzaldehyde (0.15 g, 1.13 mmol, 1.4 equiv.) were placed in a 500 mL flask and 250 mL of DCM was added under argon atmosphere. 2,3,4,5,6-Pentafluorobenzaldehyde (0.1 mL, 0.81 mmol, 1 equiv.) was added. The reaction mixture was left stirring for 15 minutes and $\text{BF}_3 \cdot \text{OEt}_2$ (0.068 mL, 0.54 mmol). The reaction mixture was left stirred under argon atmosphere with protection from light for 60 min. at rt. Afterwards DDQ (0.55 g, 2.42 mmol, 3 equiv.) was added and the flask was left stirred for additional 60 minutes. Then the solvent was removed under reduced pressure and the crude product was dissolved in toluene and chromatographed on silica gel column. The second UV-glowing fraction (R_f = 0.66, toluene) was collected, dried and recrystallized from hexane yielding 133.5 mg of red amorphous solid. Yield: 18 %. ^1H NMR (700.0 MHz, chloroform-*d*, 298 K): δ = 8.96-8.81

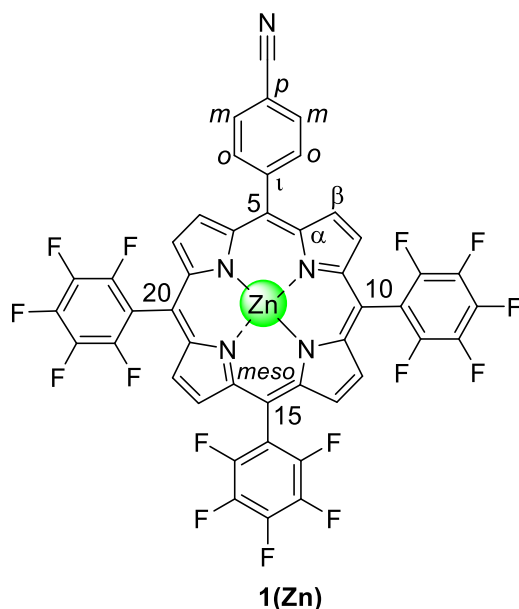
(m, 8H, β -pyrrole), 8.35 (d, $^3J = 8$ Hz, 2H, 5-*o*), 8.12 (d, $^3J = 8$ Hz, 2H, 5-*m*), -2.88 (s, 2H, NH)
 ^{13}C NMR (176.0 MHz, chloroform-*d*, 298 K): $\delta = 146.6$ (d, $^1J = 253$ Hz, 10, 15, 20-*o*), 146.0 (5-*i*), 142.4 (d, $^1J = 253$ Hz, 10, 15, 20-*p*), 137.7 (d, $^1J = 253$ Hz, 10, 15, 20-*m*), 135.0 (5-*o*), 130.9 (5-*m*), 134.6–127.0 (β signals shows large broadening due to exchange between NH tautomeric form¹²⁷⁻¹³⁰), 120.4 (5-*p*), 118.9 (CN), 116.2–115.5 (m, 10, 15, 20-*i*), 112.8 (5- meso), 103.5 (10, 20-meso), 102.7 (15-meso). The α signals are not observed because of extensive broadening due NH tautomerization¹²⁷⁻¹³⁰. ^{19}F NMR (376.5 MHz, chloroform-*d*, 298 K) $\delta = -135.4$ (dd, 2F, $^3J = 23$ Hz, $^4J = 8$ Hz, 15-*o*), -135.5 (dd, 4F, $^3J = 23$ Hz, $^4J = 8$ Hz, 10, 20-*o*), -150.1– -150.3 (m, 3F, 10, 15, 20-*p*), -160.1– -160.3 (m, 6F, 10, 15, 20-*m*), HRMS *m/z*: observed 910.1097 (expected 910.1083 calculated for $[\text{C}_{45}\text{H}_{14}\text{N}_5\text{F}_{15}+\text{H}]^+$).



(5-(4-Formyl)-10,15,20-tris(pentafluorophenyl))porphyrin (2). Route A: Under argon atmosphere, **1** (33 mg, 0.036 mmol) was dissolved in 25 mL of DCM. Then 2 equiv. of DIBAL-H (73 μL , 0.073 mmol, 1M solution in DCM) was added, and the reaction mixture was left stirring for 1h 50min. Then approx. 8 mL of saturated $\text{NH}_4\text{Cl}_{(\text{aq})}$ was added and reaction mixture was left

stirring for an additional 40 min. The organic phase was separated, washed twice with water, dried over $\text{MgSO}_{4(s)}$, filtered and evaporated under reduced pressure. The crude product was then chromatographed on silica gel with DCM as eluent. A quick moving red fraction was collected and dried yielding 12.1 mg of **2** as a red amorphous solid. Yield: 37 %. Route B: Demetallation of **2**(Zn). **2**(Zn) (34 mg, 0.035 mmol) was dissolved in 20 mL of DCM then TFA was added dropwise from a Hamilton syringe in 10 equiv. portions over 5 minute intervals of stirring time. The addition of TFA led to a change of reaction mixture color from red to violet, and then to lazure blue. The reaction was monitored by TLC and the TFA was added until no more starting material was observed on TLC plate. Then 20 mL of water was added which led to color change from lazure blue to red. The reaction mixture was left stirring for additional 10 minutes. The phases were separated, and the organic phase was washed 3x with water, dried over $\text{MgSO}_{4(s)}$, filtered and evaporated. The crude product was then chromatographed on silica gel with DCM as eluent. A fast-moving red fraction was collected and dried yielding 31.8 mg of **2** as a red amorphous solid. Yield: 93 %. ^1H NMR (700.0 MHz, chloroform-*d*, 298 K): δ = 10.41 (s, 1H, Aldehyde), 8.99–8.83 (m, 8H, β -pyrrole), 8.41 (d, 3J = 8 Hz, 2H, 5-*o*), 8.32 (d, 3J = 8 Hz, 2H, 5-*m*), -2.83 (s, 2H, NH) ^{13}C NMR (176.0 MHz, chloroform-*d*, 298 K): δ = 192.3 (Aldehyde), 147.4 (5-*i*), 146.7 (d, 1J = 253 Hz, 10, 15, 20-*o*), 142.4 (d, 1J = 253 Hz, 10, 15, 20-*p*), 137.7 (d, 1J = 253 Hz, 10, 15, 20-*m*), 136.2 (5-*p*), 135.3 (5-*o*), 134.6–128.0 (β signals shows large broadening due to exchange between NH tautomeric form¹²⁷⁻¹³⁰), 128.3 (5-*m*), 121.3 (5-meso), 116.2–115.6 (m, 10, 15, 20-*i*), 103.4 (10, 20-meso), 102.5 (15-meso), The α signals are not observed because of extensive broadening due NH tautomerization¹²⁷⁻¹³⁰. ^{19}F NMR (376.5 MHz, chloroform-*d*, 298 K) δ = -137.5 (dd, 2F, 3J = 23 Hz, 4J = 8 Hz, 15-*o*), -137.6 (dd, 4F, 3J = 23 Hz, 4J = 8 Hz, 10, 20-*o*), -152.3– -152.5 (m, 3F, 10,

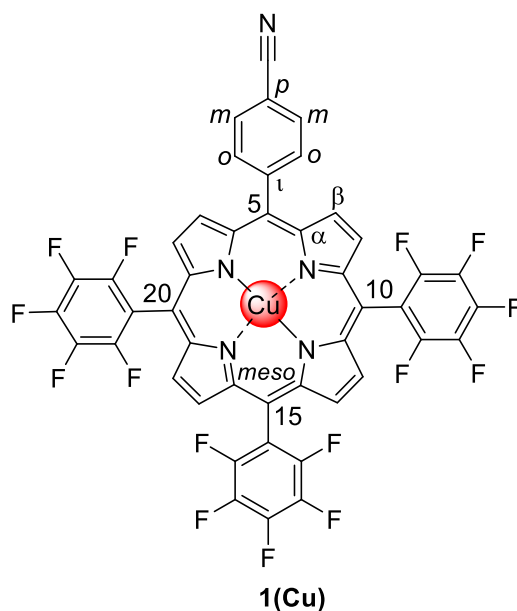
15, 20-*p*), -162.2– -162.5 (m, 6F, 10, 15, 20-*m*), HRMS *m/z*: observed 913.1075 (expected 913.1079 calculated for $[C_{45}H_{15}N_4F_{15}O+H]^+$).



(5-(4-Cyano phenyl)-10,15,20-tris(pentafluorophenyl)) porphyrinatoZn(II) (1(Zn)). 1

(40 mg, 0.043 mmol) was dissolved in 30 ml of $CHCl_3$. Then 10 equiv. (81 mg, 0.43 mmol) of $Zn(AcO)_2 \cdot 2H_2O$ dissolved in 5 ml of MeOH was added. The reaction mixture was heated to $85^\circ C$ for 2 hours. The solvents were removed under reduced pressure with a rotary evaporator, and the crude mixture dissolved in Toluene. The remaining inorganic salt was filtered off, and toluene was removed under reduced pressure with the rotary evaporator. The crude product was chromatographed on silica gel with DCM as an eluent. The main pink fraction was collected and evaporated, yielding 41.3 mg of amorphous violet solid. Yield: 99 %. 1H NMR (700.0 MHz, chloroform-*d*, 298 K): δ = 9.05-9.00 (m, 4H, β -pyrrole), 8.98-8.92 (m, 4H, β -pyrrole) 8.34 (d, 3J = 8 Hz, 2H, 5-*o*), 8.01 (d, 3J = 8 Hz, 2H, 5-*m*), ^{13}C NMR (176.0 MHz, chloroform-*d*, 298 K): δ = 150.6 (α -pyrrole), 150.1 (2x α -pyrrole), 150.1 (α -pyrrole), 147.1 (5-*t*), 146.7 (d, 1J = 253 Hz, 10,

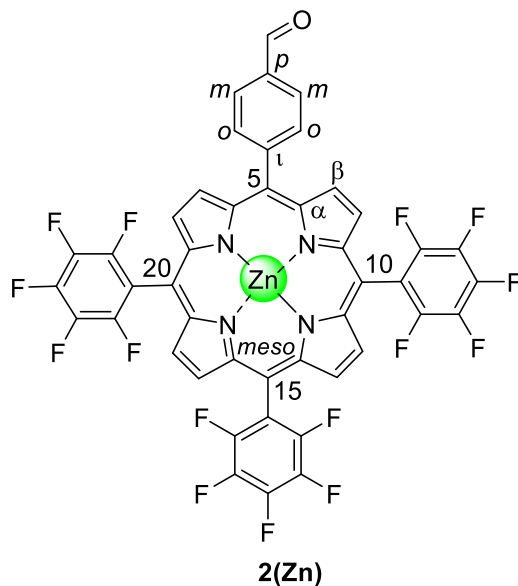
15, 20-*o*), 142.2 (d, $^1J = 253$ Hz, 10, 15, 20-*p*), 137.7 (d, $^1J = 253$ Hz, 10, 15, 20-*m*), 134.9 (5-*o*), 133.5 (β -pyrrole 7, 23), 132.2 (β -pyrrole 12, 18 or 13, 17), 132.0 (β -pyrrole 12, 18 or 13, 17), 131.2 (β -pyrrole 8, 22), 130.5 (5-*m*), 121.0 (5-*p*), 118.5 (CN), 117.0-116.5 (m, 10, 15, 20-*t*), 111.8 (5-meso), 104.0 (10, 20-meso), 103.2 (15-meso). ^{19}F NMR (376.5 MHz, chloroform-*d*, 298 K) $\delta = -135.6$ — -136.0 (m, 6F, 10, 15, 20-*o*), -150.7 — -151.0 (m, 3F, 10, 15, 20-*p*), -160.4 — -160.8 (m, 6F, 10, 15, 20-*m*), HRMS *m/z*: observed 1016.0140 (expected 1016.0127 calculated for $[\text{C}_{45}\text{H}_{12}\text{N}_5\text{F}_{15}\text{Zn}+\text{HCOO}]^-$).



(5-(4-Cyanoophenyl)-10,15,20-tris(pentafluorophenyl)) porphyrinatoCu(II) (1(Cu)).

Based on previously reported literature procedure¹³¹ **1** (36 mg, 0.039 mmol) was dissolved in 30 mL of CHCl_3 . Then 5 equiv. (39.4 mg, 0.20 mmol) of $\text{Cu}(\text{AcO})_2 \cdot \text{H}_2\text{O}$ dissolved in 5 mL of MeOH was added. The reaction mixture was heated to 85°C for 30 minutes. Then the solvents were removed under reduced pressure with a rotary evaporator and the crude mixture was chromatographed on a silica gel column with Toluene as the eluent. The main red fraction was

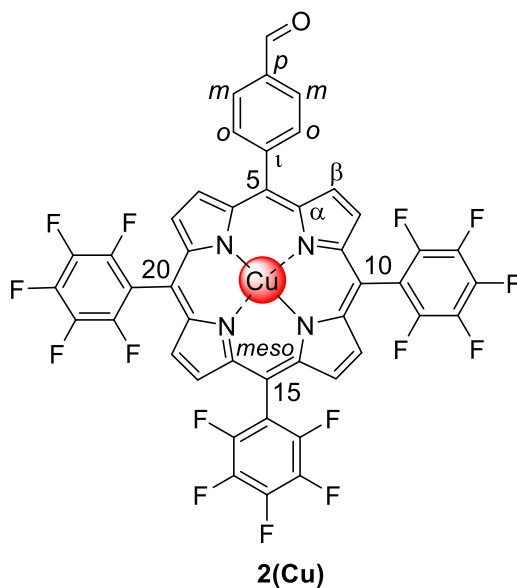
collected and evaporated, yielding 35.6 mg of amorphous red solid. Yield: 94 %. HRMS m/z : observed 970.0151 (expected 970.0155 calculated for $[\text{C}_{45}\text{H}_{12}\text{N}_5\text{F}_{15}\text{Cu}]^+$)



(5-(4-Formyl)-10,15,20-tris(pentafluorophenyl)) porphyrinatoZn(II) (2(Zn)). Under argon atmosphere **1(Zn)** (50 mg, 0.051 mmol) was dissolved in 25 mL of DCM. Then 2 equiv. of DIBAL-H (103 μL , 0.103 mmol, 1M solution in DCM) was added, and the reaction mixture was left stirring for 1h 50min. Then approx. 8 mL of saturated $\text{NH}_4\text{Cl}_{(\text{aq})}$ was added and reaction mixture was left stirring for an additional 40 min. The organic phase was separated, washed twice with water, dried over $\text{MgSO}_{4(\text{s})}$, filtered and evaporated under reduced pressure. The crude product was then chromatographed on silica gel with DCM as eluent. A fast-moving pink fraction was collected and dried yielding 47.1 mg of **2(Zn)** as a violet amorphous solid. Yield: 95 %.

^1H NMR (700.0 MHz, chloroform- d , 298 K): δ = 10.06 (s, 1H, Aldehyde), 9.03-8.99 (m, 4H, β -pyrrole 12, 13, 17, 18), 8.98 (d, 2H, 3J = 4,8 Hz, β -pyrrole 7, 23), 8.94 (d, 2H, 3J = 4,8 Hz, β -pyrrole 8, 22), 8.38 (d, 3J = 8 Hz, 2H, 5- o), 8.20 (d, 3J = 8 Hz, 2H, 5- m), ^{13}C NMR (176.0 MHz, chloroform- d , 298 K): δ = 192.4 (Aldehyde), 150.5 (α -pyrrole), 150.3 (α -pyrrole), 150.13 (α -

pyrrole), 150.06 (α -pyrrole), 148.4 (5-*t*), 146.7 (d, $^1J = 253$ Hz, 10, 15, 20-*o*), 142.2 (d, $^1J = 253$ Hz, 10, 15, 20-*p*), 137.6 (d, $^1J = 253$ Hz, 10, 15, 20-*m*), 135.7 (5-*p*), 135.1 (5-*o*), 133.8 (β -pyrrole 7, 23), 132.2 (β -pyrrole 12, 18 or 13, 17), 131.9 (β -pyrrole 12, 18 or 13, 17), 131.1 (β -pyrrole 8, 22), 128.1 (5-*m*), 122.0 (5-meso), 117.0-116.3 (m, 10, 15, 20-*t*), 104.1 (10, 20-meso), 103.2 (15-meso), ^{19}F NMR (376.5 MHz, chloroform-*d*, 298 K) $\delta = -135.8$ — -136.0 (m, 6F, 10, 15, 20-*o*), -151.0 — -151.2 (m, 3F, 10, 15, 20-*p*), -160.7 — -160.9 (m, 6F, 10, 15, 20-*m*), HRMS *m/z*: observed 1019.0123 (expected 1019.0142 calculated for $[\text{C}_{45}\text{H}_{13}\text{N}_4\text{OF}_{15}\text{Zn} + \text{HCOO}]^-$).



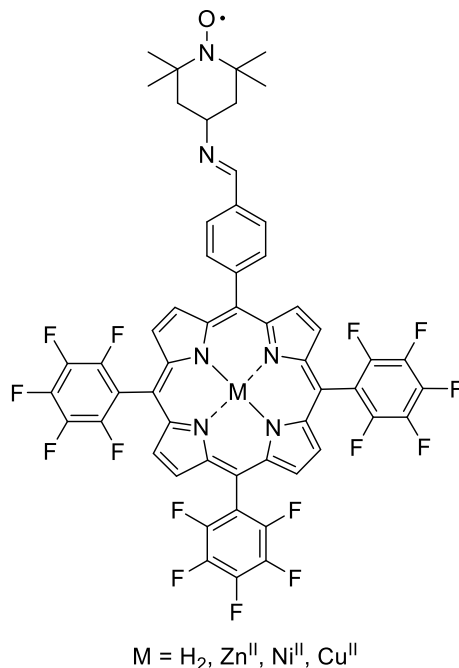
(5-(4-Formyl)-10,15,20-tris(pentafluorophenyl)) porphyrinatoCu(II) (2(Cu)). Route A:

Under argon atmosphere 1(Cu) (15 mg, 0.015 mmol) was dissolved in 25 mL of DCM. Then 4 equiv. of DIBAL-H (62 μL , 0.062 mmol, 1M solution in DCM) was added, and the reaction mixture was left stirring for 1h 50min. Then approx. 8 mL of saturated NH_4Cl (aq) was added and reaction mixture was left stirring for an additional 40 min. The organic phase was separated, washed twice with water, dried over MgSO_4 (s), and filtered followed by evaporation under reduced pressure. The crude product was then chromatographed on silica gel with DCM as eluent.

A fast-moving red fraction was collected and dried yielding 10.8 mg of 2(Cu) as a red amorphous solid. Yield: 74 %. Route B: 2 (30 mg, 0.033 mmol) was dissolved in 30 mL of CHCl₃. Then 5 equiv. (33 mg, 0.16 mmol) of Cu(AcO)₂•H₂O dissolved in 5 mL of MeOH was added. The reaction mixture was heated to 85°C for 1 hour. The solvents were removed under reduced pressure with a rotary evaporator and the crude mixture was chromatographed on silica gel column using Toluene as an eluent. The main red fraction was collected and evaporated yielding 28.2 mg of red amorphous solid. Yield: 88 %. HRMS m/z: observed 973.0151 (expected 973.0151 calculated for [C₄₅H₁₃N₄F₁₅OCu]-).

(5-(4-Formyl)-10,15,20-tris(pentafluorophenyl)) porphyrinatoNi(II) (2(Ni)). 2 (15 mg, 0.016 mmol) and 15 equiv. (61.3 mg, 0.25 mmol) of Ni(AcO)₂•4H₂O was dissolved in 5 ml of glacial acetic acid. The reaction mixture was heated to 130°C for 6 hours. Then the product was extracted with EtOAc, washed 3 times with water, dried over MgSO_{4(s)}, filtered and evaporated under reduced pressure. The crude product was recrystallized from DCM/hexane yielding 13 mg of red crystalline solid. Yield: 84 %. ¹H NMR (700.0 MHz, chloroform-*d*, 298 K): δ = 10.35 (s, 1H, Aldehyde), 8.80 (d, 2H, ³J = 4,8 Hz, β-pyrrole 7, 23), 8.79-8.76 (m, 4H, β-pyrrole 12, 13, 17, 18), 8.72 (d, 2H, ³J = 4,8 Hz, β-pyrrole 8, 22), 8.25 (d, ³J = 8 Hz, 2H, 5-*m*), 8.21 (d, ³J = 8 Hz, 2H, 5-*o*), ¹³C NMR (176.0 MHz, chloroform-*d*, 298 K): δ = 192.2 (Aldehyde), 146.4 (d, ¹J = 253 Hz, 10, 15, 20-*o*), 146.3 (5-*i*), 143.2 (α-pyrrole), 143.0 (α-pyrrole), 142.9 (α-pyrrole), 142.7 (α-pyrrole), 142.3 (d, ¹J = 253 Hz, 10, 15, 20-*p*), 137.7 (d, ¹J = 253 Hz, 10, 15, 20-*m*), 136.2 (5-*p*), 134.4 (5-*o*), 134.1 (β-pyrrole 7, 23), 132.5 (β-pyrrole 12, 18 or 13, 17), 132.3 (β-pyrrole 12, 18 or 13, 17), 131.6 (β-pyrrole 8, 22), 128.5 (5-*m*), 119.9 (5-meso), 115.0-114.6 (m, 10, 15, 20-*i*), 102.9 (10, 20-meso), 102.2 (15-meso), ¹⁹F NMR (376.5 MHz, chloroform-*d*, 298 K) δ = -134.6 (dd, 2F, ³J = 23 Hz, ⁴J = 8 Hz, 15-*o*), -134.7 (dd, 4F, ³J = 23 Hz, ⁴J = 8 Hz, 10, 20-*o*), -149.3– -149.6 (m,

3F, 10, 15, 20-*p*), -159.1– -159.4 (m, 6F, 10, 15, 20-*m*), HRMS *m/z*: observed 968.0216 (expected 968.0209 calculated for $[\text{C}_{45}\text{H}_{13}\text{N}_4\text{F}_{15}\text{ONi}]^-$).



Synthesis of TEMPO appended porphyrins (3(M)). General Procedure: Porphyrin (0.037 mmol) is dissolved in 5 ml of DCM. Then 0.5 g of neutral Alumina is added, followed by 10 equiv. of 4-Amino-2,2,6,6-tetramethylpiperidinyloxy, free radical (64 mg, 0.373 mmol). The reaction mixture is sonicated for 2h. The Alumina is filtrated off, and solvent is removed under reduced pressure with a rotary evaporator. The crude residue is dissolved in toluene and chromatographed on a SX-3 size-exclusion column. The first red fraction is collected and dried, yielding of red amorphous solid in $\geq 95\%$.

3.5.2 Time-Resolved Continuous-Wave Electron Paramagnetic Resonance (TREPR)

Spectroscopy

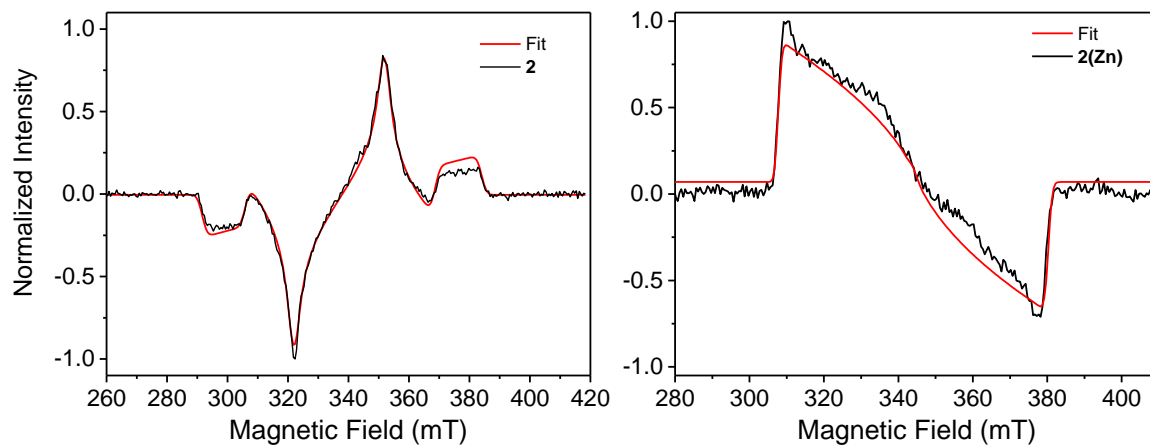
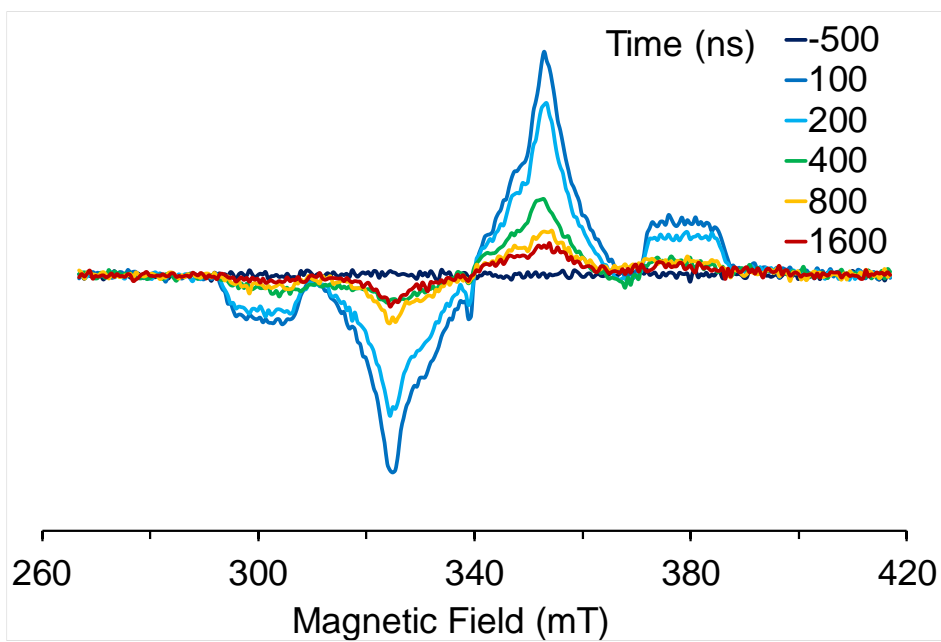


Figure 3.7. TREPR spectra obtained using direct detection at 85K in mTHF for (a) 2, (b) 2(Zn) after a 7 ns laser pulse, with the fit to ISC-Triplet models.

a)



b)

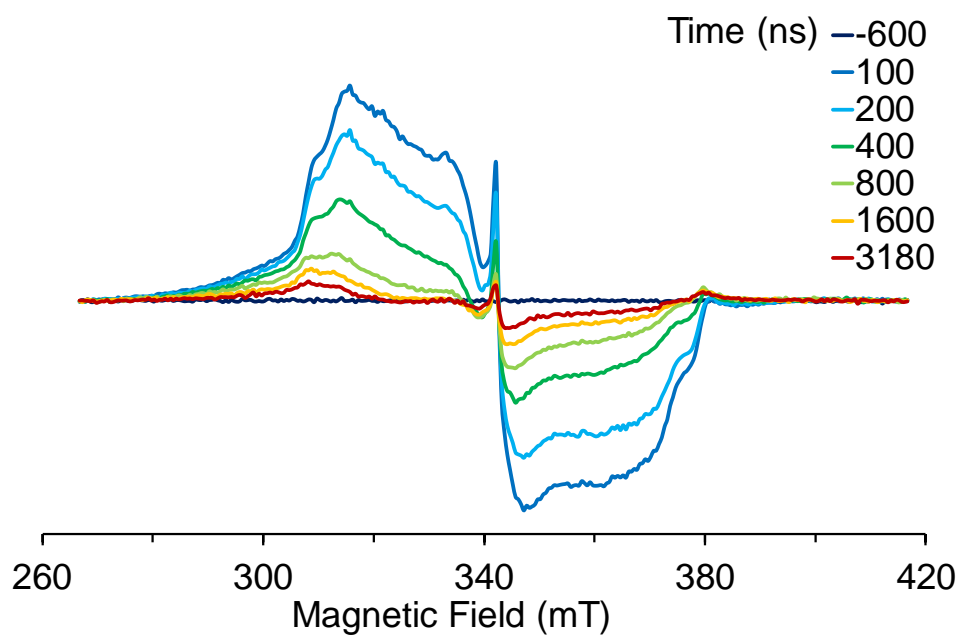


Figure 3.8. TREPR spectra obtained using direct detection at 85K in mTHF for (a) 3, (b) 3(Zn) after a 7 ns laser pulse.

3.5.3 Echo-Detected Transient Nutation Spectra

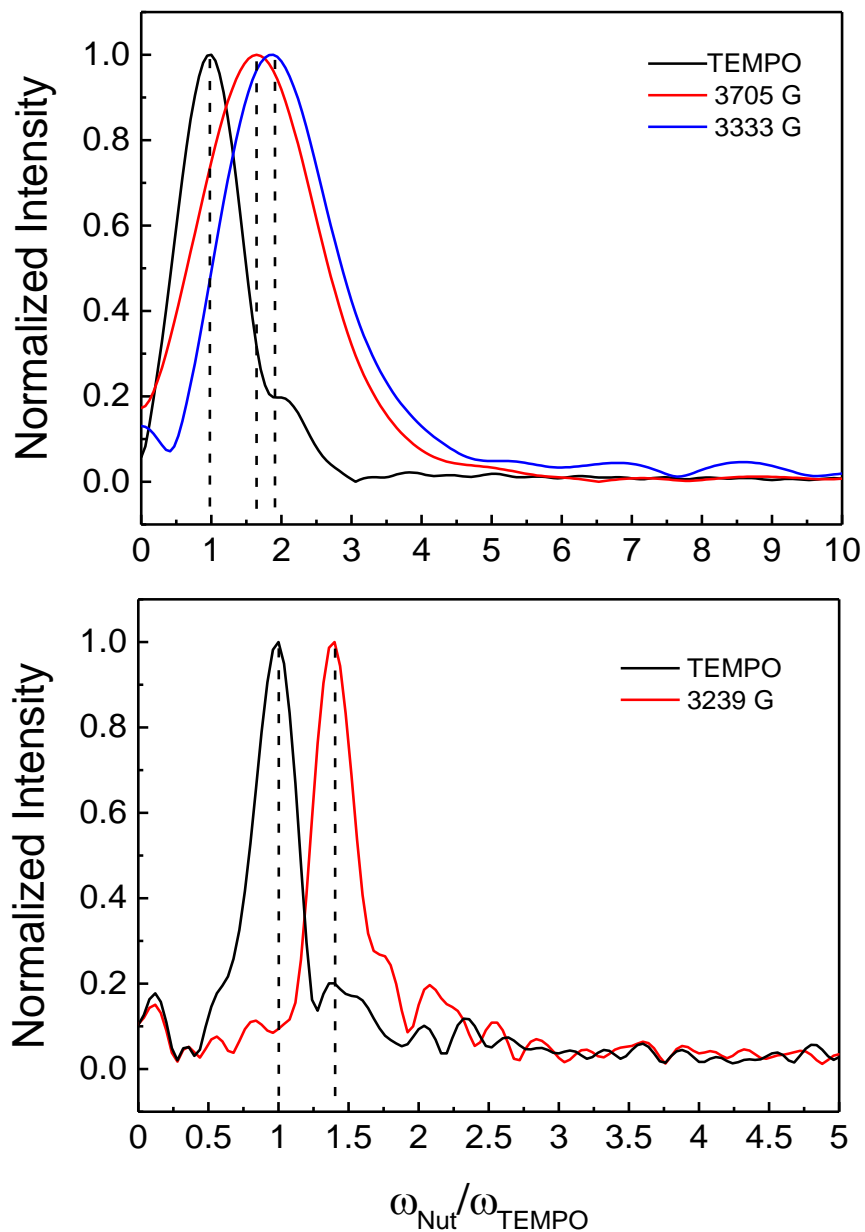


Figure 3.9. Echo-detected transient nutation spectra collected at 85K in mTHF for (Top) 3(Zn), (Bottom) 3 following the 510 nm and 550 nm, 7 ns, 2.5 mJ laser pulse, respectively. Peak positions are marked with dashed lines.

3.5.4 Transient Absorption Spectra

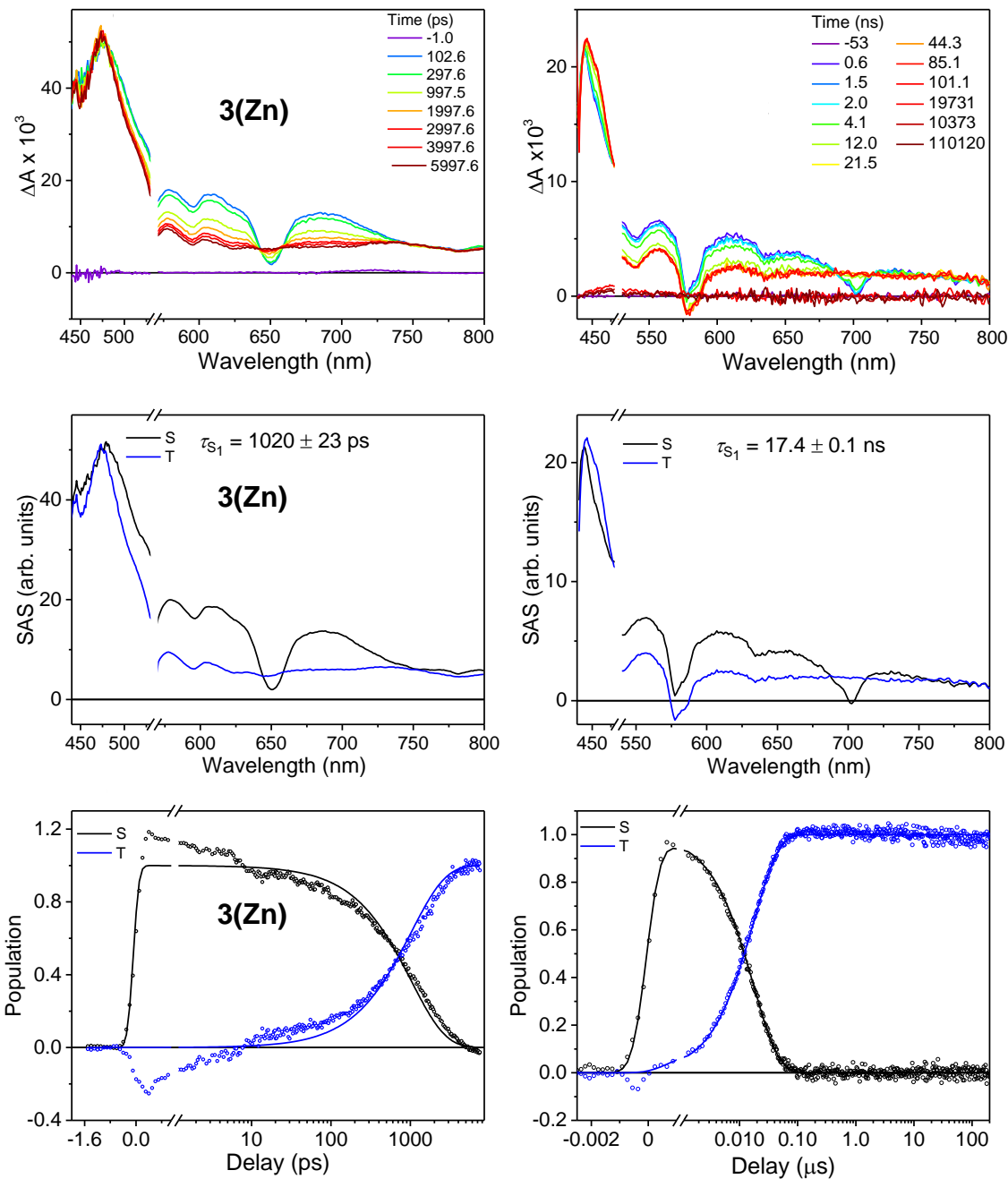


Figure 3.10. Transient absorption spectra, species-associated spectra and the global fitting of 3 and 3(Zn). (a) Transient absorption spectra of 3 and 3(Zn) in 2-methyl THF at 85 K following $\lambda_{ex} = 550$ nm and $\lambda_{ex} = 510$ nm respectively. (b) Species-associated spectra of 3 and 3(Zn) resulting from the global fitting of the data to an A \rightarrow B model. (c) Population curves and the fitting for 3 and 3(Zn) yielded from singular value decomposition to an A \rightarrow B model.

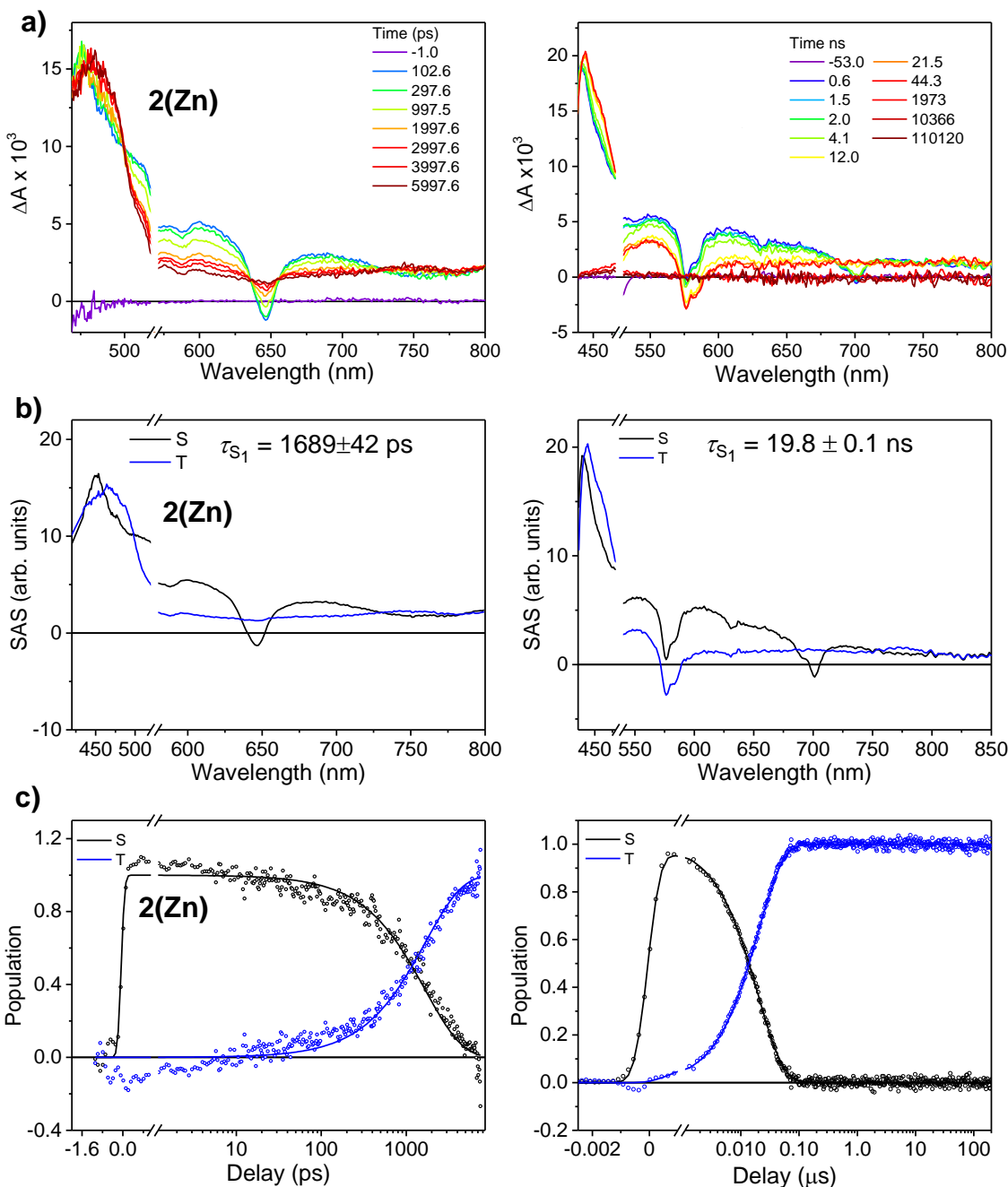


Figure 3.11. Transient absorption spectra, species-associated spectra and the global fitting of 2 and 2(Zn). (a) Transient absorption spectra of 2 and 2(Zn) in 2-methyl THF at 85 K following $\lambda_{ex} = 550$ nm and $\lambda_{ex} = 510$ nm respectively. (b) Species-associated spectra of 2 and 2(Zn) resulting from the global fitting of the data to an A \rightarrow B model. (c) Population curves and the fitting for 2 and 2(Zn) yielded from singular value decomposition to an A \rightarrow B model.

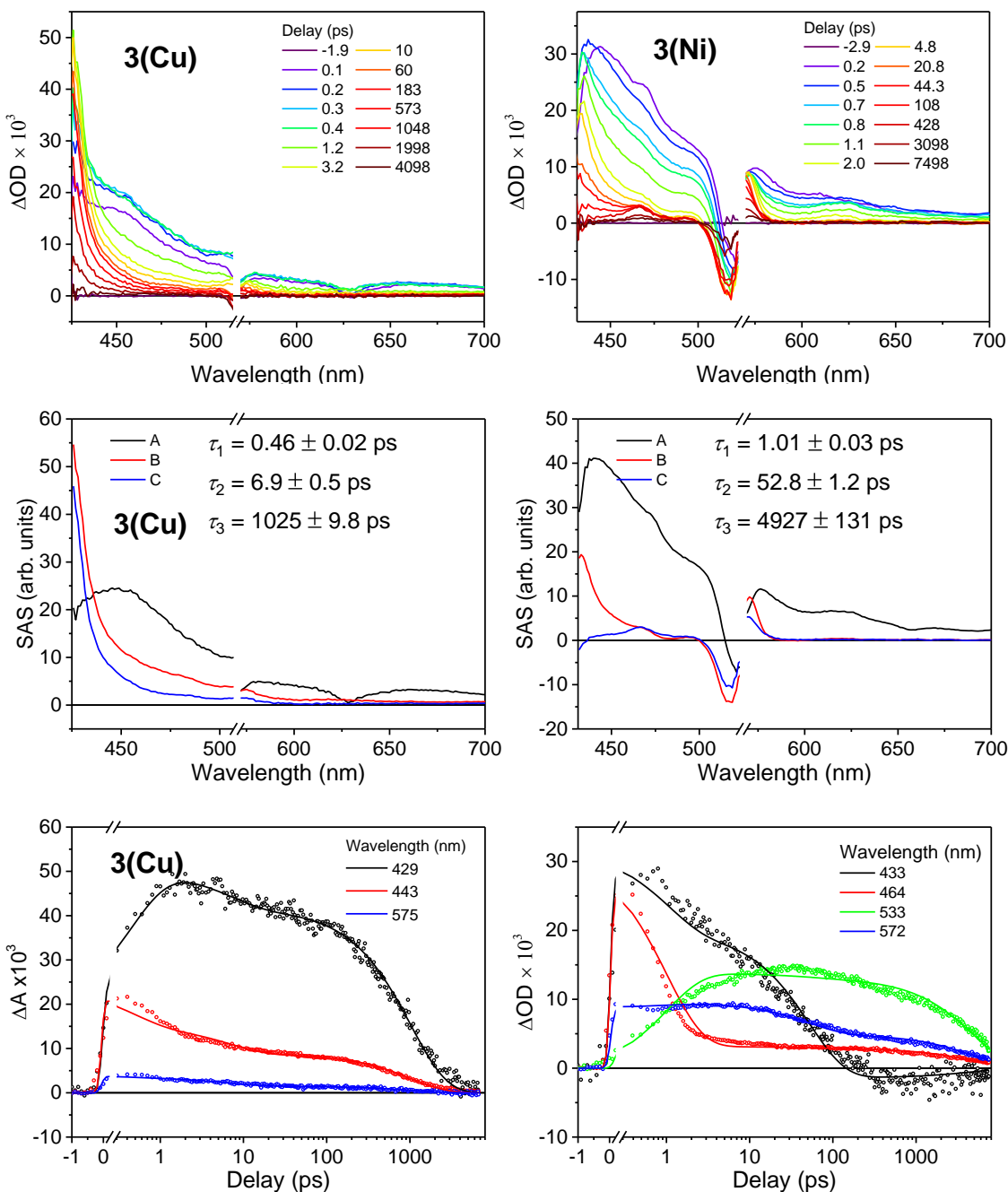


Figure 3.12. Femtosecond transient absorption spectra, species-associated spectra and the global fitting of 3(Cu) and 3(Ni). (a) Femtosecond transient absorption spectra of 3(Cu) and 3(Ni) in 2-methyl THF at 85 K following $\lambda_{ex} = 550$ nm and $\lambda_{ex} = 525$ nm respectively. (b) Species-associated spectra of 3(Cu) and 3(Ni) resulting from global fitting of the data to an A \rightarrow B \rightarrow C \rightarrow GS model. (c) Time traces at specified wavelengths for 3(Cu) and 3(Ni) and the global fitting to an A \rightarrow B \rightarrow C \rightarrow GS model.

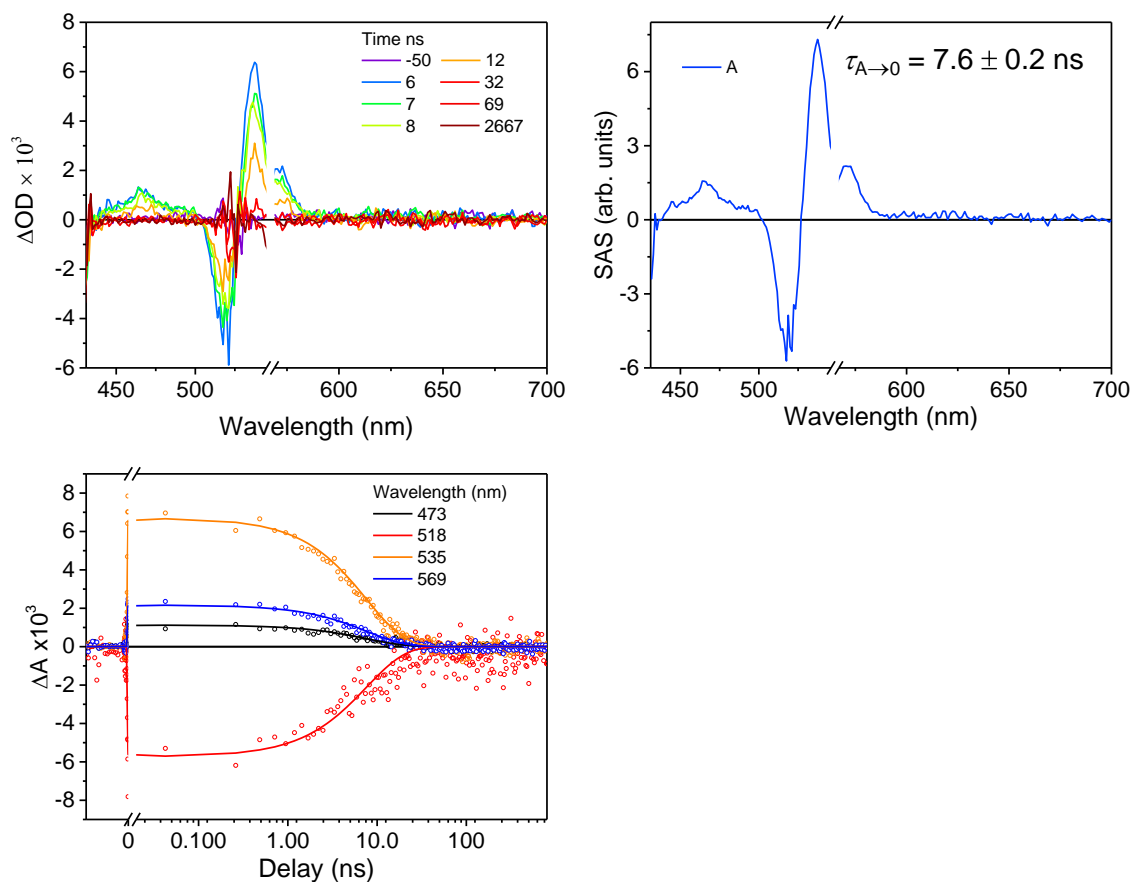


Figure 3.13. Nanosecond transient absorption spectra, species-associated spectra and the global fitting of 3(Ni). (a) Nanosecond transient absorption spectra of 3(Ni) in 2-methyl THF at 85 K following $\lambda_{\text{ex}} = 550$ nm. (b) Species-associated spectra of 3(Ni) resulting from global fitting of the data to an $A \rightarrow \text{GS}$ model. (c) Time traces at specified wavelengths for 3(Ni) and the global fitting to an $A \rightarrow \text{GS}$ model.

3.5.5 Computational Data

3 Doublet Ground State

F 2.7630330013 -4.9927858153 -2.2924631009
 F 0.3017445876 4.8911573879 -2.0525527705
 F 1.8491396706 4.9481455337 2.4236742216
 F 6.8538458043 -0.0288407766 2.0981537702
 F 6.4494528606 1.1171616384 -2.4803937435
 F 1.7050670694 -5.1753071617 2.3206051028
 F 3.0439674611 -7.6820245071 -2.3296285050
 F 2.6623014246 -9.1279826551 -0.0476757888
 F 1.9906581246 -7.8634256081 2.2751437386
 F 9.1273097332 1.4453861506 -2.6293725878
 F 10.6806547075 1.0423435282 -0.4234199896
 F 9.5289112671 0.3059380895 1.9421579084
 F 1.5223581736 7.6318070028 2.4968301558

F 0.5909802924 8.9560246741 0.3028180576
 F -0.0208415415 7.5741899488 -1.9709072602
 O -10.3854996340 2.0982533040 0.2765689946
 N 3.3119183093 -1.3797606364 -0.0144868107
 N 2.9111199341 1.5177557287 0.0355994621
 N -0.0062493686 1.2142496443 0.1962165260
 N 0.3936829540 -1.6818471817 0.1220100937
 N -10.3829751921 0.8451102825 -0.0084355324
 N -8.2173830544 -1.5716382623 -0.5605999487
 C -10.3685653346 0.4340479173 2.4035729123
 C -9.0824749121 1.1558560301 -2.0594515185
 C 3.7506960411 3.6912813937 -0.0084708292
 C 4.8137053233 2.8585817659 -0.0781902893

C 2.5664931836	-5.6762059512	-1.1573910123	C -1.2665144247	3.0778246351	0.2688242128
C 2.7191316964	-7.0603722413	-1.1906449642	C 0.0783455258	2.5844535579	0.2029155526
C 2.5224228928	-7.8004647694	-0.0271831930	C 1.2568231738	3.3454373857	0.1479815071
C 2.1783474328	-7.1535096580	1.1574508956	C 1.0832429118	4.8313986608	0.1839874615
C 2.0356944839	-5.7680317655	1.1661578290	C 1.3862680922	5.5705743725	1.3318409600
C 2.2213855515	-4.9963280409	0.0147727015	C 1.2285259280	6.9533374380	1.3823572068
C 2.0511404395	-3.5097082691	0.0354254923	C 0.7494312089	7.6311146617	0.2635469719
C 3.2274677194	-2.7516264945	-0.0168400063	C 0.4374745613	6.9244295460	-0.8954226307
C 4.5737786922	-3.2436224914	-0.0817939414	C 0.6083969826	5.5421666020	-0.9227689581
C 5.4180953602	-2.1682203282	-0.1233244232	H -0.4518016256	-4.9351492711	0.1405760013
C 4.6228896645	-0.9752613693	-0.0784889054	H -9.0845284696	1.0398528736	-3.1489933854
C 7.1841953947	0.9114148456	-1.3801629989	H -8.1777375372	0.6861064831	-1.6685752612
C 8.5629822034	1.0871188738	-1.4708499802	H -9.0649406893	2.2206936840	-1.8170221842
C 9.3577553560	0.8807670480	-0.3455222555	H -9.2743981011	0.4659925411	2.4085224431
C 8.7694861848	0.5031816722	0.8591315377	H -10.7011570076	-0.2394988199	3.2011562475
C 7.3879239092	0.3366955309	0.9252943614	H -10.7329395690	1.4408894744	2.6100035821
C 6.5623549990	0.5348797106	-0.1856397399	H -12.8917658231	-0.4310535980	0.1740075764
C 5.0798805217	0.3491551978	-0.1007098115	H 4.8491284328	-4.2879777406	-0.0914886932
C 4.2722223238	1.5020707334	-0.0510075583	H 6.4963327377	-2.1876407611	-0.1819676872
C 2.5668336273	2.8385458187	0.0658972145	H 5.8591666639	3.1261486067	-0.1398490856
C 0.7374123197	-3.0012637726	0.1009859379	H 3.7574019582	4.7720468578	-0.0140342223
C -0.4459031711	-3.8544260254	0.1511078864	H -1.5403032221	4.1222460407	0.2960793612
C -1.5112910482	-3.0226252394	0.2108044590	H 2.5163784414	-0.7502796185	0.0241688027
C -0.9718242520	-1.6654670785	0.1857140574	H 0.7886141393	0.5844741302	0.1503383332
C -3.9783945601	-1.1431792383	-0.8347202250	H -3.4340053968	-1.3413021338	-1.7538436702
C -5.3556394377	-1.3206358123	-0.7912084566	H -5.9040743908	-1.6559593090	-1.6654651141
C -10.3478943304	-1.0227759332	-1.6570649468	H -11.3794262408	-1.3923086452	-1.7248520651
C -11.5854491910	1.1375845378	-2.1570178249	H -9.8602961786	-1.2613913735	-2.6078091074
C -10.3535217522	0.5117556773	-1.4715083464	H -11.5465276564	0.9522576457	-3.2363800157
C -12.4467587271	0.0061256217	1.0744516418	H -12.5214089546	0.7172304672	-1.7753563392
C -10.9033380741	-0.0772988768	1.0546002202	H -11.5951666292	2.2171769648	-1.9857238742
C -10.4348499076	-1.5436295856	0.7952701163	H -12.7609629672	1.0517465228	1.1459419346
C -9.6598001035	-1.7918188219	-0.5159256267	H -12.8422824771	-0.5388365429	1.9395513823
C -7.5315571521	-1.2486020555	0.4618618975	H -11.3229582001	-2.1837904671	0.7505555308
C -6.0689482935	-1.0665982381	0.3916619045	H -9.8590237928	-1.9088443566	1.6525065127
C -5.3665782586	-0.6291419866	1.5225658477	H -9.7698715848	-2.8597274251	-0.7561776501
C -3.9855455528	-0.4445404951	1.4768199395	H -7.9697433704	-1.0806125939	1.4549673530
C -3.2713513969	-0.7023063460	0.2984048662	H -5.9058723907	-0.4307623047	2.4463080620
C -1.7853374643	-0.5151574712	0.2433517071	H -3.4525826229	-0.1090367866	2.3619881441
C -1.3201909468	0.8092164452	0.2484566173	H -2.5571679716	-3.2866217713	0.2700382470
C -2.1139385199	2.0029656312	0.2881644411	H -3.1928460082	2.0201042580	0.3234014496

3(Zn) Doublet Ground State

Zn 1.5703732513	-0.0784311298	0.0947142863	F 9.0276709747	1.3718881412	-2.6787140899
F 2.6822070219	-4.9708489411	-2.2998616778	F 10.5870944397	1.0072622070	-0.4706275801
F 0.1857816448	4.8919449011	-2.0065834153	F 9.4414721120	0.3238084833	1.9135377214
F 1.7589119163	4.9344168108	2.4603816248	F 1.4145915498	7.6163795712	2.5506407593
F 6.7640017950	0.0053931403	2.0860285325	F 0.4610430661	8.9462288391	0.3697243999
F 6.3476464154	1.0579997786	-2.5131788989	F -0.1550470396	7.5730721663	-1.9081171689
F 1.6681358686	-5.1715389589	2.3221055651	O -10.4868738495	2.0953936481	0.2157809552
F 2.9771945131	-7.6592759400	-2.3470771637	N 3.1760142944	-1.3364212023	-0.0094564132
F 2.6239249029	-9.1132854512	-0.0661144279	N 2.8281414816	1.5284201402	0.0374089899
F 1.9661426006	-7.8586373513	2.2665048515	N -0.0328443293	1.1777960151	0.2322159153

N 0.3129435056	-1.6851258606	0.1414137474	C -3.3419331232	-0.6821774273	0.3393344431
N -10.4701171069	0.8369636440	-0.0441290884	C -1.8559545380	-0.4969566231	0.2843770200
N -8.2804906197	-1.5748107370	-0.5301031502	C -1.3604612844	0.8180710979	0.2952941261
C -10.4708800582	0.4734012154	2.3752674812	C -2.1856492081	2.0031645388	0.3518180415
C -9.1516670457	1.1174665663	-2.0872773588	C -1.3458993381	3.0726493135	0.3322739926
C 3.6511351243	3.6844777700	-0.0048262302	C -0.0014235253	2.5512350164	0.2480029654
C 4.7184118250	2.8471238835	-0.0871419306	C 1.1587639694	3.3413401907	0.1808364934
C 2.500065463	-5.6589144468	-1.1651077824	C 0.9786523144	4.8259391230	0.2252968081
C 2.6599343390	-7.0420500427	-1.2035334273	C 1.2846706664	5.5605282753	1.3749179295
C 2.4779413629	-7.7864292275	-0.0402838315	C 1.1178744534	6.9418864569	1.4344001337
C 2.1415267526	-7.1446415113	1.1492764268	C 0.6276425853	7.6225058160	0.3221898087
C 1.9916013575	-5.7599305005	1.1628034291	C 0.3137786936	6.9202262355	-0.8390438000
C 2.1633280354	-4.9842220727	0.0122591723	C 0.4938243799	5.5393884000	-0.8750817949
C 1.9868397835	-3.4988558601	0.0386872622	H -0.5197242386	-4.9207688456	0.1509714943
C 3.1454090804	-2.7113908349	-0.0165220928	H -9.1410366492	0.9802663647	-3.1743032073
C 4.4920070050	-3.2312750365	-0.0922181259	H -8.24479253397	0.6624506813	-1.6772066269
C 5.3278450784	-2.1606204814	-0.1387822790	H -9.1447320949	2.1869097827	-1.8655315697
C 4.5000611919	-0.9771182030	-0.0850775421	H -9.3770274929	0.5142177446	2.3872406029
C 7.0867811061	0.8702451391	-1.4120450038	H -10.8040730039	-0.1875217940	3.1831131781
C 8.4659402521	1.0384436242	-1.5114442911	H -10.8451911528	1.4809256747	2.5595773175
C 9.2638316378	0.8520312813	-0.3848368231	H -12.9709816363	-0.4510062899	0.1433597639
C 8.6785410712	0.5020769266	0.8296559751	H 4.7627996479	-4.2773724831	-0.1050570404
C 7.2966303915	0.3426200421	0.9040195782	H 6.4062632768	-2.1700411237	-0.2066866269
C 6.4686123902	0.5193505610	-0.2083013187	H 5.7623956184	3.1173496745	-0.1573197819
C 4.9862905170	0.3387464602	-0.1139422674	H 3.6617188570	4.7649952865	-0.0055829256
C 4.1986491492	1.4986601198	-0.0600115811	H -1.6141423593	4.1187813029	0.3696174000
C 2.4699991612	2.8555292844	0.0779566044	H -3.5016563380	-1.3122493941	-1.7159451620
C 0.6711886598	-3.0109892725	0.1116151250	H -5.9706905686	-1.6323380729	-1.6320211072
C -0.5097534602	-3.8403646437	0.1654626971	H -11.4331148871	-1.4409391354	-1.7252807864
C -1.5796001287	-3.0036790850	0.2352024811	H -9.9067337257	-1.3163249618	-2.5964780587
C -1.0616172836	-1.6545724200	0.2149589945	H -11.6017027802	0.8719466966	-3.2846937631
C -4.0472141991	-1.1194406604	-0.7963022828	H -12.5897206038	0.6554923704	-1.8295859947
C -5.4240802361	-1.2994413306	-0.7557174140	H -11.6748726957	2.1597521851	-2.0586863000
C -10.4048767467	-1.0626347163	-1.6551146551	H -12.8564007402	1.0491065430	1.0906934254
C -11.6536953585	1.0772450062	-2.2095450788	H -12.9339691966	-0.5278632569	1.9110975079
C -10.4236958842	0.4751921942	-1.4998536056	H -11.3936235562	-2.1831063830	0.7655982416
C -12.5355246052	0.0043492846	1.0394259153	H -9.9405996492	-1.8803691311	1.6762439066
C -10.9914487609	-0.0684966297	1.0325189881	H -9.8222695596	-2.8773090607	-0.7130448498
C -10.5102660707	-1.5360365925	0.8064386174	H -8.0457841975	-1.0624268602	1.4821606979
C -9.7216280706	-1.8040981328	-0.4929028472	H -5.9803453643	-0.4221693228	2.4840566341
C -7.6018384336	-1.2380438857	0.4927632676	H -3.5269999218	-0.0973610994	2.4047187751
C -6.1395605900	-1.0511876370	0.4269851357	H -2.6241490126	-3.2709254646	0.2991387518
C -5.4393408122	-0.6167002388	1.5604633902	H -3.2647758578	2.0109773860	0.3960468939
C -4.0582277521	-0.4311440688	1.5178668534			

**Chapter 4 – Optical Spin Polarization of a Radical Serving as a Molecular Qubit through
Weak Exchange Coupling to Photogenerated Triplet States**

4.1 Introduction

Spin-bearing molecules are drawing increasing attention for their potential to serve as fundamental building blocks, qubits, in quantum information science (QIS).¹⁻⁵ Taking advantage of synthetic tunability,^{6, 7} advances have been achieved in extending the coherence times,^{12, 13, 16} scaling up the number of qubits^{11, 14, 15, 17} and optical addressability of electron spins in organic molecules^{132, 133} or metal complexes.^{34, 35} However, these molecular qubits are usually limited to thermally polarized electron spins whose initial states are ill-defined at room temperature due to the thermal fluctuations.²⁶ Thus, high magnetic field and millikelvin temperatures are often required to initialize the qubits.¹⁸ The challenge of achieving well-defined qubit state can be overcome by optical initialization, a strategy commonly used in qubit platforms that are based on defect centers in solid-state material such as nitrogen-vacancy (NV) center, where optical pumping of the ground state and spin-selective excited states relaxations allow for population buildup at one specific spin state to realize qubit initialization, or spin polarized initial state.²⁷⁻²⁹

Photochemical processes in molecular qubit systems are also spin-selective^{19, 30} and have shown promise to create well-defined initial qubit states. For instance, sub-nanosecond photo-induced electron transfer in donor-acceptor molecules generates entangled spin (qubit) pair with pure initial quantum state.^{20, 31-33} Resonant excitation of pseudo-tetragonal chromium (Cr^{4+}) complexes to their singlet excited states have also been shown to selectively relax back to $m_s = \pm 1$ ground state sublevels to create spin polarization (SP).^{34, 35}

Moreover, it has been demonstrated that chromophores appended with radicals can initialize the ground state doublet of the radicals through the exchange interactions between the chromophore triplet excited states and the radicals.³⁶⁻⁴¹ The initialized or, spin polarized ground state doublet was proposed to be a result of the reverse quartet mechanism³⁶ in most of the strongly

coupled chromophore-radical systems, in which the exchange coupling (J) is much larger than the Zeeman splitting, yielding well-defined excited doublet and quartet states that are separated by $|3J|$.⁴² However, such chromophore-radical systems in the weak-coupling regime remain unexplored.^{43,44} In this regime, the excited triplet states of the chromophore have vanishing orbital overlap with the singly occupied molecular orbital (SOMO) of the radical either due to relative long distance or orbital symmetry mismatch, resulting in exchange coupling magnitudes much smaller than the Zeeman splitting. Whether such weak exchange coupling in a chromophore-radical system can effectively create a spin-polarized ground-state doublet and the associated mechanism of SP in this regime both remain unknown.

In this work, a series of C₆₀ fullerene derivatives containing α,γ -bisdiphenylene- β -phenylallyl (BDPA) radical¹³⁴ are synthesized and used to explore ground-state SP of BDPA through its weak exchange coupling with ^{3*}C₆₀. As an allyl radical, BDPA has an unpaired electron that is predominantly located at the α and γ positions while the SOMO of BDPA has a node at β position¹³⁵ that can effectively reduce the exchange coupling between BDPA and ^{3*}C₆₀. The choice of C₆₀ as the chromophore allows for efficient generation of its triplet states,¹³⁶ providing nuclear-spin-free environments, and ease of distance- and orientation-tunability using the Prato reaction.¹³⁷

Selective photoexcitation of C₆₀ results in over ten-fold spin polarization (SP) of BDPA that is observed by pulsed electron paramagnetic resonance (EPR) spectroscopy at room temperature. Opposite SP patterns are observed for molecules with different bridges between C₆₀ and BDPA. Transient absorption spectroscopy and other pulsed EPR measurements further reveal that SP of BDPA comes from SP transfer of excited C₆₀ triplet states through weak exchange couplings over a 1 nm distance.

4.2 Experimental Details

4.2.1 Steady-State Spectroscopy.

UV-visible absorption spectra were obtained using a Shimadzu UV-1800 spectrometer in a quartz cuvette with a 1 mm path length.

4.2.2 Transient Absorption Spectroscopy.

Femtosecond transient absorption (fsTA) experiments were performed using the instruments described in previous accounts.⁵³ The 450 nm ~100 fs pump pulse was generated using a commercial collinear optical parametric amplifier (TOPAS-Prime, Light-Conversion, LLC).. The pump pulse was depolarized to suppress polarization-dependent dynamics in the signal. The pump pulses had energies of 1 μ J/pulse. Spectra were collected using a customized Helios/EOS spectrometer (Ultrafast Systems, LLC). All transient absorption data sets were collected on toluene solutions with a path length of 1 mm and an optical density of ~0.8 at 450 nm. All samples were put through three freeze-pump-thaw cycles to remove oxygen. Solution samples were stirred during run time to avoid degradation from localized heating. All datasets were background-subtracted to remove scatter from the pump pulse and corrected for time-zero offsets and group delay dispersion using Surface Explorer (Ultrafast Systems, LLC). The femtosecond transient absorption data were then each subjected to a global wavelength fitting analysis using an $A \rightarrow B \rightarrow C$ model, while the nanosecond transient absorption (nsTA) data were fit to an $A \rightarrow G$ model. The kinetic traces were fit at 5-6 wavelengths across the relevant spectral features of the species formed in each of the experiments.

4.2.3 Continuous-Wave EPR Spectroscopy

All EPR measurements were performed in ~ 100 μ M solutions of C₆₀-BDPA dyads in toluene. Solutions (~ 20 μ L) were loaded into quartz tubes (2.40 mm o.d., 2.00 mm i.d.), subjected

to three freeze–pump–thaw cycles on a vacuum line (10^{-4} Torr), and sealed with a hydrogen torch. All EPR measurements were made at X-band (~ 9.6 GHz) on a Bruker Elexsys E680 X/W EPR spectrometer with a split ring resonator (ER4118XMS3) at room temperature. Light from the pulsed laser was coupled through a fiber placed outside the cryostat window (1 mJ/pulse, 7 ns, 10 Hz), with some portion of the light passing through the coils of the resonator and exciting the sample.

TREPR Measurements using continuous wave (CW) microwaves and direct detection were performed. Following photoexcitation, kinetic traces of transient magnetization under CW microwave irradiation were pre-amplified with a video amplifier and obtained in both imaginary and real channels (quadrature detection). Time traces were recorded over a range of magnetic fields to give 2D spectra. Spectra were processed by first subtracting the signal prior to the laser pulse for each kinetic trace (at a given magnetic field point), and then subtracting the signal average at off-resonant magnetic field points from the spectra obtained at a given time.

4.2.4 Pulsed EPR.

Echo-detected delay after flash measurements were recorded by using the sequence $h\nu-T_{\text{daf}}-\pi/2-\tau-\pi-\tau$ -echo with incremented T_{daf} (DAF \equiv delay after flash) unless otherwise stated, $\tau = 160$ ns, and a π -pulse length of 32 ns. The spin echo was integrated to give the echo amplitude as a function of T_{daf} . For ground state polarization measurements, a Hahn echo pulse sequence was used, and the laser pulse was positioned at the maximum polarization (8 μ s).

4.3 Results and Discussion

4.3.1 Synthesis

Details of the synthetic procedures and characterization of **1H**, **2H**, **3H** and **4H** and the protocol of generating **1**, **2**, **3** and **4** (Figure 4.1) are given in the Section 4.5. Supplementary Information.

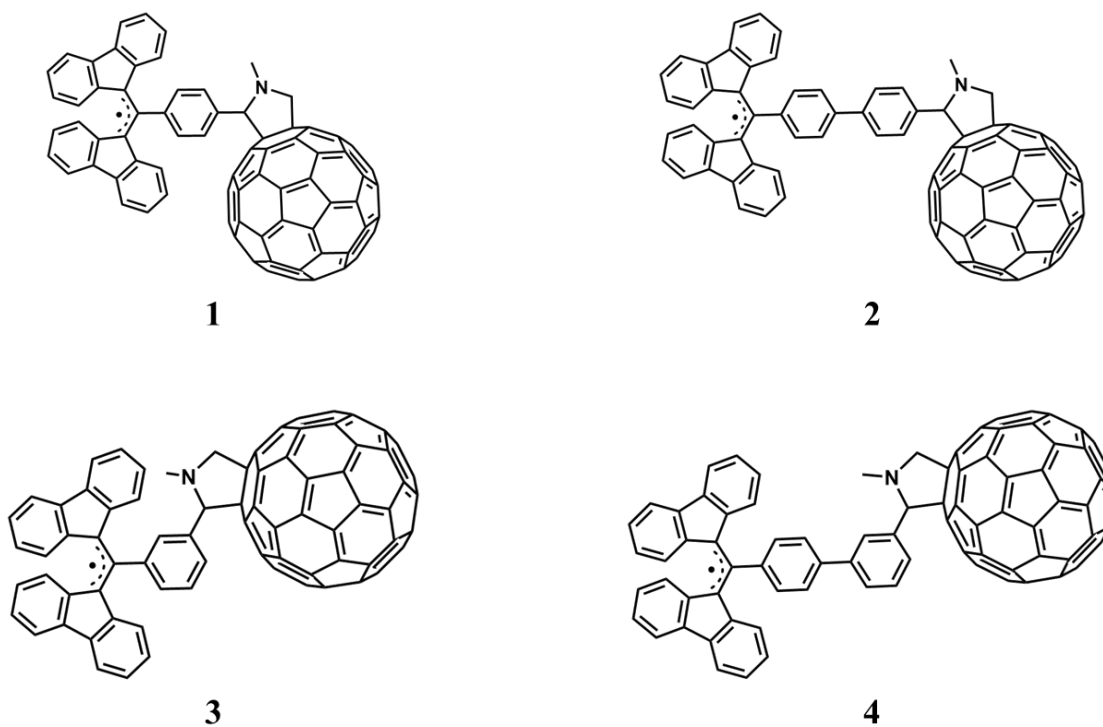


Figure 4.1. Structural formulas of the compounds **1** (C₆₀-BDPA), **2** (C₆₀-ph-BDPA), **3** (m-C₆₀-BDPA) and **4** (m-C₆₀-ph-BDPA)

4.3.2 Steady-State Spectroscopy.

The steady-state absorption spectra of **1**, **2**, **3** and **4** in toluene are shown in Figure 4.2. The strong absorption peak at 500 nm originates from the BDPA radical, which does not change from **1-4**, which is indicative of weak electronic coupling between C₆₀ and BDPA. The broad absorption

that almost covers the entire visible region with stronger absorption at lower wavelengths is characteristic of C_{60} .^{138, 139}

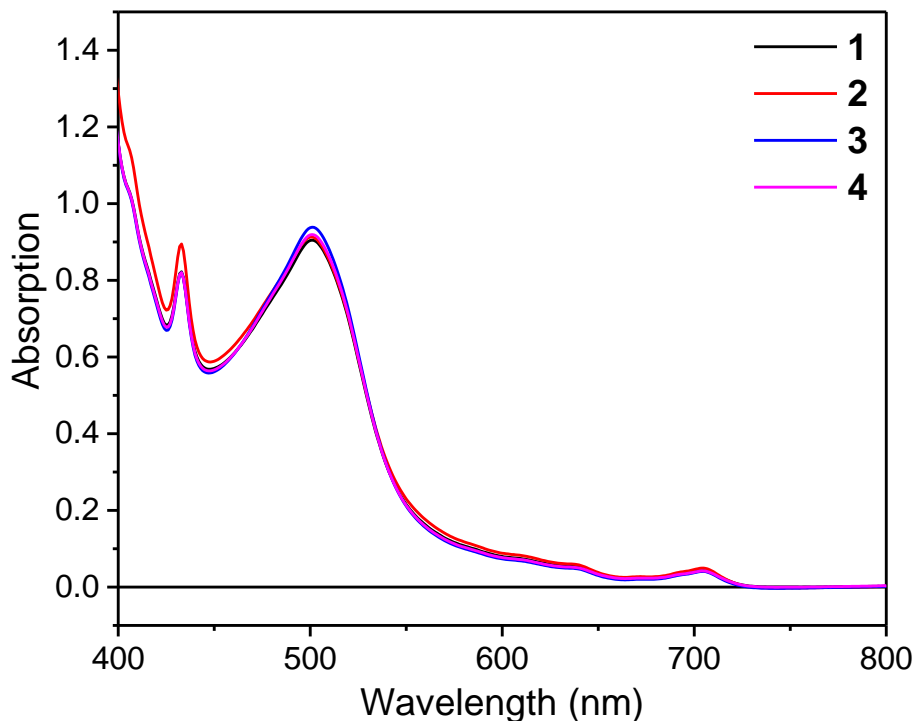


Figure 4.2. UV-vis spectra of compound 1-4 in toluene solution at room

4.3.3 Transient Absorption Spectroscopy.

Femtosecond and nanosecond transient absorption spectroscopies were used to elucidate the excited state dynamics of **1**, **2**, **3** and **4**. The samples were excited using 450 nm laser pulses to avoid directly exciting BDPA and ensure a substantial amount of sample was promoted to the excited singlet state of C_{60} ($^1C_{60}$). The fsTA data show many of the same spectral features across the four samples, but with different excited state dynamics (Figure 4.3.). Immediately after photoexcitation, the spectra show features of $^1C_{60}$ with broad absorption bands centered at 730 nm and 1020 nm.^{138, 140} The ground-state bleach of BDPA at 500 nm also appears in the first 20

ps, indicative of co-excitation of BDPA. However, the small amount of $^1\text{BDPA}$ decays independently to the ground state and does not affect the overall dynamics of excited C_{60} . At later times, as the 1020 nm feature gradually decays, the 730 nm absorption band gradually shifts to 700 nm, which tracks the intersystem crossing process as the triplet state of C_{60} ($^3\text{C}_{60}$) forms.¹⁴⁰⁻
¹⁴² The spectral features of $^3\text{C}_{60}$ are present throughout the ~ 7 ns pump-probe time delay range of the fsTA experiment and gradually decay in the nsTA experiment on the μs timescale.

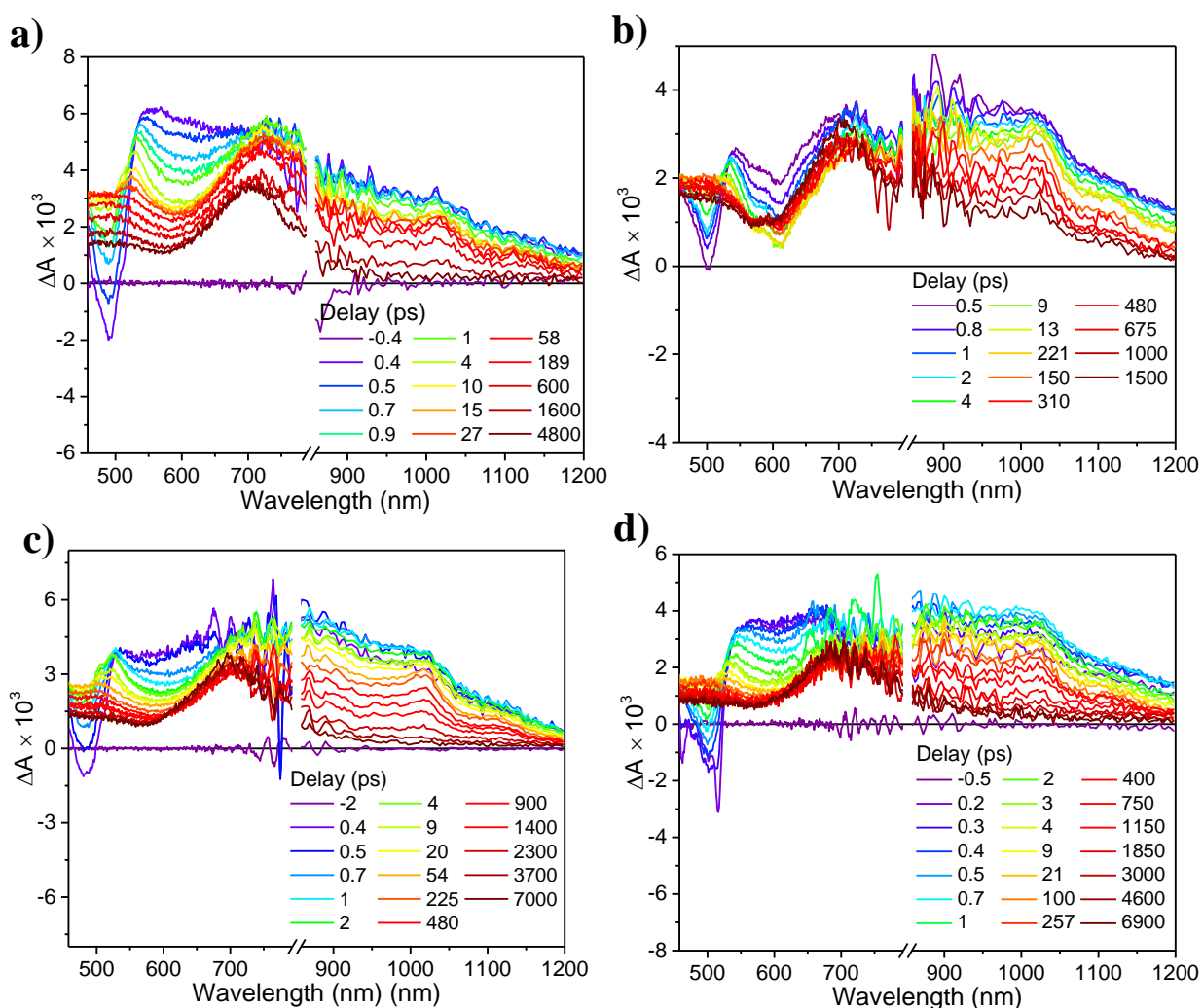


Figure 4.3. Transient absorption spectra of 1 (a), 2 (b), 3(c) and 4(d) in toluene at 298 K following $\lambda_{\text{ex}} = 450$ nm excitation.

Global fitting fsTA data to a kinetic model (see Section 4.5 for details) yields time constants $\tau_{A \rightarrow B}$, $\tau_{B \rightarrow C}$ and τ_C , and the corresponding evolution-associated spectra (EAS) of states A, B and C, representing the convoluted spectrum of $^1C_{60}$ and BDPA excited states (A), $^1C_{60}$ (B) and $^3C_{60}$ (C), respectively. The time constants $\tau_{B \rightarrow C}$ of compound **1-4** capture the decay of $^1C_{60}$ and are summarized in Table 4.1.

Table 4.1. Transient Absorption Species Associated Kinetics for 1-4 in toluene at 298 K

Compound	$\tau_{B \rightarrow C}$ (ps), $^1C_{60}$	τ_C (μ s), $^3C_{60}$
1	762 ± 41	5.0 ± 0.1
2	1275 ± 64	2.0 ± 0.1
3	887 ± 53	3.5 ± 0.1
4	1060 ± 30	5.6 ± 0.1

The difference in the decay rates of $^1C_{60}$ in **1-4** indicates the exchange couplings (J) between $^3C_{60}$ and BDPA varies across the four compounds. In the presence of the BDPA radical, the formation of $^3C_{60}$ is accelerated through the enhanced intersystem crossing (EISC) mechanism,^{37, 38, 143-145} which is modulated by the electronic coupling between $^1C_{60}$ and BDPA. As indicated by the UV-Vis and TA spectra of **1-4**, the structural difference in **1-4** has little effect on the electronic structure of C_{60} and its excited states, the electronic coupling between BDPA and $^1C_{60}$, as well as J , are mostly dictated by how much the singly occupied molecular orbital (SOMO) of BDPA is extended to the carbon at which C_{60} is connected to BDPA. The reported time constants for $^1C_{60}$ decay in fullerene and pyrrolidinofullerenes are around 1.2 ns.¹⁴⁰ Therefore, the decrease of $\tau_{B \rightarrow C}$ exhibits in **1**, **3** and **4** indicates that the weak coupling the system slightly accelerates the ISC process whereas in **2** the coupling is almost negligible such that $\tau_{B \rightarrow C}$ of **2** is virtually the same as the literature values. Moreover, $\tau_{B \rightarrow C}$ of **2** or **4** are longer than that of **1** or **3** respectively, which

indicates that the presence of an extra phenyl group in **2** and **4** between C₆₀ and BDPA drastically attenuates overlap between the SOMO of BDPA and the orbitals that contribute to ^{1*}C₆₀, thereby reducing the EISC effect. Placing BDPA in a meta orientation as in **3** or **4**, comparing to **1** and **2**, reduces the π-electron coupling due to decreased π spin density at the tertiary carbon that connects C₆₀ and BDPA, however, this also brings C₆₀ closer to BDPA. Table 4.3 summarizes the distance measured from the center of C₆₀ to the β carbon of BDPA in geometry-optimized **1-4** with B3LYP/6-31G* level of theory (Section 4.5.4). Compound **2** sees 29 % increase in C₆₀-BDPA distance than **4**, while **1** sees 17% distance increase than **3**. Therefore, we speculate that the through-space coupling between ^{1*}C₆₀ and BDPA may contribute to EISC, as τ_{B→C} of **2** is 20% longer than that of **4**, whereas **1** and **3** shows similar τ_{B→C}.

4.3.4 Time-Resolved EPR spectroscopy.

Intense TREPR spectra of spin polarized BDPA were observed for **1**, **3** and **4** in toluene at room temperature (Figure 4.5a) following the photo excitation of C₆₀ at 450 nm. However, compound **2** did not yield any measurable signal under the same conditions, which can be explained by the negligible *J* between ^{3*}C₆₀ and BDPA, as was discussed in the previous section. The TREPR for **1** shows an emissive Lorentzian-shaped spectrum that resonances at around 341.6 mT (*g* = 2.003), while both **3** and **4** show absorptive spectra with the same shape and resonance. All three spectra exhibit a linewidth of 7 G across various laser pulse delays, matching with the broadening of BDPA due to the proton hyperfine couplings.¹⁴⁶ Due to the weak exchange coupling between the ^{3*}C₆₀ and BDPA, the TREPR spectra for **1**, **3** and **4** originate from the spin-polarized ground-state doublet, as confirmed by the transient nutation (Section 4.5.3). The emissive TREPR spectrum of **1** indicates the preferential population of *m_s* = 1/2 state while the absorptive spectra of **3** and **4** suggest that the *m_s* = -1/2 state of the doublet is more populated.

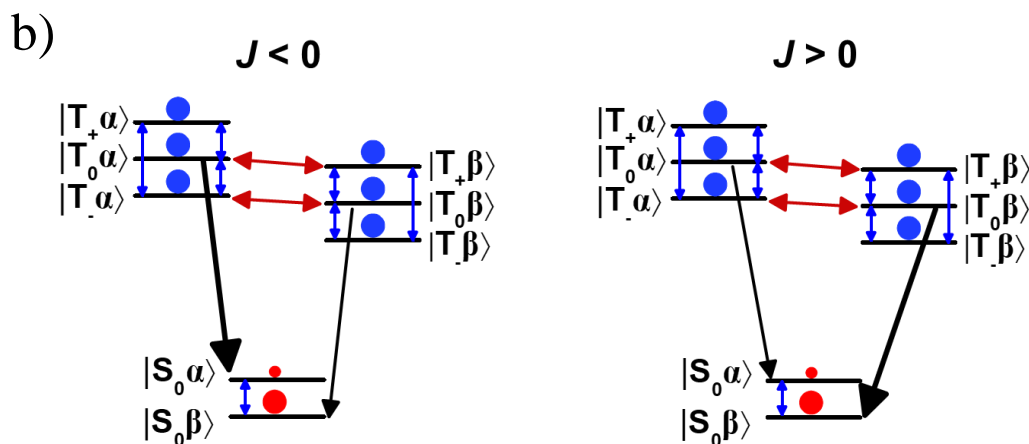
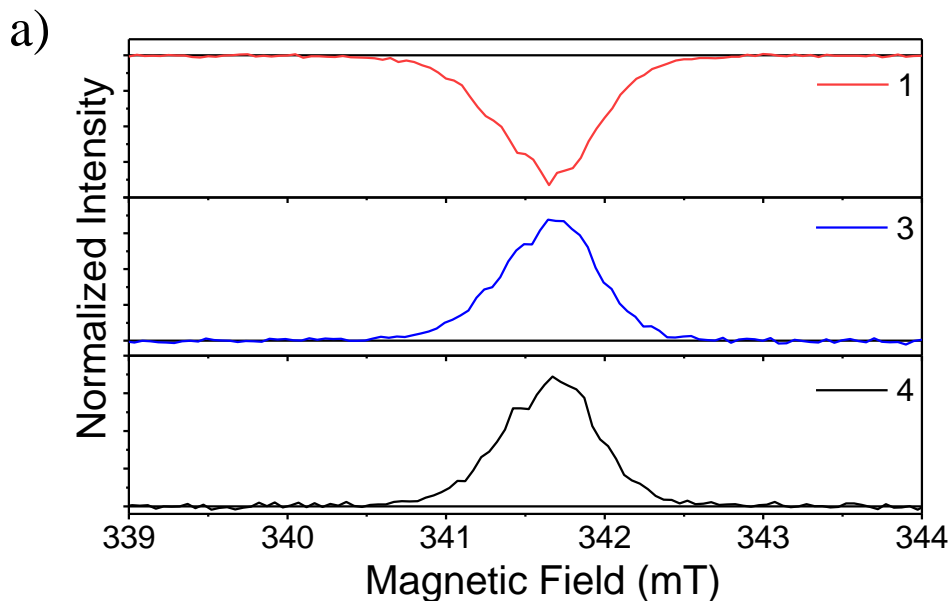


Figure 4.4. (a) TREPR spectrum of 1, 2, 3 and 4 at X-band in toluene solution at 298 K, 100 ns after a 7 ns, 450 nm laser pulse. b) Energy level diagrams of triplet-radical pair in the weak exchange coupling regime with $J > 0$ (left) or $J < 0$ (right). The arrows indicate possible flip-flop transitions in the excited states and the ISC from the excited states to the ground states. The blue and red circles indicate the initial and final populations respectively.

Due to the fast rotational motion of the molecules in solution phase, the dipolar interaction between $^3\text{C}_{60}$ and BDPA is effectively zero. The SP of BDPA can only be mediated by the exchange interaction between $^3\text{C}_{60}$ and BDPA, transferring the SP of $^3\text{C}_{60}$ to either $m_s = -1/2$ or $m_s = 1/2$ sublevel of BDPA ground state. The generation of $^3\text{C}_{60}$ involves SO-ISC process such

that only T_0 state are effectively populated. Figure 4.5 b shows the energy level diagram of weakly coupled triplet-doublet pair and the corresponding doublet ground state in the presence of magnetic field. The exchange coupling between ${}^3\text{C}_{60}$ and BDPA results in the state mixing between $T_0\alpha$ and $T_+\beta$, as well as $T_0\beta$ and $T_+\alpha$, transferring the population from $T_0\beta$ to $T_+\alpha$ preferentially (or $T_0\alpha$ to $T_+\beta$.) As the system relaxes to the ground state, spin polarized BDPA is eventually yielded. Such preferential population of the ground state doublet is consistent with previous reported chromophore-radical system: when the chromophore and the radical are linked by 1,4-phenylene, the anti-ferromagnetic exchange coupling ($J > 0$) between the chromophore and radical results in excited-state relaxation pathways that selectively populate $m_s = 1/2$, while systems with 1,3-phenylene bridge exhibits ferromagnetic coupling ($J < 0$) such that when the excited quartet and doublet states relax, the ground state $m_s = -1/2$ is populated.^{37, 38, 147}

4.3.5 Spin Dynamics of Spin Polarized BDPA.

Since constant microwave irradiation in TREPR obscures the dynamics of the spin polarized BDPA, a pulsed EPR experiment was implemented, with pulse sequence of $h\nu - T_{\text{daf}} - \pi/2 - \tau - \pi - \tau - \text{echo}$, where $h\nu$ is a 7-ns laser pulse, T_{daf} is an incremented delay after flash (DAF), τ is 200 ns and a π pulse is 32 ns in length. The integrated spin echo was plotted with T_{daf} to show the spin polarization dynamics of BDPA for **1**, **3** and **4** (Figure 4.5). The observed echo signals reproduce the spin polarization patterns observed in TREPR. Namely, upon photo excitation, **1** shows negative (emissive) signal whereas **3** and **4** show absorptive signals. Notably, the T_{daf} traces precisely capture the SP buildup and decay, and the dynamics are not complicated by the spin-spin relaxation or magnetic precession which are otherwise present in TREPR. Fitting the time traces with a biexponential decay yields time constant τ_1 and τ_2 as SP buildup and decay respectively.

Table 4.2. Polarization Kinetics and Spin-Lattice Relaxation for 1,3 and 4 in toluene at 298 K

Compound	τ_1 (μs)	τ_2 (μs)	T_1 (μs), BDPA
1	2.3 ± 0.1	38.2 ± 0.2	29 ± 2.8
3	2.0 ± 0.1	77.0 ± 0.4	58.5 ± 3.5
4	2.5 ± 0.1	75.2 ± 0.6	69.5 ± 3.2

The SP buildup process is due to the difference of relaxation pathways to the BDPA ground state sublevels $m_{-1/2}$ and $m_{+1/2}$. Therefore, the SP buildup rate is the difference between population buildup rates of ground state $m_{-1/2}$ and $m_{+1/2}$ sublevels as shown in equation 1:

$$\frac{1}{\tau_1} = \pm \left(\frac{1}{\tau_{-1/2}} - \frac{1}{\tau_{+1/2}} \right) \quad (1)$$

where $\tau_{-1/2}$ and $\tau_{+1/2}$ are population buildup time constants for ground state sublevels $m_{-1/2}$ and $m_{+1/2}$ respectively, and \pm denotes whether $m_{-1/2}$ or $m_{+1/2}$ is preferentially populated. If the SP buildup is solely associated with excited-state relaxation, namely decay of 3*C60 in this case, τ_1 should be longer than the 3*C60 lifetime τ_C which is measured using nsTA spectroscopy. However, in all the examples with measurable SP signals, τ_1 is shorter than τ_T (Table 4.2), which indicates that SP buildup pathways are more allowed transitions with shorter transition time constant than τ_C . In the weak coupling limit, the excited quartet states and double states with $m_s = \pm 1/2$ are ill-defined such that in Figure 4b, the states $T+\beta$, $T0\beta$, $T+\alpha$ and $T0\alpha$ are better described as the superpositions of excited doublet ($D_{\pm 1/2}$) and excited quartet ($Q_{\pm 1/2}$) states. As the excited states relax back to the ground state doublet ($D0$), the relaxation pathways from levels with more $D_{\pm 1/2}$ characters will be faster, since the transitions between $D_{\pm 1/2}$ and $D0$ states are spin-allowed. The decays of SP (τ_2) of 1, 3 and 4 has much longer time constants that are significantly longer

than the τ_1 and τ_C , which suggests that the decay of SP does not involve any excited state dynamics, but rather a property of the BDPA ground state. The measured spin-lattice relaxation (SLR) time (T_1) of BDPA matches with the τ_2 . Therefore, one can conclude that the decay of SP is through SLR mechanism.

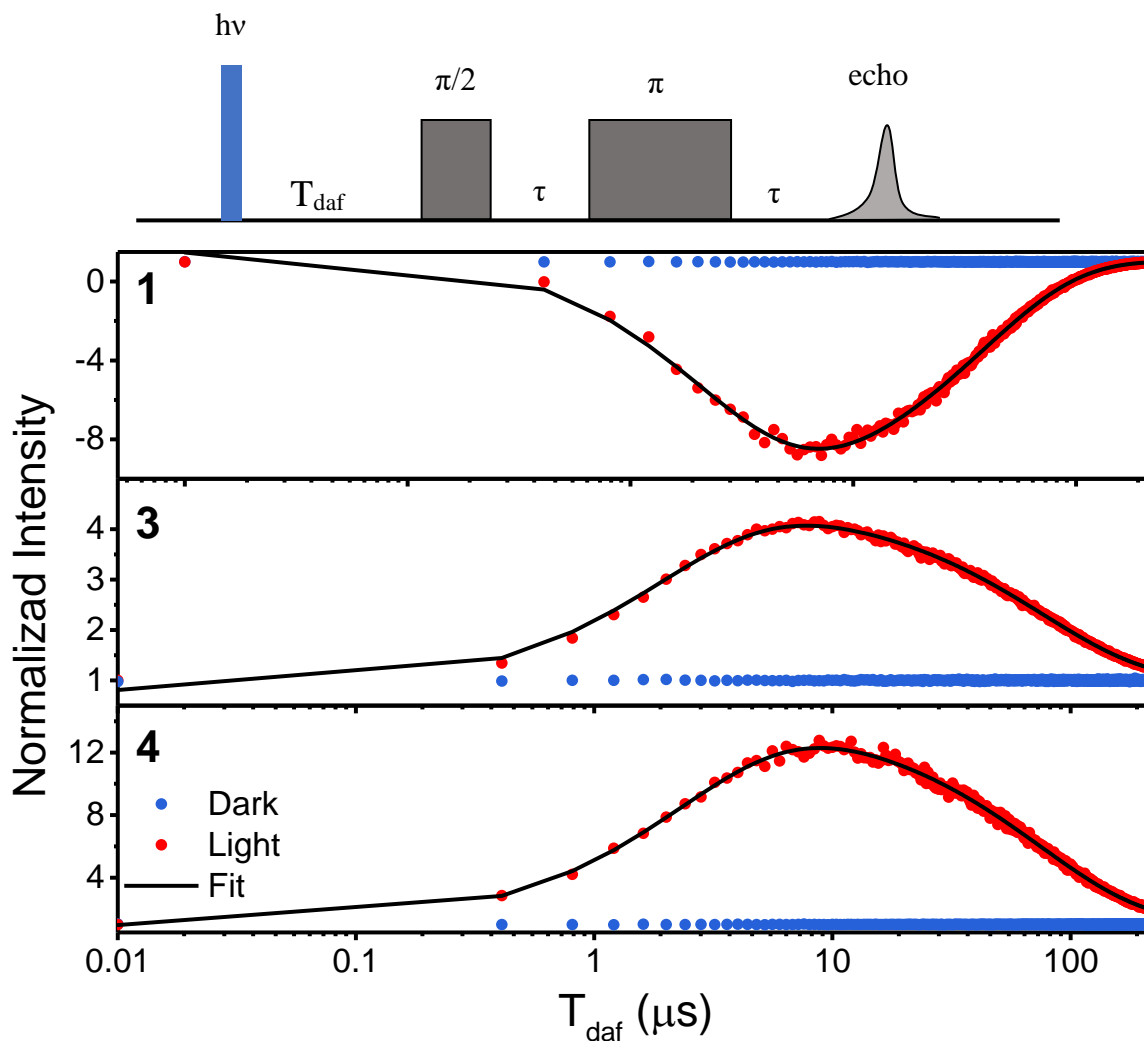


Figure 4.5. Spin dynamics of ground state polarization of BDPA probed by the pulse sequence shown at the top.

4.3.6 Ground State Spin Polarization Enhancement at Room Temperature.

Pulsed EPR allows for the measurement of relative SP by comparing the spin echo intensity with or without photoexcitation. However, the absolute value of SP remains undetectable due to the lack of knowledge on the number of molecules being promoted to the excited states, since much of the laser power is lost in the cryostat and the microwave resonator. Figure 4.6 shows the spin echo (SE) detected using the same pulse sequence as the DAF experiment, where the T_{daf} is set to where the maximum SP is measured for each sample and the SE intensity is normalized to the SE measured in the absence of laser pulse. **1** and **4** the SP is enhanced by 20- and 10-fold, respectively, after photoexcitation, which suggests efficient SP transfer from spin-polarized $^3C_{60}$ to BPDA occurs in the weak exchange coupling regime.

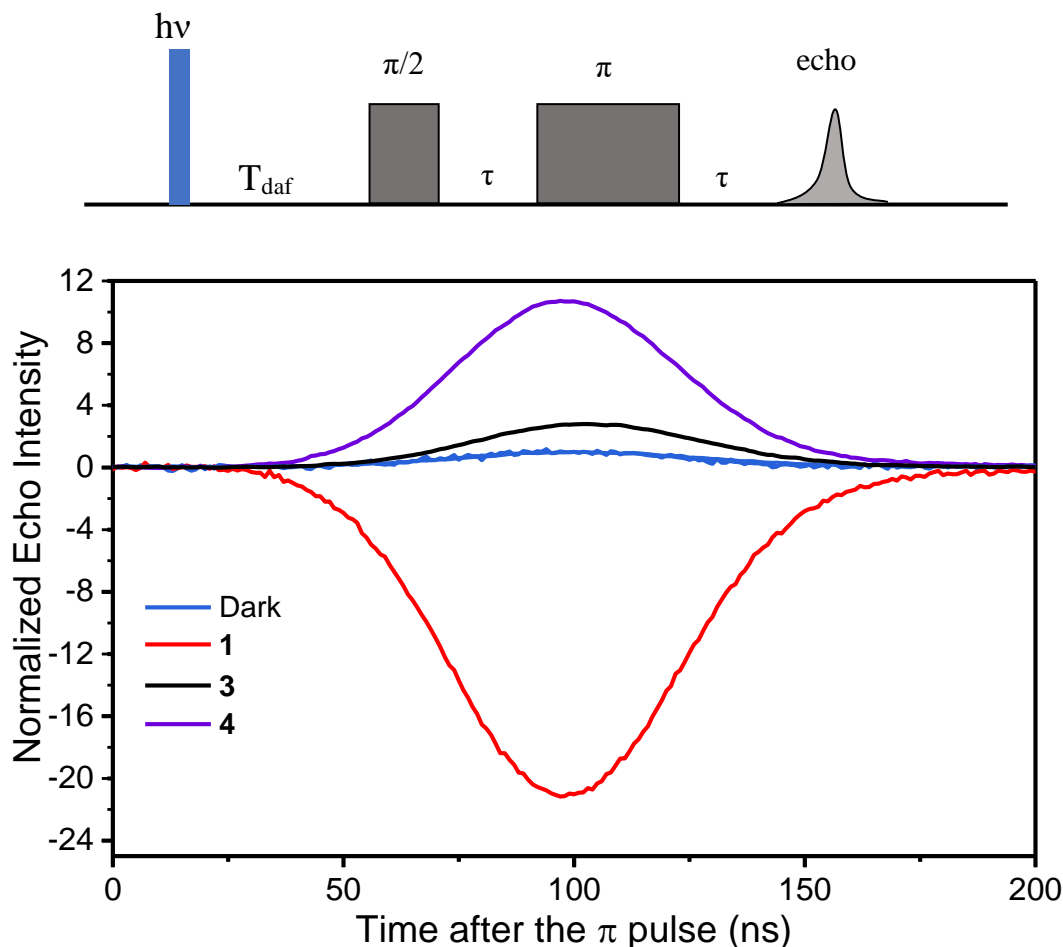


Figure 4.6. Spin echo of **1**, **3** and **4** detected at 341.7 mT using the pulse sequence shown at the top with $T_{\text{daf}} \sim 8 \mu\text{s}$. The signal was normalized to the spin echo without laser pulse i.e., at thermal equilibrium.

However, despite the closer distance between C_{60} and BDPA, the enhancement factor measured in **3** is only 2.5, which indicates that an increased ferromagnetic exchange coupling may cause less efficient spin polarization transfer. Similar trend was observed by Kirk et al. in systems composed of a nitronyl nitroxide radical and a chromophoric metal complex linked by bridges with various length. They proposed that the large energy gap between the excited quartet (Q) and doublet (D) states due to the exchange coupling in the strong coupling limit attenuates Q-D mixing, thus impeding the efficient SP transfer to the ground state. In the weak coupling regime ($|J| <$

0.03 cm^{-1}), the small Q-D energy gap should not have significant effect on reducing the Q-D mixing. However, the more efficient mixing between $T_{0\alpha}$ and $T_{+\beta}$ (or $T_{0\beta}$ and $T_{-\alpha}$) due to the increased magnitude of J when $J < 0$ effectively reduce the doublet character of $T_{0\alpha}$ and $T_{0\beta}$ states (Figure 4.19), which may decrease the transition rates to the ground state doublet and reduced the magnitude of SP in the ground states. Nevertheless, the ground state SP of BDPA that results from spin-selective relaxation of $^3\text{C}_{60}$ spin sublevels is equivalent to cooling **1**, **3** and **4** to 15 K, 31 K and 125 K, respectively (Figure 4.7).

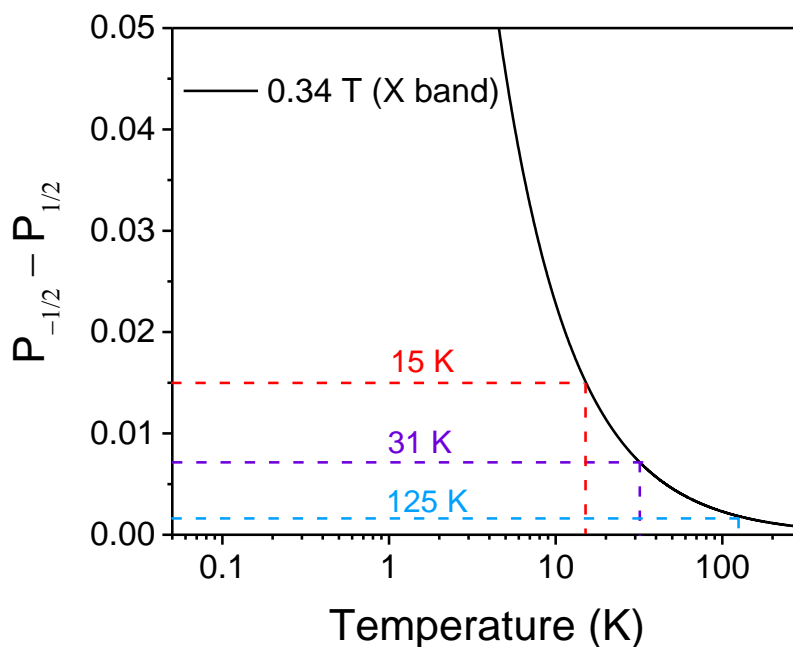


Figure 4.7. Temperature dependence of SP of a ground-state spin doublet in the presence of 0.34 T external field at thermal equilibrium (black curve). The dotted line marked the ground-state SP and the corresponding effective temperature of BDPA in **1** (red), **3** (blue) and **4** (purple) $8 \mu\text{s}$ after the photoexcitation.

4.4 Conclusion

In this study, we investigated ground state SP of covalently linked C_{60} and BDPA molecules with different distance and orientation between the chromophore and the radical.

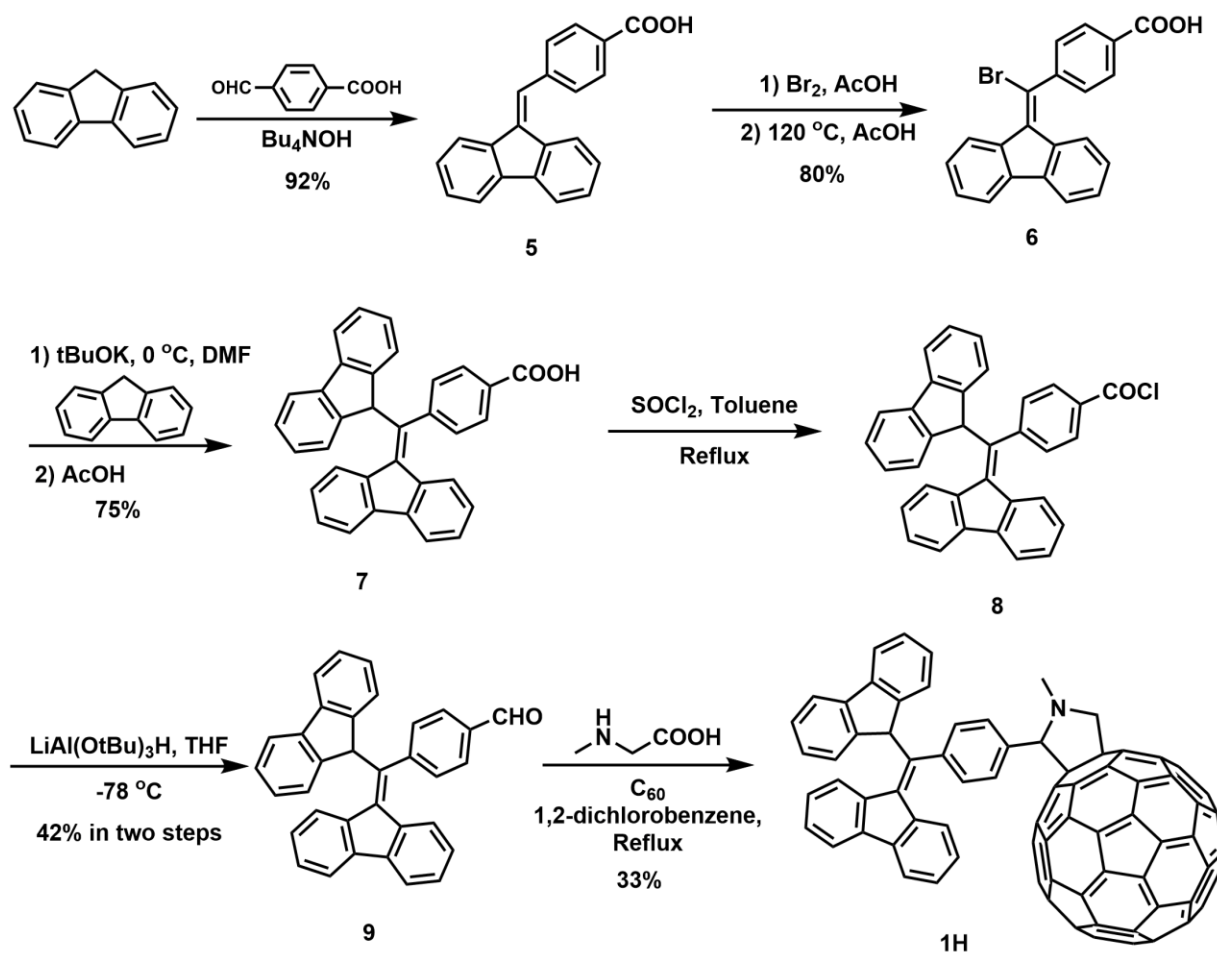
Optical spectroscopic measurements confirmed the weak exchange coupling between the $^3C_{60}$ and BDPA, and we used TREPR and pulsed EPR measurements to demonstrate that efficient ground state SP of BDPA can happen in such weak coupling regime with optical excitation at room temperature.

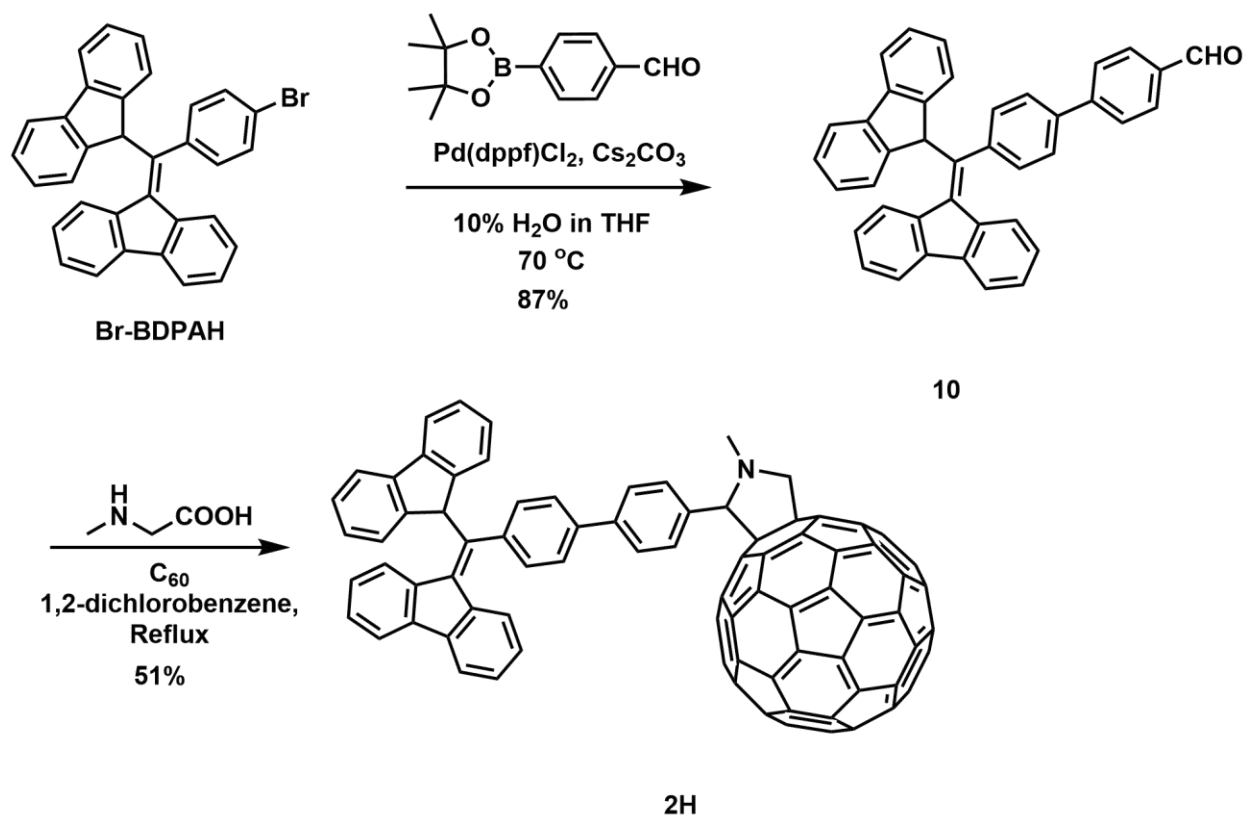
The SP dynamics and of BDPA the SP enhancement factors were measured using pulsed EPR spectroscopy. Comparing with previous reported chromophore-radical systems that fall into the strong exchange coupling regime and investigated exclusively using only TREPR methods, our work demonstrates that up to 20-fold SP enhancement can be realized in the weak exchange-coupled chromophore-radical systems with optical excitation at room temperature and hence establish the viability of such systems for qubit initialization and sensing applications.

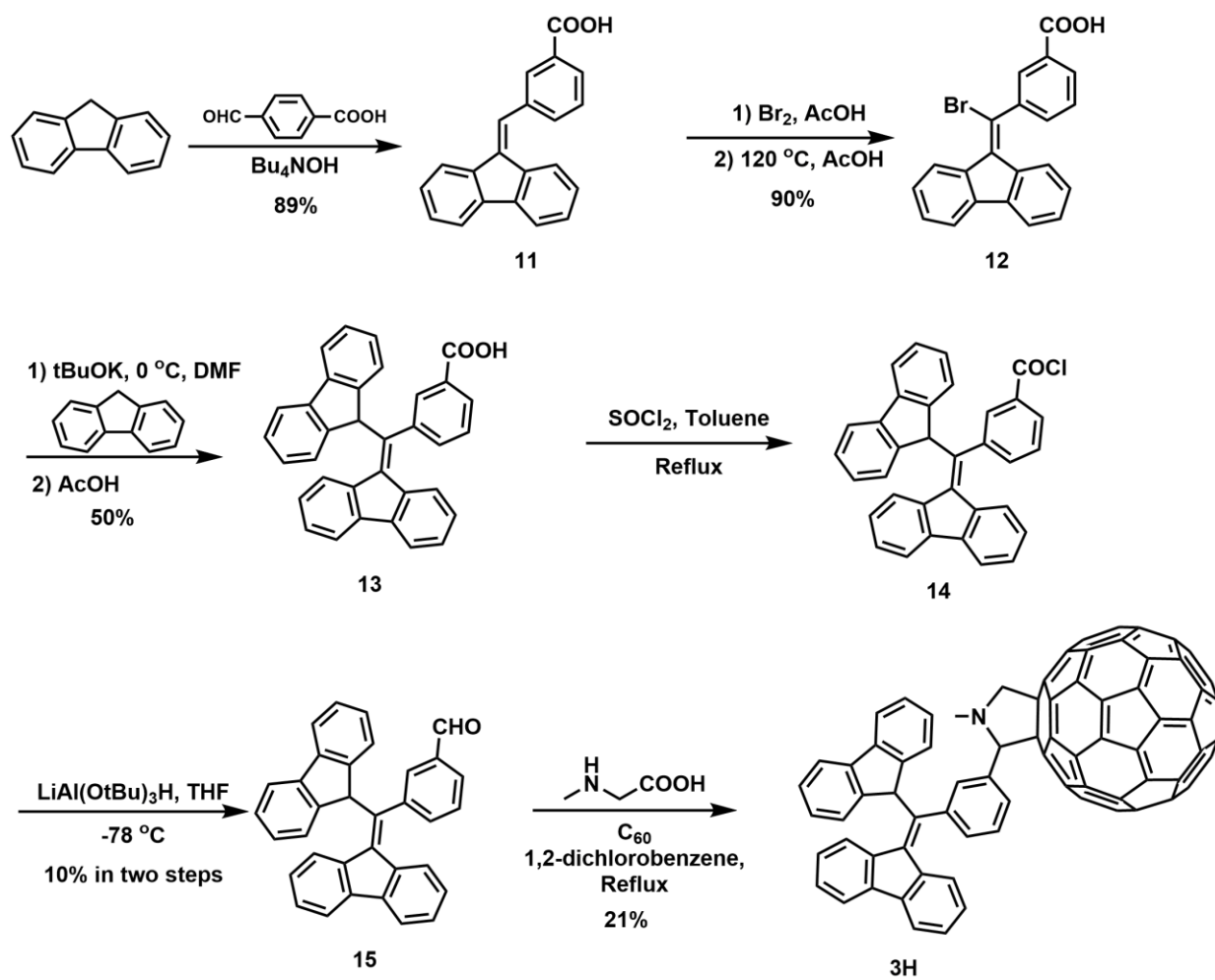
4.5 Supplementary Information

4.5.1. Synthesis and Characterization

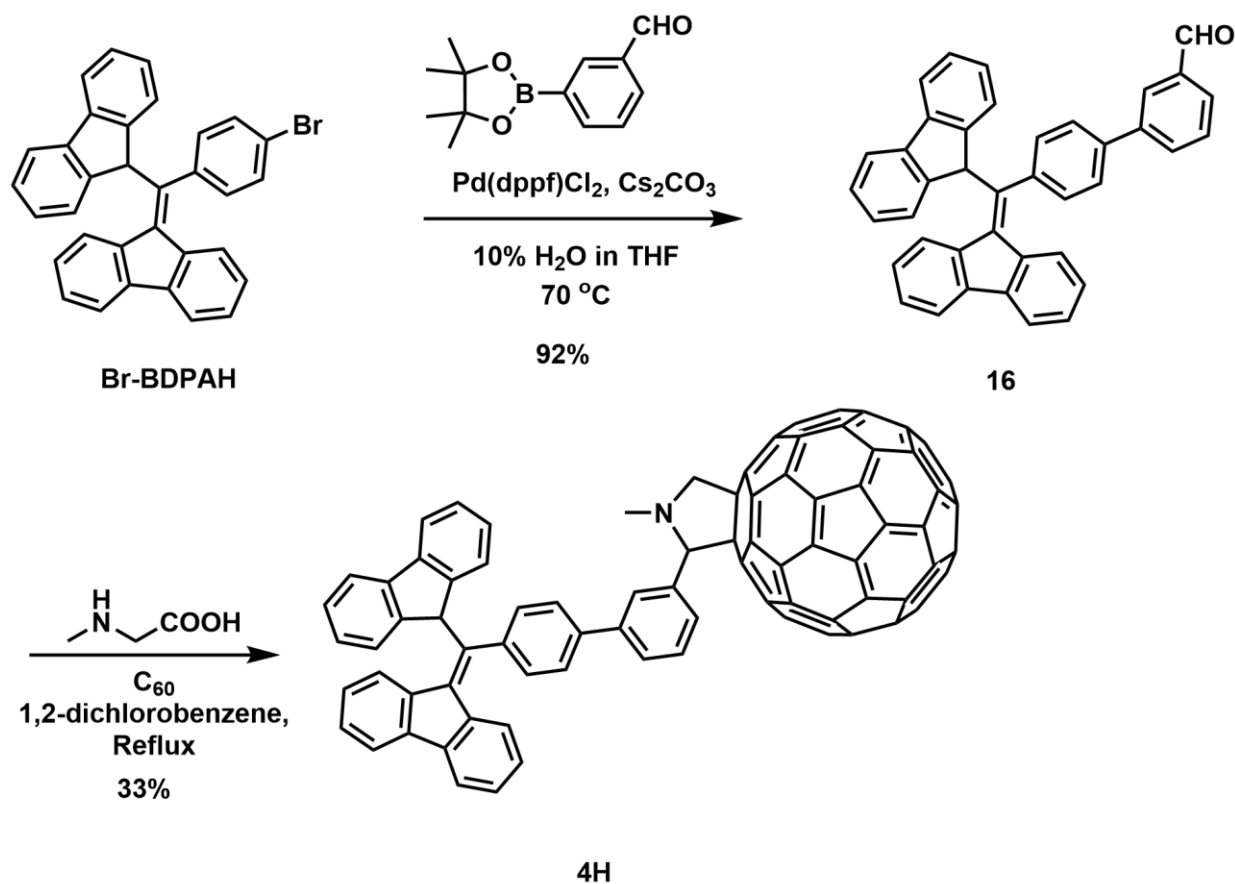
All chemicals were purchased from Sigma-Aldrich, Inc. unless noted otherwise. 1H and ^{13}C NMR spectra were acquired with a Bruker Avance III 500 MHz instrument equipped with a DCH CryoProbe. Mass spectroscopy was performed using a Bruker Autoflex III MALDI-TOF. Purification was performed using silica gel from Sorbent Technologies (Atlanta, GA). The synthesis of **1H**, **2H**, **3H** and **4H** are outlined in the Scheme S1., Scheme S2., Scheme S3. and Scheme S4. 1, 2, 3 and 4 are generated using a procedure modified from the literature.³⁰ Instead of using 1,5-diazabicyclo[4.3.0]non-5-ene, dimethylformamide was used as base to prevent nucleophilic addition to C_{60} .^{148, 149}

Scheme 4.1. Synthetic Scheme of **1H**

Scheme 4.2. Synthetic Scheme of **2H**



Scheme 4.3. Synthetic Scheme of 3H



Scheme 4.4. Synthetic Scheme of 4H

Compound 1H. 50 mg of **9**, 20 mg of sarcosine and 160 mg of C_{60} was placed in a two-neck round-bottom flask equipped with a stir bar and a water condenser. The starting materials were pump-purged three times before 10 mL of *o*-dichlorobenzene was added. The reaction was heated up to 130 °C for 3 hours before the solvent was removed on vacuum. The crude product was purified three times using silica gel chromatography to completely remove C_{60} using 25 % CH_2Cl_2 in hexane as eluents. ^1H NMR (500 MHz, CD_2Cl_2) δ : 8.37 (d, $J = 8.0$ Hz, 1H), 7.80 (d, $J = 7.6$ Hz, 1H), 7.75 – 7.52 (m, 2H), 7.51 – 7.44 (m, 3H), 7.39 (t, $J = 7.4$ Hz, 2H), 7.29 (td, $J = 7.6, 1.3$ Hz, 2H), 7.12 (s, 6H), 6.62 (s, 2H), 6.39 (s, 1H), 5.89 (d, $J = 7.9$ Hz, 1H), 4.83 (d, $J = 9.4$ Hz, 1H), 4.69 (s, 1H), 4.10 (d, $J = 9.4$ Hz, 1H), 2.78 – 2.36 (br, 3H). ^{13}C NMR (126 MHz, $\text{C}_2\text{Cl}_4\text{D}_2$) δ

147.34, 146.37, 146.34, 146.23, 146.19, 146.17, 146.15, 146.00, 145.96, 145.84, 145.61, 145.58, 145.54, 145.53, 145.38, 145.36, 145.19, 145.17, 144.72, 144.65, 144.41, 143.18, 143.13, 142.98, 142.75, 142.71, 142.69, 142.63, 142.60, 142.57, 142.25, 142.23, 142.18, 142.08, 141.96, 141.86, 141.83, 141.72, 141.58, 141.13, 140.14, 139.80, 138.69, 138.61, 135.83, 127.69, 125.26, 120.19, 120.13, 83.30, 77.00, 69.86. MS (MALDI-TOF) m/z : $[M^+]$ calculated for $C_96H_{27}N$ 1194.22; found 1194.282.

Compound 2H. A round-bottom flask equipped with a magnetic stir bar was added 30 mg of xx, 19 mg of sarcosine and 120 mg of C_{60} . After three pump-purge cycles, 10 mL of *o*-dichlorobenzene was added, and the reaction was brought up to 130 °C. 12 hours later, the solvent was removed under vacuum and the crude product was purified by silica gel chromatography three times to completely remove C_{60} using 25% CH_2Cl_2 in hexane as eluents. 1H NMR (500 MHz, CD_2Cl_2) δ : 8.36 (d, $J = 8.0$ Hz, 1H), 7.84 – 7.65 (m, 4H), 7.59 (dt, $J = 7.6, 1.0$ Hz, 2H), 7.55 (d, $J = 7.5$ Hz, 2H), 7.51 (d, $J = 8.1$ Hz, 2H), 7.40 (td, $J = 7.5, 0.9$ Hz, 1H), 7.31 – 7.17 (m, 7H), 7.13 (td, $J = 7.5, 1.0$ Hz, 1H), 6.71 (ddd, $J = 8.4, 7.3, 1.2$ Hz, 1H), 6.68 – 6.64 (m, 2H), 6.43 (s, 1H), 5.93 (dt, $J = 8.0, 0.9$ Hz, 1H), 4.91 (d, $J = 9.4$ Hz, 1H), 4.89 (s, 1H), 4.20 (d, $J = 9.4$ Hz, 1H), 2.71 (s, 3H). ^{13}C NMR (126 MHz, CD_2Cl_2) δ : 156.96, 154.57, 153.96, 147.61, 147.15, 146.94, 146.62, 146.57, 146.54, 146.48, 146.44, 146.41, 146.25, 146.12, 145.95, 145.92, 145.82, 145.80, 145.64, 145.62, 145.59, 145.53, 145.51, 145.46, 145.03, 144.94, 144.91, 144.73, 144.71, 144.52, 143.44, 143.30, 143.00, 142.88, 142.84, 142.62, 142.50, 142.43, 142.35, 142.29, 142.26, 142.15, 142.01, 141.87, 141.53, 140.43, 140.19, 140.15, 140.09, 139.79, 139.21, 139.10, 138.98, 138.40, 137.26, 136.78, 136.59, 136.29, 136.13, 129.40, 129.16, 128.58, 127.87, 127.83, 127.68, 127.36, 126.94, 126.37, 126.32, 125.78, 125.55, 120.35, 120.23, 119.43, 83.52, 77.63, 70.30. MS (MALDI-TOF) m/z : $[M^+]$ calculated for $C_{102}H_{31}N$ 1270.25; found 1269.316.

The synthesis of **Compound 3H** follows the exact same route and procedures as **1H** except for using 3-formylbenzoic acid instead of 4-formylbenzoic acid in the first step.

The synthesis of **Compound 4H** follows the same route and procedures as **2H** except for using 3-formylphenylboronic acid pinacol ester in the first step.

Compound 3H. ^1H NMR (500 MHz, $\text{C}_2\text{Cl}_4\text{D}_2$) δ 8.57 – 8.41 (m, 1H), 7.97 – 7.83 (m, 2H), 7.78 – 7.64 (m, 4H), 7.52 (t, $J = 7.1$ Hz, 2H), 7.44 (dd, $J = 14.7, 7.9$ Hz, 3H), 7.39 – 7.32 (m, 2H), 7.24 (d, $J = 7.5$ Hz, 2H), 7.09 (q, $J = 9.9$ Hz, 2H), 6.92 (s, 1H), 6.56 (s, 1H), 5.92 (s, 1H), 4.91 (d, $J = 9.5$ Hz, 1H), 4.53 (s, 1H), 4.11 (d, $J = 9.5$ Hz, 1H), 2.21 (s, 3H). ^{13}C NMR (126 MHz, $\text{C}_2\text{Cl}_4\text{D}_2$) δ 146.51, 146.47, 146.31, 146.29, 146.22, 146.11, 145.96, 145.60, 145.54, 145.52, 145.38, 145.33, 145.24, 145.23, 145.14, 143.12, 142.56, 142.55, 142.22, 142.16, 142.13, 142.06, 142.03, 141.97, 141.74, 128.52, 120.45, 120.18, 120.08, 99.61, 79.96, 79.75, 79.52, 77.61, 68.09, 65.86, 54.00, 31.74, 31.28, 29.90, 25.81, 22.89, 15.58, 14.47. MS (MALDI-TOF) m/z : $[\text{M}^+]$ calculated for $\text{C}_{96}\text{H}_{27}\text{N}$ 1194.22; found 1194.282.

Compound 4H. ^1H NMR (500 MHz, $\text{C}_2\text{Cl}_4\text{D}_2$) δ 8.34 (d, $J = 8.1$ Hz, 1H), 7.81 (d, $J = 7.8$ Hz, 1H), 7.67 (d, $J = 7.6$ Hz, 1H), 7.61 (d, $J = 7.6$ Hz, 2H), 7.53 (d, $J = 7.5$ Hz, 2H), 7.45 – 7.38 (m, 2H), 7.33 – 7.25 (m, 3H), 7.25 – 7.18 (m, 5H), 7.18 – 7.08 (m, 3H), 6.79 – 6.72 (m, 1H), 6.70 – 6.64 (m, 2H), 6.40 (s, 1H), 5.91 (d, $J = 7.9$ Hz, 1H), 4.92 (d, $J = 9.5$ Hz, 1H), 4.88 (s, 1H), 4.18 (d, $J = 9.5$ Hz, 1H), 2.73 (s, 3H). ^{13}C NMR (126 MHz, $\text{C}_2\text{Cl}_4\text{D}_2$) δ : 155.12, 152.87, 152.27, 152.17, 146.12, 145.52, 145.33, 145.13, 145.10, 145.02, 144.99, 144.94, 144.92, 144.87, 144.75, 144.60, 144.35, 144.19, 144.14, 144.11, 144.04, 143.96, 143.78, 143.52, 143.39, 143.24, 143.16, 142.87, 141.96, 141.91, 141.80, 141.51, 141.39, 141.37, 141.09, 141.04, 141.00, 140.94, 140.90, 140.84, 140.75, 140.73, 140.53, 140.51, 140.39, 139.98, 138.99, 138.68, 138.52, 138.24, 137.74, 137.50, 136.93, 136.75, 135.33, 135.07, 134.82, 134.61, 128.08, 127.80, 127.26, 126.54, 126.52, 126.47,

126.39, 126.07, 126.04, 125.76, 125.30, 125.28, 124.87, 124.84, 124.41, 124.35, 124.07, 119.23, 119.09, 118.97, 118.15, 82.48, 75.93, 51.66. MS (MALDI-TOF) m/z: [M⁺] calculated for C₁₀₂H₃₁N 1270.25; found 1269.316.

Compound 5. In a round-bottom flask equipped with a stir bar was added with 2 g (12 mmol) fluorene, 1.5 g (10 mmol) 4-formylbenzoic acid and 15 mL of THF. To this mixture was 3.5 ml (5 mmol) of 40% Bu₄N⁺OH⁻ in H₂O added dropwise under stirring, forming a yellow clear solution which was heated to 70 °C until it turned green. The mixture was then diluted with 20 mL of water and washed with hexane to remove extra fluorene and the aqueous layer was transferred to a flask, to which 15 mL of 1M HCl was added dropwise to precipitate the product. Finally, product was collected using vacuum filtration, washed with water, and dried overnight, yielding 2.7 g (90%) of yellowish crystalline powder.

Compound 6. 2.5 g (8.3 mmol) of **5** and 12 mL of AcOH was added to a round-bottom flask equipped with a stir bar. To this stirring suspension was 1.34 g (8.3 mmol) of Br₂ added dropwise. Upon addition of Br₂, a brown solution was formed, then the reaction was warmed up to 120 °C. An hour later, the reaction was cooled down to ~ 100 °C and 10 drops of water was added to the solution. The mixture was then stored in a fridge for 30 minutes to crash out the product, which was then collected with vacuum filtration and washed with methanol to yield 2.8 g (88%) of product.

Compound 7. In a two-neck round-bottom flask equipped with a stir bar was added 2 g (5.3 mmol) of **6** and 880 mg (5.3 mmol) of fluorene. 1.8 g (16 mmol) of tBuOK was loaded in a swivel feeding arm attached to the side neck of the flask. The organic solid was then dissolved in 40 mL of DMF to form a dark green solution, which was subsequently bubbled with N₂ for 10 min and cooled down to 0 °C in an ice bath. After the flask is connected to a Schlenk line in a N₂

atmosphere, the feeding arm was rotated and tBuOK was gently tapped into the DMF solution. A dark blue solution formed, and the reaction was kept at 0 °C for an hour before 15 mL of 1M HCl was added. To the resulting orange solution was added with freshly prepared 20% Na₂S₂O₄ aqueous solution till the orange color fade away. The reaction was then brought up to 100 °C, to which 3 mL of water was added. The product precipitated after the reaction was cooled down to r.t. and was collected by filtration and washed with 1:1 methanol/water, yielding 1.85 g (75%) of light orange powder.

Compound 8. In a two-neck round-bottom flask equipped with a stir bar and a water condenser that is connected to the Schlenk line was added 300 mg of **7**. The flask was pump-purged three times and 20 ml of toluene was added to dissolve the starting material, forming a yellow solution. At room temperature, 0.02 ml of SOCl₂ was added to the solution dropwise, and the reaction temperature was brought up to 80 °C. 12 hours later, the solution turned orange. After toluene was removed on a rotary evaporator 310 mg of orange oil was yielded. The product was carried to the next step without further purification.

Compound 9. 310 mg of compound xx was placed in a flame-dried two-neck round-bottom flask equipped with a stir bar and pump-purged three times before 12 mL of THF was added to dissolve the compound. The flask was then cooled down to -78 °C in a dry ice- acetone bath for 10 minutes before 200 mg LiAl(OtBu)₃H was added. 12 hours later, THF was removed on a rotary evaporator. The crude product was purified by silica gel column chromatography with 50 % CH₂Cl₂ in hexane as eluents to yield 154 mg of product. ¹H NMR (500 MHz, CD₂Cl₂) δ: 9.76 (s, 1H), 8.38 (d, J = 7.7 Hz, 1H), 7.82 (d, J = 8.4 Hz, 1H), 7.68 (d, J = 7.6 Hz, 1H), 7.59 (d, J = 7.6 Hz, 2H), 7.55 – 7.52 (m, 2H), 7.46 – 7.38 (m, 3H), 7.33 – 7.26 (m, 3H), 7.21 (td, J = 7.5, 1.2 Hz, 2H), 7.15 (td, J = 7.5, 1.0 Hz, 1H), 6.78 (d, J = 7.9 Hz, 2H), 6.70 (td, J = 7.7, 1.2 Hz, 1H), 6.44

(s, 1H), 5.78 (d, $J = 8.0$ Hz, 1H). ^{13}C NMR (126 MHz, CD_2Cl_2) δ : 191.79, 145.06, 143.73, 143.19, 141.86, 141.26, 139.93, 138.43, 136.18, 135.16, 129.29, 128.99, 128.56, 127.79, 127.71, 127.47, 127.14, 126.62, 126.00, 125.27, 125.24, 120.04, 119.97, 119.26.

Br-BDPAH was synthesized previously and was used directly for synthesizing **10** and **16**.

Compound 10. A round-bottom flask equipped with a magnetic stir bar was charged with 400 mg of compound xx, 224 mg 4-Formylphenylboronic acid pinacol ester, 786 mg of Cs_2CO_3 and 60 mg of $\text{Pd}(\text{dppf})\text{Cl}_2$. After three pump-purge cycles, 15 mL of 10:1 THF/ H_2O mixture that was bubbled with N_2 for 10 minutes was added to the flask and brought up to 70°C . 12 hours later, 6ml of N_2 purged 2:1 Toluene/ AcOH mixture was added to neutralize the base in the reaction and protonate the BDPA anion. The solvent was removed on a rotary evaporator and the crude product was purified by silica gel column chromatography to attain 370 mg of product. ^1H NMR (500 MHz, CD_2Cl_2) δ : 10.04 (s, 1H), 8.49 (dd, $J = 8.0, 0.9$ Hz, 1H), 7.94 (dt, $J = 7.4, 1.1$ Hz, 1H), 7.92 (d, $J = 8.4$ Hz, 2H), 7.80 (dt, $J = 7.5, 1.0$ Hz, 1H), 7.75 – 7.71 (m, 4H), 7.68 (dd, $J = 7.5, 0.9$ Hz, 2H), 7.53 (td, $J = 7.5, 0.9$ Hz, 1H), 7.45 – 7.37 (m, 5H), 7.34 (td, $J = 7.5, 1.2$ Hz, 2H), 7.26 (td, $J = 7.5, 1.0$ Hz, 1H), 6.89 – 6.81 (m, 3H), 6.58 (s, 1H), 6.02 (dt, $J = 8.0, 0.9$ Hz, 1H). ^{13}C NMR (126 MHz, CD_2Cl_2) δ : 191.72, 145.94, 144.16, 144.08, 141.92, 141.21, 139.81, 139.17, 138.77, 138.58, 138.10, 136.40, 135.29, 130.04, 129.29, 128.33, 127.58, 127.38, 127.24, 127.07, 126.58, 126.54, 126.02, 125.36, 125.23, 120.03, 119.91, 119.13.

Compound 11. ^1H NMR (500 MHz, $\text{DMSO}-d_6$) δ : 13.40-12.90 (br, 1H), 8.15 (s, 1H), 8.02-7.96 (m, 3H), 7.91-7.84 (m, 3H), 7.65 (t, $J = 7.5$ Hz, 1H), 7.45-7.35 (m, 4H), 7.12 (td, $J = 7.5$ Hz, 0.96 Hz, 1H). ^{13}C NMR (126 MHz, DMSO) δ : 166.66, 142.43, 140.77, 139.42, 137.14, 136.93, 135.71, 132.81, 132.07, 130.48, 130.28, 129.91, 128.92, 127.61, 127.34, 125.65, 124.02, 123.27, 120.39, 120.19.

Compound 12. ^1H NMR (500 MHz, DMSO- d_6) δ : 13.64-12.96 (br, 1H), 8.78 (d, $J = 7.5$ Hz, 1H), 8.11 (dt, $J = 7.5$ Hz, 1.5 Hz, 1H), 7.97 (t, $J = 1.5$ Hz, 1H), 7.95 (d, $J = 7.5$ Hz, 1H), 7.87 (d, $J = 7.5$ Hz, 1H), 7.77 (td, $J = 7.5$ Hz, 1.5 Hz, 1H), 7.73 (t, $J = 7.5$ Hz, 1H), 7.54 (td, $J = 7.5$ Hz, 1.0 Hz, 1H), 7.47 (td, $J = 7.5$ Hz, 1.0 Hz, 1H), 7.30 (td, $J = 7.5$ Hz, 1.0 Hz, 1H), 6.92 (td, $J = 7.5$ Hz, 1.0 Hz, 1H), 6.05 (d, $J = 7.5$ Hz, 1H). ^{13}C NMR (126 MHz, DMSO- d_6) δ : 166.66, 142.43, 140.77, 139.42, 137.14, 136.92, 135.71, 132.80, 132.08, 130.48, 130.28, 129.91, 128.92, 127.61, 127.34, 125.64, 124.02, 123.27, 120.38, 120.19.

Compound 13. ^1H NMR (500 MHz, CD_2Cl_2) δ : 8.39 (d, $J = 7.5$ Hz, 1H), 7.82 (d, $J = 7.5$ Hz, 1H), 7.72 (dt, $J = 7.5, 1.5$ Hz, 1H), 7.68 (d, $J = 7.5$ Hz, 1H), 7.60-7.53 (m, 4H), 7.41 (td, $J = 7.5, 0.9$ Hz, 1H), 7.35 (t, $J = 1.5$ Hz, 1H), 7.31 (td, $J = 7.5, 1.5$ Hz, 1H), 7.28-7.18 (m, 4H), 7.15 (td, $J = 7.5, 1.5$ Hz, 1H), 7.03 (t, $J = 7.5$ Hz, 1H), 6.81 (dt, $J = 7.5, 1.5$ Hz, 1H), 6.70 (td, $J = 7.5, 1.5$ Hz, 1H), 6.44 (s, 1H), 5.73 (d, $J = 7.5$ Hz, 1H). ^{13}C NMR (126 MHz, CD_2Cl_2) δ : 169.80, 143.85, 143.79, 143.24, 141.99, 141.78, 141.25, 139.90, 138.98, 138.59, 138.48, 136.49, 133.84, 130.45, 128.88, 128.50, 128.46, 128.05, 127.69, 127.67, 127.42, 127.16, 127.08, 126.63, 126.07, 125.91, 125.25, 125.12, 120.04, 119.98, 119.94, 119.24.

Compound 15. ^1H NMR (500 MHz, CD_2Cl_2) δ : 9.58 (s, 1H), 8.40 (d, $J = 7.5$ Hz, 1H), 7.82 (d, $J = 7.5$ Hz, 1H), 7.68 (d, $J = 7.5$ Hz, 1H), 7.58 (d, $J = 7.5$ Hz, 3H), 7.54 (t, $J = 7.5$ Hz, 2H), 7.42 (t, $J = 7.5$ Hz, 1H), 7.31 (t, $J = 7.5$ Hz, 1H), 7.29 – 7.25 (m, 2H), 7.24 – 7.18 (m, 2H), 7.14 (t, $J = 7.5$ Hz, 1H), 7.09 (t, $J = 7.5$ Hz, 1H), 7.07 (s, 1H), 6.85 (d, $J = 7.5$ Hz, 1H), 6.69 (t, $J = 7.5$ Hz, 1H), 6.46 (s, 1H), 5.73 (d, $J = 8.0$ Hz, 1H).

Compound 16. ^1H NMR (500 MHz, $\text{C}_2\text{Cl}_4\text{D}_2$) δ : 9.95 (s, 1H), 8.38 (d, $J = 8.1$ Hz, 1H), 7.93 (t, $J = 1.8$ Hz, 1H), 7.83 (dd, $J = 7.7, 1.2$ Hz, 1H), 7.75 – 7.71 (m, 2H), 7.70 (d, $J = 7.6$ Hz, 1H), 7.60 (d, $J = 7.5$ Hz, 2H), 7.55 (d, $J = 7.4$ Hz, 2H), 7.50 (t, $J = 7.7$ Hz, 1H), 7.43 (td, $J = 7.5,$

0.9 Hz, 1H), 7.35 – 7.30 (m, 2H), 7.28 (dd, $J = 7.5, 1.2$ Hz, 2H), 7.26 – 7.21 (m, 4H), 7.18 (td, $J = 7.4, 1.0$ Hz, 1H), 6.78 (ddd, $J = 8.4, 7.4, 1.3$ Hz, 1H), 6.69 (d, $J = 8.0$ Hz, 2H), 6.43 (s, 1H). ^{13}C NMR (126 MHz, $\text{C}_2\text{Cl}_4\text{D}_2$) δ : 192.83, 144.77, 144.04, 141.99, 141.30, 141.22, 139.79, 138.90, 138.68, 138.49, 137.85, 136.79, 136.12, 133.05, 129.74, 129.22, 129.06, 128.55, 127.81, 127.79, 127.73, 127.65, 127.28, 126.97, 126.40, 126.07, 125.58, 125.29, 120.45, 120.31, 120.22, 119.42.

4.5.2. Transient Absorption Spectroscopy

All datasets were background-subtracted to remove scattered pump light and spontaneous emission and corrected for group delay dispersion and time-zero using Surface Xplorer (Ultrafast Systems, LLC). The fsTA data were globally fitted to an $\text{A} \rightarrow \text{B} \rightarrow \text{C}$ model. The nsTA data were fit to an $\text{A} \rightarrow \text{G}$ model.

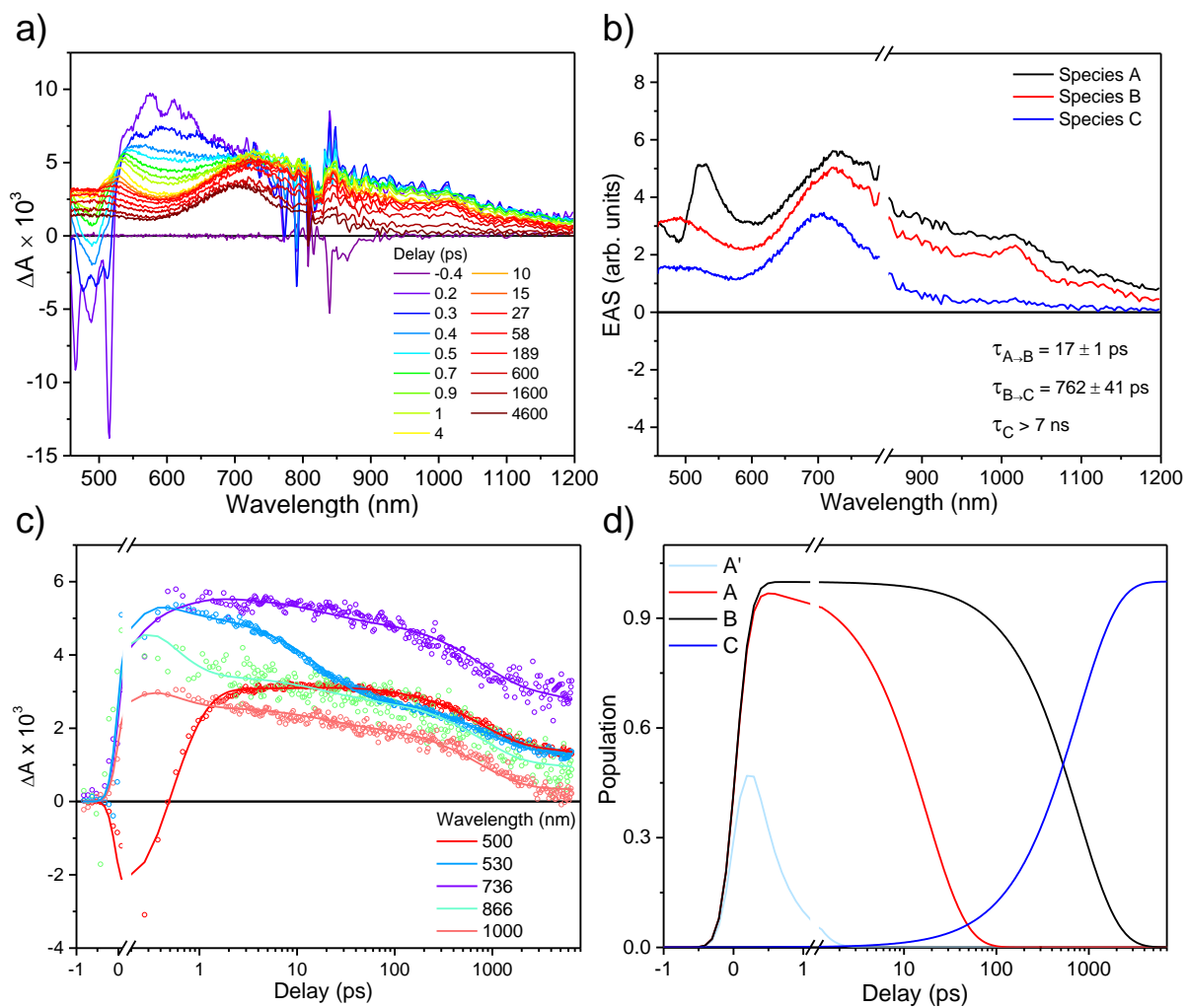


Figure 4.8. Transient absorption spectra of 1. a) FSTA data of 1 at 298 K in toluene solution following $\lambda_{\text{ex}} = 450$ nm excitation. b) Evolution-associated spectra (EAS) of 1. c) Comparison of the kinetic traces to the fit at selected probe wavelengths. d) Population models for the species in the EAS.

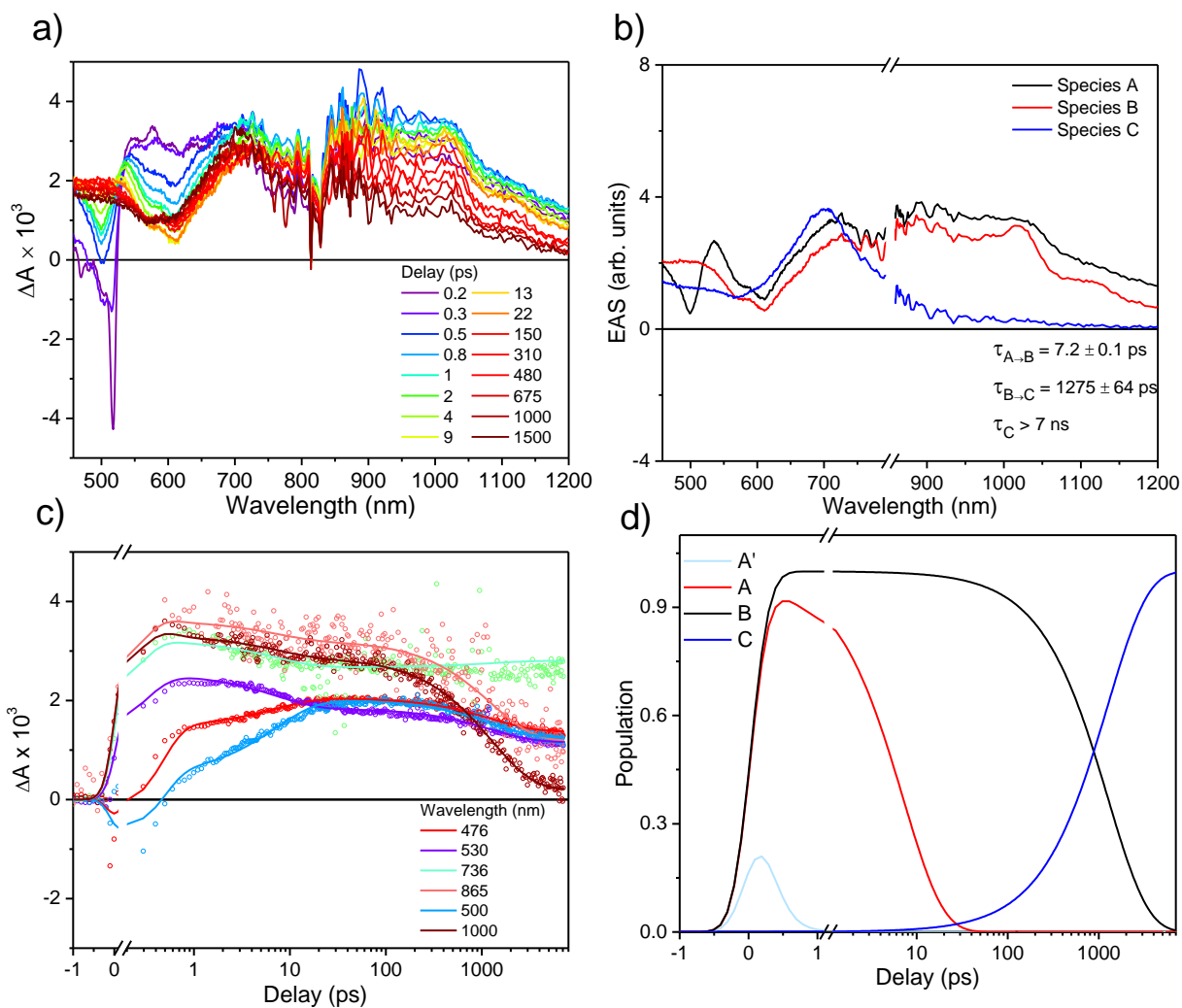


Figure 4.9. Transient absorption spectra of 2. a) FsTA data of 2 at 298 K in toluene solution following $\lambda_{\text{ex}} = 450$ nm excitation. b) Evolution-associated spectra (EAS) of 2. c) Comparison of the kinetic traces to the fit at selected probe wavelengths. d) Population models for the species in the EAS.

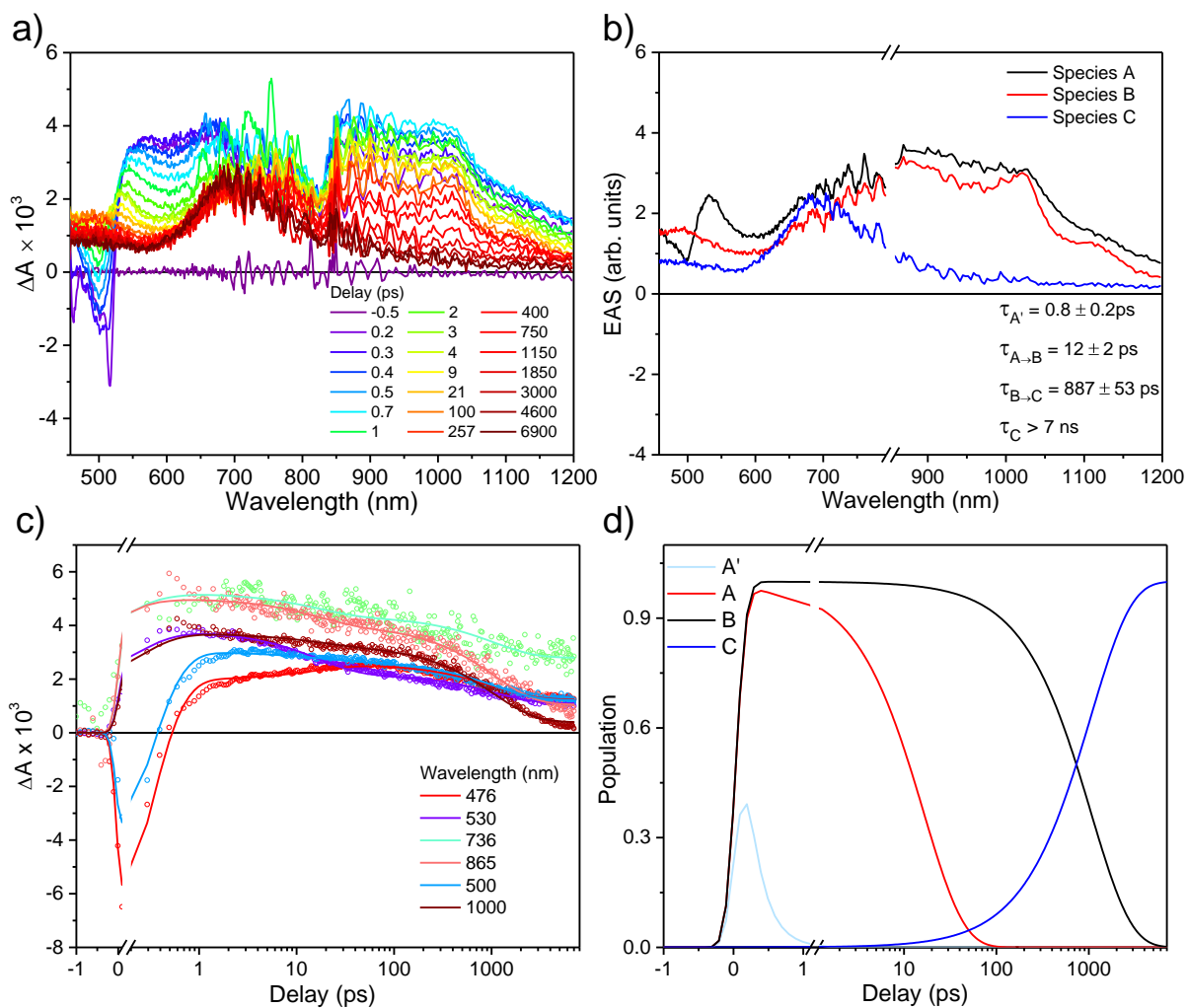


Figure 4.10. Transient absorption spectra of 3. a) fsTA data of 3 at 298 K in toluene solution following $\lambda_{\text{ex}} = 450$ nm excitation. b) Evolution-associated spectra (EAS) of 3. c) Comparison of the kinetic traces to the fit at selected probe wavelengths. d) Population models for the species in the EAS.

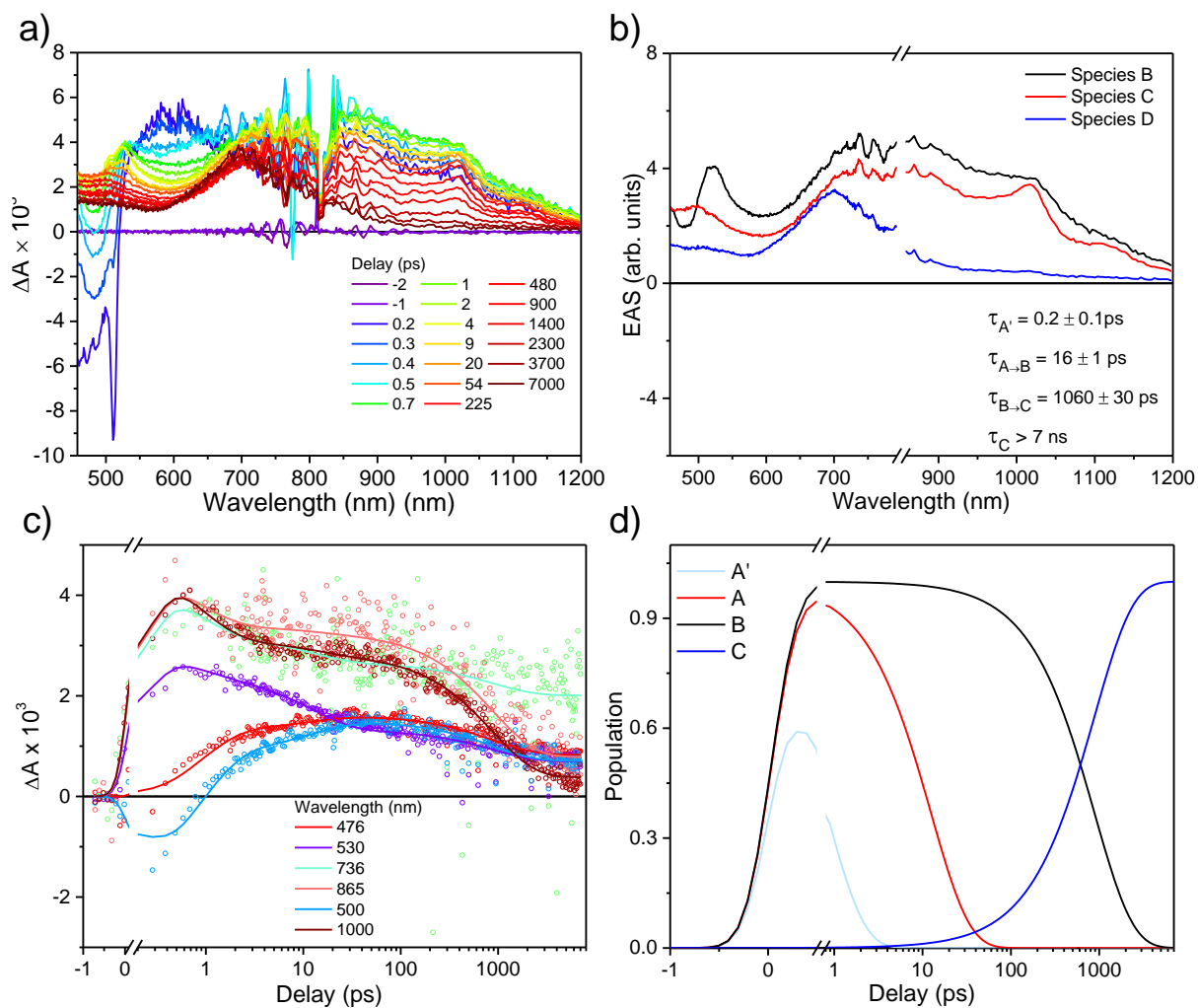


Figure 4.11. Transient absorption spectra of 4. a) FsTA data of 4 at 298 K in toluene solution following $\lambda_{\text{ex}} = 450$ nm excitation. b) Evolution-associated spectra (EAS) of 4. c) Comparison of the kinetic traces to the fit at selected probe wavelengths. d) Population models for the species in the EAS.

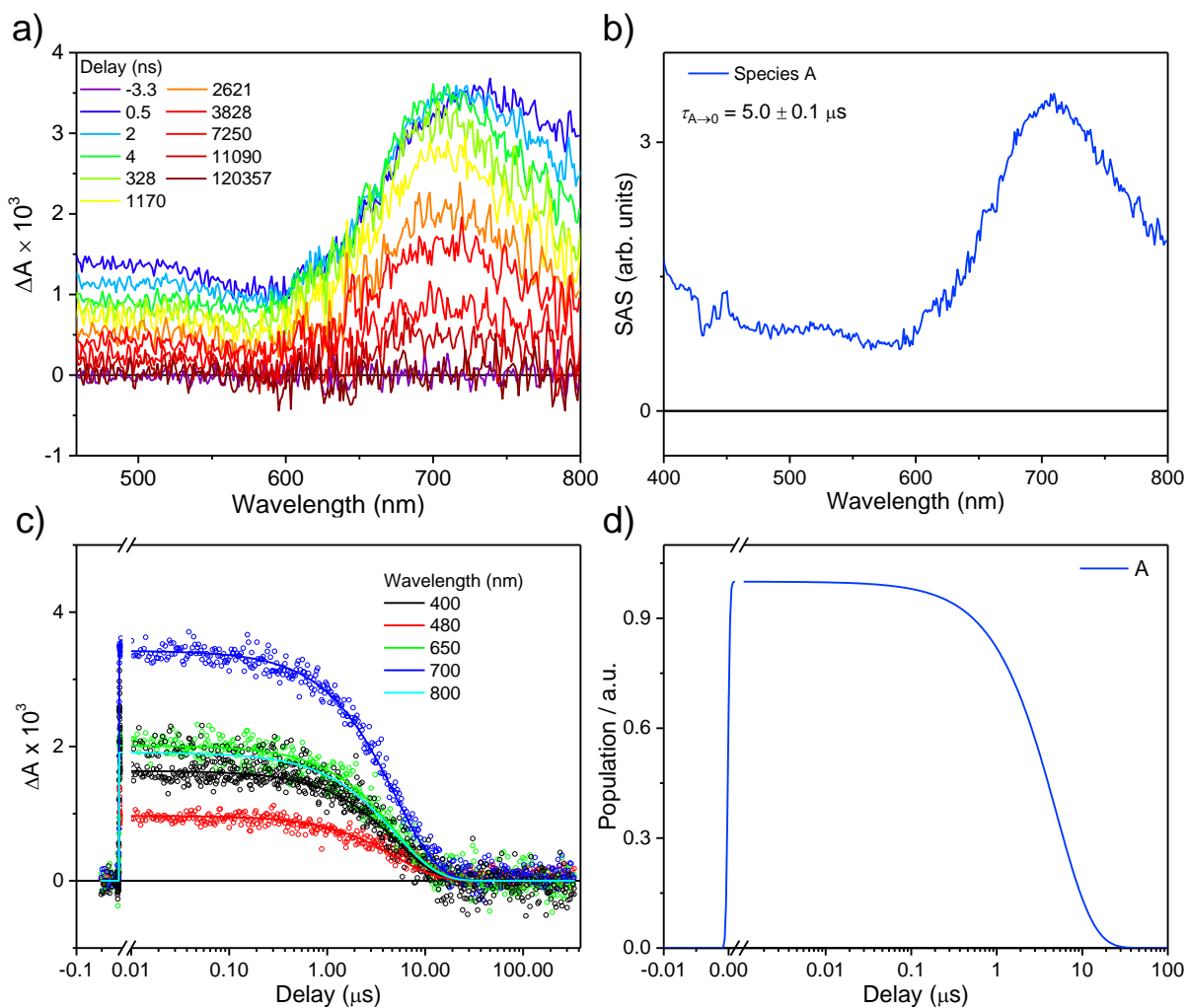


Figure 4.12. Transient absorption spectra of 1. a) NsTA data of 1 at 298 K in toluene solution following $\lambda_{\text{ex}} = 450 \text{ nm}$ excitation. b) Species-associated spectra (SAS) of 1. c) Comparison of the kinetic traces to the fit at selected probe wavelengths. d) Population models for the species in the SAS.

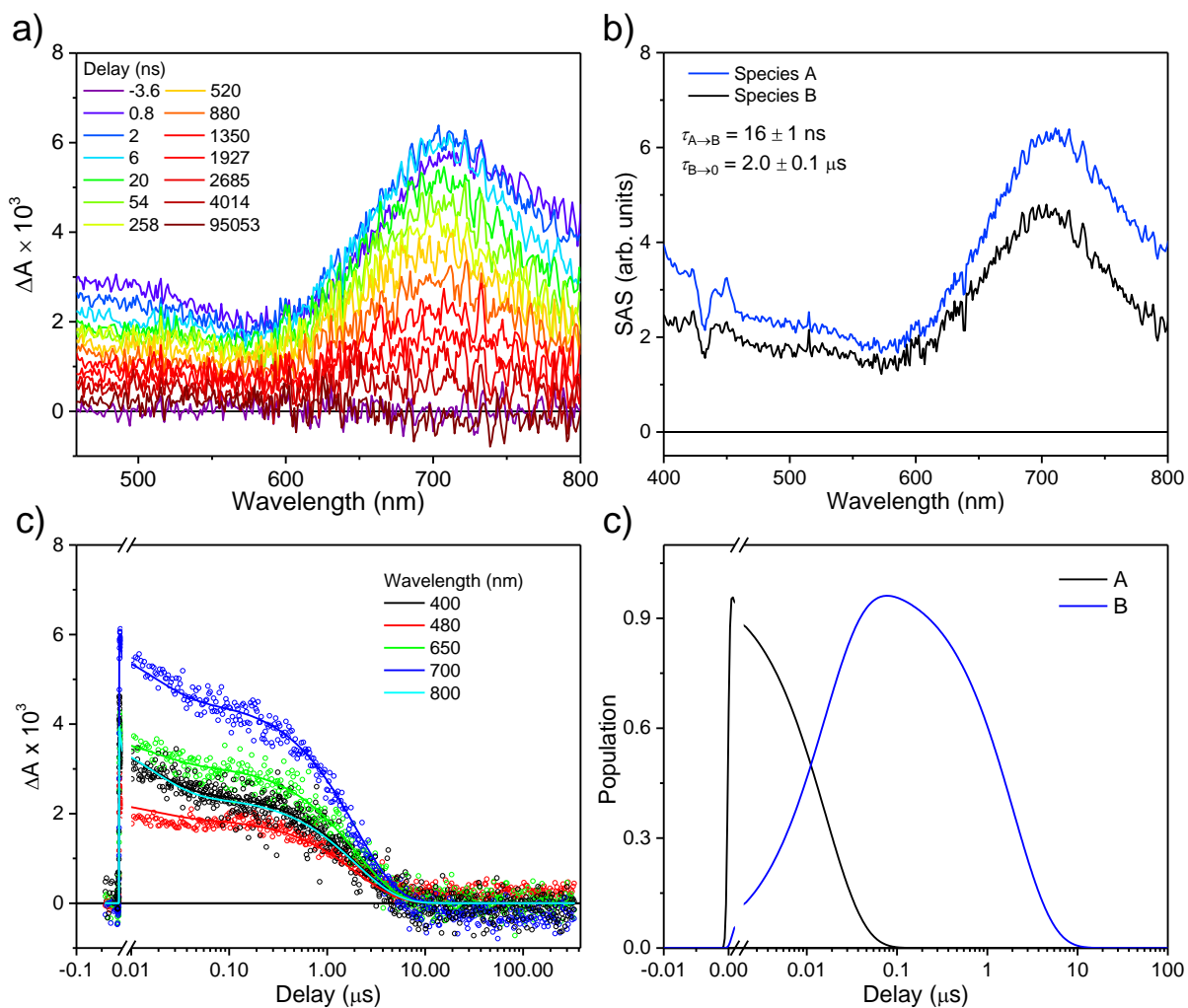


Figure 4.13. Transient absorption spectra of 2. a) NsTA data of 2 at 298 K in toluene solution following $\lambda_{\text{ex}} = 450$ nm excitation. b) Species-associated spectra (SAS) of 2. c) Comparison of the kinetic traces to the fit at selected probe wavelengths. d) Population models for the species in the SAS.

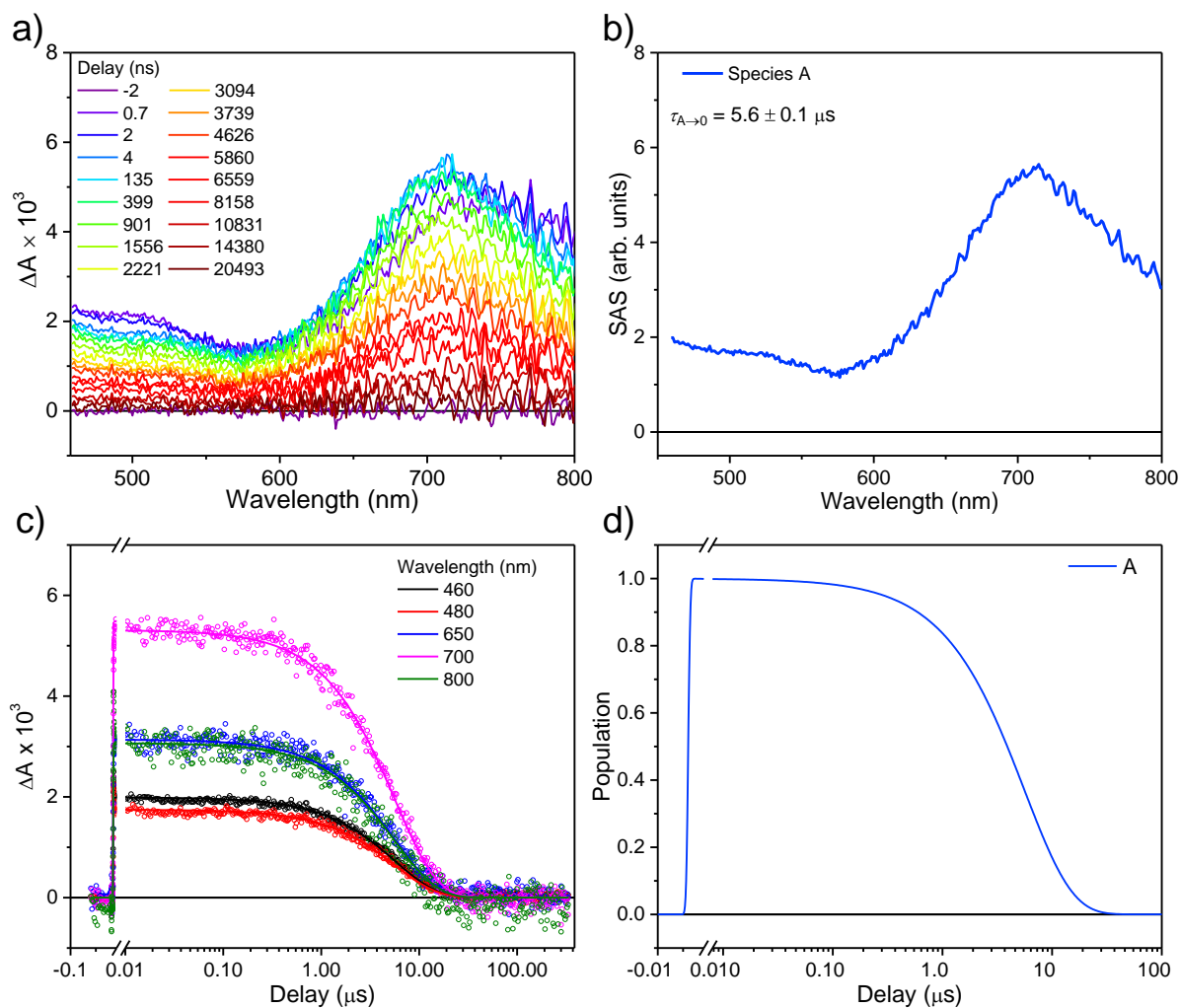


Figure 4.14. Transient absorption spectra of 3. a) NsTA data of 3 at 298 K in toluene solution following $\lambda_{\text{ex}} = 450 \text{ nm}$ excitation. b) Species-associated spectra (SAS) of 3. c) Comparison of the kinetic traces to the fit at selected probe wavelengths. d) Population models for the species in the SAS.

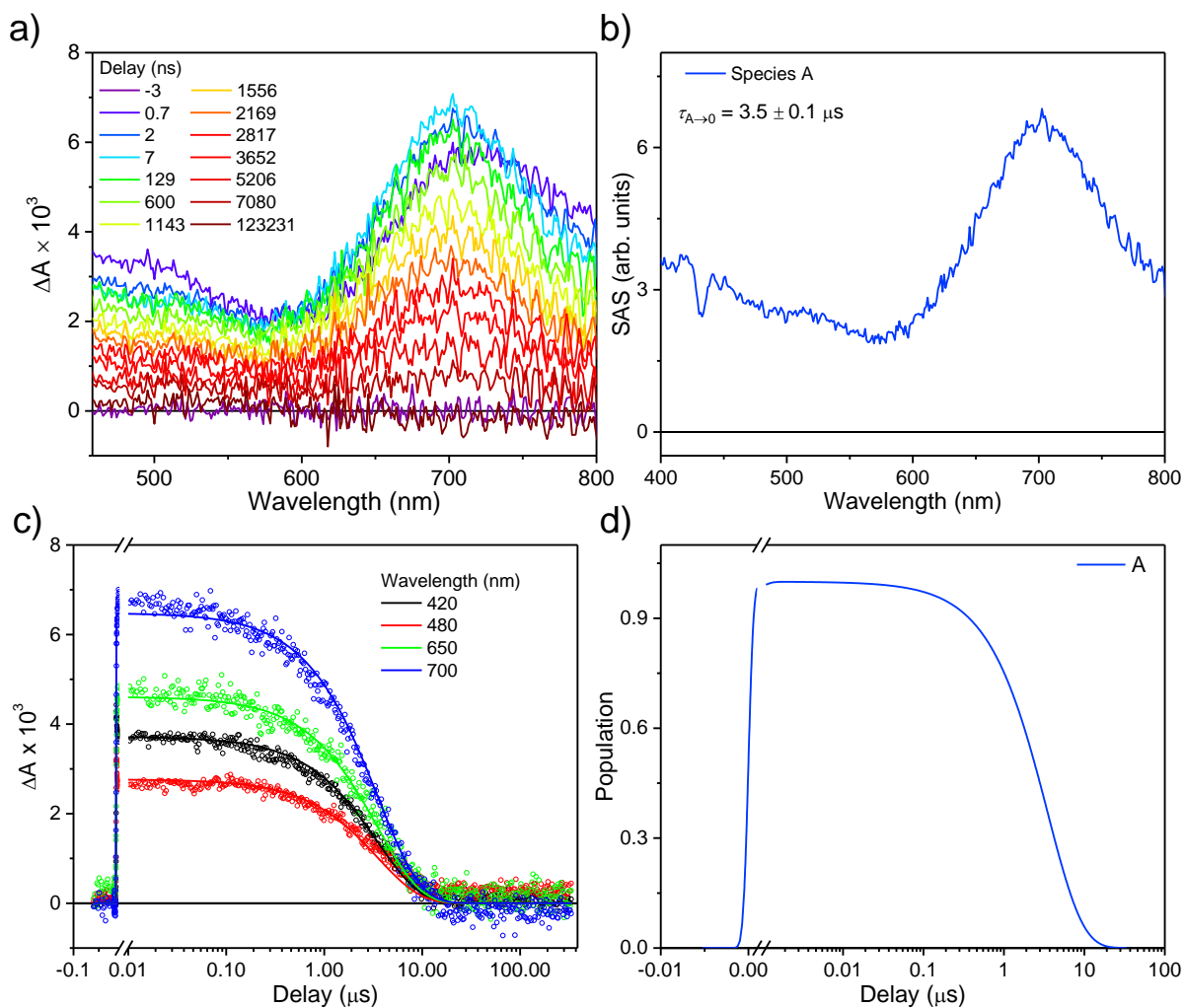


Figure 4.15. Transient absorption spectra of 4. a) NsTA data of 4 at 298 K in toluene solution following $\lambda_{\text{ex}} = 450 \text{ nm}$ excitation. b) Species-associated spectra (SAS) of 4. c) Comparison of the kinetic traces to the fit at selected probe wavelengths. d) Population models for the species in the SAS.

4.5.3 Electron Paramagnetic Resonance (EPR) Spectroscopy

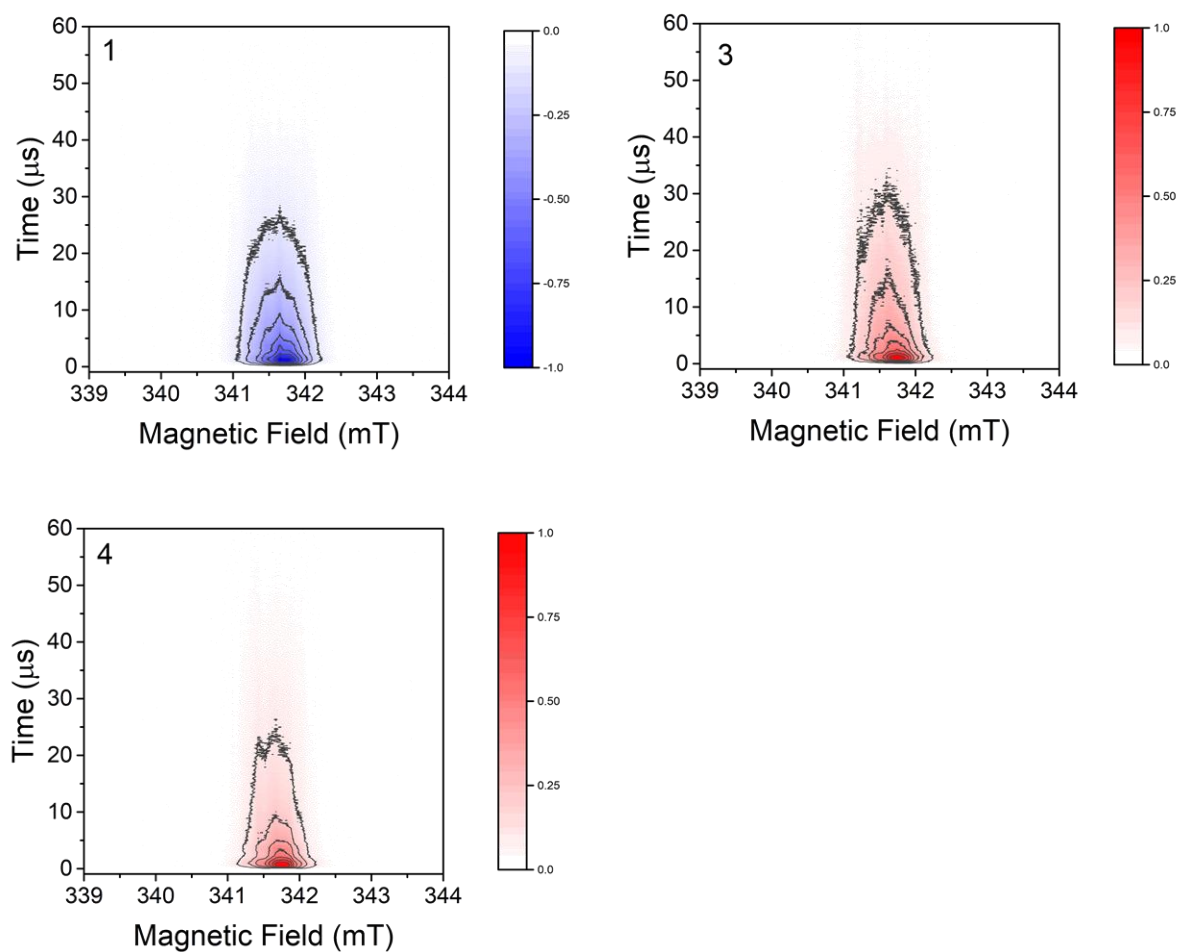


Figure 4.16. Time-Resolved EPR of 1 (a), 3 (b) and 4 (c) in toluene at room temperature.

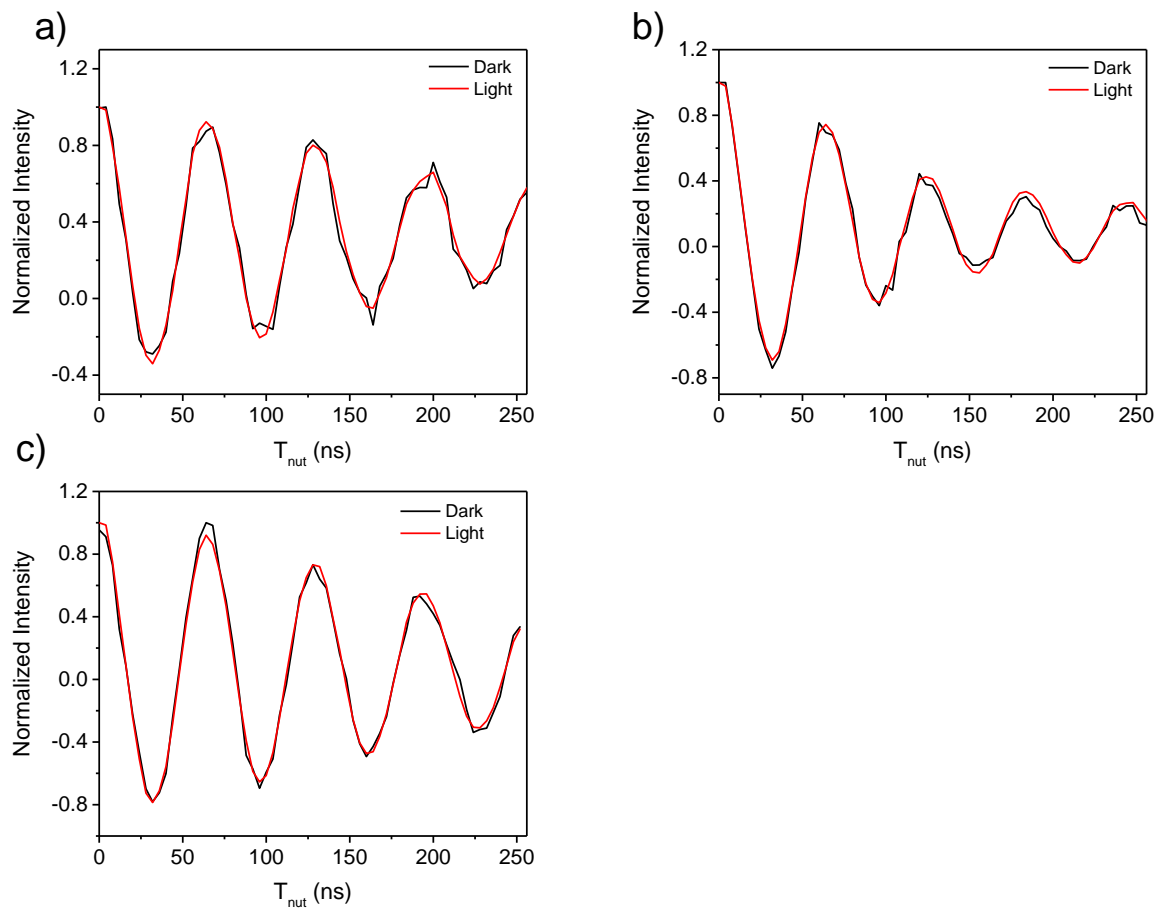


Figure 4.17. Transient nutation of 1 (a), 3 (b) and 4 (c) with (red) and without (black) light excitation ($T_{daf} = 1\mu s$)

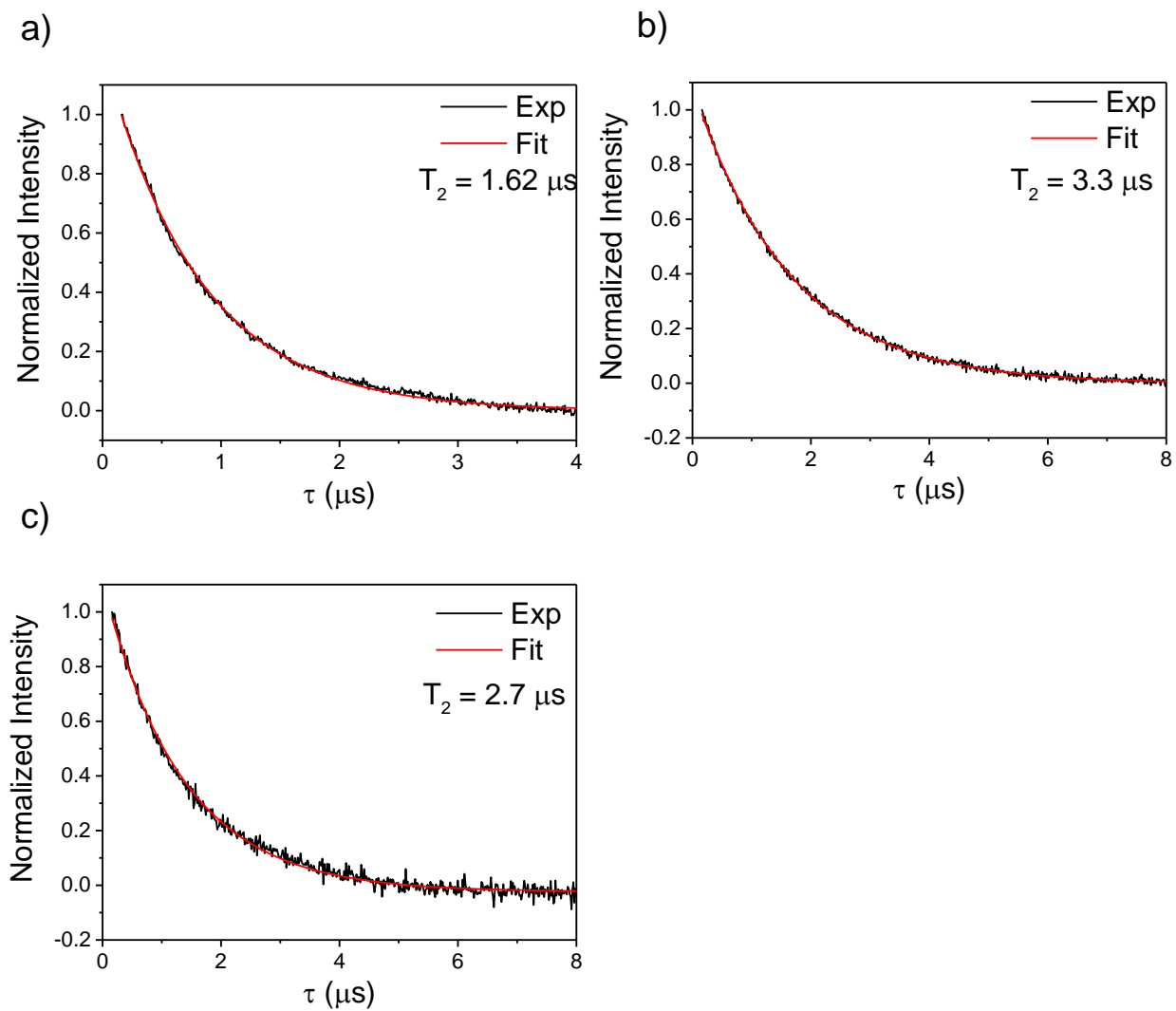


Figure 4.18. T_2 relaxation measurement of the steady state BDPA in 1 (a), 3 (b) and 4 (c) using the pulse sequence $\pi/2$ - τ - π - τ -echo, where $\tau = 160$ ns and π pulse is 32 ns.

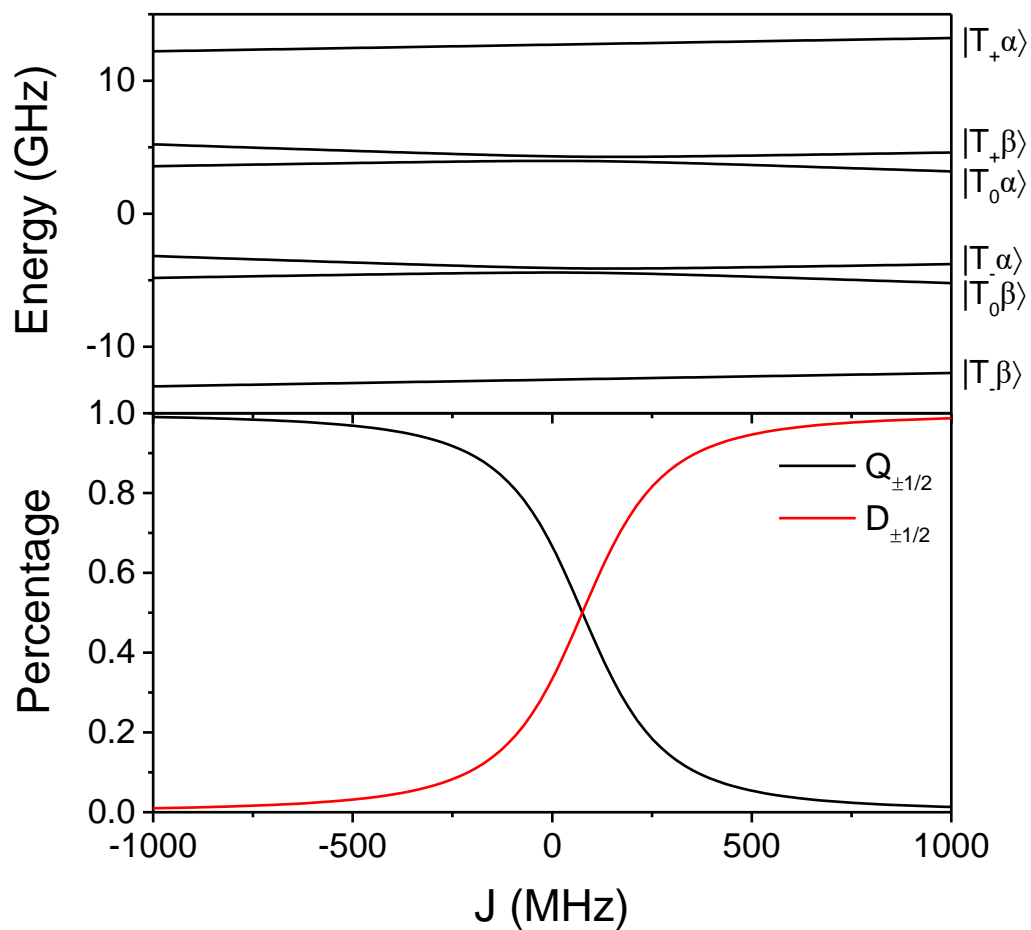


Figure 4.19. Exchange coupling dependence of energies of spin sublevels of a radical-triplet pair system (top) and the doublet (quartet) character in percentage of the $T_0\beta$ and $T_0\alpha$ levels (bottom)

4.5.4 Computational Data

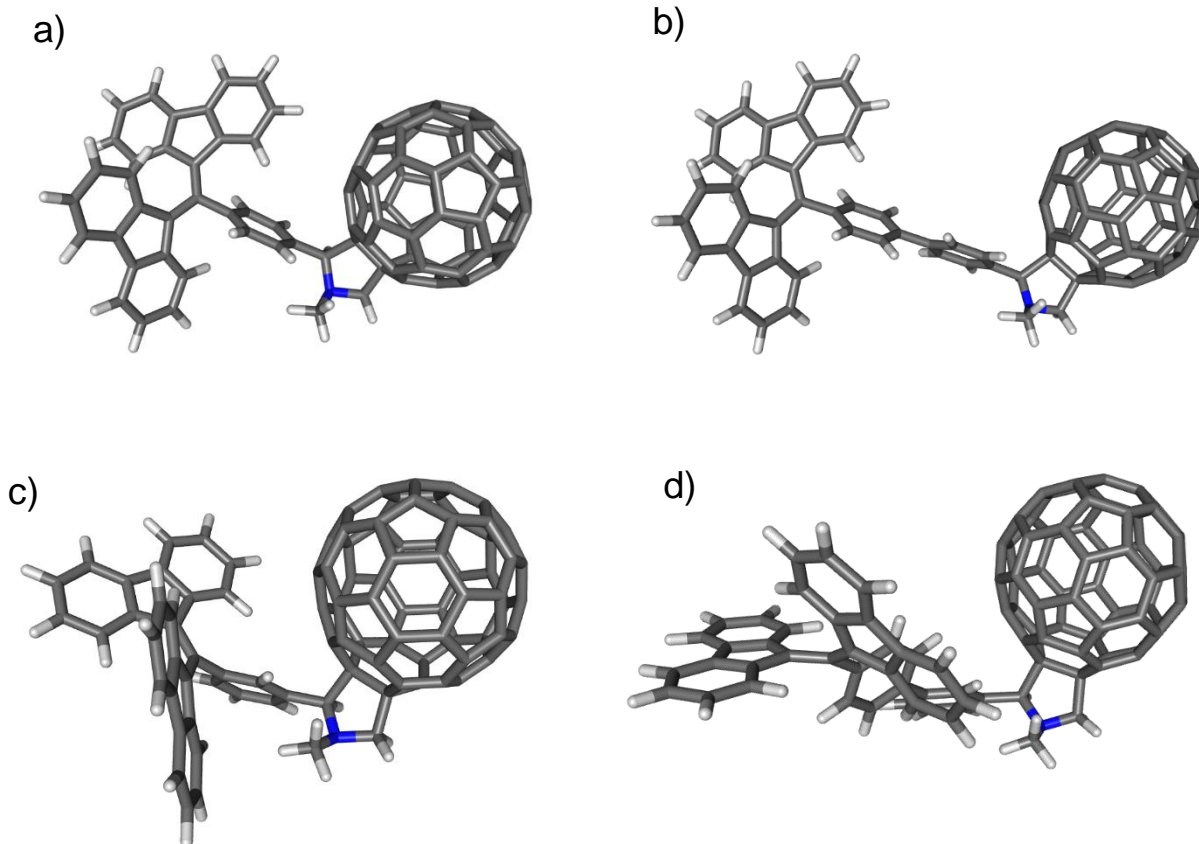


Figure 4.20. Optimized structure for 1 (a), 2 (b), 3 (c) and 4 (d) with B3LYP/6-31G* level of theory

Table 4.3. C₆₀ to BDPA distance measured from the center of C₆₀ to α -carbon of BDPA

Compound	1	2	3	4
C ₆₀ to BDPA Distance	9.6 Å	13.9 Å	8.2 Å	10.8 Å

Optimized structure of **1** on the doublet ground state.

N	-0.4837915	-3.8478419	-1.5237916	C	-5.9469474	1.4405065	-0.6020921
C	-6.9062447	3.4826676	-1.2687550	C	-5.7925942	0.0704338	-0.2882028
C	-7.1941541	2.1204902	-0.9829200	C	-4.4984031	-0.5889625	-0.6433853
C	-8.4883209	1.6307625	-1.1955138	C	-3.7480299	-1.2602076	0.3343602
C	-9.4838522	2.5032498	-1.6397984	C	-2.5246925	-1.8469369	0.0245678
C	-9.1995195	3.8517324	-1.8865362	C	-2.0211811	-1.8210253	-1.2870503
C	-7.9033006	4.3467001	-1.7104162	C	-2.7835219	-1.1645159	-2.2645107

C	-3.9916058	-0.5454179	-1.9503208	C	0.2823982	0.3158416	0.2973450
C	-6.7762597	-0.7155768	0.3586105	C	0.5869652	0.7583865	-1.0493391
C	-7.7281061	-0.2677662	1.3863818	C	3.7506501	3.6535011	0.6122314
C	-7.8986650	0.9719871	2.0142629	C	0.9551367	-0.3953195	-1.8232662
C	-8.8374170	1.0942616	3.0404644	C	1.9693748	-0.2885210	-2.7528419
C	-9.5955715	-0.0066786	3.4565479	C	2.6324667	0.9801939	-2.9652844
C	-9.4118104	-1.2589075	2.8611458	C	2.9929902	-1.3501557	-2.8694544
C	-8.4782569	-1.3879802	1.8375434	C	7.0180314	-0.8937728	-0.8849301
C	-8.0366015	-2.5644384	1.0864344	C	2.8171626	3.4726138	-0.4101950
C	-6.9841473	-2.1646916	0.2157332	C	5.3928147	-2.3598836	-1.7336006
C	-6.4203773	-3.1085478	-0.6542679	C	5.4455637	-1.2091758	-2.6027322
C	-6.8807445	-4.4266651	-0.6262483	C	1.5414086	2.8397016	-0.1227739
C	-7.9021958	-4.8139702	0.2490163	C	5.1577469	3.3946574	0.3649389
C	-8.4908125	-3.8790870	1.1068359	C	5.5769222	2.9645338	-0.8955538
C	-4.8865804	2.4581614	-0.6840325	C	1.1973347	1.9999708	-1.2592750
C	-5.4745733	3.7006213	-1.0531983	C	2.2471656	2.1142115	-2.2418295
C	-4.7104783	4.8601675	-1.1344245	C	4.2591863	-0.7088631	-3.1501563
C	-3.3445999	4.7949930	-0.8398984	C	4.0410372	0.7251617	-3.2107581
C	-2.7601627	3.5831316	-0.4551442	C	3.2534985	3.0216659	-1.7218063
C	-3.5207602	2.4151053	-0.3686818	C	6.4475994	-0.2977906	-2.0822059
C	2.9932618	-2.5350950	2.4303910	C	6.5833467	1.9187003	-1.0094182
C	2.5870122	-1.3722685	3.1986061	C	4.6071539	2.7723309	-1.9564383
C	3.5463635	-0.5051114	3.7227281	C	6.2347155	1.0809538	-2.1405236
C	5.3523391	-1.8781051	2.7474009	C	5.0089641	1.6034107	-2.7221633
C	4.3522909	-2.7867926	2.2173207	C	3.4436598	3.2118278	1.9634774
C	1.3692886	-0.8445544	2.6128073	C	4.6620580	2.6804161	2.5485568
C	3.3313807	0.9321738	3.6685246	C	5.7230096	2.7950033	1.5619239
C	6.4161535	-1.7601284	1.7631219	C	0.5974915	1.1320562	1.3888029
C	4.7889697	-3.2259414	0.9146660	C	1.2477079	2.4150577	1.1726722
C	2.0315803	-2.7380529	1.3679990	C	4.9583798	-0.7592094	3.4841649
C	7.0425217	-0.5294704	1.5564193	C	5.6109705	0.5178169	3.2713259
C	6.6325290	0.6316767	2.3262530	C	6.6871189	1.7915987	1.4526891
C	1.1554981	0.5371549	2.5784306	C	7.3496709	-0.0876797	0.2056108
C	4.6052707	1.5638401	3.3847251	C	7.1283486	1.3463106	0.1417879
C	2.1585887	1.4416385	3.1079281	C	-0.6825935	-2.4074992	-1.6860909
C	6.0681950	-2.5958537	0.6268922	C	0.9192062	-4.0293279	-1.8359958
C	3.8456603	-3.3926711	-0.1058029	C	-0.9279434	-4.5128625	-0.2995484
C	2.4405559	-3.1771407	0.1266186	H	-8.7234708	0.5869070	-1.0196004
C	1.0106954	-1.6739979	1.4825399	H	-10.4912106	2.1277590	-1.7970709
C	4.1549364	-2.9485976	-1.4520521	H	-9.9879855	4.5157806	-2.2306014
C	1.7348157	-2.8278487	-1.1897214	H	-7.6796834	5.3878972	-1.9287837
C	0.4586913	-1.1131081	0.3505585	H	-4.1207343	-1.2999881	1.3536771
C	6.3641646	-2.1726201	-0.6679977	H	-1.9554742	-2.3106900	0.8210217
C	2.2158399	2.6064732	2.2388290	H	-2.4194018	-1.1270786	-3.2883314
C	2.9437095	-2.4531554	-2.0451895	H	-4.5531946	-0.0296078	-2.7236527
C	0.6226765	-1.6792837	-1.0622792	H	-7.3104125	1.8320731	1.7151825

H	-8.9767235	2.0573625	3.5237786	H	-1.7006188	3.5480852	-0.2171413
H	-10.3210374	0.1086749	4.2573346	H	-3.0452577	1.4924361	-0.0580281
H	-9.9806386	-2.1188466	3.2057801	H	1.0564820	-3.9732949	-2.9231801
H	-5.6346690	-2.8300038	-1.3471602	H	1.2859484	-5.0015160	-1.4982908
H	-6.4395207	-5.1593288	-1.2966421	H	-0.6819264	-5.5756190	-0.3882367
H	-8.2468164	-5.8446022	0.2555471	H	-2.0132190	-4.4316926	-0.2114381
H	-9.2979840	-4.1773070	1.7714080	H	-0.4714859	-4.1370611	0.6300445
H	-5.1657792	5.8074505	-1.4123582	H	-0.5719002	-2.2292291	-2.7629905
H	-2.7359436	5.6931989	-0.9006395				

Optimized structure of **2** on the doublet ground state.

C	9.8395705	-3.4906581	-0.8117566	C	7.9540298	-5.1485931	-0.1528501
C	9.9416979	-2.0766380	-0.7130199	C	6.6656520	-5.2486639	0.3815024
C	11.0866460	-1.4351183	-1.2005405	C	5.9638951	-4.0972463	0.7576703
C	12.1272391	-2.2018019	-1.7287699	C	6.5244366	-2.8289548	0.5935858
C	12.0314204	-3.5968223	-1.7930221	H	11.1729891	-0.3547498	-1.1755514
C	10.8790410	-4.2485541	-1.3427243	H	13.0203861	-1.7056768	-2.0985596
C	8.6748038	-1.5436219	-0.1857713	H	12.8515730	-4.1761897	-2.2085216
C	8.3433987	-0.1839908	-0.0047593	H	10.7953303	-5.3297406	-1.4201162
C	6.9224655	0.2392005	-0.1800774	H	6.8482058	1.3668031	1.6546698
C	6.2907522	1.0491475	0.7786383	H	4.5135038	2.0920388	1.3681930
C	4.9681785	1.4492760	0.6199638	H	2.3098134	1.3577682	1.4126304
C	4.2234385	1.0644596	-0.5082549	H	0.0016078	2.1024240	1.1449146
C	2.8162097	1.4998510	-0.6801279	H	0.6154889	2.4777737	-3.0933274
C	1.9525924	1.6212737	0.4211507	H	2.9422302	1.7514855	-2.8209803
C	0.6339352	2.0405912	0.2661682	H	4.3018927	-0.0761443	-2.3401210
C	0.1199596	2.3608524	-1.0003024	H	6.6443185	-0.7815567	-2.0572045
C	0.9806125	2.2302313	-2.0994491	H	10.3754302	-1.3955038	1.9373592
C	2.2991549	1.8107049	-1.9477172	H	12.3072260	-1.1239497	3.4541579
C	4.8581612	0.2571276	-1.4687350	H	13.4501519	1.0644489	3.6690491
C	6.1784642	-0.1500694	-1.3066032	H	12.6441711	3.0348753	2.3848262
C	9.2908956	0.8153881	0.3450724	H	7.6386284	2.4470382	-1.4581887
C	10.4338326	0.6590740	1.2528854	H	8.1023016	4.8321399	-1.8941748
C	10.8716835	-0.4340358	2.0109197	H	9.9867915	5.9833829	-0.7689411
C	11.9598221	-0.2754847	2.8710680	H	11.4654971	4.7396151	0.7949705
C	12.6046740	0.9612242	2.9942427	H	8.5067448	-6.0451928	-0.4221816
C	12.1576925	2.0697865	2.2670344	H	6.2112141	-6.2265882	0.5158865
C	11.0748627	1.9195147	1.4066642	H	4.9689648	-4.1889348	1.1849249
C	10.3674425	2.8935684	0.5730469	H	5.9664347	-1.9517065	0.9004216
C	9.2708379	2.2302476	-0.0466299	C	-5.0087456	1.9488532	2.7503975
C	8.4639513	2.9348298	-0.9512427	C	-4.5195345	0.7044607	3.3144467
C	8.7308365	4.2826883	-1.1985523	C	-5.4117615	-0.3145138	3.6482182
C	9.7961973	4.9332466	-0.5643960	C	-7.3100011	1.0633648	2.8778488
C	10.6260043	4.2368374	0.3209377	C	-6.3806975	2.1280498	2.5459366
C	7.8032870	-2.7104137	0.0319070	C	-3.2521599	0.3878301	2.6803122
C	8.5189080	-3.8882144	-0.3207768	C	-5.0773238	-1.6972476	3.3482396

C	-8.3458692	1.0388133	1.8578696	C	-7.0783426	-3.0538634	-1.5649365
C	-6.8335854	2.7562821	1.3288488	C	-2.7893909	-1.6999929	-1.6252961
C	-4.0524250	2.4121868	1.7690221	C	-3.8115464	-1.7200063	-2.6428892
C	-8.8647144	-0.1808591	1.4197677	C	-6.0364280	1.0522140	-3.0983828
C	-8.3732232	-1.4250797	1.9852523				
C	-2.9244428	-0.9444794	2.4090816	C	-5.6993650	-0.3261771	-3.4035173
C	-6.2906203	-2.3670142	2.9217330	C	-4.7472688	-2.7822202	-2.3208714
C	-3.8578266	-2.0051061	2.7414953	C	-8.2005956	0.2868135	-2.1854532
C	-8.0519236	2.0886507	0.8975531	C	-8.1669436	-2.0885297	-1.5228404
C	-5.8924239	3.1753916	0.3815002	C	-6.1133011	-2.6010596	-2.5468734
C	-4.4781316	3.0305569	0.6134104	C	-7.8730392	-1.0385302	-2.4790534
C	-2.9478664	1.4302285	1.7234722	C	-6.5987162	-1.3506732	-3.1082404
C	-6.1424847	2.9548606	-1.0306150	C	-4.9754748	-3.6386472	1.2659137
C	-3.7257363	2.9808385	-0.7209213	C	-6.2418407	-3.3172364	1.8995681
C	-2.3308846	1.1274327	0.5267585	C	-7.2738810	-3.3372300	0.8775695
C	-8.2910859	1.8794685	-0.4599441	C	-2.3018526	-1.2718615	1.1488724
C	-3.8069962	-2.9952290	1.6779241	C	-2.8420333	-2.5424229	0.6918738
C	-4.8853068	2.6721477	-1.6666098	C	-6.8362999	-0.1339966	3.4176781
C	-2.5211289	1.9202332	-0.7707709	C	-7.3785042	-1.4007127	2.9654818
C	-2.0398323	-0.2518955	0.2286215	C	-8.3173733	-2.4113083	0.9192260
C	-2.2873778	-0.4713810	-1.1827578	C	-9.1139552	-0.3981724	0.0038557
C	-5.2242442	-3.8574084	-0.1501914	C	-8.7749331	-1.7756403	-0.3050707
C	-2.7380027	0.7683241	-1.7523403	C	-1.2908591	2.8538903	-1.2476648
C	-3.7251617	0.7495179	-2.7164381	N	-1.5942939	4.2161369	-0.8086446
C	-4.2784131	-0.5096016	-3.1666855	C	-3.0074005	4.3504683	-1.0971965
C	-4.8314203	1.7311895	-2.6724691	H	-3.1405032	4.5109616	-2.1742663
C	-8.8353937	0.6129845	-0.9174226	H	-3.4491968	5.1991159	-0.5697758
C	-4.2939678	-3.4231870	-1.0967921	H	-1.4185157	2.8782266	-2.3375783
C	-7.3223534	2.3283633	-1.4461287	C	-1.2003852	4.6300048	0.5378624
C	-7.2687306	1.3524886	-2.5070866	H	-1.4884445	5.6779651	0.6666135
C	-3.0794824	-2.7530511	-0.6655684	H	-0.1141343	4.5692165	0.6325115
C	-6.6442748	-3.6691667	-0.3891880	H	-1.6545479	4.0494019	1.3559715

Optimized structure of **3** on the ground state.

N	0.4100016	0.9226028	4.1365595	C	2.1091575	1.8679454	2.5053457
C	4.9288058	-3.6463307	1.7573061	C	2.7353133	3.1065203	2.7117018
C	4.9558939	-2.6291556	0.7644421	C	4.0576423	3.3201639	2.3214738
C	4.8549907	-2.9821393	-0.5867696	C	5.5417181	0.2398293	-0.4421274
C	4.7796150	-4.3318656	-0.9350598	C	6.7928254	-0.3373052	-0.9597997
C	4.7861932	-5.3293137	0.0474259	C	7.7037980	-1.2379528	-0.3942397
C	4.8507431	-4.9896125	1.4027935	C	8.8746487	-1.5513267	-1.0878327
C	4.9733042	-1.3174049	1.4268499	C	9.1543338	-0.9667256	-2.3284979
C	4.9293303	-0.0481569	0.7986008	C	8.2695072	-0.0404938	-2.8899304
C	4.7753224	2.3016780	1.7001118	C	7.1002797	0.2750266	-2.2048081
C	4.1791891	1.0487378	1.4854316	C	6.0374879	1.2320864	-2.5174367
C	2.8552042	0.8441616	1.9058069	C	5.1117190	1.2359446	-1.4372371

C	3.9658307	2.0389785	-1.5232721	C	-5.3856081	2.2173478	1.2956958
C	3.7729530	2.8409366	-2.6501637	C	-0.7851216	2.1357886	-2.7824510
C	4.7019449	2.8458357	-3.6969134	C	-4.2005030	1.4563413	-4.0066420
C	5.8385657	2.0330504	-3.6370493	C	-4.8700398	2.3650660	-3.1841542
C	4.9510325	-1.5906397	2.8704885	C	-0.7173677	2.8632713	-1.5252810
C	4.9561533	-2.9998078	3.0709494	C	-1.9123670	3.6617776	-1.3988427
C	5.0078364	-3.5417984	4.3512683	C	-4.2770309	3.0683247	1.2276926
C	5.0635060	-2.6799166	5.4515848	C	-3.9563563	3.7371299	-0.0203228
C	5.0825476	-1.2924507	5.2642294	C	-2.7329799	3.4336566	-2.5738074
C	5.0332368	-0.7398494	3.9821705				
C	-2.1986033	-2.5549229	0.8934568	C	-6.2024789	1.9916195	0.1171275
C	-1.5688837	-2.7216157	-0.4036264	C	-5.9633066	1.9109575	-2.3363958
C	-2.3460551	-2.9632438	-1.5362939	C	-4.1223887	3.3691507	-2.4533169
C	-4.4019217	-2.8763273	-0.1722573	C	-5.8908544	2.6354754	-1.0822972
C	-3.5895662	-2.6411282	1.0070600	C	-4.7479533	3.5325483	-1.1506090
C	-0.4343412	-1.8191231	-0.4757186	C	-2.2508341	0.1578022	-4.2144287
C	-2.0263382	-2.2994250	-2.7899842	C	-3.3864756	-0.7449476	-4.1367807
C	-5.6102043	-2.0765004	-0.0511680	C	-4.5908459	0.0569529	-4.0095342
C	-4.2850353	-1.7002105	1.8506935	C	0.2662965	0.1941983	-1.6811238
C	-1.4596202	-1.5556069	1.6336510	C	-0.3035911	0.8297046	-2.8581801
C	-6.1598899	-1.4673292	-1.1805890	C	-3.7938802	-3.0348685	-1.4191463
C	-5.5271666	-1.6356975	-2.4769247	C	-4.3671547	-2.4046703	-2.5924394
C	-0.1168137	-1.1964675	-1.6869687	C	-5.6391663	-0.3785486	-3.1977589
C	-3.2743385	-1.9496211	-3.4397737	C	-6.6639537	-0.1060404	-1.0998745
C	-0.9328921	-1.4341818	-2.8633783	C	-6.3410542	0.5664639	-2.3457922
C	-5.5388387	-1.3476186	1.2034297	C	0.6630467	1.7203027	2.9390879
C	-3.5541776	-0.7249673	2.5393541	C	-1.0351744	0.9147807	4.2282600
C	-2.1175404	-0.6654988	2.4545397	C	1.0455143	-0.3907815	4.2565459
C	-0.3516356	-1.0906133	0.7717044	H	4.8336802	-2.2216449	-1.3592274
C	-4.0586103	0.6337868	2.6177896	H	4.7108406	-4.6096327	-1.9832218
C	-1.6280116	0.7534787	2.7591125	H	4.7263780	-6.3743514	-0.2445485
C	0.0394089	0.2326369	0.7878264	H	4.8275677	-5.7654323	2.1641622
C	-6.0227025	-0.0424891	1.2811008	H	2.4080807	-0.1258955	1.7238976
C	-1.0488065	-0.1796438	-3.5895707	H	2.1790057	3.9127333	3.1835733
C	-2.9331602	1.5283018	2.5786460	H	4.5231481	4.2863800	2.4950012
C	-0.4178757	1.2600541	1.8292056	H	7.5121427	-1.6918856	0.5714684
C	0.3150021	0.8858837	-0.4667406	H	9.5781645	-2.2570491	-0.6546005
C	-0.1849683	2.2442264	-0.3888507	H	10.0709527	-1.2240022	-2.8524367
C	-2.7550975	1.5202347	-4.1337042	H	8.5013918	0.4331307	-3.8405189
C	-0.7778755	2.4247606	0.9074625	H	3.2265984	2.0450645	-0.7314478
C	-1.9269457	3.1785003	1.0255945	H	2.8851215	3.4643083	-2.7133528
C	-2.5109408	3.8028633	-0.1420714	H	4.5341340	3.4762675	-4.5660091
C	-3.0376940	2.7158461	1.8864827	H	6.5485025	2.0227788	-4.4604360
C	-6.5975915	0.5917096	0.1074854	H	5.0157675	-4.6189917	4.4972879
C	-2.0352972	2.4895233	-3.4316279	H	5.1031290	-3.0895799	6.4572792
C	-5.2730024	0.9684338	2.0087385	H	5.1417364	-0.6339612	6.1266381

H 5.0624469 0.3370547 3.8594725
 H -1.3762100 1.8809647 4.6208623
 H -1.3931048 0.1300747 4.8987765
 H 0.3194970 2.7297563 3.1993175

H 0.7359726 -0.8277077 5.2108012
 H 2.1306560 -0.2734545 4.2838536
 H 0.7942616 -1.1055412 3.4582420
 H 5.7993831 2.4667685 1.3794843

Optimized structure of **4** on the ground state.

C -6.7231461 3.5277262 0.5936222
 C -7.0913625 2.4134756 -0.2089172
 C -7.7688409 2.6276131 -1.4152330
 C -8.1103738 3.9299344 -1.7848035
 C -7.7711465 5.0193496 -0.9736935
 C -7.0659998 4.8230722 0.2184053
 C -6.5397532 1.1905196 0.3924156
 C -6.6183004 -0.1207611 -0.1347507
 C -5.4658261 -1.0431236 0.0905569
 C -5.6655217 -2.3516706 0.5619265
 C -4.5908678 -3.2118338 0.7669497
 C -3.2733726 -2.7997852 0.5049386
 C -2.1894192 -5.0687010 0.3637455
 C -2.1220671 -3.7121893 0.7181913
 C -0.9292153 -3.2234893 1.2730709
 C 0.1897007 -4.0436736 1.4637148
 C 0.0938204 -5.3916076 1.0908824
 C -1.0871985 -5.8997052 0.5501964
 C -3.0745800 -1.4917899 0.0292936
 C -4.1480549 -0.6298190 -0.1693280
 C -7.7294945 -0.6085100 -0.8655992
 C -9.1430527 -0.2718757 -0.6432174
 C -9.7625087 0.5450555 0.3103968
 C -11.1563967 0.6179973 0.3452754
 C -11.9377707 -0.1265925 -0.5465040
 C -11.3333394 -0.9724306 -1.4821502
 C -9.9446273 -1.0476901 -1.5248762
 C -9.0535431 -1.8686402 -2.3468168
 C -7.7152944 -1.6227298 -1.9298838
 C -6.6596424 -2.2464127 -2.6097147
 C -6.9450507 -3.1265541 -3.6552802
 C -8.2665345 -3.3837409 -4.0392146
 C -9.3291904 -2.7464804 -3.3903018
 C -5.8196355 1.6207680 1.6001047
 C -5.9571866 3.0303473 1.7382177
 C -5.4302247 3.6969744 2.8398155
 C -4.7665103 2.9599719 3.8259811
 C -4.6478759 1.5697852 3.7115578
 C -5.1737353 0.8930199 2.6092717
 H -8.0287505 1.7967368 -2.0614096

H -8.6440827 4.0976175 -2.7163315
 H -8.0455246 6.0257700 -1.2783961
 H -6.7809307 5.6735553 0.8327441
 H -6.6743246 -2.6882379 0.7819336
 H -4.7718663 -4.2087491 1.1596818
 H -0.8909562 -2.1829783 1.5716669
 H 0.9493257 -6.0479942 1.2292070
 H -1.1430814 -6.9459969 0.2624064
 H -2.0706394 -1.1577845 -0.2176759
 H -3.9699267 0.3725089 -0.5476219
 H -9.1736590 1.1172320 1.0185951
 H -11.6388074 1.2595369 1.0775982
 H -13.0213950 -0.0567669 -0.5033131
 H -11.9432373 -1.5694263 -2.1556505
 H -5.6287465 -2.0536075 -2.3356784
 H -6.1278203 -3.6161424 -4.1781610
 H -8.4678145 -4.0731541 -4.8547921
 H -10.3530755 -2.9295557 -3.7066165
 H -5.5402300 4.7737669 2.9418460
 H -4.3496060 3.4690778 4.6908480
 H -4.1422419 1.0068109 4.4914984
 H -5.0780071 -0.1848707 2.5443895
 C 2.1688867 1.9243682 2.4600847
 C 1.4377840 2.3816508 1.2923040
 C 1.9625812 3.3910306 0.4850537
 C 3.9577205 3.5400015 1.9312783
 C 3.4018208 2.5019031 2.7793148
 C 0.7806813 1.2347948 0.6918449
 C 1.8616670 3.2879562 -0.9619713
 C 5.3942089 3.3321625 1.8514590
 C 4.4828963 1.6521526 3.2177843
 C 1.9683681 0.4982802 2.5935410
 C 6.0682014 3.5685558 0.6518507
 C 5.3336365 4.0253068 -0.5153542
 C 0.6684645 1.1468608 -0.6994662
 C 3.0928774 3.7998453 -1.5310720
 C 1.2263492 2.1881327 -1.5421503
 C 5.7203727 2.1620552 2.6482274
 C 4.2749213 0.2711180 3.3160987
 C 2.9918266 -0.3155655 3.0271401

C	1.0981202	0.0638347	1.4799794	C	7.6369003	0.2392476	0.3240593
C	5.3026798	-0.6485624	2.8641541	C	7.2151522	1.2986393	-1.8624860
C	3.1602252	-1.7844329	2.6235254	C	6.1457914	-0.5562957	-2.8336294
C	1.2984420	-1.1588836	0.8727097	C	7.5396900	0.1317168	-1.0649175
C	6.7069579	1.2772759	2.2161574	C	6.8719627	-1.0154387	-1.6602225
C	1.8041157	1.5532280	-2.7152541	C	2.9902483	2.0452218	-3.2629325
C	4.6530187	-1.7987253	2.2972160	C	3.6481827	3.1897000	-2.6577275
C	2.2083707	-2.2625478	1.4211104	C	5.0828790	2.9758059	-2.7348501
C	1.2297965	-1.2372321	-0.5639288	C	0.9002835	-0.1233560	-1.3436795
C	2.2523999	-2.1599379	-1.0155017	C	1.6003561	0.1206528	-2.5942739
C	4.0195206	1.1216709	-3.7145419	C	3.2532221	3.9779350	0.8082753
C	2.9551132	-2.6434004	0.1415558	C	3.9537866	4.2264965	-0.4370105
C	4.3196509	-2.8355748	0.0701801	C	5.9084045	3.3844344	-1.6863252
C	5.0281681	-2.5803055	-1.1659114	C	7.0968091	2.6447103	0.2016423
C	5.1950996	-2.4011177	1.1817764	C	6.9968157	2.5307824	-1.2421287
C	7.4111810	1.5223227	0.9702372	C	1.4884441	-3.5543029	2.0763615
C	3.8199298	-0.2560445	-3.5996197	N	1.4815655	-3.3465522	3.5249256
C	6.4999368	-0.1567137	2.3331995	C	2.7968634	-2.8015410	3.7907622
C	7.0735122	-0.7940105	1.1736330	H	3.5345214	-3.6135874	3.7684912
C	2.5858155	-0.7646997	-3.0271342	H	2.8446600	-2.3263062	4.7732933
C	5.3119203	1.6972507	-3.3858733	H	2.2271731	-4.3490866	1.9111172
C	6.3539546	0.8729584	-2.9564334	C	0.3708226	-2.6046338	4.1227997
C	2.9149717	-1.9333948	-2.2269498	H	0.5312856	-2.5699480	5.2047923
C	4.3389189	-2.1478052	-2.3038422	H	-0.5624664	-3.1419036	3.9409448
C	6.4191108	-1.8910180	0.6024949	H	0.2502457	-1.5707666	3.7629571
C	6.3195946	-2.0008733	-0.8416509	H	-3.0972808	-5.4621285	-0.0850435
C	4.9055215	-1.1136357	-3.1500052				

**Chapter 5 – Quantum Gate Operation on a Spectral Addressable Photogenerated
Molecular Electron Spin-Qubit Pair**

5.1 Introduction

New computation, communication and sensing technologies provided by quantum information science (QIS) are drawing considerable attention.¹⁻³ Identification and characterization of new molecular systems to serve as qubits in these applications have motivated chemists to contribute in this field^{4,5} by taking advantage of synthetic tunability^{6,7} and ease of spin state readout using microwave pulses⁸⁻¹⁰ of electron spins in molecular systems. These molecular systems employ multiple electron spin qubits comprising interacting organic radicals^{8,9,18-21} and/or metal complexes^{11,16,22-25} and have achieved advances in extending coherence lifetimes¹¹⁻¹³ and scaling up the number of qubits.¹⁴⁻¹⁷ However, thermally polarized electron spins²⁶ with well-defined initial spin states only available at high magnetic fields and temperatures < 3 K.¹⁸

Spin-selective photochemical processes^{150,151} in molecular qubit systems have shown significant promise for creating well-defined initial qubit states. For instance, sub-nanosecond photo-induced electron transfer in donor-acceptor molecules generates an entangled spin (qubit) pair in a pure initial quantum state.^{32,152-154} Sub-nanosecond photo-driven electron transfer from a molecular donor to an acceptor has been shown to generate a radical pair (RP) having two entangled electron spins that can serve as a spin qubit pair (SQP) in a well-defined pure initial singlet quantum state^{31,32} even at room temperature.³³ Together with pulse electron paramagnetic resonance (pulse-EPR) techniques, we have shown that photo-generated RPs can mediate quantum state teleportation,¹⁹ implement a CNOT gate,²⁰ and transfer polarization to a third spin.⁴⁵⁻⁴⁸ Moreover, qubit-specific addressability can be achieved in an SQP system using electronic g -factor engineering.^{18,21,23} In addition, resonant excitation of pseudo-tetragonal chromium (Cr^{4+}) complexes to their singlet excited states has also been shown to selectively relax back to the $m_s = \pm 1$ triplet ground state sublevels to create spin polarization.^{35,155}

However, previous molecular donor-acceptor molecules that produce spectrally addressable RP used radical cations or anions with significant g anisotropy and large hyperfine coupling (HFC) of nuclear spins such as protons and nitrogen atoms, which results in significant spectral overlap from molecules with non-ideal orientations. Spectral broadening caused by HFC also poses limitation on the selection of donors and acceptors, such that radicals with significant g factor deviation from the free electron are used, which results in difficulty in constructing microwave pulses with large bandwidths.

Here, we addressed these issues by designing and synthesizing a donor-acceptor(1)-acceptor(2) (D-A₁-A₂) molecule with significant reduced HFC by using fully deuterated *peri*-xanthenoxanthene (PXX) as D, naphthalenemonoimide (NMI) as A₁, and a nuclear-spin-free C₆₀ fullerene as A₂. Selective photoexcitation of PXX results in sub-nanosecond, two-step electron transfer to form a long-lived PXX^{•+}-NMI-C₆₀^{•-} radical ion pair (RP), which is an initially entangled spin qubit pair (SQP). Alignment of the SQP in the nematic liquid crystal 4-cyano-4'-(n-pentyl)biphenyl (5CB) effectively eliminates spectral complexities due to the anisotropic g tensors of both PXX^{•+} and C₆₀^{•-}, which results in well-resolved resonances for each electron spin and thus providing a platform for quantum gate operations. We demonstrate both single-qubit gate and two-qubit CNOT gate operations using both selective and non-selective Gaussian-shaped microwave pulses and broadband spectral detection of the results of gate operations.

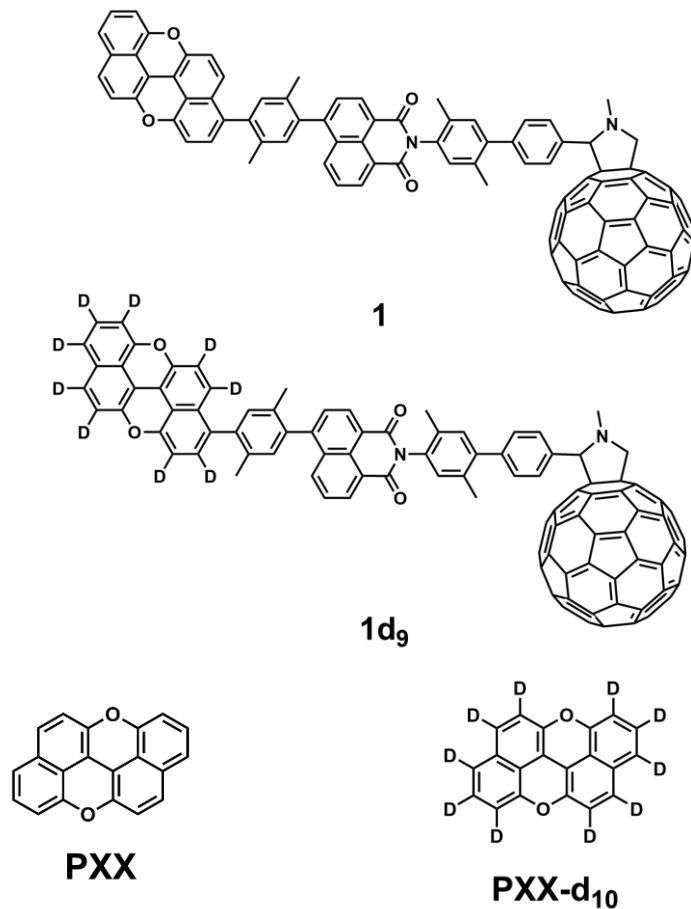


Figure 5.1. Structures of the compounds used in this study.

5.2 Experimental Methods

5.2.1 Synthesis

Detailed synthetic procedures and characterization of **1** and **1-d₉** are given in the Supporting Information (SI). PXX cation radical (PXX^{•+}) and PXX-*d*₁₀ cation radical (PXX^{•+}-*d*₁₀) were generated through chemical oxidation by adding sub-stoichiometric amount (0.8 equivalent) of nitrosonium tetrafluoroborate to a 100 μM dichloromethane solution of PXX or PXX-*d*₁₀. The sample of radical solutions were used immediately for EPR measurements.

5.2.2 Steady-state optical spectroscopy

UV-visible absorption spectra were obtained using a Shimadzu UV-1800 spectrometer in a quartz cuvette with a 1 mm path length.

5.2.3 Steady-state continuous-wave EPR spectroscopy (CW-EPR)

CW-EPR measurements were performed on ~20 μL , 100 μM of samples in dichloromethane solution that were loaded into quartz tubes (2.40 mm o.d., 2.00 mm i.d.), subjected to three freeze-pump-thaw cycles on a vacuum line (10^{-4} Torr), and sealed with a hydrogen torch. Measurements at X-band (9.5 GHz) were performed with a Bruker Elexsys E580, equipped with a 4122SHQE resonator. Scans were performed with magnetic field modulation amplitude of 0.1 G, modulation frequency of 60 kHz and non-saturating microwave power of 1.5 mW.

5.2.4 Time-resolved EPR (TREPR) spectroscopy

Measurements were made at X-band (~9.6 GHz) on a Bruker Elexsys E680 X/W EPR spectrometer with a split ring resonator (ER4118X-MS3). The temperature was set by an Oxford Instruments CF935 continuous flow optical cryostat with liquid nitrogen. Direct detection using CW microwaves was performed following photoexcitation. Kinetic traces of transient magnetization under CW microwave irradiation were detected in quadrature. Time traces were recorded over a range of magnetic fields to give a 2D spectra. Spectra were processed by first subtracting the signal prior to the laser pulse for each kinetic trace (at a given magnetic field point), and then subtracting the signal average at off-resonant magnetic field points from the spectra obtained at a given time.

5.2.5 Pulse-EPR spectroscopy

Shaped microwave pulses were generated using a commercial Bruker SpinJet II arbitrary waveform generator (AWG) module. A Gaussian-shaped pulse was used for both selective and nonselective turning angle operations due to a more uniform excitation across the field-swept echo-detected spectrum than traditional square-shaped pulses. The excitation profile of a Gaussian 20 ns and 80 ns length pulse was observed to provide sufficient bandwidth for the nonselective and selective excitations, respectively, of the SQP necessary to perform the CNOT gate pulse sequence (See SI). The turning angle of these pulses was controlled by their amplitude as output by the AWG. These amplitudes were kept within a linear response regime of the traveling wave tube (TWT) amplifier. The resonator response profile and the TWT response profile and amplitude for the pulse turning angles given specific pulse lengths were calibrated with the EPR signal from the triplet state of C_{60} ($^3C_{60}$) as an internal standard generated by photoexcitation of the sample.

5.3 Results and Discussion

5.3.1 Steady-state absorption spectroscopy

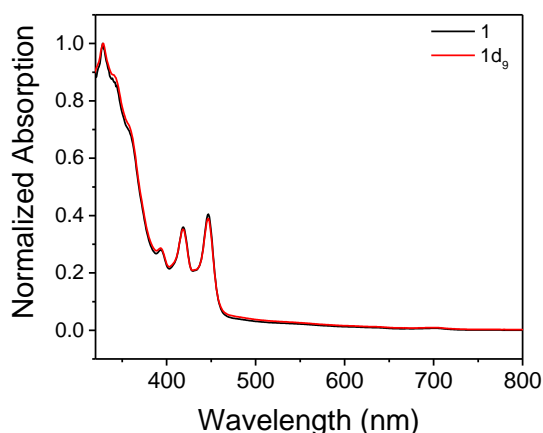


Figure 5.2. UV-vis spectra of 1 and 1-d9 1d9 in toluene solution at 295 K

Steady-state absorption spectra of **1** and **1-d₉** in toluene are shown in **Figure 5.2**. Since deuteration does not change the electronic structure of PXX, **1** and **1-d₉** have identical absorption spectra with characteristic vibrational progression at 400 nm, 420 nm and 450 nm that belong to PXX^{58, 156}. The strong absorption below 360 nm and broad absorption that almost covers the entire visible region with stronger absorption at longer wavelengths is characteristic of C₆₀.^{138, 139}

5.3.2 Transient absorption spectroscopy.

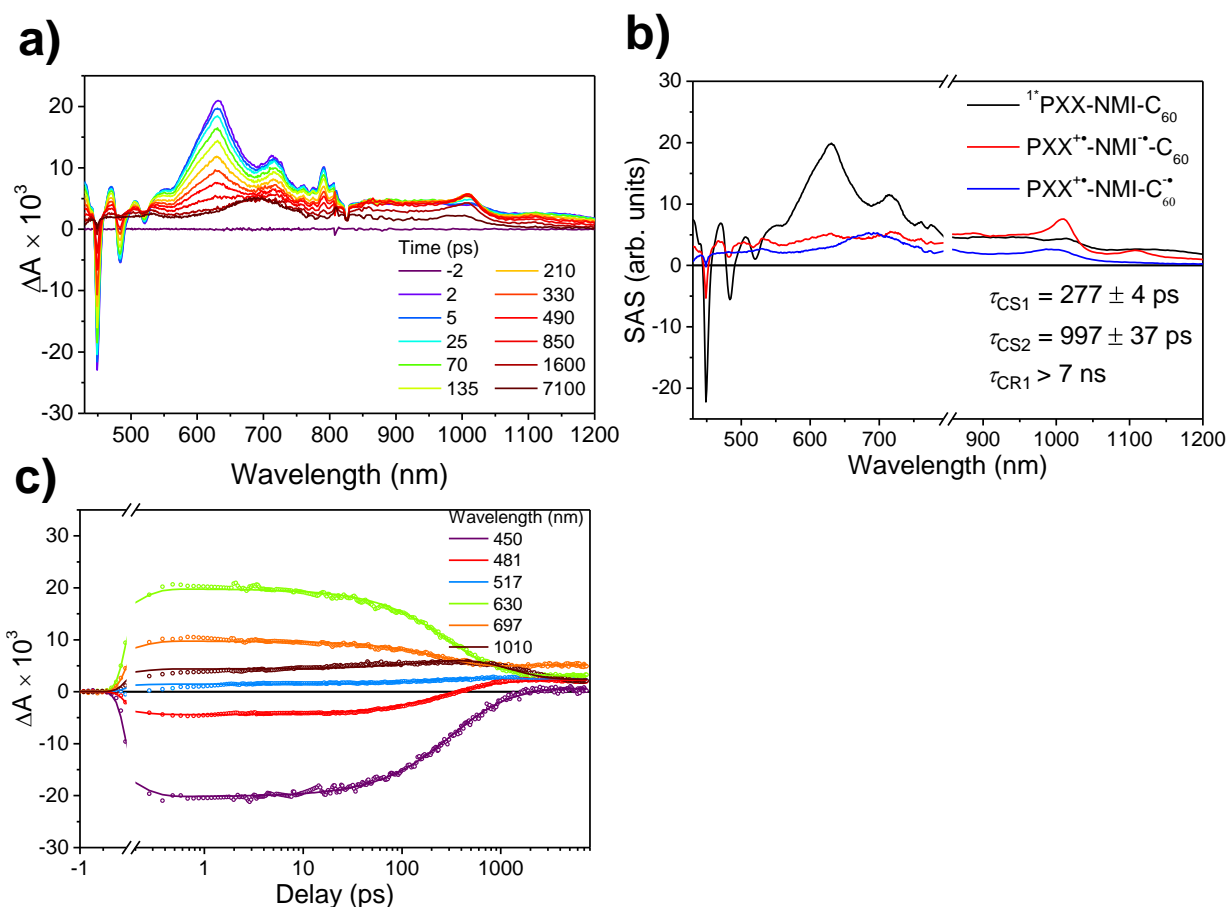


Figure 5.3. Transient absorption spectra of **1**. a) fsTA data of **1** at 85 K in mTHF solution following $\lambda_{\text{ex}} = 450$ nm excitation. b) Species-associated spectra (SAS) of **1**. c) Comparison of the kinetic traces to the fit at selected probe wavelengths.

Femtosecond and nanosecond transient absorption spectroscopies (fsTA and nsTA) are used to monitor the photo-induced electron transfer dynamics of **1** in 2-methyltetrahydrofuran (mTHF) at 85K (**Figure 5.3**). The singlet excited state of PXX (^1PXX) formed immediately after the laser excitation as shown by its characteristic absorption at 650 nm, the ground-bleach at 450 nm and stimulated emission at 480 and 520 nm. The subsequent charge transfer reaction $^1\text{PXX-NMI-C}_{60} \rightarrow \text{PXX}^{*+}\text{-NMI}^{\bullet-}\text{-C}_{60}$ results in the appearance of absorption at 530 nm and 1000 nm^{58, 156}. The absorption peak eventually broadened due to coexistence of $\text{C}_{60}^{\bullet-}$ and PXX^{*+} , which is evidence that the second charge transfer reaction $\text{PXX}^{*+}\text{-NMI}^{\bullet-}\text{-C}_{60} \rightarrow \text{PXX}^{*+}\text{-NMI-C}_{60}^{\bullet-}$ occurs. Inevitable co-excitation of C_{60} also produces C_{60} triplet excited state ($^3\text{C}_{60}$) which has an absorption at 680 nm that appears on a longer time scale¹³⁸ (**Figure 3a**). Global fitting of the fsTA data using an $A \rightarrow B \rightarrow C$ model yields the time constant for the first and second charge transfer reactions $\tau_{\text{CS1}} = 277 \pm 4$ ps, and $\tau_{\text{CS2}} = 997 \pm 31$ ps respectively. The RP $\text{PXX}^{*+}\text{-NMI-C}_{60}^{\bullet-}$ eventually decays to the $^3\text{C}_{60}$ with time constant of 2.0 ± 0.2 μs (Figure S1).

5.3.3 Steady-state EPR spectroscopy

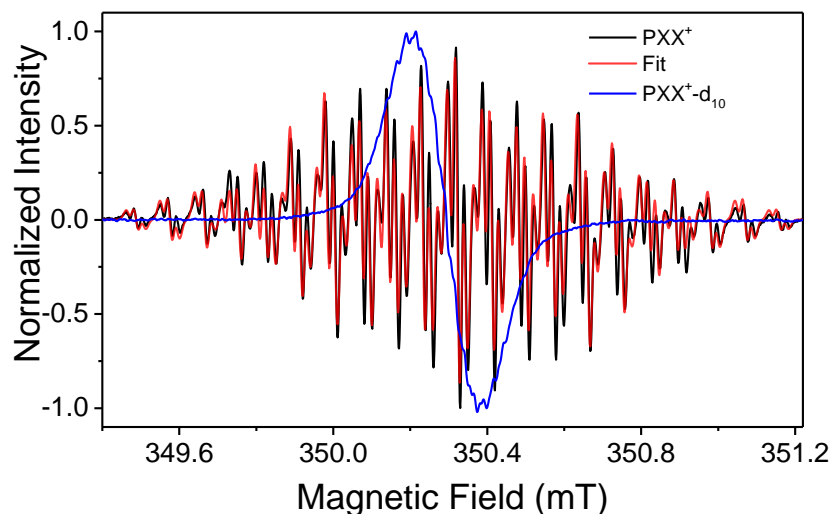


Figure 5.4. CW-EPR spectra of PXX radical cation and PXX-d10 radical cation in dichloromethane solution at 295 K. The spectral fitting of PXX radical cation is shown in red.

Chemically generated $\text{PXX}^{+\bullet}$ and $\text{PXX}^{+\bullet}\text{-d}_{10}$ in dichloromethane solution were characterized by CW-EPR spectroscopy (**Figure 5.4**). The unpaired electron in $\text{PXX}^{+\bullet}$ is coupled to ten protons, yielding an experimental EPR spectrum with 64 lines. The isotropic hyperfine coupling constants (HFCs) of the five inequivalent protons were obtained from fitting the experimental spectrum and are summarized in Table S1. The EPR spectrum of $\text{PXX}^{+\bullet}\text{-d}_{10}$ exhibits significant spectral narrowing resulting from the ~ 6.5 -fold reduction in gyromagnetic ratio of deuterons relative to protons. The structure that appears atop of the derivative spectrum of $\text{PXX}^{+\bullet}\text{-d}_{10}$ result from unresolved deuteron HFCs.

5.3.4 TREPR spectroscopy

To evaluate the feasibility of $\text{PXX}^{+\bullet}\text{-d}_9\text{-NMI-C}_{60}^{\bullet-}$ as a potential SQP system for quantum gate operations, TREPR measurements were performed on both **1** and **1-d₉** in mTHF and 5CB at

85 K. The spectra were recorded in direct detection, where positive signals are enhanced absorptive (*a*) transitions and negative signals are emissive (*e*) ones. **Figure 5.5** shows the corresponding TREPR spectra at 200 ns after a 7 ns, 450 nm laser pulse. The large difference in *g* tensors between PXX^+ and $\text{C}_{60}^{\bullet-}$ allows for spectral separation of the two radicals at the 0.35 T magnetic field characteristic of X-band EPR spectroscopy. However, significant line broadening at lower field was observed for **1** due to the unresolved HFCs from the protons of PXX. The higher field portion of the spectrum with transitions primarily from $\text{C}_{60}^{\bullet-}$ has a narrow *aea* polarization pattern that owing to the nuclear-spin-free nature of $\text{C}_{60}^{\bullet-}$ and its axial *g* tensor, which is likely due to the pyrrolidino-functionalization of C_{60} that distorts its symmetry.

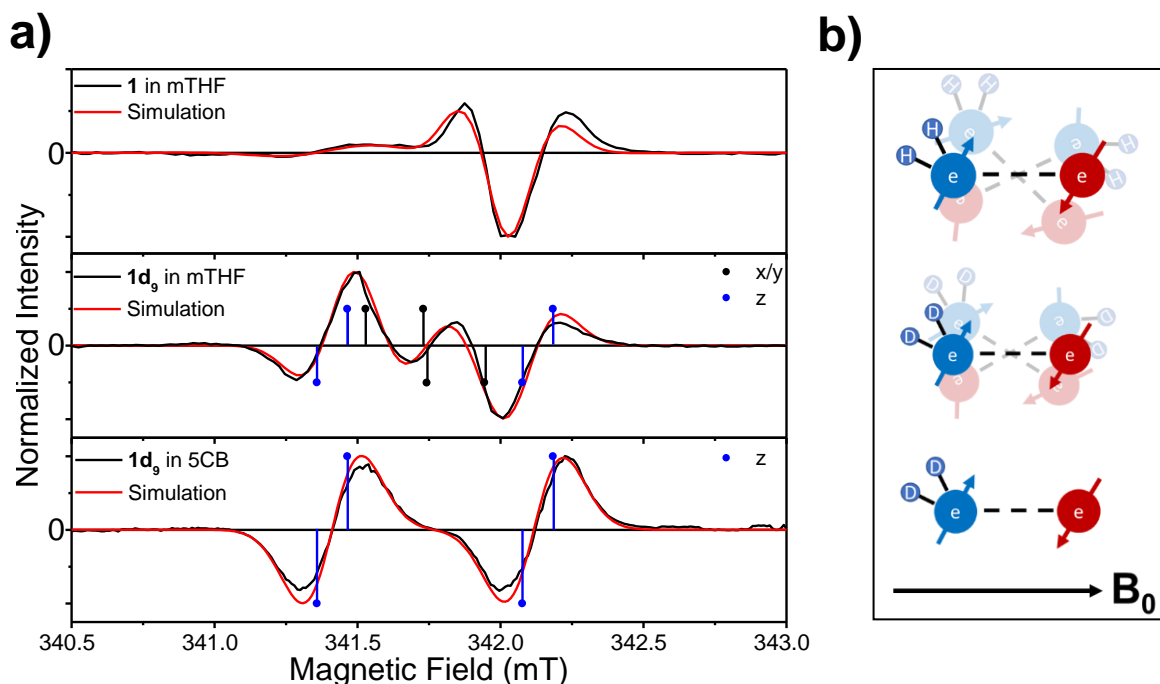


Figure 5.5. (a) TREPR spectra and spectral simulation of **1** in mTHF solution (top), 1-d₉1d₉ in mTHF solution (middle) and 1-d₉1d₉ in 5CB aligned along the magnetic field at 85 K, 200 ns after a 7 ns, 450 nm laser pulse. The vertical lines connected to the dots show the transitions of RPs whose principal axes, *x*, *y* or *z*, are parallel to the magnetic field, where *z* is defined as the direction that connects the two spins, and *x* and *y* are perpendicular to *z* (b) Schematics of RPs randomly orient in the solution with one of the electron spins in the RP coupled to multiple protons (top), randomly oriented RPs with one of the electron spins in the RP coupled to multiple deuterons (middle), and deuterated RPs *z*-axis is aligned along the magnetic field direction (bottom).

Compared to **1**, the lower field features in the TREPR spectrum of **1-d₉** in mTHF is narrowed in the absence of proton HFC. The entire TREPR spectrum of **1-d₉** is almost centrosymmetric and shows an *eaeaea* polarization pattern, which deviates from the ideal *eaea* pattern predicted for the four spin transitions of spin-correlated RPs. This deviation is attributed to the axial *g* tensors of both PXX⁺⁺ and C₆₀^{•-}. The Zeeman splitting of an electron spin in an anisotropic molecule is a function of the molecular orientation with respect the external magnetic field, likewise, the TREPR spectrum of an ensemble of RPs, such as those in **1-d₉**, are randomly oriented in the frozen matrix resulting in a powder pattern composed of transitions in RPs that are in all different orientations (**Figure 5.5 a**).

To eliminate the spectral complexity from random molecular orientations, **1-d₉** is dissolved in 5CB and the sample is aligned by the magnetic field, then frozen. The aligned sample shows a well-resolved *eaea* polarization pattern spanning roughly 35 MHz that permits qubit addressability and non-selective excitation, necessary for quantum gate operations. The two TREPR spectra of **1-d₉** can be globally simulated using the same spin model with a dipolar coupling constant $D = -3$ MHz and two axial *g* tensors: [2.0045 2.0045 2.0031] and [2.0003 2.0003 2.0021] for PXX⁺⁺ and C₆₀^{•-} respectively. The spectral simulation of **1** in frozen mTHF used a 20 MHz PXX⁺⁺ linewidth to account for unresolved proton HFCs (see Section 5.5).

5.3.5 EPR spectral readout with nonselective pulses

The strategies of *g* factor engineering, deuteration and alignment of **1-d₉** produced well-resolved RP EPR spectra, allowing for uniform excitation of the entire EPR spectrum using a 20 ns Gaussian-shaped microwave pulse. Instead of using traditional field-sweep detection for the EPR spectrum, the TREPR spectrum in the frequency domain of **1-d₉** in 5CB can be attained by measuring the entire spin echo time trace in the direct dimension¹⁵⁷ at the center field of the

spectrum and performing a Fourier transform to obtain the spin echo. To ensure the same bandwidths between the two pulses, the turning angles of the $\pi/2$ and π pulse were determined by adjusting the pulse amplitude instead of the pulse lengths (**Figure 5.6a**). The spin echo of the RP signal, shown in **Figure 5.6b**, has strong oscillations, which carries all the spectral information in the time domain, similar to a free induction decay (FID). The TREPR spectrum of **1-d9** in 5CB is well-reproduced in the frequency domain (**Figure 5.6c**), which demonstrate this technique as a feasible detection scheme for quantum gate operations.

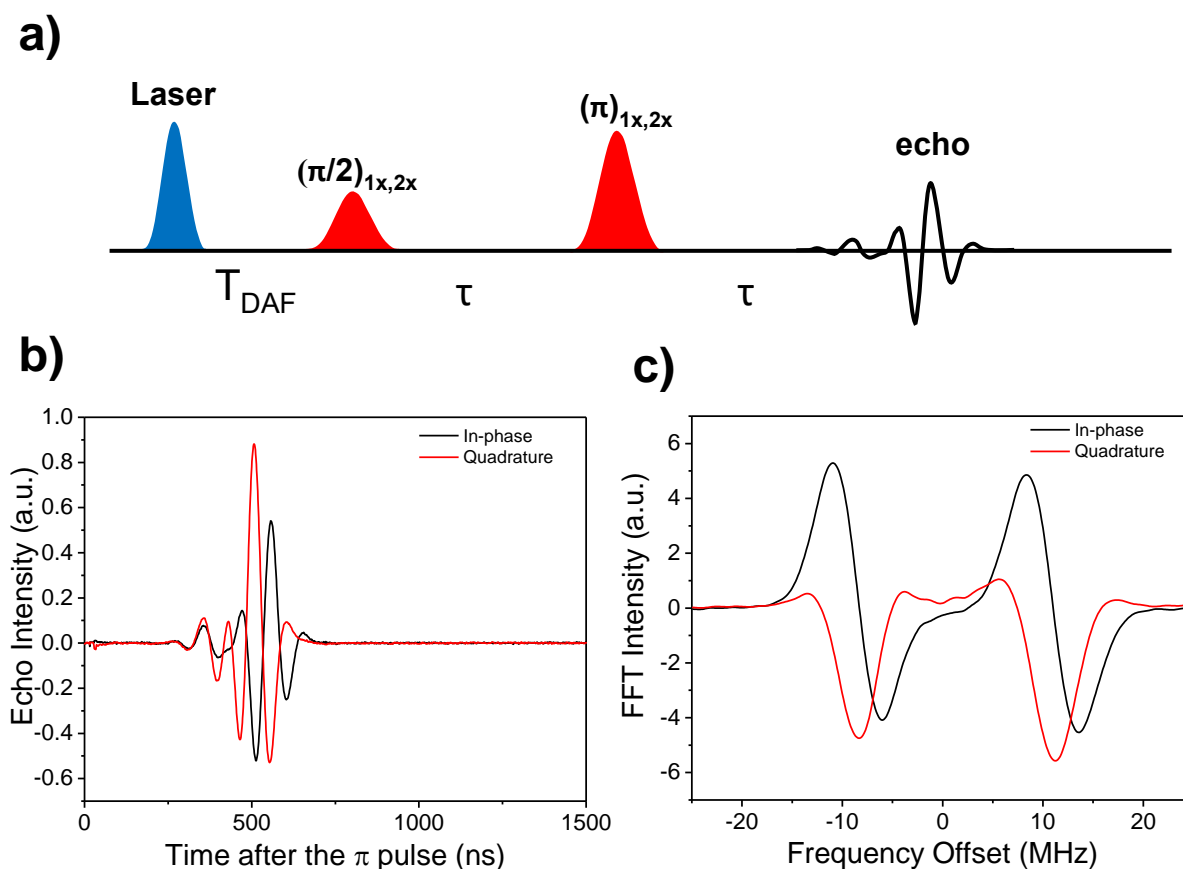


Figure 5.6. Pulse sequence used to measure the EPR spectrum of the SQP produced by photoexcitation of **1-d9**. (b) Spin echo of the RP showing FID-like behavior due to the broadband microwave excitation. Both in-phase and quadrature part of the signal was collected. (c) Frequency domain of the spin echo producing the entire RP spectrum.

5.3.6 Single-qubit operation

Single-qubit operations are performed using an 80 ns Gaussian-shaped, frequency selective pulse. The amplitude of this pulse is incremented to perform a nutation that is targeted on either $C_{60}^{\cdot-}$ or $PXX^{\cdot+}$, depending on the frequency offset of the pulse (See Section 5.5 **Figure 5.13**). The effect of the single-qubit nutation pulse can be monitored using the detection scheme mentioned in the previous section. **Figure 5.7a** shows the pulse sequence used in this experiment, where the nutation pulse has a frequency offset of -9 MHz that selectively operates on $C_{60}^{\cdot-}$. The frequency spectrum of the RP produced after photoexciting **1-d9** is plotted against the turning angle of the nutation pulse (**Figure 5.7b**).

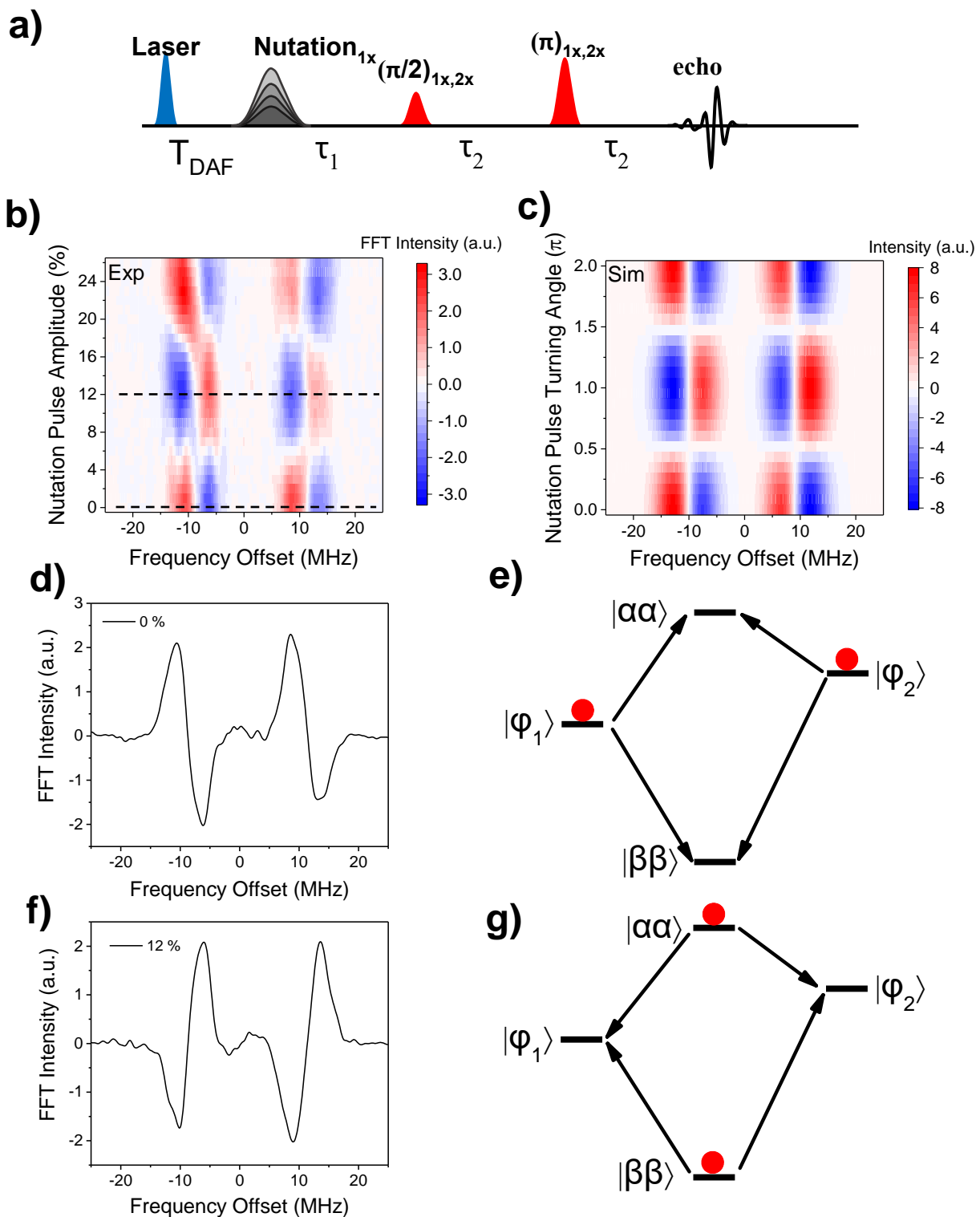


Figure 5.7. (a) Pulse sequence of single-qubit nutation. (b) Frequency spectra after a single-qubit nutation pulse on C60^{•-}. (c) Frequency space simulation on the effect of single-qubit pulse with varying turning angles. (d) and (f) Experimental spectra slices at the dashed line in (b). (e) and (f) Spin level diagrams and level populations of the RP with and without a π pulse respectively.

The nutation behavior occurs not only in $C_{60}^{\bullet-}$ but also in PXX^{*+} (**Figure 5.7b**), which can be simulated accurately in frequency domain (**Figure 5.7c**). This nutation effect can be attributed to the spin correlation between $C_{60}^{\bullet-}$ and PXX^{*+} electron spins¹⁵⁸. The PXX^{*+} - d_9 -NMI- $C_{60}^{\bullet-}$ RP generated after photoexciting **1-d9** has an initial singlet state, which results in the spin population in the $|\varphi_1\rangle$ and $|\varphi_2\rangle$ eigen states of the RP in the high field limit¹⁵⁹ (**Figure 5.7e**). The absorptive and emissive transitions of $C_{60}^{\bullet-}$ can be assigned to $|\varphi_1\rangle$ to $|\alpha\alpha\rangle$ and $|\varphi_2\rangle$ to $|\beta\beta\rangle$ respectively. The nutation pulse π pulse that applies to transitions of $C_{60}^{\bullet-}$ effectively flip spin populations from $|\varphi_1\rangle$ state to $|\alpha\alpha\rangle$ state, and $|\varphi_2\rangle$ state to $|\beta\beta\rangle$ state simultaneously (**Figure 5.7g**), causing the entire spectrum to flip accordingly (**Figure 5.7f**). Same behavior was observed when the nutation pulse is applied to PXX^{*+} (See Section 5.5, **Figure 5.16**).

5.3.7 The three-pulse CNOT gate

Due to the limited 2 μ s RP lifetime in **1-d9** at 85 K, the original pulse sequence proposed by Salikhov¹⁶⁰ for CNOT gate cannot be implemented in our system. However, the initial singlet RP state allows for reduction of the number of the pulses necessary to implement the CNOT gate (see SI). Here, a three-pulse CNOT gate is used and the spectrum after the gate is read out detected using a broadband Hahn echo pulse sequence as described previously. (**Figure 8a**). The pulse sequence is composed of three Gaussian-shaped microwave pulses, two of which are 80 ns selective $\pi/2$ pulses at the frequencies of the control and target qubits, and one 20 ns non-selective π pulse that excites all four transitions of the SQP. The two evolution times $L = \pi/(2j)$ can be determined experimentally using out-of-phase ESEEM measurements (see SI), where j is the effective total spin-spin interaction and is confirmed by incrementing L in this pulse sequence. **Figures 5.8b** and **5.8c** show the spectral changes that occur when L is incremented with $C_{60}^{\bullet-}$ or PXX^{*+} acting as the control qubit, respectively. The SQP spectra after the pulse sequence oscillate

at the same period as the out-of-phase ESEEM (See Section 5.5, **Figure 5.15**), suggesting that state mixing mediated by j is important for CNOT gate implementation. Furthermore, when $L = 55$ ns, the CNOT gate occurs; however, the frequency spectra after the CNOT gate, shown in **Figures 5.8d** and **Figure 5.8e** do not match completely with the simulation, which indicates a reduced fidelity due to imperfection of pulses and decoherence. Limited by the RP lifetime, the quantum state tomography used for fidelity measurement cannot be performed after the CNOT gate. Therefore, longer linker between NMI and C_{60} may be needed to improve the RP lifetime for future quantum state tomography experiments.

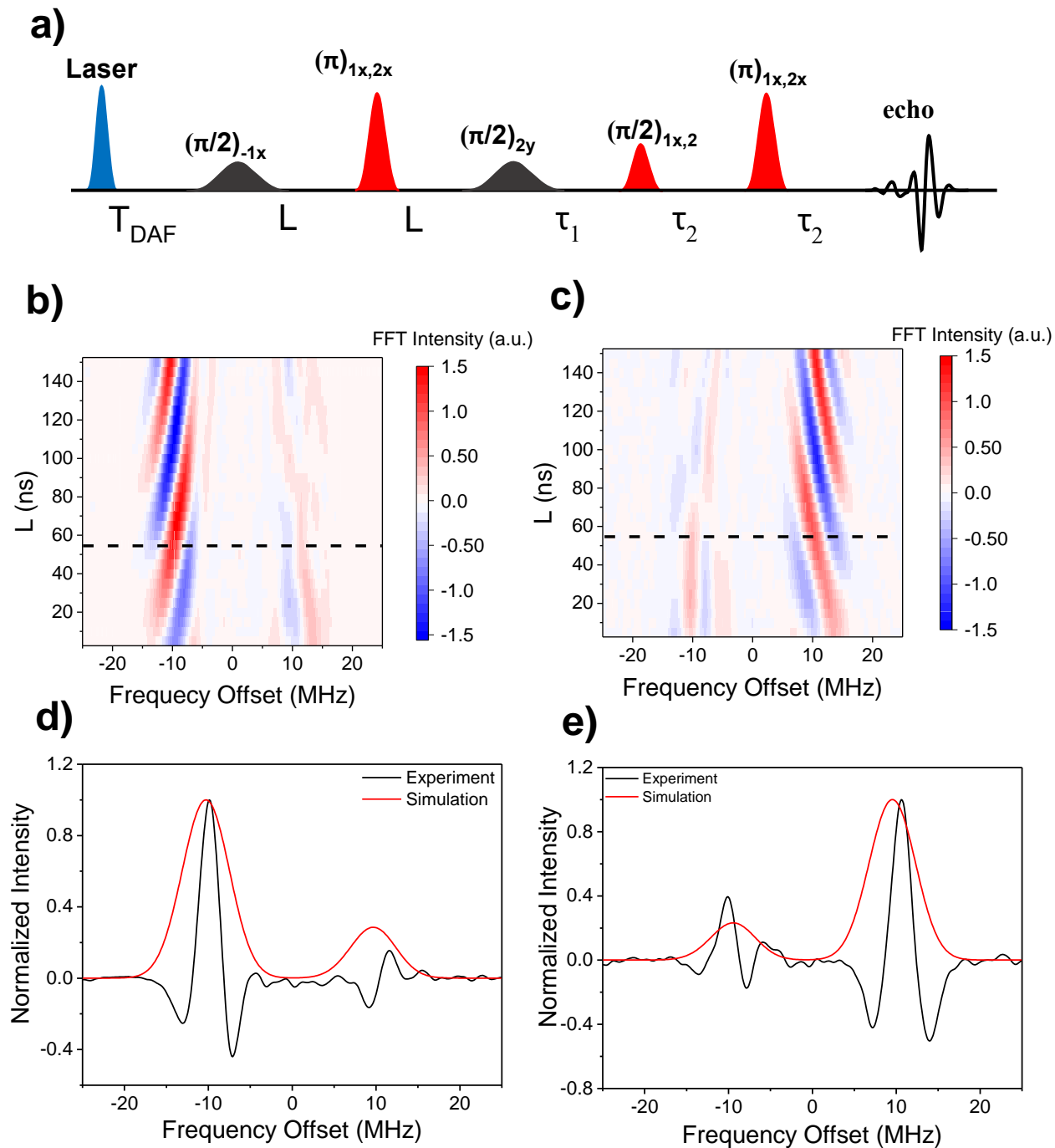


Figure 5.8. (a) Pulse sequence for CNOT gate and detection. Frequency spectra after the three-pulse CNOT gate operation with incremental L is plotted in (b) and (c) using $C60\bullet-$ or $PXX\bullet+-d9$ as the control qubit respectively. The slice marked by the dashed line in (b) and (c) are shown in (d) and (e) respectively and simulation is shown in red.

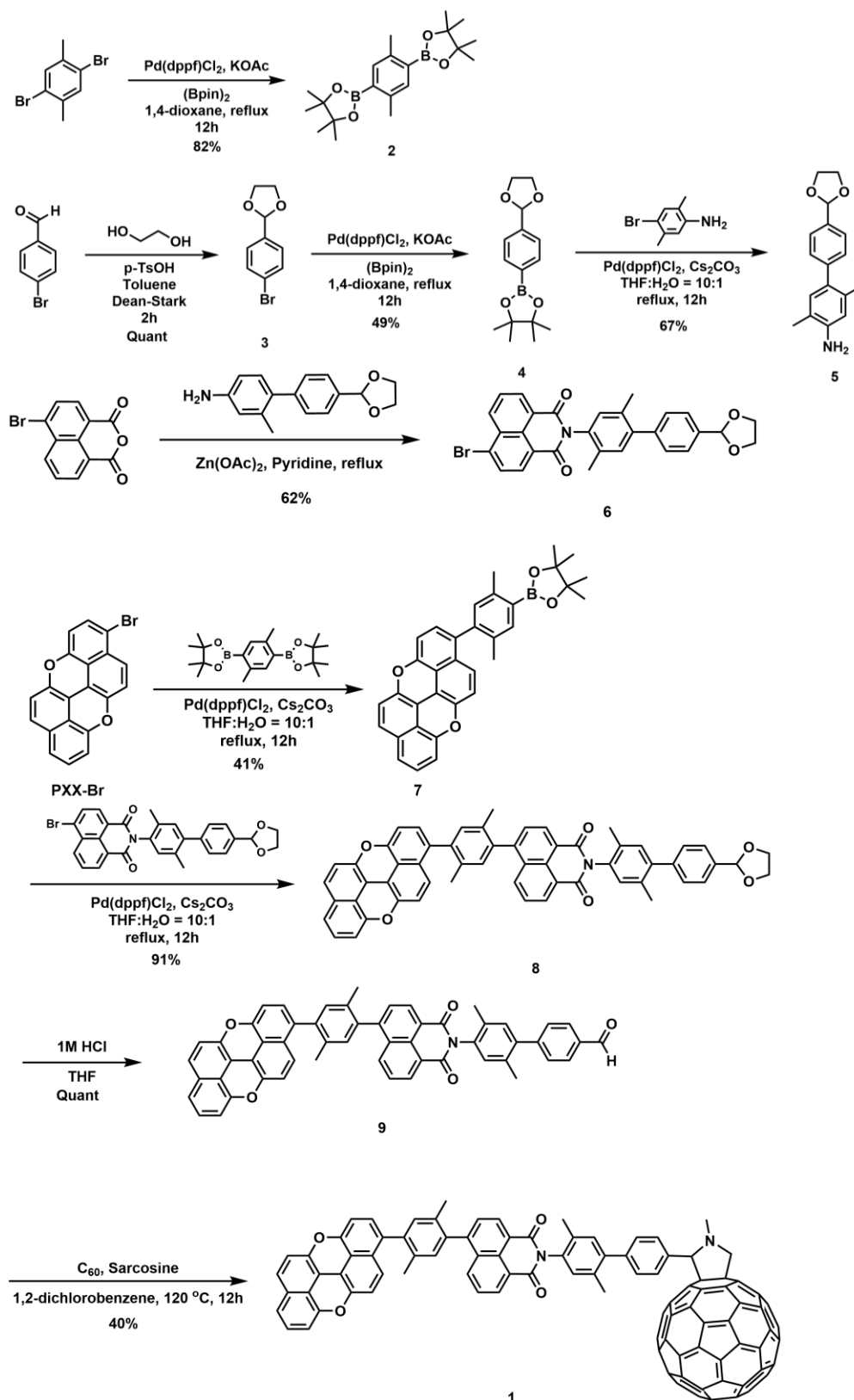
5.4 Conclusions

In this study, we synthesized a donor-acceptor molecule that can be photoexcited to produce a RP with spectrally separated radical cation and anion resonances due to their distinct g tensors. Deuteration of the PXX donor and molecular alignment in 5CB results in an SQP having four spectrally separated narrow transitions, providing a platform for quantum logic gate operations. Single-qubit gate and two-qubit CNOT gate, which form a complete set of gates necessary for quantum computation, are demonstrated using this system.

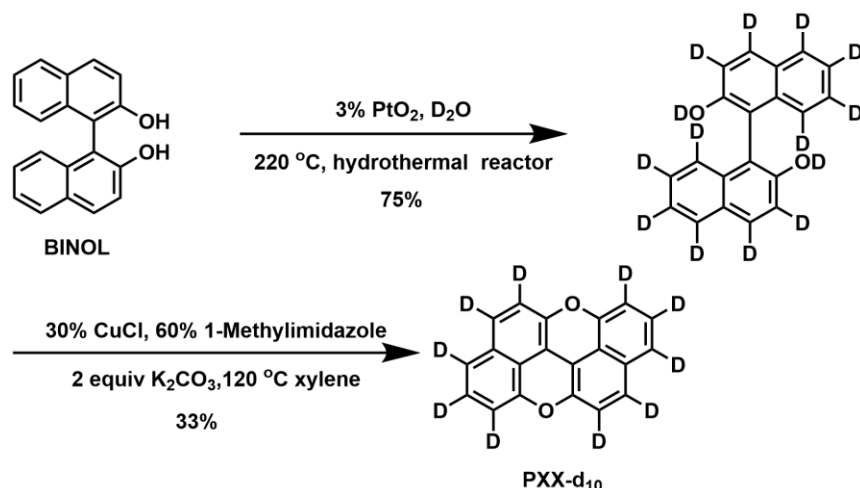
5.5 Supplementary Information

5.5.1. Synthesis and Characterization

All chemicals were purchased from Sigma-Aldrich, Inc. unless noted otherwise. ^1H and ^{13}C NMR spectra were acquired with a Bruker Avance III 500 MHz instrument equipped with a DCH CryoProbe. Mass spectroscopy was performed using a Bruker Rapiflex MALDI-TOF. Purification was performed using silica gel from Sorbent Technologies (Atlanta, GA). The synthesis of Compound 1 or 1d is outlined in Scheme S1 and the synthesis of PXX-d10 is outlined in Scheme S2



Scheme 5.1. Synthesis route of 1.



Scheme 5.2. Synthesis route of PXX-d₁₀.

Compound 2 In a 100-ml round bottom flask equipped with a magnetic stir bar was added 1 g (3.8 mmol) of 1,4-dibromo-2,5-dimethylbenzene, 3.8 g (15 mmol) of Bis(pinacolato)diboron, 136 mg (0.2 mmol) of Pd(dppf)Cl₂ and 2.2 g (23 mmol) of potassium acetate. The solid mixture was pump-purged three times under a nitrogen atmosphere before 20 ml of N₂-degassed 1,4-dioxane was injected into the flask and brought to reflux. 12 hours later, the solvent was removed under vacuum and the crude product was purified using silica gel column chromatography with 50% dichloromethane in hexane as eluents, yielding 1.2 g (82%) of white powder as product. ¹H NMR (500 MHz, CDCl₃) δ 7.56 (s, 2H), 2.50 (s, 6H), 1.36 (s, 24H). ¹³C NMR (126 MHz, CDCl₃) δ 140.58, 136.94, 83.43, 24.91, 21.52.

Compound 3 In a 50-ml round bottom flask equipped with a stir bar and a Dean-Stark trap was placed with 1 g (5.5 mmol) of 4-bromobenzaldehyde 2.4 ml (44 mmol) of anhydrous ethylene glycol, 70 mg (0.28 mmol) of p-toluenesulfonic acid, 0.5 ml of silica gel and 12 ml of toluene. The reaction was brought up to 110 °C for 2 hours till the solvent in the Dean-Stark trap is no longer turbid. The mixture was poured into 20 ml of ethyl acetate and washed with water (10 ml × 3) and brine (5 ml). The organic layer was dried with anhydrous Na₂SO₄ and removed under vacuum to

yield 1.25 g of colorless oil as product. ^1H NMR (500 MHz, CDCl_3) δ 7.52 – 7.46 (m, 2H), 7.37 – 7.30 (m, 2H), 5.75 (s, 1H), 4.13 – 4.05 (m, 2H), 4.05 – 3.97 (m, 2H). ^{13}C NMR (126 MHz, CDCl_3) δ 136.96, 131.55, 128.23, 123.30, 103.07, 65.36.

Compound 4 In a 100-ml round bottom flask equipped with a magnetic stir bar was added 1 g (4.4 mmol) of **3**, 1.2 g (9 mmol) of Bis(pinacolato)diboron, 78 mg (0.38 mmol) of $\text{Pd}(\text{dppf})\text{Cl}_2$ and 1.1 g (13 mmol) of potassium acetate. The solid mixture was pump-purged three times under a nitrogen atmosphere before 20 ml of N_2 -degassed 1,4-dioxane was injected into the flask and brought to reflux. 12 hours later, the solvent was removed under vacuum and the crude product was purified using silica gel column chromatography with dichloromethane as eluents, yielding 501 mg (49%) of white powder as product. ^1H NMR (500 MHz, CDCl_3) δ 7.80 (d, $J = 8.1$ Hz, 2H), 7.45 (d, $J = 8.1$ Hz, 2H), 5.82 (s, 1H), 4.13 – 4.06 (m, 2H), 4.06 – 3.98 (m, 2H), 1.32 (s, 12H). ^{13}C NMR (126 MHz, CDCl_3) δ 140.80, 138.08, 128.76, 125.71, 103.61, 84.37, 83.89, 65.30, 24.91.

Compound 5 500 mg of **4**, 470 mg of 4-bromo-2,5-dimethylaniline, 70 mg of $\text{Pd}(\text{dppf})\text{Cl}_2$ and 2.3 g of cesium carbonate was placed in a 50-ml round bottomed flask that was equipped with a stir bar and condenser. After pump-purge cycles, the solid was protected in an N_2 atmosphere and 20 ml of degassed 10% water in tetrahydrofuran solution was added to the reaction vessel and refluxed for 12 hours. The reaction mixture was then extracted with dichloromethane and washed with water. After the solvent was removed from the organic layer under vacuum, the crude product was purified using silica gel chromatography with dichloromethane as eluent to yield 300 mg (61%) of off-white waxy solid as product. ^1H NMR (500 MHz, CDCl_3) δ 7.48 – 7.45 (m, 2H), 7.32 – 7.28 (m, 2H), 6.91 (s, 1H), 6.58 (s, 1H), 5.83 (s, 1H), 4.21 – 4.10 (m, 2H), 4.10 – 4.00 (m, 2H), 3.58 (br, 2H), 2.16 (s, 3H), 2.14 (s, 3H). ^{13}C NMR (126 MHz, CDCl_3) δ 134.47, 133.79, 132.85, 131.27, 129.39, 128.26, 126.30, 123.19, 122.30, 103.75, 65.46, 29.74, 20.15, 17.19.

Compound 6 120 mg of 4-Bromo-1,8-naphthalic anhydride, 170 mg of **5**, 20 mg of zinc acetate and 10 ml of pyridine were added to a 25-ml round bottomed flask that was equipped with a magnetic stir bar and a water condenser. The reaction was heated to 100 °C for 24 hours before the solvent was removed using a rotary evaporator. The crude product was passing through a silica gel column with dichloromethane as eluent to yield 78 mg (32%) of off-white powder as the product. ¹H NMR (500 MHz, CDCl₃) δ 8.72 (dd, J = 7.3, 1.1 Hz, 1H), 8.65 (dd, J = 8.5, 1.1 Hz, 1H), 8.48 (d, J = 7.8 Hz, 1H), 8.09 (d, J = 7.8 Hz, 1H), 7.90 (dd, J = 8.5, 7.3 Hz, 1H), 7.53 (d, J = 8.1 Hz, 2H), 7.40 (d, J = 8.3 Hz, 2H), 7.22 (s, 1H), 7.09 (s, 1H), 5.86 (s, 1H), 4.22 – 4.12 (m, 2H), 4.12 – 4.02 (m, 2H), 2.24 (s, 3H), 2.13 (s, 3H). ¹³C NMR (126 MHz, CDCl₃) δ 163.56, 142.36, 142.29, 136.45, 134.47, 133.79, 133.25, 132.85, 132.59, 131.76, 131.27, 130.88, 130.85, 130.04, 129.98, 129.68, 129.54, 129.39, 128.26, 126.30, 123.19, 122.30, 103.75, 65.46, 20.15, 17.19.

Compound 7 100 mg of PXX-Br, 150 mg of **2**, 10 mg of Pd(dppf)Cl₂ and 76 mg of potassium carbonate were placed in a 100-ml round bottomed flask that was equipped with a magnetic stir bar and a condenser. After the solid mixture was pump-purged three times and protected in a nitrogen atmosphere, 20 ml of degassed tetrahydrofuran was injected into the reaction vessel and heated up till reflux for 12 hours. The solvent was then removed under vacuum and the crude product was purified using silica gel chromatography with 50 % dichloromethane in hexane as eluent to yield 70 mg of product. ¹H NMR (500 MHz, CDCl₃) δ 7.68 (s, 1H), 7.31 (d, J = 9.0 Hz, 1H), 7.10 – 7.07 (m, 2H), 7.00 (s, 1H), 6.95 – 6.91 (m, 2H), 6.86 (d, J = 9.2 Hz, 1H), 6.80 (d, J = 9.3 Hz, 1H), 6.70 (t, J = 7.8 Hz, 1H), 6.65 – 6.61 (m, 1H), 2.52 (s, 3H), 2.02 (s, 3H), 1.36 (s, 12H).

Compound 8 35 mg of **6**, 70 mg of **7**, 55 mg of cesium carbonate and 2 mg of Pd(dppf)Cl₂ was placed in a 25-ml round bottomed flask and pump-purged three times with N₂ before 10 ml of

N₂-degassed 10 % water in tetrahydrofuran solution was injected. The reaction was brought up to reflux for 12 hours before the solvent was removed using a rotary evaporator. The crude product was purified using a silica gel chromatography with dichloromethane as eluent to yield 46 mg of product. ¹H NMR (500 MHz, CDCl₃) δ 8.76 – 8.66 (m, 2H), 8.11 – 8.02 (m, 1H), 7.83 – 7.71 (m, 2H), 7.54 (d, J = 8.1 Hz, 2H), 7.42 (d, J = 8.0 Hz, 2H), 7.35 (dt, J = 9.0, 1.7 Hz, 1H), 7.25 (s, 1H), 7.23 – 7.21 (m, 1H), 7.20 (s, 1H), 7.14 (s, 1H), 7.13 – 7.10 (m, 2H), 7.09 – 7.02 (m, 2H), 6.99 – 6.96 (m, 1H), 6.93 (s, 1H), 6.78 (dd, J = 7.8, 2.5 Hz, 1H), 6.67 (ddd, J = 5.3, 4.5, 3.1 Hz, 1H), 5.87 (s, 1H), 4.22 – 4.14 (m, 2H), 4.09 – 4.04 (m, 2H), 2.26 (s, 3H), 2.20 (s, 3H), 2.12 (s, 3H), 2.03 (s, 3H). MS (MALDI-TOF) m/z: [M⁺] calculated for C₅₇H₃₉NO₆ 833.28; found 835.316.

Compound 9 80 mg of **8** was dissolved in 15 ml of tetrahydrofuran in a 20-ml scintillation vial with the addition of 0.1 ml of 37 % hydrochloric acid and stirred at room temperature. Three hours later, the deprotection was completed as monitored by NMR. The reaction was quenched by sodium bicarbonate and extracted with dichloromethane. The product in the organic layer was used directly for the next step after the solvent was removed under vacuum. ¹H NMR (500 MHz, CDCl₃) δ 10.02 (s, 1H), 8.72 – 8.62 (m, 2H), 8.02 (td, J = 7.6, 1.2 Hz, 1H), 7.90 (d, J = 8.0 Hz, 2H), 7.77 – 7.67 (m, 2H), 7.53 (d, J = 8.0 Hz, 2H), 7.29 (dd, J = 9.0, 2.3 Hz, 1H), 7.22 (s, 1H), 7.18 (s, 1H), 7.15 (s, 1H), 7.13 (d, J = 2.3 Hz, 1H), 7.06 (p, J = 2.7 Hz, 2H), 7.04 – 7.00 (m, 1H), 7.00 – 6.96 (m, 1H), 6.95 – 6.90 (m, 1H), 6.86 (t, J = 8.7 Hz, 1H), 6.72 (dd, J = 7.8, 2.4 Hz, 1H), 6.61 (td, J = 4.7, 3.1 Hz, 1H), 2.23 (s, 3H), 2.17 (s, 3H), 2.08 (s, 3H), 2.01 (s, 3H). MS (MALDI-TOF) m/z: [M⁺] calculated for C₅₅H₃₅NO₅ 789.25; found 789.566.

Compound 1 In a 50-ml round bottomed flask equipped with a magnetic stir bar and a water condenser was placed with 50 mg of **9**, 17 mg of sarcosine and 136 mg of C₆₀ that were pump-purged three times with N₂. 20 ml of 1,2-dichlorobenzene was added to the flask and heated

to 120 °C for 15 hours. After the reaction was cooled down, the solvent was removed under vacuum and the crude product was purified with silica gel column chromatography using 15% of dichloromethane in hexane to remove unreacted C₆₀ first then flash with dichloromethane to obtain the crude product. The crude product was then purified with the same chromatography procedure two extra times to completely remove C₆₀ to yield 20 mg of dark brown solid as product. ¹H NMR (500 MHz, CDCl₃) δ 8.74 – 8.66 (m, 2H), 8.05 (ddd, J = 7.8, 6.5, 1.2 Hz, 1H), 7.86 (s, 2H), 7.79 – 7.70 (m, 2H), 7.45 (dd, J = 5.4, 2.6 Hz, 2H), 7.35 (dt, J = 9.1, 1.8 Hz, 1H), 7.28 (s, 1H), 7.22 (d, J = 5.5 Hz, 1H), 7.19 (dd, J = 6.2, 4.1 Hz, 1H), 7.12 (dq, J = 5.2, 2.4 Hz, 3H), 7.09 – 7.05 (m, 1H), 7.05 – 7.01 (m, 1H), 6.97 (dt, J = 9.1, 1.9 Hz, 1H), 6.95 – 6.88 (m, 1H), 6.78 (dd, J = 7.8, 2.5 Hz, 1H), 6.67 (ddd, J = 5.4, 4.5, 3.2 Hz, 1H), 5.02 (d, J = 9.3 Hz, 1H), 5.00 (s, 1H), 4.30 (d, J = 9.4 Hz, 1H), 2.89 (s, 3H), 2.18 (s, 6H), 2.12 (s, 3H), 2.05 (s, 3H). ¹³C NMR (126 MHz, CDCl₃) δ 146.50, 146.46, 146.42, 145.49, 145.38, 145.32, 145.28, 145.26, 144.99, 144.94, 144.92, 144.90, 144.76, 144.62, 144.60, 144.58, 144.51, 144.48, 144.44, 144.40, 144.35, 144.30, 144.22, 143.76, 143.49, 143.25, 143.17, 143.16, 142.26, 142.12, 142.05, 141.96, 141.72, 141.64, 141.55, 141.28, 141.25, 141.23, 141.03, 140.94, 140.79, 140.58, 140.44, 139.21, 139.14, 138.97, 138.62, 134.32, 133.21, 132.21, 131.36, 129.31, 82.29, 39.20, 28.76, 19.14, 18.62, 16.16, 13.10. MS (MALDI-TOF) m/z: [M⁺] calculated for C₁₁₇H₄₀N₂O₄ 1537.30; found 1537.492.

BINOL-d₁₂ Deuteration of BINOL follows the literature procedure. Briefly, in a 125-ml Parr Acid Digestion Vessel was placed 2 g of BINOL, 20 ml of D₂O and 30 mg of PtO₂. (2% equiv.). The sealed vessel was placed in an air circulating dry oven and heated up to 220 °C for 48 hours. The vessel was then cooled down to room temperature and 100 ml of dichloromethane was added to dissolve the product. After filtration, the filtrate was collected, and the solvent removed under vacuum. The crude product underwent another deuteration cycle for complete deuteration

(> 95%) to yield 1.6 g (75%) of product that was used directly for the next step. MS (MALDI-TOF) m/z: $[M^+]$ calculated for $C_{20}H_{13}O_2$ 299.18; found 299.276.

PXX-d₁₀ Synthesis of PXX-d₁₀ follows the literature procedure. MS (MALDI-TOF) m/z: $[M^+]$ calculated for $C_{20}D_{10}O_2$ 292.13; found 292.242.

Compound 1d Synthesis of **1d** follows the same route as **1** except for using deuterated PXX-Br as the precursor. MS (MALDI-TOF) m/z: $[M^+]$ calculated for $C_{117}H_{31}D_9N_2O_4$ 1546.36; found 1546.408.

5.5.2. Transient Absorption Spectroscopy

Femtosecond visible transient absorption (fsTA) spectroscopy experiments were conducted using a commercial regeneratively amplified Ti:sapphire laser system (Tsunami oscillator/Spitfire amplifier, Spectra-Physics, described previously⁴ equipped with a commercial collinear optical parametric amplifier (TOPAS-Prime, Light-Conversion LLC). Before interaction with the sample, the probe was split using a neutral density filter so that one portion interacted with the sample and one portion provided a reference spectrum. The pump (450 nm, 1 μ J/pulse, 120 fs) was sent through a commercial depolarizer (DPU-25-A, Thorlabs, Inc.) to suppress the effects of rotational dynamics and chopped at 500 Hz. The pump was focused to about 0.2 mm diameter and the probe to about 0.1 mm diameter at the sample. The reference probe and the transmitted probe were coupled into optical fibers and detected using a customized Helios spectrometer and Helios software (Ultrafast Systems, LLC). Nanosecond visible transient absorption (nsTA) spectroscopy experiments were performed using the pump pulse described for the fsTA experiments paired with a photonic crystal fiber ultra-broadband probe generated by a customized EOS spectrometer (Ultrafast Systems, LLC). The temporal resolution was about 120-280 fs in the fsTA experiments and about 600-900 ps in the nsTA experiments. Visible fsTA

spectra were collected for 3 s at each pump-probe time delay; nsTA spectra were collected using similar durations. Samples for room-temperature TA experiments were dissolved in toluene and prepared with an optical density of 0.8 at 500 nm in 2 mm quartz cuvettes fused to a glass bulb. This bulb was used to subject each sample to four freeze-pump-thaw cycles under vacuum (10^{-4} Torr) to remove oxygen. Samples were stirred to minimize the effects of local heating and degradation.

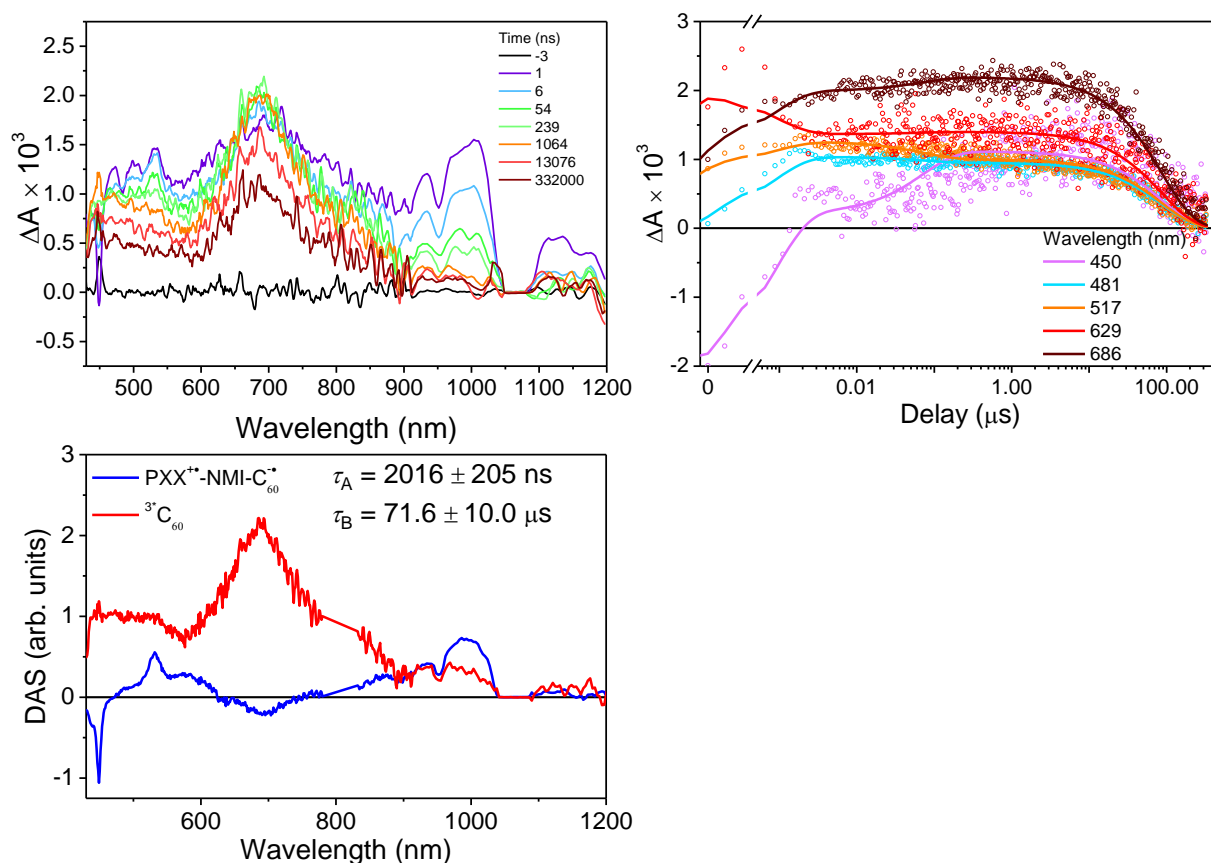


Figure 5.9. Transient absorption spectra of 1. a) nsTA data of 1 at 85 K in mTHF solution following $\lambda_{\text{exc}} = 414$ nm excitation. b) Decay-associated spectra (DAS) of 1. c) Comparison of the kinetic traces to the fit at selected probe wavelengths.

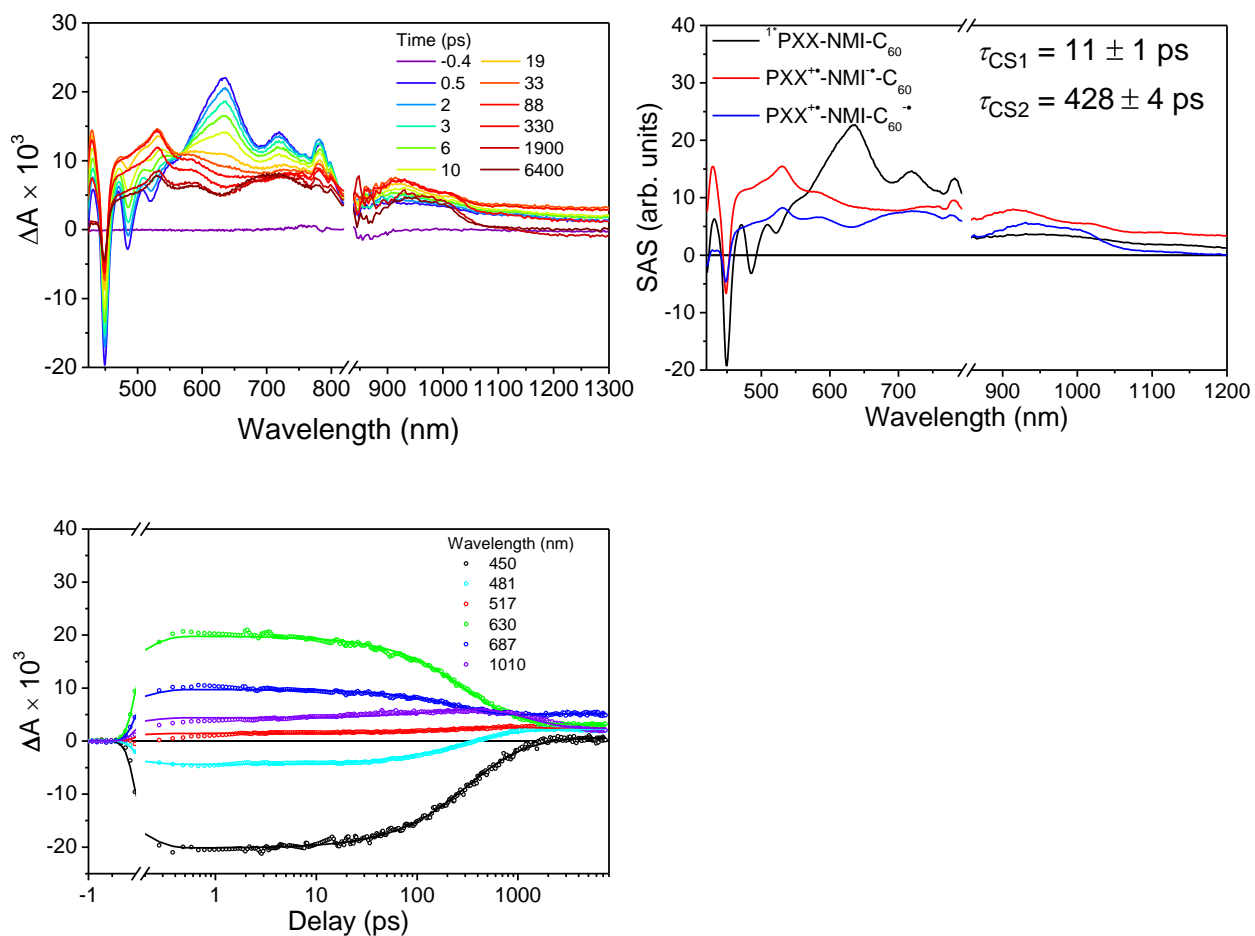


Figure 5.10 Transient absorption spectra of 1. a) fsTA data of 1 at 294 K in toluene solution following $\lambda_{\text{ex}} = 414$ nm excitation. b) Species-associated spectra (SAS) of 1. c) Comparison of the kinetic traces to the fit at selected probe wavelengths.

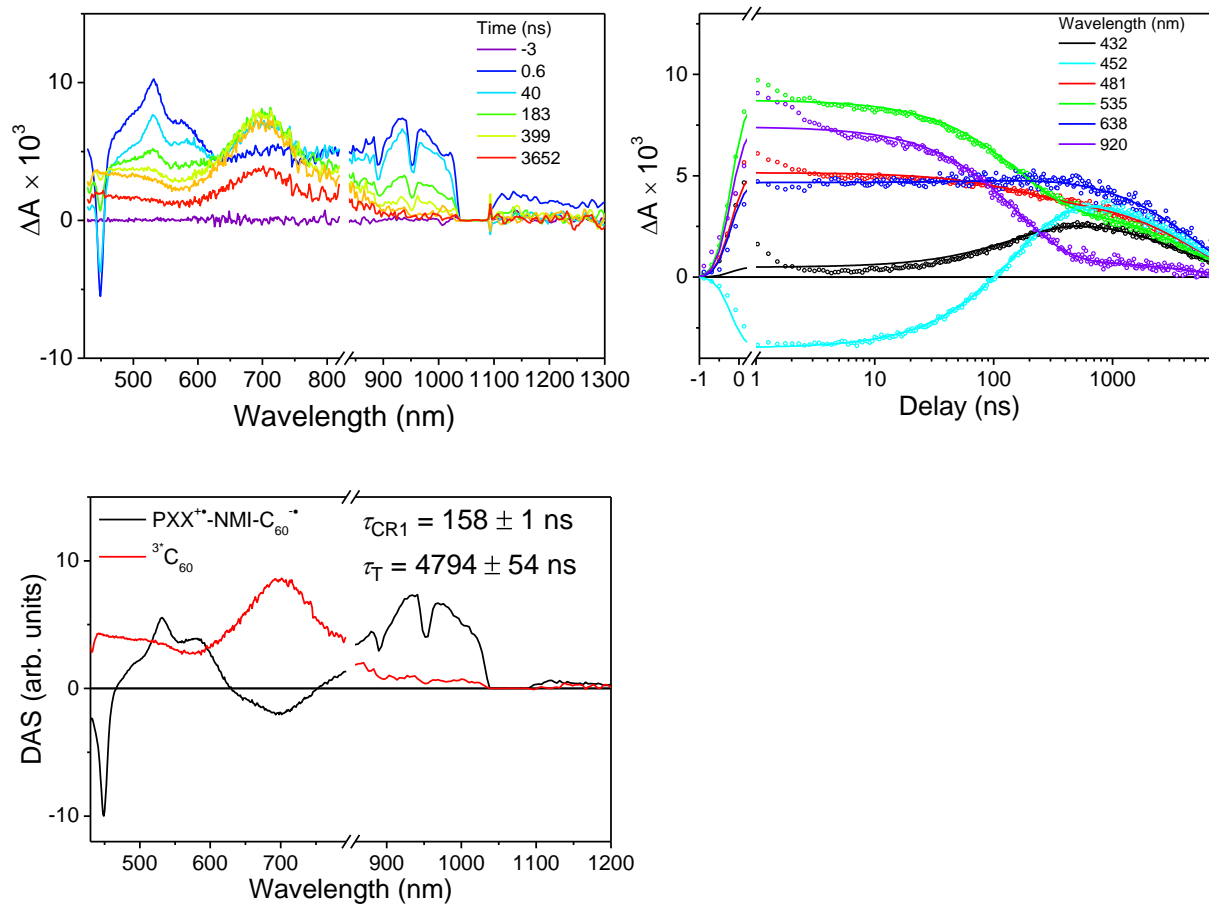


Figure 5.11. Transient absorption spectra of 1. a) nsTA data of 1 at 294 K in toluene solution following $\lambda_{\text{ex}} = 414$ nm excitation. b) Decay-associated spectra (DAS) of 1. c) Comparison of the kinetic traces to the fit at selected probe wavelengths.

5.5.3. Electron Paramagnetic Spectroscopy

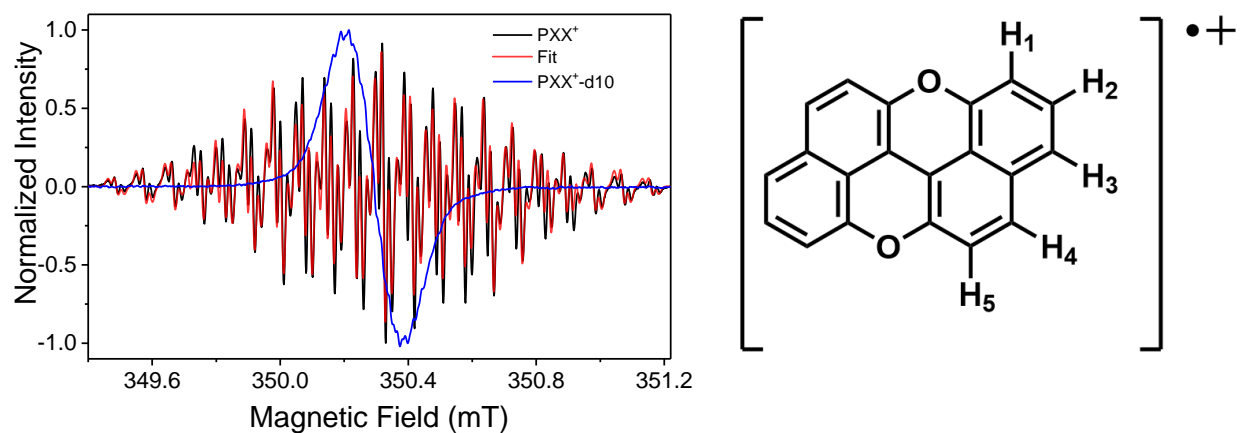


Figure 5.12. CW-EPR of PXX•⁺ and PXX•⁺-d10 in dichloromethane solution at 294 K and the structure formula of PXX showing five chemically inequivalent protons.

Table 5.1. Proton Hyperfine Couplings Extracted From CW-EPR Spectrum of PXX Radical Cation

Proton	H1	H2	H3	H4	H5
Hyperfine Coupling (MHz)	5.00	0.51	6.37	9.47	2.45
Calculated Hyperfine Coupling (MHz)	6.19	0.29	9.28	11.21	4.28

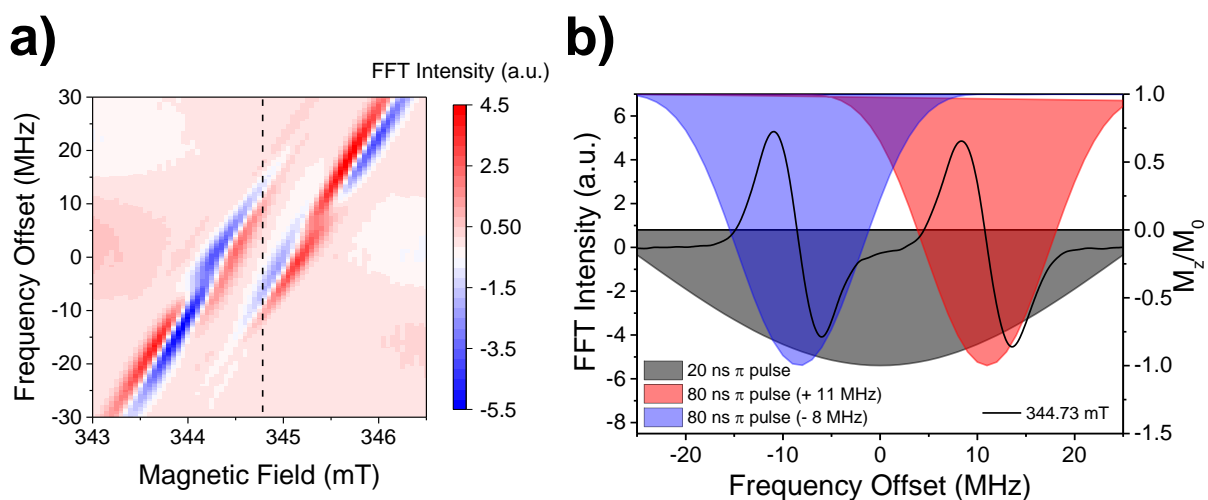


Figure 5.13. (a) Echo detected field sweep of 1-d9 in 5CB aligned along the magnetic field. 20 ns Gaussian-shaped $\pi/2$ and π pulse are used in the experiment. Fourier transform of the echo at each

field position gives the corresponding frequency spectra and were plot against the magnetic field. The features with frequencies larger than 20 MHz or lower than -20 MHz belong to 3^*C60 . (b) Frequency spectra of 1-d9 1d9 at the field position indicated by the dashed line in (a) showing the complete EPR spectrum of the RP. The shaded area shows the bandwidths of Gaussian-shaped microwave pulses, indicating the feasibility of selective and non-selective excitation.

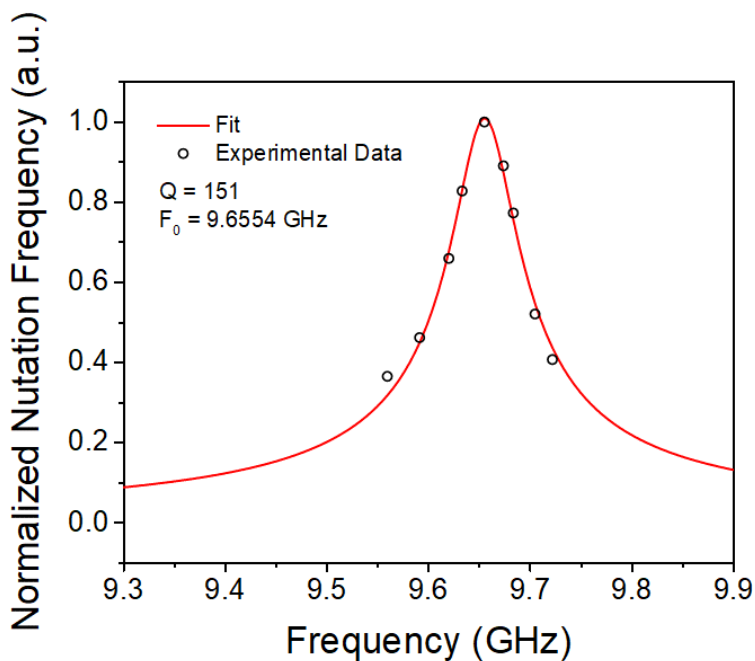


Figure 5.14. Resonator profile characterized by a three-pulse nutation experiment at various frequency. The nutation frequencies versus microwave frequencies plot isare fitted with a resonator model to give the center frequency F_0 and the quality factor Q .

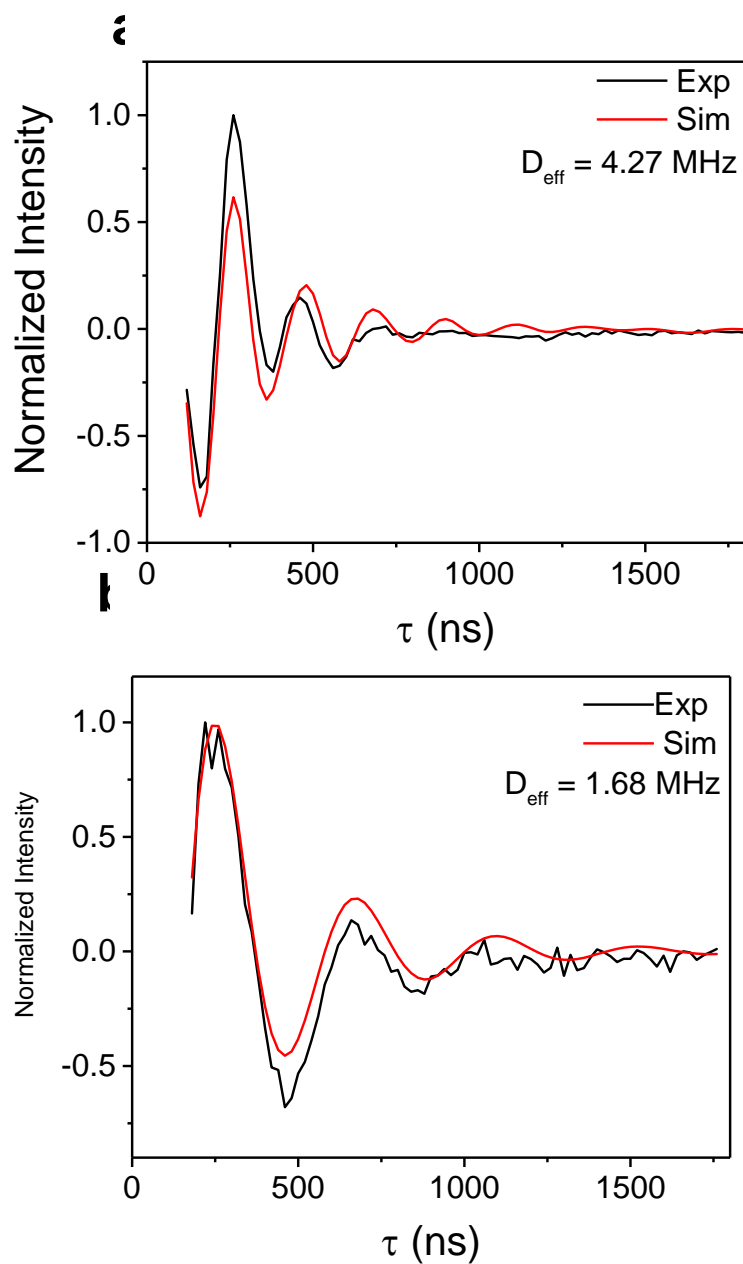


Figure 5.15. Out-of-phase ESEEM measurement on 1-d9 at 85 K in 5CB liquid crystal that is (a) aligned along the magnetic field, or (b) aligned perpendicular to the field.

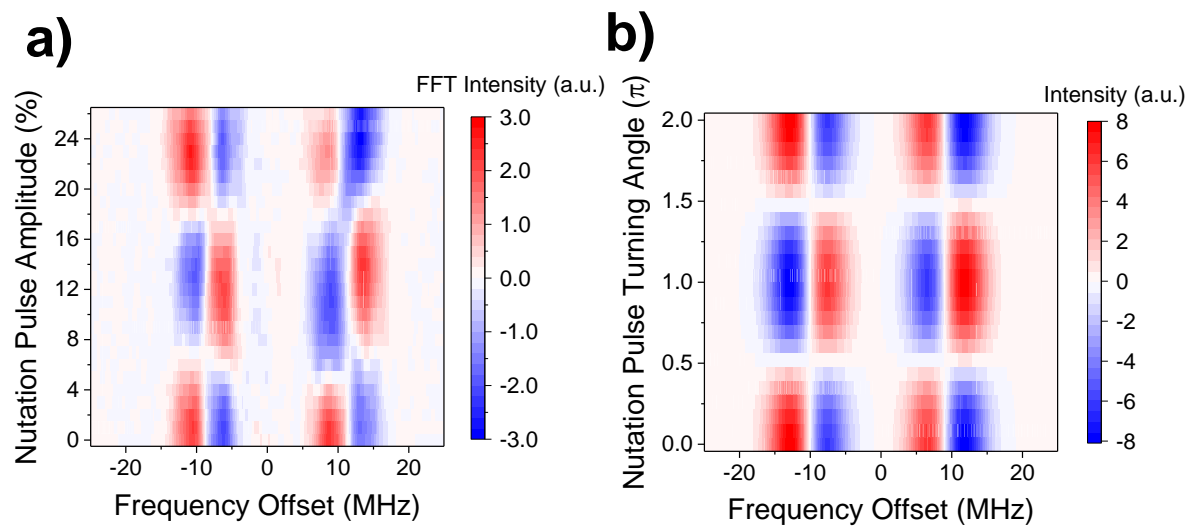


Figure 5.16. (a) Single-qubit gate operation using a three-pulse nutation pulse sequence with a selective nutation pulse that excites $PXX\bullet+$ and a non-selective Hahn echo sequence that detects the entire EPR spectrum. (b) Frequency domain simulation of the experiment.

Reference

- (1) Harrow, A. W.; Montanaro, A. Quantum computational supremacy. *Nature* **2017**, *549* (7671), 203-209.
- (2) Degen, C. L.; Reinhard, F.; Cappellaro, P. Quantum sensing. *Reviews of Modern Physics* **2017**, *89* (3).
- (3) Biamonte, J.; Wittek, P.; Pancotti, N.; Rebentrost, P.; Wiebe, N.; Lloyd, S. Quantum machine learning. *Nature* **2017**, *549* (7671), 195-202.
- (4) Wasielewski, M. R.; Forbes, M. D. E.; Frank, N. L.; Kowalski, K.; Scholes, G. D.; Yuen-Zhou, J.; Baldo, M. A.; Freedman, D. E.; Goldsmith, R. H.; Goodson Iii, T.; et al. Exploiting chemistry and molecular systems for quantum information science. *Nature Reviews Chemistry* **2020**, *4* (9), 490-504.
- (5) Atzori, M.; Sessoli, R. The Second Quantum Revolution: Role and Challenges of Molecular Chemistry. *Journal of the American Chemical Society* **2019**, *141* (29), 11339-11352.
- (6) Troiani, F.; Affronte, M. Molecular spins for quantum information technologies. *Chem Soc Rev* **2011**, *40* (6), 3119-3129.
- (7) Liu, Y.; Toma, F. M. Catalyst: Qubits from the Bottom Up. *Chem* **2020**, *6* (4), 795-798.
- (8) Takui, T.; Berliner, L.; Hanson, G. *Electron spin resonance (ESR) based quantum computing*; Springer, 2016.
- (9) Sato, K.; Nakazawa, S.; Rahimi, R.; Ise, T.; Nishida, S.; Yoshino, T.; Mori, N.; Toyota, K.; Shiomi, D.; Yakiyama, Y.; et al. Molecular electron-spin quantum computers and quantum information processing: pulse-based electron magnetic resonance spin technology applied to matter spin-qubits. *Journal of Materials Chemistry* **2009**, *19* (22).

- (10) Coronado, E. Molecular magnetism: from chemical design to spin control in molecules, materials and devices. *Nature Reviews Materials* **2020**, *5* (2), 87-104.
- (11) Zadrozny, J. M.; Niklas, J.; Poluektov, O. G.; Freedman, D. E. Millisecond Coherence Time in a Tunable Molecular Electronic Spin Qubit. *ACS Cent Sci* **2015**, *1* (9), 488-492.
- (12) Lombardi, F.; Lodi, A.; Ma, J.; Liu, J.; Slota, M.; Narita, A.; Myers, W. K.; Mullen, K.; Feng, X.; Bogani, L. Quantum units from the topological engineering of molecular graphenoids. *Science* **2019**, *366* (6469), 1107-1110.
- (13) Shiddiq, M.; Komijani, D.; Duan, Y.; Gaita-Ariño, A.; Coronado, E.; Hill, S. Enhancing coherence in molecular spin qubits via atomic clock transitions. *Nature* **2016**, *531* (7594), 348-351.
- (14) Yu, C. J.; Krzyaniak, M. D.; Fataftah, M. S.; Wasielewski, M. R.; Freedman, D. E. A concentrated array of copper porphyrin candidate qubits. *Chem Sci* **2019**, *10* (6), 1702-1708.
- (15) Gaita-Ariño, A.; Luis, F.; Hill, S.; Coronado, E. Molecular spins for quantum computation. *Nature Chemistry* **2019**, *11* (4), 301-309.
- (16) Zadrozny, J. M.; Gallagher, A. T.; Harris, T. D.; Freedman, D. E. A Porous Array of Clock Qubits. *J Am Chem Soc* **2017**, *139* (20), 7089-7094.
- (17) Fernandez, A.; Ferrando-Soria, J.; Pineda, E. M.; Tuna, F.; Vitorica-Yrezabal, I. J.; Knappke, C.; Ujma, J.; Muryn, C. A.; Timco, G. A.; Barran, P. E.; et al. Making hybrid [n]-rotaxanes as supramolecular arrays of molecular electron spin qubits. *Nature Communications* **2016**, *7* (1), 10240.
- (18) Nakazawa, S.; Nishida, S.; Ise, T.; Yoshino, T.; Mori, N.; Rahimi, R. D.; Sato, K.; Morita, Y.; Toyota, K.; Shiomi, D.; et al. A synthetic two-spin quantum bit: g-engineered exchange-

coupled biradical designed for controlled-NOT gate operations. *Angew Chem Int Ed Engl* **2012**, *51* (39), 9860-9864.

(19) Rugg, B. K.; Krzyaniak, M. D.; Phelan, B. T.; Ratner, M. A.; Young, R. M.; Wasielewski, M. R. Photodriven quantum teleportation of an electron spin state in a covalent donor–acceptor–radical system. *Nature Chemistry* **2019**, *11* (11), 981-986.

(20) Nelson, J. N.; Zhang, J.; Zhou, J.; Rugg, B. K.; Krzyaniak, M. D.; Wasielewski, M. R. CNOT gate operation on a photogenerated molecular electron spin-qubit pair. *J Chem Phys* **2020**, *152* (1), 014503.

(21) Olshansky, J. H.; Zhang, J.; Krzyaniak, M. D.; Lorenzo, E. R.; Wasielewski, M. R. Selectively Addressable Photogenerated Spin Qubit Pairs in DNA Hairpins. *J Am Chem Soc* **2020**, *142* (7), 3346-3350.

(22) Aguila, D.; Barrios, L. A.; Velasco, V.; Roubeau, O.; Repolles, A.; Alonso, P. J.; Sese, J.; Teat, S. J.; Luis, F.; Aromi, G. Heterodimetallic [LnLn'] lanthanide complexes: toward a chemical design of two-qubit molecular spin quantum gates. *J Am Chem Soc* **2014**, *136* (40), 14215-14222.

(23) Fernandez, A.; Moreno Pineda, E.; Muryn, C. A.; Sproules, S.; Moro, F.; Timco, G. A.; McInnes, E. J. L.; Winpenny, R. E. P. g-Engineering in Hybrid Rotaxanes To Create AB and AB₂ Electron Spin Systems: EPR Spectroscopic Studies of Weak Interactions between Dissimilar Electron Spin Qubits. *Angewandte Chemie International Edition* **2015**, *54* (37), 10858-10861.

(24) Atzori, M.; Chiesa, A.; Morra, E.; Chiesa, M.; Sorace, L.; Carretta, S.; Sessoli, R. A two-qubit molecular architecture for electron-mediated nuclear quantum simulation. *Chem Sci* **2018**, *9* (29), 6183-6192.

- (25) Bayliss, S. L.; Laorenza, D. W.; Mintun, P. J.; Kovos, B. D.; Freedman, D. E.; Awschalom, D. D. Optically addressable molecular spins for quantum information processing. *Science* **2020**, *370* (6522), 1309.
- (26) Warren, S., W. The Usefulness of NMR Quantum Computing. *Science* **1997**, *277* (5332), 1688-1690.
- (27) Awschalom, D. D.; Hanson, R.; Wrachtrup, J.; Zhou, B. B. Quantum technologies with optically interfaced solid-state spins. *Nat. Photonics* **2018**, *12* (9), 516-527.
- (28) Doherty, M. W.; Manson, N. B.; Delaney, P.; Jelezko, F.; Wrachtrup, J.; Hollenberg, L. C. L. The nitrogen-vacancy colour centre in diamond. *Phys. Rep.* **2013**, *528* (1), 1-45.
- (29) Plakhotnik, T.; Aman, H. NV-centers in nanodiamonds: How good they are. *Diamond Relat. Mater.* **2018**, *82*, 87-95.
- (30) Rugg, B. K.; Phelan, B. T.; Horwitz, N. E.; Young, R. M.; Krzyaniak, M. D.; Ratner, M. A.; Wasielewski, M. R. Spin-Selective Photoreduction of a Stable Radical within a Covalent Donor-Acceptor-Radical Triad. *J. Am. Chem. Soc.* **2017**, *139* (44), 15660-15663.
- (31) Thurnauer, M. C.; Norris, J. R. An electron spin echo phase shift observed in photosynthetic algae: possible evidence for dynamic radical pair interactions. *Chemical Physics Letters* **1980**, *76* (3), 557-561.
- (32) Buckley, C. D.; Hunter, D. A.; Hore, P. J.; McLauchlan, K. A. Electron spin resonance of spin-correlated radical pairs. *Chemical Physics Letters* **1987**, *135* (3), 307-312.
- (33) Chen, H. F.; Gardner, D. M.; Carmieli, R.; Wasielewski, M. R. Controlling the orientation of spin-correlated radical pairs by covalent linkage to nanoporous anodic aluminum oxide membranes. *Chem Commun (Camb)* **2013**, *49* (77), 8614-8616.

- (34) Bayliss, S. L.; Laorenza, D. W.; Mintun, P. J.; Kovos, B. D.; Freedman, D. E.; Awschalom, D. D. Optically addressable molecular spins for quantum information processing. *Science (Washington, DC, U. S.)* **2020**, *370* (6522), 1309-1312.
- (35) Laorenza, D. W.; Kairalapova, A.; Bayliss, S. L.; Goldzak, T.; Greene, S. M.; Weiss, L. R.; Deb, P.; Mintun, P. J.; Collins, K. A.; Awschalom, D. D.; et al. Tunable Cr⁴⁺ Molecular Color Centers. *Journal of the American Chemical Society* **2021**, *143* (50), 21350-21363.
- (36) Rozenshtein, V.; Berg, A.; Stavitski, E.; Levanon, H.; Franco, L.; Corvaja, C. Electron Spin Polarization of Functionalized Fullerenes. Reversed Quartet Mechanism. *J. Phys. Chem. A* **2005**, *109* (49), 11144-11154.
- (37) Giacobbe, E. M.; Mi, Q.; Colvin, M. T.; Cohen, B.; Ramanan, C.; Scott, A. M.; Yeganeh, S.; Marks, T. J.; Ratner, M. A.; Wasielewski, M. R. Ultrafast intersystem crossing and spin dynamics of photoexcited perylene-3,4:9,10-bis(dicarboximide) covalently linked to a nitroxide radical at fixed distances. *J. Am. Chem. Soc.* **2009**, *131* (10), 3700-3712.
- (38) Colvin, M. T.; Smeigh, A. L.; Giacobbe, E. M.; Conron, S. M. M.; Ricks, A. B.; Wasielewski, M. R. Ultrafast intersystem crossing and spin dynamics of zinc meso-tetraphenylporphyrin covalently bound to stable radicals. *J. Phys. Chem. A* **2011**, *115* (26), 7538-7549.
- (39) Kirk, M. L.; Shultz, D. A.; Hewitt, P.; van der Est, A. Excited State Exchange Control of Photoinduced Electron Spin Polarization in Electronic Ground States. *J. Phys. Chem. Lett.* **2022**, *13* (3), 872-878.
- (40) Kirk, M. L.; Shultz, D. A.; Hewitt, P.; Stasiw, D. E.; Chen, J.; van der Est, A. Chromophore-radical excited state antiferromagnetic exchange controls the sign of photoinduced ground state spin polarization. *Chem. Sci.* **2021**, *12* (41), 13704-13710.

- (41) Kirk, M. L.; Shultz, D. A.; Chen, J.; Hewitt, P.; Daley, D.; Paudel, S.; van der Est, A. Metal Ion Control of Photoinduced Electron Spin Polarization in Electronic Ground States. *J. Am. Chem. Soc.* **2021**, *143* (28), 10519-10523.
- (42) Kandrashkin, Y. E.; van der Est, A. The triplet mechanism of electron spin polarization in moderately coupled triplet-doublet rigid complexes as a source of the enhanced $+1/2 \leftrightarrow -1/2$ transitions. *J. Chem. Phys.* **2019**, *151* (18), 184301/184301-184301/184308.
- (43) Van der Est, A.; Asano-Someda, M.; Ragona, P.; Kaizu, Y. Light-Induced Electron Spin Polarization of a Weakly Coupled Triplet-Doublet Spin Pair in a Covalently Linked Porphyrin Dimer. *J. Phys. Chem. A* **2002**, *106* (37), 8531-8542.
- (44) Dal Farra, M. G.; Martin, C.; Bergantino, E.; Kandrashkin, Y. E.; van der Est, A.; Di Valentin, M. Electron spin polarization transfer induced by triplet-radical interactions in the weakly coupled regime. *Phys. Chem. Chem. Phys.* **2020**, *22* (35), 19982-19991.
- (45) Horwitz, N. E.; Phelan, B. T.; Nelson, J. N.; Mauck, C. M.; Krzyaniak, M. D.; Wasielewski, M. R. Spin Polarization Transfer from a Photogenerated Radical Ion Pair to a Stable Radical Controlled by Charge Recombination. *J Phys Chem A* **2017**, *121* (23), 4455-4463.
- (46) Horwitz, N. E.; Phelan, B. T.; Nelson, J. N.; Krzyaniak, M. D.; Wasielewski, M. R. Picosecond Control of Photogenerated Radical Pair Lifetimes Using a Stable Third Radical. *J Phys Chem A* **2016**, *120* (18), 2841-2853.
- (47) Colvin, M. T.; Carmieli, R.; Miura, T.; Richert, S.; Gardner, D. M.; Smeigh, A. L.; Dyar, S. M.; Conron, S. M.; Ratner, M. A.; Wasielewski, M. R. Electron spin polarization transfer from photogenerated spin-correlated radical pairs to a stable radical observer spin. *J Phys Chem A* **2013**, *117* (25), 5314-5325.

- (48) Mi, Q.; Chernick, E. T.; McCamant, D. W.; Weiss, E. A.; Ratner, M. A.; Wasielewski, M. R. Spin dynamics of photogenerated triradicals in fixed distance electron donor-chromophore-acceptor-TEMPO molecules. *J Phys Chem A* **2006**, *110* (23), 7323-7333.
- (49) Marcus, R. A. On the Theory of Oxidation - Reduction Reactions Involving Electron Transfer. I. *The Journal of Chemical Physics* **1956**, *24* (5), 966-978.
- (50) Marcus, R. A. On the Theory of Electron - Transfer Reactions. VI. Unified Treatment for Homogeneous and Electrode Reactions. *The Journal of Chemical Physics* **1965**, *43* (2), 679-701.
- (51) Weller, A. Photoinduced Electron Transfer in Solution: Exciplex and Radical Ion Pair Formation Free Enthalpies and their Solvent Dependence. *Zeitschrift für Physikalische Chemie* **1982**, *133* (1), 93-98.
- (52) Rugg, B. K.; Phelan, B. T.; Horwitz, N. E.; Young, R. M.; Krzyaniak, M. D.; Ratner, M. A.; Wasielewski, M. R. Spin-Selective Photoreduction of a Stable Radical within a Covalent Donor-Acceptor-Radical Triad. *J Am Chem Soc* **2017**, *139* (44), 15660-15663.
- (53) Young, R. M.; Dyar, S. M.; Barnes, J. C.; Juricek, M.; Stoddart, J. F.; Co, D. T.; Wasielewski, M. R. Ultrafast conformational dynamics of electron transfer in ExBox4+ subsetperylene. *J Phys Chem A* **2013**, *117* (47), 12438-12448.
- (54) Salikhov, K. M.; Golbeck, J. H.; Stehlik, D. Quantum teleportation across a biological membrane by means of correlated spin pair dynamics in photosynthetic reaction centers. *Applied Magnetic Resonance* **2007**, *31* (1-2), 237-252.
- (55) van der Est, A.; Asano-Someda, M.; Ragogna, P.; Kaizu, Y. Light-Induced Electron Spin Polarization of a Weakly Coupled Triplet–Doublet Spin Pair in a Covalently Linked Porphyrin Dimer. *The Journal of Physical Chemistry A* **2002**, *106* (37), 8531-8542.

- (56) Kandrashkin, Y. E.; van der Est, A. The triplet mechanism of electron spin polarization in moderately coupled triplet-doublet rigid complexes as a source of the enhanced $+1/2 \leftrightarrow -1/2$ transitions. *J Chem Phys* **2019**, *151* (18), 184301.
- (57) Gosztola, D.; Niemczyk, M. P.; Svec, W.; Lukas, A. S.; Wasielewski, M. R. Excited Doublet States of Electrochemically Generated Aromatic Imide and Diimide Radical Anions. *Journal of Physical Chemistry A* **2000**, *104* (28), 6545-6551.
- (58) Christensen, J. A.; Zhang, J.; Zhou, J.; Nelson, J. N.; Wasielewski, M. R. Near-Infrared Excitation of the peri-Xanthenoxanthene Radical Cation Drives Energy-Demanding Hole Transfer Reactions. *Journal of Physical Chemistry C* **2018**, *122* (41), 23364-23370.
- (59) Al-Aqar, R.; Benniston, A. C.; Harriman, A.; Perks, T. Structural Dynamics and Barrier Crossing Observed for a Fluorescent O-Doped Polycyclic Aromatic Hydrocarbon. *ChemPhotoChem* **2017**, *1* (5), 198-205.
- (60) Stoll, S.; Schweiger, A. EasySpin, a comprehensive software package for spectral simulation and analysis in EPR. *Journal of Magnetic Resonance* **2006**, *178* (1), 42-55.
- (61) Colvin, M. T.; Ricks, A. B.; Scott, A. M.; Smeigh, A. L.; Carmieli, R.; Miura, T.; Wasielewski, M. R. Magnetic field-induced switching of the radical-pair intersystem crossing mechanism in a donor-bridge-acceptor molecule for artificial photosynthesis. *J Am Chem Soc* **2011**, *133* (5), 1240-1243.
- (62) Miura, T.; Carmieli, R.; Wasielewski, M. R. Time-resolved EPR studies of charge recombination and triplet-state formation within donor-bridge-acceptor molecules having wire-like oligofluorene bridges. *The Journal of Physical Chemistry A* **2010**, *114* (18), 5769-5778.

- (63) Colvin, M. T.; Ricks, A. B.; Scott, A. M.; Co, D. T.; Wasielewski, M. R. Intersystem Crossing Involving Strongly Spin Exchange-Coupled Radical Ion Pairs in Donor-bridge-Acceptor Molecules. *The Journal of Physical Chemistry A* **2012**, *116* (8), 1923-1930.
- (64) van Willigen, H.; Jones, G.; Farahat, M. S. Time-resolved EPR study of photoexcited triplet-state formation in electron-donor-substituted acridinium ions. *The Journal of Physical Chemistry* **1996**, *100* (9), 3312-3316.
- (65) Levanon, H.; Norris, J. R. The photoexcited triplet state and photosynthesis. *Chemical Reviews* **1978**, *78* (3), 185-198.
- (66) Adrian, F.; Monchick, L. Theory of chemically induced magnetic polarization. Effects of S-T \pm 1 mixing in strong magnetic fields. *The Journal of Chemical Physics* **1979**, *71* (6), 2600-2610.
- (67) Adrian, F.; Monchick, L. Analytic formula for chemically induced magnetic polarization by S-T \pm 1 mixing in a strong magnetic field. *The Journal of Chemical Physics* **1980**, *72* (10), 5786-5787.
- (68) Honma, H.; Murai, H.; Kuwata, K. CIDEP study on photooxidation of N, N, N', N' - tetramethyl-p-phenylenediamine by maleic anhydride. Enhanced S-T-1 mixing by radical-ion pair system. *Chemical physics letters* **1992**, *195* (2-3), 239-242.
- (69) Kandrashkin, Y. E.; van der Est, A. Stimulated Electron Spin Polarization in Strongly Coupled Triplet-Doublet Spin Pairs. *Applied Magnetic Resonance* **2011**, *40* (2), 189-204.
- (70) Kamei, T.; Uryu, M.; Shimada, T. Cu-Catalyzed Aerobic Oxidative C-H/C-O Cyclization of 2,2'-Binaphthols: Practical Synthesis of PXX Derivatives. *Org. Lett.* **2017**, *19* (10), 2714-2717.
- (71) Greenfield, S. R.; Wasielewski, M. R. Near-transform-limited visible and near-IR fs pulses from OPA using Type II B-barium borate. *Opt. Lett.* **1995**, *20* (12), 1394-1396.

- (72) Ivanov, K. L.; Wagenpfahl, A.; Deibel, C.; Matysik, J. Spin-chemistry concepts for spintronics scientists. *Beilstein J Nanotechnol* **2017**, *8*, 1427-1445.
- (73) Sanvito, S. Molecular spintronics. *Chem Soc Rev* **2011**, *40* (6), 3336-3355.
- (74) The 2007 Nobel Prize in Physics was awarded to Albert Fert and Peter Grünberg for the discovery of GMR.
- (75) Ennen, I.; Kappe, D.; Rempel, T.; Glenske, C.; Hutten, A. Giant Magnetoresistance: Basic Concepts, Microstructure, Magnetic Interactions and Applications. *Sensors (Basel)* **2016**, *16* (6), 904.
- (76) Baibich, M. N.; Broto, J. M.; Fert, A.; Nguyen Van Dau, F.; Petroff, F.; Etienne, P.; Creuzet, G.; Friederich, A.; Chazelas, J. Giant magnetoresistance of (001)Fe/(001)Cr magnetic superlattices. *Phys Rev Lett* **1988**, *61* (21), 2472-2475.
- (77) Binasch, G.; Grunberg, P.; Saurenbach, F.; Zinn, W. Enhanced magnetoresistance in layered magnetic structures with antiferromagnetic interlayer exchange. *Phys Rev B Condens Matter* **1989**, *39* (7), 4828-4830.
- (78) Hicks, R. G. What's new in stable radical chemistry? *Org Biomol Chem* **2007**, *5* (9), 1321-1338.
- (79) Ratera, I.; Veciana, J. Playing with organic radicals as building blocks for functional molecular materials. *Chem Soc Rev* **2012**, *41* (1), 303-349.
- (80) Kumar, S.; Kumar, Y.; Keshri, S. K.; Mukhopadhyay, P. Recent Advances in Organic Radicals and Their Magnetism. *Magnetochemistry* **2016**, *2* (4), 42.
- (81) Mas-Torrent, M.; Crivillers, N.; Mugnaini, V.; Ratera, I.; Rovira, C.; Veciana, J. Organic radicals on surfaces: towards molecular spintronics. *Journal of Materials Chemistry* **2009**, *19* (12), 1691-1695.

- (82) Poggini, L.; Cucinotta, G.; Sorace, L.; Caneschi, A.; Gatteschi, D.; Sessoli, R.; Mannini, M. Nitronyl nitroxide radicals at the interface: a hybrid architecture for spintronics. *Rendiconti Lincei-Scienze Fisiche E Naturali* **2018**, *29* (3), 623-630.
- (83) Olshansky, J. H.; Krzyaniak, M. D.; Young, R. M.; Wasielewski, M. R. Photogenerated Spin-Entangled Qubit (Radical) Pairs in DNA Hairpins: Observation of Spin Delocalization and Coherence. *Journal of the American Chemical Society* **2019**, *141* (5), 2152-2160.
- (84) Nelson, J. N.; Zhang, J.; Zhou, J.; Rugg, B. K.; Krzyaniak, M. D.; Wasielewski, M. R. CNOT gate operation on a photogenerated molecular electron spin-qubit pair. *The Journal of Chemical Physics* **2020**, *152* (1), 014503.
- (85) Jurow, M.; Schuckman, A. E.; Batteas, J. D.; Drain, C. M. Porphyrins as Molecular Electronic Components of Functional Devices. *Coord Chem Rev* **2010**, *254* (19-20), 2297-2310.
- (86) Tran, T. T.; Chang, Y. R.; Hoang, T. K.; Kuo, M. Y.; Su, Y. O. Electrochemical Behavior of meso-Substituted Porphyrins: The Role of Cation Radicals to the Half-Wave Oxidation Potential Splitting. *J Phys Chem A* **2016**, *120* (28), 5504-5511.
- (87) Sano, S.; Sano, T.; Morishima, I.; Shiro, Y.; Maeda, Y. On the mechanism of the chemical and enzymic oxygenations of alpha-oxypurohemin IX to Fe.biliverdin IX alpha. *Proc Natl Acad Sci U S A* **1986**, *83* (3), 531-535.
- (88) Shimizu, D.; Oh, J.; Furukawa, K.; Kim, D.; Osuka, A. Triarylporphyrin meso-Oxy Radicals: Remarkable Chemical Stabilities and Oxidation to Oxophlorin pi-Cations. *J Am Chem Soc* **2015**, *137* (49), 15584-15594.
- (89) Shimizu, D.; Osuka, A. Porphyrinoids as a platform of stable radicals. *Chem Sci* **2018**, *9* (6), 1408-1423.

- (90) Dommaschk, M.; Gutzeit, F.; Boretius, S.; Haag, R.; Herges, R. Coordination-induced spin-state-switch (CISSS) in water. *Chem Commun (Camb)* **2014**, 50 (83), 12476-12478.
- (91) F. A. Cotton, G. W., C. A. Murillo, M. Bochmann, *Advanced Inorganic Chemistry*, 6th ed., Wiley Interscience, New York, 1999.
- (92) Gnezdilov, O. I.; Mambetov, A. E.; Obynochny, A. A.; Salikhov, K. M. Time-resolved EPR study of electron spin polarization and spin exchange in mixed solutions of porphyrin stable free radicals. *Appl Magn Reson* **2003**, 25 (1), 157-198.
- (93) Fujisawa, J.; Ohba, Y.; Yamauchi, S. Electron-spin polarizations generated from interactions between excited triplet porphyrins and stable radicals studied by time-resolved electron paramagnetic resonance. *J Phys Chem A* **1997**, 101 (4), 434-439.
- (94) Blank, A.; Levanon, H. *Interaction between Polarized Triplets and Stable Radicals in Liquid Solutions*; 2001. DOI: 10.1021/jp010033g.
- (95) Blank, A.; Galili, T.; Levanon, H. Triplet porphyrins as donors in intramolecular electron transfer and their intermolecular interaction with free radicals. *Journal of Porphyrins and Phthalocyanines* **2001**, 5 (1), 58-66.
- (96) Poddutoori, P. K.; Pilkington, M.; Alberola, A.; Polo, V.; Warren, J. E.; van der Est, A. Spin-spin interactions in porphyrin-based monoverdazyl radical hybrid spin systems. *Inorg Chem* **2010**, 49 (7), 3516-3524.
- (97) Rakowsky, M. H.; More, K. M.; Kulikov, A. V.; Eaton, G. R.; Eaton, S. S. Time-Domain Electron-Paramagnetic-Resonance as a Probe of Electron-Electron Spin-Spin Interaction in Spin-Labeled Low-Spin Iron Porphyrins. *J Am Chem Soc* **1995**, 117 (7), 2049-2057.
- (98) Teki, Y. Excited-State Dynamics of Non-Luminescent and Luminescent pi-Radicals. *Chemistry* **2020**, 26 (5), 980-996.

- (99) Buchachenko, A. L.; Berdinsky, V. L. Electron Spin Catalysis. *Chem. Rev.* **2002**, *102* (3), 603-612.
- (100) Zarea, M.; Ratner, M. A.; Wasielewski, M. R. Spin polarization transfer by the radical pair mechanism. *The Journal of Chemical Physics* **2015**, *143* (5), 054101.
- (101) Kandrashkin, Y.; van der Est, A. *Stimulated Electron Spin Polarization in Strongly Coupled Triplet–Doublet Spin Pairs*; 2011. DOI: 10.1007/s00723-011-0194-8.
- (102) Colvin, M. T.; Giacobbe, E. M.; Cohen, B.; Miura, T.; Scott, A. M.; Wasielewski, M. R. Competitive electron transfer and enhanced intersystem crossing in photoexcited covalent TEMPO-perylene-3,4:9,10-bis(dicarboximide) dyads: unusual spin polarization resulting from the radical-triplet interaction. *J Phys Chem A* **2010**, *114* (4), 1741-1748.
- (103) Gardner, D. M.; Chen, H. F.; Krzyaniak, M. D.; Ratner, M. A.; Wasielewski, M. R. Large Dipolar Spin-Spin Interaction in a Photogenerated U-Shaped Triradical. *J Phys Chem A* **2015**, *119* (29), 8040-8048.
- (104) Colvin, M. T.; Smeigh, A. L.; Giacobbe, E. M.; Conron, S. M. M.; Ricks, A. B.; Wasielewski, M. R. Ultrafast Intersystem Crossing and Spin Dynamics of Zinc meso-Tetraphenylporphyrin Covalently Bound to Stable Radicals. *The Journal of Physical Chemistry A* **2011**, *115* (26), 7538-7549.
- (105) Dyar, S. M.; Margulies, E. A.; Horwitz, N. E.; Brown, K. E.; Krzyaniak, M. D.; Wasielewski, M. R. Photogenerated Quartet State Formation in a Compact Ring-Fused Perylene-Nitroxide. *The Journal of Physical Chemistry B* **2015**, *119* (43), 13560-13569.
- (106) Giacobbe, E. M.; Mi, Q.; Colvin, M. T.; Cohen, B.; Ramanan, C.; Scott, A. M.; Yeganeh, S.; Marks, T. J.; Ratner, M. A.; Wasielewski, M. R. Ultrafast intersystem crossing and spin

dynamics of photoexcited perylene-3,4:9,10-bis(dicarboximide) covalently linked to a nitroxide radical at fixed distances. *J Am Chem Soc* **2009**, *131* (10), 3700-3712.

(107) Gütlich, P.; Goodwin, H. A. Spin Crossover—An Overall Perspective. In *Spin Crossover in Transition Metal Compounds I*, Gütlich, P., Goodwin, H. A. Eds.; Topics in Current Chemistry, Springer Berlin Heidelberg, 2004; pp 1-47.

(108) Balch, A. L.; Noll, B. C.; Phillips, S. L.; Reid, S. M.; Zovinka, E. P. Nickel(II) Complexes of the Octaethyloxophlorin Dianion and Octaethyloxophlorin Radical Dianion. *Inorganic Chemistry* **1993**, *32* (22), 4730-4736.

(109) Stahler, C.; Shimizu, D.; Yoshida, K.; Furukawa, K.; Herges, R.; Osuka, A. Stable Ni(II) Porphyrin meso-Oxy Radical with a Quartet Ground State. *Chemistry* **2017**, *23* (30), 7217-7220.

(110) Chernick, E. T.; Casillas, R.; Zirzmeier, J.; Gardner, D. M.; Gruber, M.; Kropp, H.; Meyer, K.; Wasielewski, M. R.; Guldi, D. M.; Tykwinski, R. R. Pentacene Appended to a TEMPO Stable Free Radical: The Effect of Magnetic Exchange Coupling on Photoexcited Pentacene. *Journal of the American Chemical Society* **2015**, *137* (2), 857-863.

(111) Weiss, E. A.; Chernick, E. T.; Wasielewski, M. R. Modulation of radical ion pair lifetimes by the presence of a third spin in rodlike donor-acceptor triads. *J Am Chem Soc* **2004**, *126* (8), 2326-2327.

(112) Chernick, E. T.; Mi, Q.; Vega, A. M.; Lockard, J. V.; Ratner, M. A.; Wasielewski, M. R. Controlling electron transfer dynamics in donor-bridge-acceptor molecules by increasing unpaired spin density on the bridge. *J Phys Chem B* **2007**, *111* (24), 6728-6737.

(113) Chernick, E. T.; Mi, Q.; Kelley, R. F.; Weiss, E. A.; Jones, B. A.; Marks, T. J.; Ratner, M. A.; Wasielewski, M. R. Electron donor-bridge-acceptor molecules with bridging nitronyl nitroxide

radicals: influence of a third spin on charge- and spin-transfer dynamics. *J Am Chem Soc* **2006**, *128* (13), 4356-4364.

(114) Krzystek, J.; Park, J. H.; Meisel, M. W.; Hitchman, M. A.; Stratemeier, H.; Brunel, L. C.; Telser, J. EPR spectra from "EPR-silent" species: high-frequency and high-field EPR spectroscopy of pseudotetrahedral complexes of nickel(II). *Inorg Chem* **2002**, *41* (17), 4478-4487.

(115) Greiner, S. P.; Rowlands, D. L.; Kreilick, R. W. Epr and Endor Study of Selected Porphyrin-Copper and Phthalocyanine-Copper Complexes. *J Phys Chem-Us* **1992**, *96* (23), 9132-9139.

(116) Gouterman, M. Study of the Effects of Substitution on the Absorption Spectra of Porphin. *J Chem Phys* **1959**, *30* (5), 1139-1161.

(117) Khudyakov, I. V.; Serebrennikov, Y. A.; Turro, N. J. Spin-orbit coupling in free-radical reactions: on the way to heavy elements. *Chemical Reviews* **1993**, *93* (1), 537-570.

(118) Yeganeh, S.; Wasielewski, M. R.; Ratner, M. A. Enhanced Intersystem Crossing in Three-Spin Systems: A Perturbation Theory Treatment. *Journal of the American Chemical Society* **2009**, *131* (6), 2268-2273.

(119) Thurnauer, M. C.; Katz, J. J.; Norris, J. R. The triplet state in bacterial photosynthesis: Possible mechanisms of the primary photo-act. *Proceedings of the National Academy of Sciences* **1975**, *72* (9), 3270.

(120) Scherz, A.; Orbach, N.; Levanon, H. Kinetic Study of the Photoexcited Triplet State of Free Base Porphyrins by EPR. *Israel Journal of Chemistry* **1974**, *12* (6), 1037-1048.

(121) Gonen, O.; Levanon, H. Time-resolved EPR spectroscopy of electron spin polarized ZnTPP triplets oriented in a liquid crystal. *The Journal of Physical Chemistry* **1985**, *89* (9), 1637-1643.

- (122) Isoya, J.; Kanda, H.; Norris, J. R.; Tang, J.; Bowman, M. K. Fourier-transform and continuous-wave EPR studies of nickel in synthetic diamond: Site and spin multiplicity. *Phys Rev B* **1990**, *41* (7), 3905-3913.
- (123) Astashkin, A. V.; Schweiger, A. Electron-spin transient nutation: a new approach to simplify the interpretation of ESR spectra. *Chem. Phys. Lett.* **1990**, *174* (6), 595-602.
- (124) Sukhanov, A. A.; Konov, K. B.; Salikhov, K. M.; Voronkova, V. K.; Mikhailitsyna, E. A.; Tyurin, V. S. Time-Resolved Continuous-Wave and Pulse EPR Investigation of Photoinduced States of Zinc Porphyrin Linked with an Ethylenediamine Copper Complex. *Appl Magn Reson* **2015**, *46* (11), 1199-1220.
- (125) Littler, B. J.; Miller, M. A.; Hung, C. H.; Wagner, R. W.; O'Shea, D. F.; Boyle, P. D.; Lindsey, J. S. Refined synthesis of 5-substituted dipyrromethanes. *J Org Chem* **1999**, *64* (4), 1391-1396.
- (126) Rao, P. D.; Dhanalekshmi, S.; Littler, B. J.; Lindsey, J. S. Rational syntheses of porphyrins bearing up to four different meso substituents. *J Org Chem* **2000**, *65* (22), 7323-7344.
- (127) Abraham, R. J.; Hawkes, G. E.; Hudson, M. F.; Smith, K. M. Nuclear Magnetic-Resonance Spectra of Porphyrins .10. C-13 Nuclear Magnetic-Resonance Spectra of Some Meso-Tetraarylporphyrins and Their Metal-Chelates. *J Chem Soc Perk T 2* **1975**, (3), 204-211.
- (128) Abraham, R. J.; Hawkes, G. E.; Smith, K. M. C-13 Nuclear Magnetic-Resonance Spectra of Coproporphyrins. *J Chem Soc Chem Comm* **1973**, (12), 401-402.
- (129) Battersby, A. R.; Mcdonald, E.; Moron, J. Studies of Porphyrin Biosynthesis by C-B Nuclear Magnetic-Resonance - Synthesis of [C-13]Porphobilinogen and Its Incorporation into Protoporphyrin-Ix. *J Chem Soc Chem Comm* **1972**, (15), 920-+.

- (130) Shaw, S. J.; Shanmugathan, S.; Clarke, O. J.; Boyle, R. W.; Osborne, A. G.; Edwards, C. A C-13 NMR spectral examination of alpha- and beta-carbon signal peak heights in some disubstituted arylporphyrins (vol 5, pg 575, 2001). *J Porphyr Phthalocya* **2001**, 5 (12), 895-895.
- (131) Kooriyaden, F. R.; Sujatha, S.; Varghese, B.; Arunkumar, C. Synthesis of electron-deficient fluorinated porphyrins through scrambling: Characterization and quantitative crystal structure analysis. *J. Fluorine Chem.* **2015**, 170, 10-16.
- (132) Goovaerts, E. Optically detected magnetic resonance (ODMR). *eMagRes* **2017**, 6 (2), 343-358.
- (133) Carbonera, D. Optically detected magnetic resonance (ODMR) of photoexcited triplet states. *Photosynthesis Research* **2009**, 102 (2), 403.
- (134) Koelsch, C. F. Syntheses with triarylvinylmagnesium bromides, α,γ -Bisdiphenylene- β -phenylallyl, a stable free radical. *J. Am. Chem. Soc.* **1957**, 79, 4439-4441.
- (135) Watanabe, K.; Yamauchi, J.; Ohya-Nishiguchi, H.; Deguchi, Y.; Takaki, H. Abnormal hyperfine splitting in the ESR spectra of $\alpha,\alpha,\gamma,\gamma$ -tetraphenylallyl-type organic stable free radicals. *Bull. Chem. Soc. Jap.* **1972**, 45 (2), 371-375.
- (136) Wasielewski, M. R.; O'Neil, M. P.; Lykke, K. R.; Pellin, M. J.; Gruen, D. M. Triplet states of fullerenes C60 and C70. Electron paramagnetic resonance spectra, photophysics, and electronic structures. *J. Am. Chem. Soc.* **1991**, 113 (7), 2774-2776.
- (137) Maggini, M.; Scorrano, G.; Prato, M. Addition of azomethine ylides to C60: synthesis, characterization, and functionalization of fullerene pyrrolidines. *J. Am. Chem. Soc.* **1993**, 115 (21), 9798-9799.
- (138) Guldi, D. M.; Prato, M. Excited-state properties of C60 fullerene derivatives. *Acc. Chem. Res.* **2000**, 33 (10), 695-703.

- (139) Leach, S.; Vervloet, M.; Despres, A.; Breheret, E.; Hare, J. P.; Dennis, T. J.; Kroto, H. W.; Taylor, R.; Walton, D. R. M. Electronic spectra and transitions of the fullerene C₆₀. *Chem. Phys.* **1992**, *160* (3), 451-466.
- (140) Thomas, K. G.; Biju, V.; George, M. V.; Guldi, D. M.; Kamat, P. V. Excited-State Interactions in Pyrrolidinofullerenes. *J. Phys. Chem. A* **1998**, *102* (28), 5341-5348.
- (141) Ebbesen, T. W.; Tanigaki, K.; Kuroshima, S. Excited-state properties of the carbon sixty-atom molecule. *Chem. Phys. Lett.* **1991**, *181* (6), 501-504.
- (142) Dimitrijevic, N. M.; Kamat, P. V. Triplet excited state behavior of fullerenes: pulse radiolysis and laser flash photolysis of fullerenes (C₆₀ and C₇₀) in benzene. *J. Phys. Chem.* **1992**, *96* (12), 4811-4814.
- (143) Colvin, M. T.; Giacobbe, E. M.; Cohen, B.; Miura, T.; Scott, A. M.; Wasielewski, M. R. Competitive Electron Transfer and Enhanced Intersystem Crossing in Photoexcited Covalent TEMPO-Perylene-3,4:9,10-bis(dicarboximide) Dyads: Unusual Spin Polarization Resulting from the Radical-Triplet Interaction. *J. Phys. Chem. A* **2010**, *114* (4), 1741-1748.
- (144) Yeganeh, S.; Wasielewski, M. R.; Ratner, M. A. Enhanced Intersystem Crossing in Three-Spin Systems: A Perturbation Theory Treatment. *J. Am. Chem. Soc.* **2009**, *131* (6), 2268-2273.
- (145) Grzegorzec, N.; Mao, H.; Michel, P.; Junge, M. J.; Lorenzo, E. R.; Young, R. M.; Krzyaniak, M. D.; Wasielewski, M. R.; Chernick, E. T. Metalated Porphyrin Stable Free Radicals: Exploration of Electron Spin Communication and Dynamics. *J Phys Chem A* **2020**, *124* (30), 6168-6176.
- (146) Meyer, V.; Eaton, S. S.; Eaton, G. R. X-band Electron Spin Relaxation Times for Four Aromatic Radicals in Fluid Solution and Comparison with Other Organic Radicals. *Appl. Magn. Reson.* **2014**, *45* (10), 993-1007.

- (147) Blaettler, C.; Jent, F.; Paul, H. A novel radical-triplet pair mechanism for chemically induced electron polarization (CIDEP) of free radicals in solution. *Chem. Phys. Lett.* **1990**, *166* (4), 375-380.
- (148) Skiebe, A.; Hirsch, A.; Klos, H.; Gotschy, B. [DBU]C60. Spin pairing in a fullerene salt. *Chem. Phys. Lett.* **1994**, *220* (1-2), 138-140.
- (149) Klos, H.; Rystau, I.; Schuetz, W.; Gotschy, B.; Skiebe, A.; Hirsch, A. Doping of C60 with tertiary amines: TDAE, DBU, DBN. A comparative study. *Chem. Phys. Lett.* **1994**, *224* (3-4), 333-337.
- (150) Rugg, B. K.; Phelan, B. T.; Horwitz, N. E.; Young, R. M.; Krzyaniak, M. D.; Ratner, M. A.; Wasielewski, M. R. Spin-Selective Photoreduction of a Stable Radical within a Covalent Donor–Acceptor–Radical Triad. *Journal of the American Chemical Society* **2017**, *139* (44), 15660-15663.
- (151) Rugg, B. K.; Krzyaniak, M. D.; Phelan, B. T.; Ratner, M. A.; Young, R. M.; Wasielewski, M. R. Photodriven quantum teleportation of an electron spin state in a covalent donor-acceptor-radical system. *Nat. Chem.* **2019**, *11* (11), 981-986.
- (152) Thurnauer, M. C.; Norris, J. R. An electron spin echo phase shift observed in photosynthetic algae : Possible evidence for dynamic radical pair interactions. *Chemical Physics Letters* **1980**, *76*, 557-561.
- (153) Chen, H.-F.; Gardner, D. M.; Carmieli, R.; Wasielewski, M. R. Controlling the orientation of spin-correlated radical pairs by covalent linkage to nanoporous anodic aluminum oxide membranes. *Chemical Communications (Cambridge, United Kingdom)* **2013**, *49* (77), 8614-8616.

- (154) Nelson, J. N.; Zhang, J.; Zhou, J.; Rugg, B. K.; Krzyaniak, M. D.; Wasielewski, M. R. CNOT gate operation on a photogenerated molecular electron spin-qubit pair. *Journal of Chemical Physics* **2020**, *152* (1), 014503/014501-014503/014507.
- (155) Bayliss, S. L.; Laorenza, D. W.; Mintun, P. J.; Kovos, B. D.; Freedman, D. E.; Awschalom, D. D. Optically addressable molecular spins for quantum information processing. *Science* **2020**, *370* (6522), 1309-1312.
- (156) Mao, H.; Young, R. M.; Krzyaniak, M. D.; Wasielewski, M. R. Controlling the Dynamics of Three Electron Spin Qubits in a Donor-Acceptor-Radical Molecule Using Dielectric Environment Changes. *J. Phys. Chem. Lett.* **2021**, *12* (9), 2213-2218.
- (157) Bowman, M. K.; Maryasov, A. G. The Direct Dimension in Pulse EPR. *Applied Magnetic Resonance* **2021**, *52* (8), 1041-1062.
- (158) Harvey, S. M.; Wasielewski, M. R. Photogenerated Spin-Correlated Radical Pairs: From Photosynthetic Energy Transduction to Quantum Information Science. *J Am Chem Soc* **2021**, *143* (38), 15508-15529.
- (159) Tang, J.; Thurnauer, M. C.; Norris, J. R. Electron spin echo envelope modulation due to exchange and dipolar interactions in a spin-correlated radical pair. *Chem. Phys. Lett.* **1994**, *219* (3-4), 283-290.
- (160) Volkov, M. Y.; Salikhov, K. M. Pulse Protocols for Quantum Computing with Electron Spins as Qubits. *Applied Magnetic Resonance* **2011**, *41* (2), 145-154.

Curriculum Vitae

Haochuan Mao

Northwestern University

Center for Molecular Quantum Transduction (CMQT)

Institute for Sustainability and Energy at Northwestern (ISEN)

2145 Sheridan Road, Evanston, IL 60208

Tel: +1(773)-961-6447

Email: Haochuanmao2022@u.northwestern.edu

EDUCATION

2017 **B.Sc., Chemistry**

Nanjing University, Nanjing, Jiangsu, P.R.China

Thesis: Synthesis and Characterization of Boron-Centered Diradicals and Triradicals

RESEARCH EXPERIENCE

2017 - present **Northwestern University**, Evanston, Illinois, United States

Graduate Student

Advisor: **Prof. Michael R. Wasielewski**

2014 – 2017 **Nanjing University**, Nanjing, Jiangsu, P.R.China

Undergraduate Student

Advisor: **Prof. Xinping Wang**

Summer 2016 **The University of Sydney**, Camperdown, NSW, Australia

Visiting Student

Advisor: **Prof. Matthew H. Todd**

PUBLICATIONS

Mao, H.; Young, R. M.; Krzyaniak, M. D.; Wasielewski, M. R., Controlling the Dynamics of Three Electron Spin Qubits in a Donor-Acceptor-Radical Molecule Using Dielectric Environment Changes. *Journal of Physical Chemistry Letters* **2021**, *12* (9), 2213-2218.

Jiao, Y.; Dordevic, L.; **Mao, H.;** Young, R. M.; Jaynes, T.; Chen, H.; Qiu, Y.; Cai, K.; Zhang, L.; Chen, X. Y.; Feng, Y.; Wasielewski, M. R.; Stupp, S. I.; Stoddart, J. F., A Donor-Acceptor [2]Catenane for Visible Light Photocatalysis. *Journal of the American Chemical Society* **2021**, *143* (21), 8000-8010.

Chen, X. Y.; **Mao, H.;** Feng, Y.; Cai, K.; Shen, D.; Wu, H.; Zhang, L.; Zhao, X.; Chen, H.; Song, B.; Jiao, Y.; Wu, Y.; Stern, C. L.; Wasielewski, M. R.; Stoddart, J. F., Radically Enhanced Dual Recognition. *Angewandte Chemie International Edition* **2021**, *60* (48), 25454-25462.

Guo, Q. H.; Zhou, J.; **Mao, H.;** Qiu, Y.; Nguyen, M. T.; Feng, Y.; Liang, J.; Shen, D.; Li, P.; Liu, Z.; Wasielewski, M. R.; Stoddart, J. F., TetrazineBox: A Structurally Transformative Toolbox. *Journal of the American Chemical Society* **2020**, *142* (11), 5419-5428.

Grzegorzec, N. *; **Mao, H. *;** Michel, P.; Junge, M. J.; Lorenzo, E. R.; Young, R. M.; Krzyaniak, M. D.; Wasielewski, M. R.; Chernick, E. T., Metalated Porphyrin Stable Free Radicals: Exploration of Electron Spin Communication and Dynamics. *The Journal of Physical Chemistry A* **2020**, *124* (30), 6168-6176.

Cao, W.; McCallum, N. C.; Ni, Q. Z.; Li, W.; Boyce, H.; **Mao, H.;** Zhou, X.; Sun, H.; Thompson, M. P.; Battistella, C.; Wasielewski, M. R.; Dhinojwala, A.; Shawkey, M. D.; Burkart, M. D.; Wang, Z.; Gianneschi, N. C., Selenomelanin: An Abiotic Selenium Analogue of Pheomelanin. *Journal of the American Chemical Society* **2020**, *142* (29), 12802-12810.

Cao, W.; Mantanona, A. J.; **Mao, H.;** McCallum, N. C.; Jiao, Y.; Battistella, C.; Caponetti, V.; Zang, N. Z.; Thompson, M. P.; Montalti, M.; Stoddart, J. F.; Wasielewski, M. R.; Rinehart, J. D.; Gianneschi, N. C., Radical-Enriched Artificial Melanin. *Chemistry of Materials* **2020**, *32* (13), 5759-5767.

Cai, K.; **Mao, H.;** Liu, W. G.; Qiu, Y.; Shi, Y.; Zhang, L.; Shen, D.; Chen, H.; Jiao, Y.; Wu, H.; Liu, Z.; Feng, Y.; Stern, C. L.; Wasielewski, M. R.; Goddard, W. A., 3rd; Stoddart, J. F., Highly Stable Organic Bisradicals Protected by Mechanical Bonds. *Journal of the American Chemical Society* **2020**, *142* (15), 7190-7197.

Wang, L.; Fang, Y.; **Mao, H.;** Qu, Y.; Zuo, J.; Zhang, Z.; Tan, G.; Wang, X., An Isolable Diboron-Centered Diradical with a Triplet Ground State. *Chemistry—A European Journal* **2017**, *23* (28), 6930-6936.

REFERENCES**Prof. Michael R. Wasielewski**

Department of Chemistry, Northwestern University

Tel: +1(847)-467-1423

Email: m-wasielewski@northwestern.edu

Prof. J. Fraser Stoddart

Department of Chemistry, Northwestern University

Tel: +1(847)-491-3793

Email: stoddart@northwestern.edu